University College London

Department of Electronic and Electrical Engineering

PhD Thesis

Computational Analysis and Fabrication of Metasurfaces for Applications in Linear and Nonlinear Optics

Student:
Daniel Timbrell

Supervisor:
Prof. Nicolae Panoiu
Prof. Paul Warburton

May 2018

I, Daniel Timbrell, confirm that the work presented in this thesis is my own. Where information has been derived from other sources, I confirm that this has been indicated in the work.

Abstract

We present theoretical and computational findings regarding second harmonic generation within plasmonic and all-dielectric metamaterials. An in-depth analysis of the surface and bulk contributions to the second harmonic signal in centrosymmetric meta-atoms is undertaken, whereby it is found that a common assumption of neglecting the bulk portion of dielectric structures is unjustified.

An all-dielectric metamaterial unit cell is also presented. The power radiated by the electromagnetic dipoles are calculated alongside the electric quadrupole for both the linear and nonlinear regime for a $LiTaO_3$ meta-atom. A nonlinear resonance that is engendered by the linear toroidal dipole is also shown to be toroidal in nature.

A structure consisting of gold split ring resonators embedded in a dielectric is designed to have a strong nonlinear toroidal dipole. The optical spectra of the metamaterial array are simulated, with the powers radiated by the electric, magnetic and toroidal dipoles being compared at the second harmonic, whereby the toroidal dipole dominates.

In a separate investigation, we analyse computationally and experimentally optical meta-atoms that generate two distinct resonances in frequency-space for applications in laser protection. Different polarisation-dependent designs are incorporated to produce a polarisation-independent meta-atom. The optical response of this cross-shaped structure is calculated and compared with a fabricated structure. The simulation and fabrication process is analysed in detail. Additional to this investigation, a notch filter is designed through using DiffractMOD's MOST optimizer and subsequently manufactured in the London Centre for Nanotechnology. The transmission coefficients are again measured.

Furthermore, a Bragg/metamaterial composite is briefly introduced and analysed. This new composite is intended to improve performance on the previous transmission notch filter by having the metamaterial effectively act as a substitute for a number of layers of the Bragg filter.

Acknowledgements

First and foremost, I will always be indebted to Prof. Nicolae C. Panoiu for his guidance in dealing with my laboratory shenanigans and his infinite patience regarding my paper submissions. This thesis would certainly not exist were it not for his tutelage, dedication and genuine care.

To my secondary supervisor, Prof. Paul Warburton, praise must also be given. Many a time I came to a roadblock in my fabrication procedures and many a time he insightfully pointed me in the right direction. I must also thank him for his comments in my transfer viva, along with Dr. Hidekazu Kurebayashi.

Both Andrew Hurst and Andrew Wood were both incredibly helpful in steering my fabrication efforts toward something manufacturable.

The financial support of EPSRC and Qioptiq enabled me to shelter and feed myself in London, by no means an easy feat! I am forever grateful.

I would like to thank everyone in Nicolae's group for their help and friendship, Dr. Jian Wei You, Dr. Jie You, Dr. Martin Weismann, Dr. Abiola Oladipo, Dr. Spyros Lavdas, Dr. Ahmed Al-Jarro, and Qun Ren. Jian and Martin in particular were always full of ideas when I needed help. Dr. Nuno Braz also helped me tremendously throughout the entire PhD.

Helen Moore supported me like no other throughout some very tough times and I cannot thank her enough.

Finally, to all my friends and family that have shown support and love: from the bottom of my heart, thank you.

Journal articles related to the PhD dissertation

D. Timbrell, J. W. You, Y. S. Kivshar, and N. C. Panoiu, "A comparative analysis of surface and bulk contributions to second-harmonic generation in centrosymmetric nanoparticles", Sci. Rep. **8**, 3586 (2018).

D. Timbrell, J. W. You, and N. C. Panoiu, "Toroidal-dipole second-harmonic generation from a toroidal metasurface", Opt. Lett. (In preparation).

Conference contributions related to the PhD dissertation

1. D. Timbrell, N. V. S. Braz, P. A. Warburton, and N. C. Panoiu, "Resonantly Enhanced Nonlinear Toroidal Moments in Plasmonic Metamaterials", PIERS, Prague, (2015).

2. D. Timbrell, M. Weismann, N. V. S. Braz, P. A. Warburton, and N. C. Panoiu, "Toroidal dipoles generated in nonlinear plasmonic metamaterials", Metamaterials 2015, (2015).

3. D. Timbrell and N. C. Panoiu "Second-harmonic generation from toroidal moments of all-dielectric metasurfaces", META 2016, Malaga, (2016).

4. D. Timbrell and N. C. Panoiu "Second-harmonic generation from toroidal optical modes of dielectric nano-structures", Photon 16, Leeds, (2016).

5. D. Timbrell, J. W. You, Y. S. Kivshar, and N. C. Panoiu, "Surface versus bulk contribution to second-harmonic generation in centrosymmetric meta-atoms", PIERS, Saint Petersburg, (2017).

6. D. Timbrell, J. W. You, Y. S. Kivshar, N. C. Panoiu, "Comparison of surface and bulk contributions to SHG in meta-atoms made of centrosymmetric materials", Quantum Electronics and Laser Science Fundamental Science, San Jose, California, (2017)

List of Abbreviations

ACS	Absorption cross section
Au	Gold
c	Speed of light in vacuum (299,792.458 km/s)
CAD	Computer-aided design
CST	Computer simulation technology studio suite
EBL	Electron beam lithography
FDTD	Finite difference time domain
FIT	Finite integration technique
FF	Fundamental frequency
FTIR	Fourier Transform Infrared Spectroscopy
FWHM	Full width at half maximum
HSQ	Hydrogen silsesquioxane
$LiTaO_3$	Lithium tantalate
NTFF	Near-to-far field
PMMA	Poly(methyl methacrylate)
RCS	Radar cross section
RCWA	Rigorous coupled-wave analysis
SH	Second harmonic
SHG	Second harmonic generation
SEM	Scanning electron microscope
Si	Silicon
SRR	Split ring resonator

XOR	Exclusively 'OR' (Boolean)
ϵ_0	Electric permittivity of vacuum (8.854×10^{-12} F/m)
γ	Collision rate of electrons
$\chi^{(2)}$	Nonlinear electric susceptibility tensor
ω	Fundamental frequency in radians
Ω	Second harmonic frequency in radians

Contents

List of Figures

Chapter 1

Introduction

The role which electromagnetic waves play in aiding mankind cannot be overstated. From medical instruments to global communication to surveillance equipment to energy sources, the applications arising from light-manipulation have truly been revolutionary. The desire, therefore, to master light, to completely control every possible parameter of its constitution, is patently justified. So ingrained in our day-to-day lives are these items, one resounding fact holds true: the greater our understanding of light, the higher the quality of mankind's existence.

Building upon the universal importance of light-control, therefore, this thesis sets out to investigate and achieve two main goals on influencing light, the first of which can be summarised with the following question: supposing we desire to block two mid-IR frequencies of light, ω_1 and ω_2, as narrowly as possible, can a metamaterial be designed to easily achieve this, and what are - if any - the limitations?

The second objective is to design and analyse meta-atoms that cause strong nonlinear optical signals. Specifically, there are two main studies within this objective: Firstly, are current assumptions of the negligibility of bulk centrosymmetric media justified? Secondly, can strong nonlinear toroidal dipoles be excited within plasmonic and dielectric metamaterials? While our first aim sets out to engineer a light, inexpensive multi-functional laser-protection product, the second looks to the world of the theoretical for the prospect of new physics.

In 1880, Alexander Graham Bell and Sumner Tainter reported their invention of the photophone to the American Association for the Advancement of Science [1]. By using the human voice as a means of varying the intensity of an electromagnetic source focused on a selenium receiver, the receiver could, due to the selenium's changing conductivity, transmit the words uttered by the speaker. Bell and Tainter themselves utilized this invention, communicating at a distance of 213m [2]. Thus the first demonstration of wireless communication was achieved. Today, the use of wireless communication at microwave

frequencies has permeated into nearly every culture. Mobile phones, tablets and most computers contain small transmitters and receivers for almost instant communication with anyone, even in outer space.

Even when hardware is required, the utilization of electromagnetic waves is prevalent due to the work of Schultz and Keck, who in 1970 created an optical fibre with surprisingly low losses [3]. A quote from the paper by F. P. Kapron et al. encapsulates the significance of their achievement: "The preceding measurements show that waveguides can be constructed which have radiation losses very close to the intrinsic material scattering loss" [4]. Henceforth, electromagnetic waves became one of the foundations on which society is based.

The state of electromagnetic affairs could not be how it is today were it not for the invention of the laser, first experimentally demonstrated in 1960 by T. H. Maiman [5]. Light amplification by stimulated emission of radiation is a process whereby a narrow beam of light consisting of several excited modes centered around a particular wavelength is generated. This beam is *coherent*, meaning there is a fixed phase relationship between the electromagnetic field values temporally and/or spatially. The unusually-high intensity of laser light meant that a new probe with which to study materials had been created. It is therefore unsurprising that during the 1960s numerous reports of previously-unseen optical activities in materials were published, including, among others, second harmonic generation [6], third harmonic generation [7] and optical parametric oscillation [8].

Also published in this fruitful decade was the seed which would blossom into the entire field of metamaterials: namely, the idea of negative refraction. First proposed by Veselago in 1968 [9], he suggested that if a medium were to have simultaneously negative values for the real part of the electric permittivity and magnetic permeability, its interaction with an incoming electromagnetic wave would cause the wave to be refracted to the *same* side of the normal, as contrary to our every-day experiences. While it was well-known at the time [10] that the noble metals' permittivity functions were negative for a wide range of frequencies, figuring out how to control a material's magnetic response to external radiation was a hurdle that would not be cleared until near the end of the millenium.

In 1999 Sir John Pendry of Imperial College London dramatically increased the ability to control light when he designed and demonstrated that a split ring resonator is a structure with a profound magnetic response [11]. The ring, with its natural inductance due to its metallic nature, is split in order to imbue it with a capacitance, in effect becoming a resonant LC-circuit. By tuning the structural parameters of the unit cell, this resonance causes the magnetic permeability to become negative. A year later, a material with a negative refractive index was fabricated [12]. This unit-cell is henceforth known as a meta-atom, the basis of a metamaterial; a material designed to have properties

which are not found within nature. Since this monumental work, split ring resonators have been utilized for a vast array of metamaterial applications, including perfect light absorbers [13,14], narrow-band resonators [15], and for generating magnetic responses at optical frequencies [16, 17]. The ground-breaking work of Pendry et al. have made the split ring resonator one of the most common metamaterial units.

The field of metamaterials has garnered significant attention since it was proposed that they could be responsible for the world's first invisibility cloak. By considering the permittivity and permeability functions of the metamaterial as anisotropic tensors, it is possible to create a metamaterial which steers the incoming light. This has been achieved with split ring resonators at microwaves for a specific frequency [18], but the frequency-dependence and shape of these functions means that an invisibility cloak designed for even a small range of frequencies is currently not feasible without additional gain media, electromagnetically induced transparency or chirality.

Metals are not a required basis for a metamaterial structure [19]. Rather than relying on a current generated by the metal's free electrons, dielectric structures can be utilized whereby the nature of their excited displacement currents are responsible for their electromagnetic responses.

Metamaterials have enabled the toroidal multipole moments to be analysed in significant detail. This electromagnetic phenomenon, first discovered in 1957 by Zel'dovich [20] and subsequently linked to violations of Newton's Third Law [21] and atomic parity non-conservation [22], is often over-shadowed by the electric and magnetic multipole moments, due to their comparative strength. The power radiated by the toroidal moments can deliberately be exacerbated through considerations of a metamaterial unit cell. Since the first toroidal metamaterial was fabricated in 2010 [23], toroidal moments have been measured at microwaves [24–26] and at optical frequencies [27–29], and have been shown to be able to yield extremely high quality factors [26], and pronounced chiral activity [30]. Systems whereby the toroidal field cancels with the electric field are known as anapole moments. These non-radiating configurations have been put forward as an explanation for dark matter [31], and have also been produced in toroidal metamaterials [32] containing no metallic elements.

Although just a handful of unique phenomena engendered by metamaterials have been mentioned, it is clear that they have forever changed the potential of future technology. In recent years, companies specialising in metamaterial products have been established, such as Echodyne [33], Kymeta [34], and Metamaterial Technologies [35]. Their services include visor-protectors, increasing the efficiency of solar panel absorption, and scanning arrays for radar applications. In order to help produce metamaterial antennae which can acquire, steer and lock any beam to a satellite, Kymeta have recently been awarded 62

million dollars [36]. This number alone speaks volumes of how sought-after the promises of metamaterials are.

The outline of this thesis is as follows. Chapter 2 describes the main workings of electromagnetism and plasmonics, including Maxwell's equations, the derivation of the damped permittivity functions, and the functions of second harmonic generation. The fundamentals of optical metamaterials are then analysed, with a number of applications being explained. Investigations into how to host a toroidal moment within a metamaterial are also undertaken. The range of software packages and computational methods that were utilized throughout this thesis, including how to simulate and calculate the relevant structural responses at the fundamental frequency and second harmonic within plasmonic and all-dielectric metamaterials are the subjects of Chapter 3. Chapter 4 discusses in detail the differences between surface and bulk contributions to the second harmonic signal in both plasmonic and all-dielectric centrosymmetric meta-atoms. A strong nonlinear toroidal dipole generated by a linear toroidal resonance in a $LiTaO_3$ meta-atom is studied in Chapter 5. The details of metamaterial fabrication are delineated in Chapter 6 along with analysis of the optical measurements of these fabricated metamaterials. Finally, in Chapter 7 we sumarize the main results of our work and present some future perspectives.

Bibliography

[1] N Jones, "First 'Radio' Built by San Diego Resident Partner of Inventor of Telephone. Keeps Notebook of Experiences With Bell", San Diego Evening Tribune **4**, (1937).

[2] S Tainter and A. G. Bell, "Selenium and the photophone", Nature **22**, 500-503 (1880).

[3] J. Hecht, *City of Light: The Story of Fiber Optics* (Oxford University Press, 1999).

[4] F. Kapron, D. Keck, and R. Maurer, "Radiation losses in glass optical waveguides", Appl. Phys. Lett. **17**, 423-425 (1970).

[5] T. H. Maiman, "Stimulated optical radiation in ruby", Nature **187**, 493494 (1960).

[6] P. A. Franken, A. E. Hill, C. W. Peters, and G. Weinreich, "Generation of optical harmonics", Phys. Rev. Lett. **7**, 118-120 (1961).

[7] G. H. New and J. F. Ward, "Optical third-harmonic generation in gases", Phys. Rev. Lett. **19**, 556-559 (1967).

[8] J. A. Giordmaine, and R. C. Miller, "Tunable coherent parametric oscillation in $LiNbO_3$ at optical frequencies", Phys. Rev. Lett. **14**, 973-976 (1965)

[9] V. G. Veselago, "The electrodynamics of substances with simultaneously negative values of ϵ and μ", Sov. Phys. Usp. **10**, 509-514 (1968).

[10] R. L. Olmon, B. Slovick, T. W. Johnson, D. Shelton, S.-H. Oh, G. D. Boreman and M. B. Raschke, "Optical dielectric function of gold", Phys. Rev. B **86**, 235147 (2012).

[11] J. B. Pendry, A. J. Holden, D. J. Robbins, and W. J. Stewart, "Magnetism from conductors and enhanced nonlinear phenomena", IEEE Transactions on Microwave Theory and Techniques **47**, 2075-2084 (1990).

[12] R. A. Shelby, D. R. Smith, and S. Schultz,"Experimental verification of a negative index of refraction", Science **292**, 77-79 (2001).

[13] N. I. Landy, S. Sajuyigbe, J. J. Mock, and D. R. Smith, and W. J. Padilla, "Perfect metamaterial absorber", Phys. Rev. Lett. 207402, **100** (2008).

[14] X. Liu, T. Starr, A. F. Starr, and W. J. Padilla, "Infrared spatial and frequency selective metamaterial with near-unity absorbance", Phys. Rev. Lett. **104**, 207403 (2010).

[15] B. Wang, Z. Xie, S. Feng, B. Zhang, and Y. Zhang, "Ultrahigh Q-factor and figure of merit Fano metamaterial based on dark ring magnetic mode", Optics Communications **335**, 60-64 (2015).

[16] M. W. Klein, C. Enkrich, M. Wegener, C. M. Soukoulis, and S. Linden, "Single-slit split-ring resonators at optical frequencies: limits of size scaling", Opt. Lett. **31**, 1259-1261 (2006).

[17] T. D. Corrigan, P. W. Kolb, A. B. Sushkov, H. D. Drew, D. C. Schmadel and R. J. Phaneuf, "Optical plasmonic resonances in split-ring resonator structures: an improved LC model", Opt. Exp. **16**, 19850-19864 (2008).

[18] W. Cai and V. Shalaev, *Optical Metamaterials. Fundamentals and Applications* (Springer US, 2009)

[19] A. A. Basharin, M. Kafesaki, E. N. Economou, C. M. Soukoulis, V. A. Fedotov, V. Savinov, and N. I. Zheludev, "Dielectric metamaterials with toroidal dipolar response", Phys. Rev. X **5**, 011036 (2015).

[20] Y. B. Zel'dovich, Zh. Eksp. Teor. Fiz. **33**, 1531 (1957) [Sov. Phys.JETP 6, 1184 (1958)].

[21] G. N. Afanasiev, "Simplest sources of electromagnetic fields as a tool for testing the reciprocity-like theorems", Sci. Rep. **3**, 539-559 (2013).

[22] C. S. Wood, S. C. Bennett, D. Cho, B. P. Masterson, J. L. Roberts, C. E. Tanner, and C. E. Wieman, "Measurement of parity nonconservation and an anapole moment in cesium", Science **275**, 1759-1763 (1997).

[23] K. Marinov, A. D. Boardman, V. A. Fedotov, and N. I. Zheludev, "Toroidal metamaterial", New Journal of Physics **9**, 324-202 (2007).

[24] Y. Fan, Z. Wei, H. Li, H. Chen, and C. M. Soukoulis, "Low-loss and high-Q planar metamaterial with toroidal moment", Phys. Rev. B **87**, 115417 (2013).

[25] Z. Dong, P. Ni, J. Zhu, X. Yin, and X. Zhang, "Toroidal dipole response in a multifold double-ring metamaterial", Opt. Exp. **20**, 13065-13070 (2012).

[26] V. A. Fedotov, A. V. Rogacheva, V. Savinov, D. P. Tsai, and N. I. Zheludev, "Resonant transparency and non-trivial non-radiating excitations in toroidal metamaterials", Sci. Rep. **3**, 2967 (2013).

[27] B. Ögüt, N. Talebi, R. Vogelgesang, W. Sigle, and P. A. van Aken, "Toroidal plasmonic eigenmodes in oligomer nanocavities for the visible", Nano Lett. **12**, 52395244 (2012).

[28] Y. Huang, W. T. Chen, P. C. Wu, V. Fedotov, V. Savinov, Y. Z. Ho, Y. Chau, N. I. Zheludev, and D. P. Tsai, "Design of plasmonic toroidal metamaterials at optical frequencies", Opt. Exp. **20**, 1760-1768 (2012),

[29] Z. Dong, J. Zhu, J. Rho, J. Li, C. Lu, X. Yin, and X. Zhang, "Optical toroidal dipolar response by an asymmetric double-bar metamaterial", Appl. Phys. Lett. **101**, 144105 (2012).

[30] N. Papasimakis, V. A. Fedotov, K. Marinov, and N. I. Zheludev, "Gyrotropy of a metamolecule: wire on a torus", Phys. Rev. Lett. **103**, 093901 (2009).

[31] C. M. Ho, and R. J. Scherrer, "Anapole dark matter", Phys. Lett. B **722**, 341-346 (2013).

[32] A. E. Miroshnichenko, A. B. Evlyukhin, Y. F. Yu, R. M. Bakker, A. Chipouline, A. I. Kuznetsov, B. Luk'yanchuk, B. N. Chichkov, and Y. S. Kivshar, "Nonradiating anapole modes in dielectric nanoparticles", Nat. Comm. **6**, 8069-8076 (2015).

[33] Echodyne, [Accessed September 16th 2018]; Available from: https://echodyne.com/

[34] Kymeta, [Accessed September 16th 2018]; Available from: https://kymetacorp.com/

[35] Metamaterial Technologies Inc., [Accessed September 16th 2018]; Available from: https://metamaterial.com/

[36] M. J. de la Merced, "Kymeta Raises 62 Million in Investment Led by Bill Gates", The New York Times, (2016).

Chapter 2

Background

2.1 Introduction

This chapter lays the fundamental building blocks that will be built upon in subsequent chapters to explain the physical phenomena arising from our metamaterial interactions. We begin with a discussion about Maxwell's equations, which neatly contain the laws of light. The refractive index is also introduced as one of the most useful parameters to predict a material's behaviour. In order to explain the full behaviour of the metals analysed throughout this thesis, the topic of plasmonics is introduced to explain the role of electrons in generating the linear physical effects. The theoretical discussion then moves onto nonlinear physics, which is a heavily utilised optical interaction throughout this work. The physics of both centrosymmetric and non-centrosymmetric crystals are delineated in detail.

Metamaterials are then introduced, with an in-depth description of both plasmonic and all-dielectric metamaterials being given. Many examples of metamaterials are shown and the physics of their applications is discussed. One crucial example for my thesis is the introduction of nonlinear physics and its link with metamaterials. Furthermore, the multipole expansion is explained to show the origin of the separate multipole moments that become a staple of my work. Finally, the notion of combining metamaterials with Bragg filters to form an optical composite is introduced, to show that metamaterials have the potential to reduce the number of required Bragg layers.

2.2 Maxwell's Equations

As the phenomena of classical electromagnetism are encapsulated by Maxwell's equations, it would be inaccurate to begin this chapter without immediately introducing them,

written here in S.I. units:

$$\nabla \cdot \mathbf{E} = \frac{\rho}{\epsilon_0} \tag{2.1a}$$

$$\nabla \cdot \mathbf{B} = 0 \tag{2.1b}$$

$$\nabla \times \mathbf{E} = -\frac{\partial \mathbf{B}}{\partial \mathrm{t}} \tag{2.1c}$$

$$\nabla \times \mathbf{H} = \mathbf{J} + \frac{\partial \mathbf{D}}{\partial \mathrm{t}} \tag{2.1d}$$

This final form of the equations, written without potentials, was first derived by Oliver Heaviside [1]. These four equations, known individually as: (a) Gauss's Law, (b) Gauss's Law for Magnetism, (c) Faraday's Law, and (d) Maxwell-Ampère Law, describe how the charge (ρ) and current densities ($\mathbf{J}$) are the sources of the electric field, $\mathbf{E}$, and the magnetic field, $\mathbf{H}$, where:

$$\mathbf{D} = \epsilon_0 \mathbf{E} + \mathbf{P} = \epsilon_0 (1 + \chi_\mathrm{e}) \mathbf{E} = \epsilon_0 \epsilon_\mathrm{r} \mathbf{E} \tag{2.2a}$$

$$\mathbf{B} = \mu_0 \mathbf{H} + \mathbf{M} = \mu_0 (1 + \chi_\mathrm{m}) \mathbf{H} = \mu_0 \mu_\mathrm{r} \mathbf{H} \tag{2.2b}$$

$\mathbf{P}$ and $\mathbf{M}$ are the polarization and magnetization of the medium respectively. In effect, these describe how strongly the medium reacts to the influence of electric and magnetic fields. In a vacuum, both polarization and magnetization are zero.

The relative permittivity and permeability, ϵ_r and μ_r respectively, are dependent upon the electric and magnetic susceptibility tensors, χ_e and χ_m. These tensors are analysed in more depth when we consider second harmonic generation, but it is worth noting that they are dependent upon the symmetry properties of the unit cell of the medium. ϵ_0 and μ_0 are the electric permittivity and magnetic permeability of free space respectively, which culminate in the definition of the speed of light *in vacuo*:

$$c = \frac{1}{\sqrt{\mu_0 \epsilon_0}} \tag{2.3}$$

The value adopted by the Fifteenth General Conference of Weights and Measures [2] is:

$$c = 299,792.458 \mathrm{km/s} \tag{2.4}$$

Ampère's Law without the current term and Faraday's Law can be combined to acquire an equation that describes the propagation of electromagnetic waves through free space:

$$(\nabla^2 + \mu \epsilon \omega^2) \mathbf{\Psi}(\mathbf{x}) = 0 \tag{2.5}$$

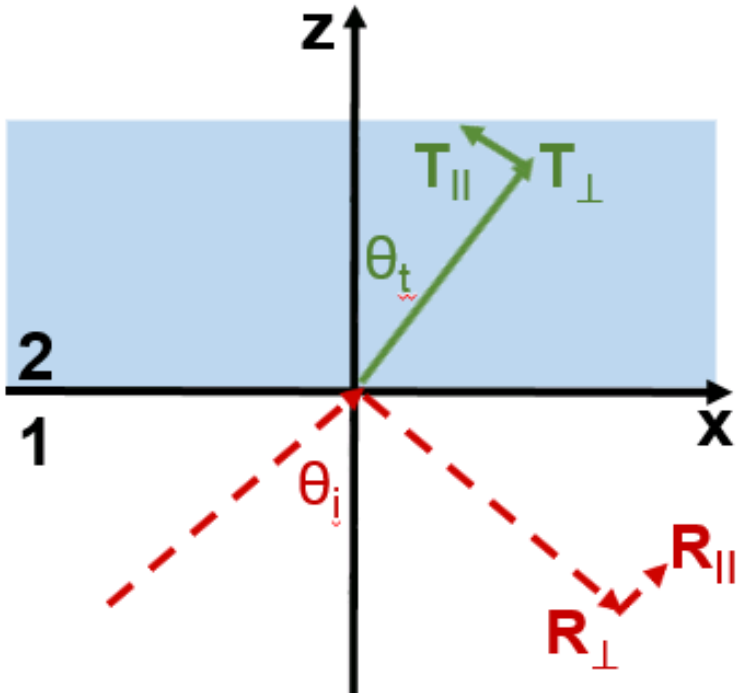

Figure 2.1: The physics of reflection and transmission. An electromagnetic wave is incident on an interface of a different material, giving rise to parallel ($X_{||}$) and perpendicular ($X_{\perp}$) components of the absorption, reflection and transmission coefficients. Here X can be any of R, T, and A. Also displayed are the angles of incidence (θ_i), reflection (θ_r) and transmission (θ_t). Adapted from [4].

Equation 2.5 is The Helmholtz wave equation, where $\Psi(\mathbf{x})$ represents either the **E**- or **B**-field. ω is the angular frequency of the light.

The direction and magnitude of the energy flow of the electromagnetic waves is encapsulated in the Poynting vector, first devised by John Henry Poynting in 1884 [3]. Explicitly, the time-averaged Poynting vector, **S**, is often used to incorporate the full length of the phase of the electromagnetic field, and is given by:

$$\mathbf{S} = \frac{1}{2}\mathbf{E} \times \mathbf{H}^* \tag{2.6}$$

where the asterisk denotes that the complex conjugate of the magnetic field is to be taken. An electromagnetic wave vector incident on an interface is often referred to as the wavevector, **k**, which naturally coincides with the direction of the Poynting vector. To see this, the reader can study the electromagnetic setups of Chapters 4 and 5 (Figures 4.1 and 5.1 repectively).

A mathematical tool that is of incredible importance within the realm of simulations (*cf.* Chapter 3) is the Fourier transform. Given the electric fields for all frequencies, one can switch between the frequency-domain and the time-domain *via* the following

equation:

$$\mathbf{E}(\mathbf{r},t) = \frac{1}{2\pi}\int_{-\infty}^{\infty}\mathbf{E}(\mathbf{r},\omega)e^{-i\omega t}\mathrm{d}\omega \tag{2.7}$$

A transverse plane wave, often utilised in the aforementioned simulations, is a solution of Equation 2.5 in the case where the medium through which the wave is propagated is a vacuum:

$$\mathbf{E}(\mathbf{r},t) = \mathbf{E}(\omega)e^{i(k\mathbf{n}\cdot\mathbf{r}-\omega t)} + \mathbf{E}^{*}(\omega)e^{-i(k\mathbf{n}\cdot\mathbf{r}-\omega t)} \tag{2.8}$$

The producers of all electromagnetic fields, the respective electric charge density and current density, ρ and $\mathbf{J}$, are bound to one another *via* the continuity equation:

$$g\frac{\partial\rho}{\partial t} + \nabla\cdot\mathbf{J} = 0 \tag{2.9}$$

This is an incredibly useful equation that is utilized many times throughout my work, as it allows a choice to be made regarding further calculations: the equations of interest can be rewritten so that they are wholly written in terms of either charge or current density distributions. It is often easier to consider entire electromagnetic systems just in terms of one parameter, as we shall particularly see in Chapters 3, 4, and 5.

Naturally, the electric and magnetic fields interact and influence a particle of charge q via the Lorentz force:

$$\mathbf{F} = \mathrm{q}(\mathbf{E} + \mathbf{v}\times\mathbf{B}) \tag{2.10}$$

where $\mathbf{F}$ is the force experienced by the particle traveling through an electromagnetic field. Hence the magnitude and direction of the charged particle's movement can be ascertained. We now move on to a more in-depth look at light-matter interactions that are relevant for my metamaterial work.

2.2.1 Index of Refraction

A material's response to external electromagnetic stimuli - whether it will be transmitted, reflected and/or absorbed, and the relevant percentages of each - is fully characterised by its complex-valued refractive index, n. For many optical metamaterial applications, it is therefore one of the most crucial parameters, as we will be designing materials to purposefully interact with light sources to, for example, transmit no light for certain wavelengths. It is important to understand the physical meaning of this parameter before a discussion of metamaterials can be undertaken. Figure 2.1 shows the physics of the problem. An incident light source with parallel and perpendicular components impinges on a medium with refractive index n.

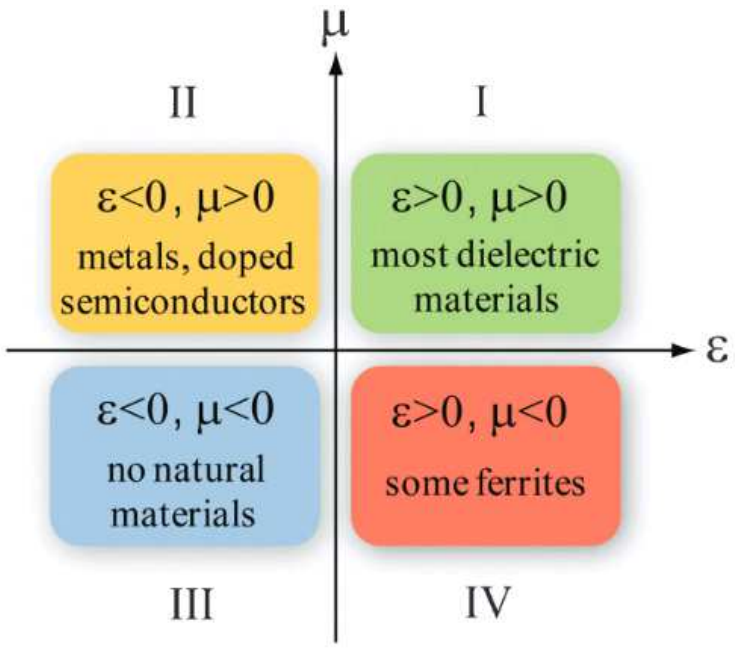

Figure 2.2: The possibilities of permittivity (ϵ) and permeability (μ) permutations. Each of the four quadrants leads to vastly different physics. Adapted from [5]. Within this thesis, we will focus on the upper-most quadrants.

It can be shown [4] that solving the above problem leads to the Fresnel formulae:

$$T_{\parallel} = \frac{2n_1 \cos\theta_i}{n_2 \cos\theta_i + n_1 \cos\theta_t} A_{\parallel} \tag{2.11a}$$

$$T_{\perp} = \frac{2n_1 \cos\theta_i}{n_1 \cos\theta_i + n_2 \cos\theta_t} A_{\perp} \tag{2.11b}$$

$$R_{\parallel} = \frac{n_2 \cos\theta_i - n_1 \cos\theta_t}{n_2 \cos\theta_i + n_1 \cos\theta_t} A_{\parallel} \tag{2.11c}$$

$$R_{\perp} = \frac{n_1 \cos\theta_i - n_2 \cos\theta_t}{n_1 \cos\theta_i + n_2 \cos\theta_t} A_{\perp} \tag{2.11d}$$

Equations 2.2a and 2.2b that we saw in the previous section come in handy here, as the electromagnetic nature of a medium can be regarded in terms of these frequency-dependent functions, where:

$$n(\omega) = n'(\omega) + ik''(\omega) = \sqrt{\epsilon(\omega)\mu(\omega)} \tag{2.12}$$

k″ is simply the imaginary part of the refractive index. When an electromagnetic wave traveling in a medium of refractive index n_1 impinges with an angle θ_1 on an interface of refractive index n_2, as in Figure 2.1, the extent to which the wave's direction is altered -

refracted - is expressed by Snell's Law, where θ_2 is the outgoing angle:

$$n_1 \sin\theta_1 = n_2 \sin\theta_2 \tag{2.13}$$

The origin of the refractive index is the microscopic dipoles present in the medium, which absorb the incoming light and consequently re-radiate it with a certain retardation. In almost all natural media, the magnetic permeability is equal to unity as the frequency approaches the optical band [5]. Physically, this means that the medium of interest does not have the physical capability of interacting with the incident magnetic field, as the magnetic dipoles inherent within the material cannot respond quickly enough to the oscillations of the magnetic field. Equation 2.12 therefore most often reduces more simply to:

$$n(\omega) = \sqrt{\epsilon(\omega)} \tag{2.14}$$

Indeed, throughout this work the parameter ϵ is of much greater importance than μ for this very reason. After some algebraic manipulation, the full relationship between the refractive index and the electric permittivity function can be delineated:

$$\epsilon' = Re(\epsilon) = n'^2 - k''^2 \tag{2.15a}$$

$$\epsilon'' = Im(\epsilon) = 2n'k'' \tag{2.15b}$$

$$n'^2 = [\epsilon' + \sqrt{\epsilon'^2 + \epsilon''^2}]/2 \tag{2.15c}$$

$$k''^2 = [-\epsilon' + \sqrt{\epsilon'^2 + \epsilon''^2}]/2 \tag{2.15d}$$

The role that the key components ϵ and μ play in electromagnetic phenomena is summarily depicted in Figure 2.2. Each of the four quadrants leads to vastly different physical regimes. The fourth quadrant, corresponding to magnetic plasmas, is outside of the research interests of this thesis due to the negligibility of permeability dispersion for the reasons previously mentioned.

So far, we have some simple building blocks for explaining electromagnetism; Maxwell's equations tell us how the electromagnetic fields influence the charges and currents and *vice versa*. Once the light meets with something substantial, we have the refractive index to rely upon, a parameter that plays a role across the entire fields of plasmonics, optics and photonics. It therefore resides at the core of all optical metamaterial considerations. When considering metals, the seemingly simple permittivity can start to become a rather more involved function. A more rigorous analysis of this parameter is hence required for a deeper insight into the framework of metamaterials. A discussion on the electron model of varying metals and this model's dependence on the workings of plasmons now follows.

2.3 Plasmonics

Within this section we take a look at the Drude free electron model and subsequently begin to build upon this simplified framework with the inclusions of more complex plasmonic behaviour in order to explain the role that plasmons play in the permittivity function of a metal. The aim of this section is to show that Equation 2.12 actually contains a complex collection of physics, and hence any attempt to truly understand what is occurring when a light source interacts with a metamaterial must reference these rather more complicated physical processes.

2.3.1 Drude Free Electron Model

The optical properties of metals stem from the behaviour of the metal's electrons [6]. A common classical model, the Drude free electron model, first derived in 1900 by Paul Drude [7], largely dictates the responses of the electrons [5]. This model considers a mobile plasma of free electrons of number density n with the positively-charged ion core being held fixed. The equation of motion for a free electron is dependent upon its effective mass, m, charge, e and damping constant, γ:

$$m\frac{d^2\mathbf{r}(t)}{dt^2} + m\gamma\frac{d\mathbf{r}(\mathrm{t})}{d\mathrm{t}} = -e\mathbf{E}_0 e^{-i\omega\mathrm{t}} \tag{2.16}$$

The damping constant is a quantity which represents the free electron collision rate, a parameter necessary for an imaginary part of ϵ. A larger value of γ implies a greater number of collisions between the electrons per second. It is essentially a term that damps the otherwise perfectly free motion of the electrons. After solving the above differential equation for $\mathbf{r}$, the displacement of the free electron can be reduced to:

$$\mathbf{r}(\mathrm{t}) = \frac{e}{m}\frac{\mathbf{E}_0 e^{-i\omega t}}{(\omega^2 + \mathrm{i}\gamma\omega)} \tag{2.17}$$

By comparing equations 2.2a and 2.17 with the fact that the polarization of a medium can also be defined by: $\boldsymbol{P} = ne\boldsymbol{r}$, we arrive at the definition of the dielectric function of the Drude free electron model:

$$\epsilon(\omega) = 1 - \frac{\omega_p^2}{\omega^2 + \gamma^2} + i\frac{\omega_p^2\gamma}{\omega(\omega^2 + \gamma^2)} \tag{2.18}$$

Here, ω_p is defined as the volume plasma frequency of the metal, the frequency at which the free electron plasma oscillates. Mathematically:

$$\omega_p = \sqrt{\frac{ne^2}{\epsilon_0 m}} \tag{2.19}$$

It is important to note that so far we have been considering *volume* plasmons, a term which describes the properties of the bulk metallic plasma. The dielectric function of the Drude free electron model does not fully resemble reality, however, a fact that should so far not be surprising; as mentioned at the outset, the Drude model is a classical model, and hence any quantum effects are naturally ignored. The neglection of extra physics is therefore traded for mathematically simplicity. Here, however, for a more complete view, the interband and intraband transitions of the electrons must be taken into consideration.

2.3.2 Interband Transitions

From the above discussion, we can now finalise the equation for the metal's dielectric function by incorporating the most pertinent quantum effect. In order to do this, we add another restraint on the freedom of the electrons. These bound electrons belong to certain quantum orbitals of the metal atoms. At a particular frequency, ω_0, these bound electrons can be excited to a higher-order quantum orbital. The response term that incorporates these quantum effects follows a Lorentz form:

$$\epsilon_{ib}(\omega) = 1 + \frac{\omega_1^2}{\omega_0^2 - \omega^2 - i\gamma\omega} \tag{2.20}$$

where γ and ω_1 are related to the damping and density of the bound electrons, respectively [5].

Once the interband and intraband transitions are accounted for, the following equation transpires [8]:

$$\epsilon_r(\omega) = \epsilon_{ib} + 1 - \frac{\omega_p^2}{\omega^2 + i\gamma\omega} \tag{2.21}$$

The final form of the dielectric function of metals arises through being aware of the fact that metals such as gold and silver have multiple transitions that must be taken into consideration. This leads to the following equation:

$$\epsilon(\omega) = \epsilon_\infty - \frac{\omega_p^2}{\omega^2 + \gamma^2} + i\frac{\omega_p^2\gamma}{\omega(\omega^2 + \gamma^2)} \tag{2.22}$$

The term ϵ_∞ is a material-dependent property and has 'swallowed' the interband/intraband frequency dependence. In the subsequent chapters when the permittivity function of a metal is mentioned, the reader is encouraged to remember that it is Equation 2.22 that lies beneath the definition.

We will now briefly analyse the dispersion relation of plasmons for all frequencies and subsequently include a brief analysis of surface plasmon polaritons.

2.3.3 Dispersion Relation of the Free Electron Gas, Additional Parameters

In the following analysis of metallic plasmas, we will limit ourselves to the frequency range where $\omega \ll \omega_p$, the limit where metals behave as in 'day-to-day' interactions [6]. This is justified, as, for example, the plasma frequency of gold is 2.183 x10^{15} Hz [9]. Within this framework, there are two regimes to consider: the high and low-frequency regions.

Beginning with high-frequencies - i.e. ω approaches ω_p - it is clear from analysing Equation 2.18 that the light's frequency begins to drown out the effect of the damping constant, leading us to a predominantly real permittivity function of an undamped plasma:

$$\epsilon(\omega) = 1 - \frac{\omega_p^2}{\omega^2} \tag{2.23}$$

In the low-frequency limit, i.e. $\omega \ll \gamma$, electron collisions play a much larger role. The metal's permittivity function now has a significant imaginary part, of comparable magnitude to the real part:

$$n \approx k = \sqrt{\frac{\epsilon_2}{2}} = \sqrt{\frac{\omega_p^2}{2\omega\gamma}} \tag{2.24}$$

When the metals have a predominantly imaginary refractive index, the metals are mainly absorbers, expressed succinctly via the absorption coefficient:

$$\alpha = \sqrt{\frac{2\omega_p^2\omega}{c^2\gamma}} \tag{2.25}$$

This parameter is directly linked to one of the fundamental concepts of this section, the skin depth of the metal:

$$\delta = \frac{2}{\alpha} = \sqrt{\frac{2}{\sigma_0\omega\mu_0}} \tag{2.26}$$

where σ_0 is the conductivity of the metal. The skin depth is effectively the distance the external light can penetrate through the metal. At room temperature this skin depth is usually around 100nm [10] for most metals, explaining why metals are opaque [5]. It can be shown [6] that by considering the transparency regime of metals, $\omega \gg \omega_p$, i.e. the regime contrary to above, the following dispersion relation holds:

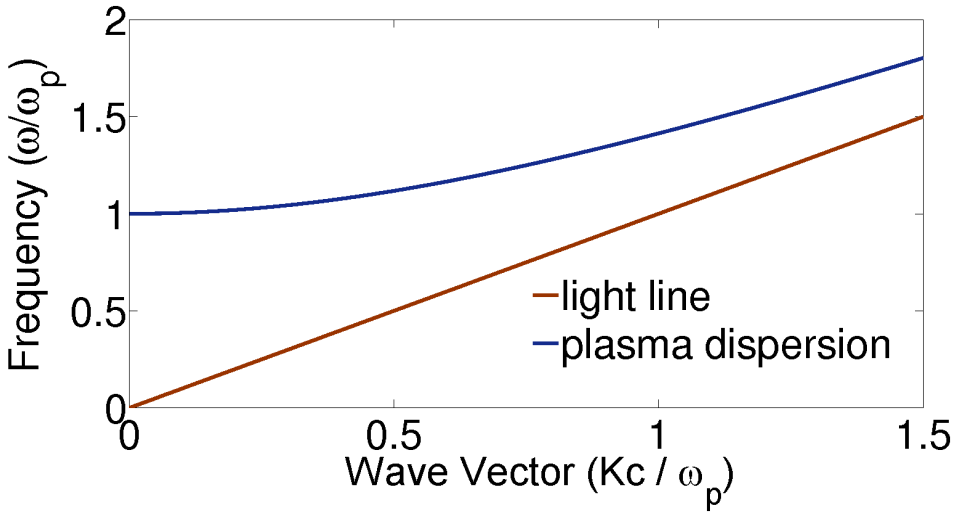

Figure 2.3: The dispersion relation of a free electron gas. As can be seen, electromagnetic wave propagation is only possible for $\omega > \omega_p$.

$$\omega^2 = \omega_p^2 + K^2 c^2 \tag{2.27}$$

where K is the wavevector of the surface plasmon.

Hence only transverse waves with frequency $\omega \gg \omega_p$ are allowed to travel through the free plasma. This dispersion relation of the free electron gas is plotted in Figure 2.3.

At this point, we are now in the position to consider surface plasmon polaritons.

2.3.4 Surface Plasmon Polaritons

Surface plasmon polaritons (SPPs) are the couplings of photons to plasmons at a dielectric-metal interface [11]. These couplings produce propagating surface waves with a permittivity-dependent wave vector and are evanescently confined.

While an in-depth mathematical framework can be found in [6, 11], we here want to highlight a key result, namely the wavevector of the SPPs:

$$\beta = k_0 \sqrt{\frac{\epsilon_1 \epsilon_2}{\epsilon_1 + \epsilon_2}} \tag{2.28}$$

where ϵ_1 and ϵ_2 are the permittivity functions of the surrounding dielectric and metal respectively. As can be seen, the frequency of oscillation of the SPPs tends towards an asymptote as the wavevector approaches infinity. This surface plasmon frequency is given by:

$$\omega_{sp} = \frac{\omega_p}{\sqrt{1 + \epsilon_2}} \tag{2.29}$$

However, as we saw in the discussion of the Drude model, above, the Drude model needs the damping to be included in order to portray the underlying physics. Once this metallic damping - including interband and intraband transitions - is taken into account, the wavevector of the SPPs is now limited to a finite maximum, as shown in Figure 2.4. It can be shown [6] that the dispersion relation for the surface plasmons, when the metal is placed in an insulator-metal-insulator 'sandwich', splits into two equations, referred to as 'symmetric' (SR) and 'antisymmetric' (LR) modes on account of the parity of the electric field at the interface. For increasing metallic thickness, these modes converge.

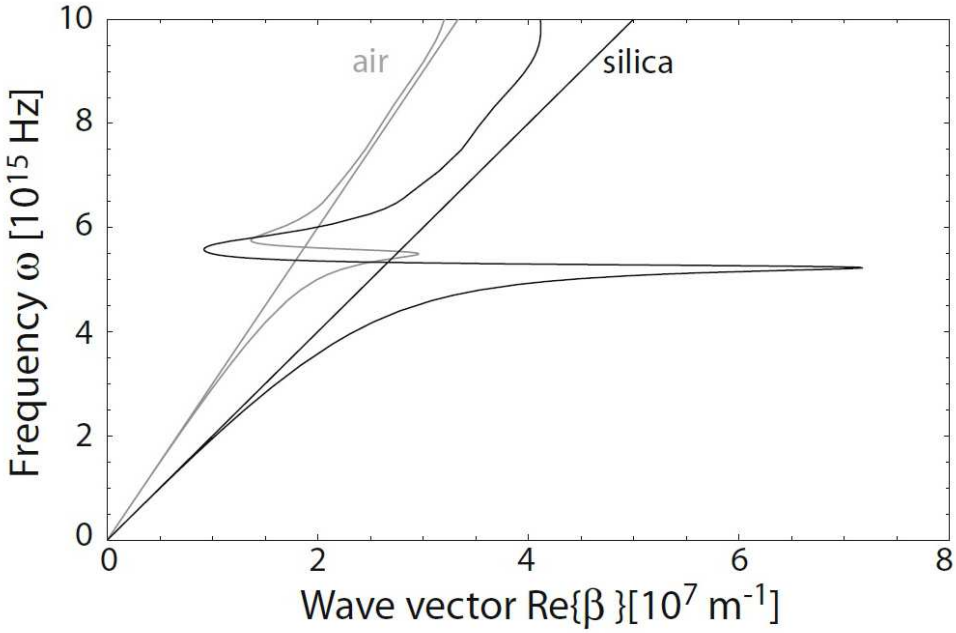

Figure 2.4: The dispersion relation of SPPs for a silver-air interface when losses are taken into account. Two surrounding dielectrics are considered: air and silica. The finite maximum for the wavevector is evident; the wavevector approaches 7 x $10^7 m^{-1}$. Taken from [6].

The extent to which the SPPs are confined is summed up by the skin-depth equation [11], which calculates the decay constant, κ_i, of the SPP perpendicular to the interface:

$$\kappa_i = \frac{\omega}{c}\sqrt{\frac{-\epsilon_i^2}{\epsilon_1 + \epsilon_2}} \tag{2.30}$$

where the index i describes the media, i.e. i=1 for z<0 and i=2 for z>0. We have seen that the metals used primarily for metamaterials - namely gold and silver - contain electronic functions rich with activity, able to sustain volume and surface oscillations. It is by taking advantage of these highly-resonant materials that allow plasmonic nanostructures to have such a wide-range of applications, including linear [12] and nonlinear [13] plas-

monic devices, optical sensor applications [14] and photochemical processes [15]. Three seminal review papers on the theory of collective electronic excitations at metal surfaces have been given by Ritchie [16], Feibelman [17] and Liebsch [18].

2.3.5 Kramers-Kronig Relations

The real and imaginary parts of the constitutive parameter are interconnected. Explicitly:

$$Re(\chi(\omega)) = \frac{2}{\pi}\int_0^\infty d\omega' Im(\chi(\omega'))\frac{\omega'}{\omega'^2 - \omega^2} \tag{2.31a}$$

$$Im(\chi(\omega)) = -\frac{2\omega}{\pi}\int_0^\infty d\omega' \frac{[Re(\chi(\omega')) - 1]}{(\omega'^2 - \omega^2)} \tag{2.31b}$$

Where the frequency-dependent constitutive parameter, $\chi(\omega)$, can represent either the permittivity or the permeability of the medium. Furthermore, ω' represent the infinite number of frequencies to be integrated over. These relations - the Kramers-Kronig relations - were first calculated independently by H. A. Kramers and R. de L. Kronig. They show that by tuning the imaginary (real) part of the constitutive parameter, the real (imaginary) part can be altered. This necessary condition arises from causality [72].

The Kramers-Kronig relations have been used in metamaterial applications. As has previously been discussed, the reflection, transmission, and absorption of a medium are dependent upon the real and imaginary parts of the permittivity and permeability functions. Hence, the Kramers-Kronig relations have been successfully used to produce wide-band metamaterial absorbers [72], reflectionless absorption [20], and omni-directional wave absorbtion [21].

2.4 Second Harmonic Generation

With the advent of masers and, subsequently, lasers, the opportunities to study light-matter interactions became manifold due to the high intensities of the light beams which were hitherto inaccessible. Optical phenomena, including second-harmonic [22] and third-harmonic [23] generation were soon observed through utilizing these lasers with metals [22] and non-metals [24].

These processes fall under the umbrella-term of nonlinear optics. The nonlinear optical interaction that is pertinent for my work is second-harmonic generation (SHG). Above, we mentioned that the permittivity function is dependent upon the symmetry properties of the crystal. The symmetry properties causes SHG to be split into two camps: centrosymmetric and non-centrosymmetric, both of which we shall analyse a little later on, but firstly a general overview of SHG shall be given.

We saw from the discussion on electromagnetic moments that the entire electromagnetic activity of a medium can be characterised by its polarization distribution (which, *via* the continuity equation 2.9, can also be expressed in terms of the current density). The full polarization function of a medium is described [25] by the equation:

$$P(t) = \epsilon_0[\chi^{(1)}E(t) + \chi^{(2)}E^2(t) + \chi^{(3)}E^3(t) + ...] \tag{2.32}$$

where this equation theoretically extends to infinity. The first term in this equation describes the linear response of the medium. The remaining terms characterise the nonlinear characteristics of the material in question. The description 'nonlinear' refers to the fact that these pieces are dependent upon higher-order terms of the electric fields. It is the second term in this equation, the term describing SHG, which concerns us within the nonlinear framework of this thesis.

Second harmonic generation is the nonlinear optical process whereby an incident electromagnetic field of frequency ω interacts with a structure to produce an outgoing field at frequency 2ω, referred to as Ω throughout this work, as depicted in Figure 2.5. This generation of the second harmonic field can be due to the metallic surfaces [26] or the bulk of media [27]. In order to study second-harmonic effects in more detail, it is crucial to gain an insight into the workings of $\chi^{(2)}$, the nonlinear electric susceptibility tensor.

$\chi^{(2)}$, more accurately written as $\chi^{(2)}_{ijk}$, has 27 components, as each subscript refers to one component from either the x, y or z-directions. The non-zero components and their respective magnitude naturally depend upon the crystal in question. When dealing with centrosymmetric media, it is the surfaces of the medium that utilise this susceptibility tensor, whereas for non-centrosymmetric media, the physics describing the bulk of the material is dependent upon $\chi^{(2)}$, as we shall show now.

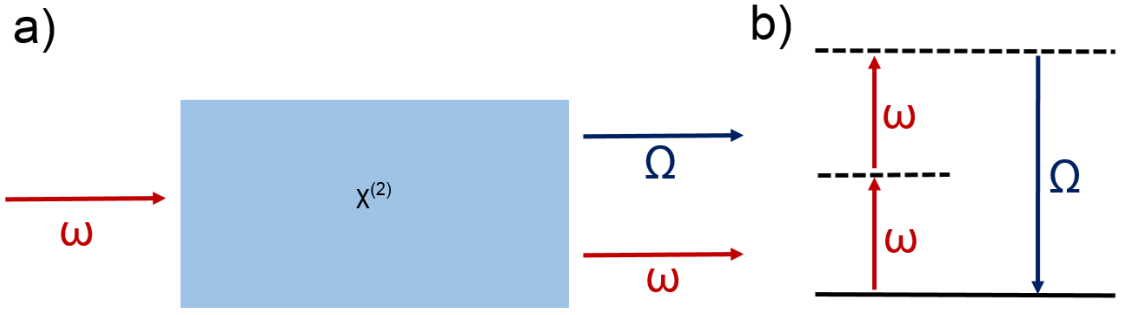

Figure 2.5: a) The principle of SHG; two photons of frequency ω combine through a medium with permittivity $\chi^{(2)}$ to produce an outgoing photon of frequency 2ω. b) The corresponding energy levels of this process. Adapted from [60].

2.4.1 Centrosymmetric

'Centrosymmetric' is a term used when the crystal in question has an inversion centre. In this regime, as shall be documented in detail in Chapter 4, the physics again branches into two categories: the processes occurring at the surface of the medium and rather different processes that occur at the bulk. The surface physics is encapsulated by the following equation:

$$\mathbf{P}^s_\Omega(\mathbf{r}) = \epsilon_0 \chi^{(2)}_s : \mathbf{E}(\mathbf{r})\mathbf{E}(\mathbf{r})\delta(\mathbf{r} - \mathbf{r}_s) \tag{2.33}$$

where the Dirac delta function ensures only the surface is considered, and hence $\chi^{(2)}_s$ is the nonlinear *surface* electric susceptibility tensor. $\mathbf{P}^s$ is the nonlinear polarization term generated at the surface.

The second component of the nonlinear polarization is generated in the bulk of the material and is written as:

$$\begin{aligned}\mathbf{P}^b_{i,\Omega}(\mathbf{r}) = \gamma \nabla_i \left[\mathbf{E}_\omega(\mathbf{r}) \cdot \mathbf{E}_\omega(\mathbf{r})\right] + \delta' \left[\mathbf{E}_\omega(\mathbf{r}) \cdot \nabla\right] \mathbf{E}_{i,\omega}(\mathbf{r}) \\ + \beta \mathbf{E}_{i,\omega}(\mathbf{r}) \left[\nabla \cdot \mathbf{E}_\omega(\mathbf{r})\right] + \zeta \mathbf{E}_{i,\omega}(\mathbf{r}) \nabla_i \mathbf{E}_{i,\omega}(\mathbf{r}),\end{aligned} \tag{2.34}$$

where γ, δ', β, and ζ are material parameters dependent upon the crystal. It is important to note that this γ is not the same as the collision-loss seen in Section 2.3. This polarization originates from electric quadrupoles and magnetic dipoles located in the bulk. This is the dominant bulk contribution in centrosymmetric media (a statement that is rigorously explored in Chapter 4), as in this case the contributions of the electric dipoles vanish, a fact that can be shown by solving the displacement equation for an electric dipole, as shown in [25].

The third term in Eq. (2.34) can usually be neglected, as in homogeneous media (all media studied throughout this thesis are homogenous) $\nabla \cdot \mathbf{E}_\omega(\mathbf{r}) = 0$. Furthermore, most theoretical models [28] predict that the second term is also negligible. For example, in the case of plane wave propagation in a homogeneous medium this term exactly cancels due to the transverse character of the field at the fundamental field. Moreover, in the case of noble metals the ratio between δ' and γ is of the order of ν/ω [29], where ν is the damping frequency, and this ratio is negligible at optical frequencies. It is important to note, however, that the degree to which the term proportional to δ' influences the SHG is still a matter of debate [29]. Based on these considerations, as we shall see later, throughout this thesis, the choice is made to set $\delta' = 0$ and to additionally neglect the third term in Eq. (2.34). Furthermore, in the case of noble metals, the anisotropy parameter has a negligible value, so that in our later calculations the choice is made to

set $\zeta = 0$ for gold.

Thus, these same nonlinear polarizations define nonlinear currents, *via* $\mathbf{J}_{\Omega}^{s,b}(\mathbf{r}) = -i\Omega\mathbf{P}_{\Omega}^{s,b}(\mathbf{r})$ (an $e^{-i\omega t}$ dependence of all harmonic fields is assumed throughout this thesis). These nonlinear currents can subsequently be used to calculate the nonlinear optical far-field by employing a near-field/far-field transformation [30], as later detailed in Chapter 3, thus enabling a complete characterization of the nonlinear scattering process.

2.4.2 Non-centrosymmetric

Comparatively, the physics that describes non-centrosymmetric SHG is simpler; only the bulk has to be considered [25], and it is of the same form as Equation 2.33:

$$\mathbf{P}_{\Omega}^{b}(\mathbf{r}) = \epsilon_0 \chi_b^{(2)} : \mathbf{E}(\mathbf{r})\mathbf{E}(\mathbf{r})\delta(\mathbf{r} - \mathbf{r}_b) \tag{2.35}$$

where the 'b' written throughout the above equation is to denote the bulk part, with the Dirac delta function again forcing all non-zero polarization values to belong to the bulk of the structure.

2.4.3 Miller's Rule

We have seen from the previous discussion that the linear permittivity of the materials to be considered is dispersive in nature. An empirical rule that describes the frequency dispersion of the nonlinear regime is Miller's Rule [25]. Miller noticed [36] that the frequency dispersion of the linear and nonlinear tensors can be arranged such that the ratio:

$$\frac{\chi^{(2)}(\omega_1 + \omega_2, \omega_1, \omega_2)}{\chi^{(1)}(\omega_1 + \omega_2)\chi^{(1)}(\omega_1)\chi^{(1)}(\omega_2)} = C \tag{2.36}$$

is constant. Explicitly, $\chi^{(1)}$ is the linear susceptibility, $\chi^{(2)}$ is any of the nonlinear surface or bulk susceptibilities, namely $\chi^{(2)}_{\perp,\perp,\perp}$,$\chi^{(2)}_{\parallel,\parallel,\perp}$,$\chi^{(2)}_{\parallel,\perp,\parallel}$, γ or ζ.

For the purposes of SHG, i.e. ω_2=2ω_1, this equation can be further simplified:

$$\frac{\chi^{(2)}(\Omega, \omega)}{\chi^{(1)}(\Omega)[\chi^{(1)}]^2} = C \tag{2.37}$$

Due to the nature of the Miller rule, the shape of the dispersion curves corresponding to the other nonlinear susceptibilities will remain the same; only the scaling constant C will change. It is clear from this equation that the dispersions in the linear regime become amplified in the nonlinear regime. Hence, care must be taken to ensure the nature of the nonlinearities are correctly determined.

The lack of experimental data with regards to nonlinear susceptibilities often leads to the nonlinear tensors being inferred from the above equations. For example, as we shall see in Chapter 4, the nonlinear experimental data of gold was measured with a wavelength of 810nm. This value can then be fed into Equation 2.37 to thereotically determine the dispersion of the surface tensor.

The sensitivity of SHG is such that the resulting wave depends upon, including others, the material roughness [31], crystal orientation [32]. As an example to exemplify this sensitivity, SHG at a silver-air interface was shown to be enhanced by a factor of 10^4 due to the surface roughness [34]. It is clear from the discussion above that laser polarization and wavelength [35] also play a crucial role in engendering a nonlinear response.

2.5 Metamaterials

2.5.1 Nomenclature and Overview

The term 'metamaterial' first appeared in scientific literature in the year 2000 following the paper of Smith et al., in which a material composite was created exhibiting a negative refractive index [37], which we shall shortly observe. Given the widespread use of the term in a quickly evolving field, it is perhaps unsurprising that there fails to be a rigorous definition that accurately describes every use of the word. For example, the European Unions Metamorphose Network, the primary sponsor of the Metamaterials Congress, defines a metamaterial as "an arrangement of artificial structural elements, designed to achieve advantageous and unusual electromagnetic properties" [38]. Such a definition, as noted by Cai and Shalaev in their seminal work *Optical Metamaterials* [5] is overly inclusive, as this definition makes no distinction between metamaterials and other man-made structures, such as photonic crystals. It is common to say that metamaterials go beyond the capabilities of nature, a fact that squares up with the very etymology of the word: The prefix 'meta' has its roots in the Greek for 'beyond' or 'transcendental'; a meaning that is ascribed to these structures due to the fact that through tuning the precise size, shape, geometry and orientation of the materials, it is thought to be possible to achieve a material with properties that go beyond the capabilities of nature. The phrase 'thought to be' is used in the preceding sentence due to a rather profound semantic thought by Cai and Shalaev, namely, that in order to assert that a material goes beyond the capabilities of nature is to assert the *non-existence* of something. As this thesis is not to be weighed down by philosophical arguments, the definition of a metamaterial within this thesis takes the form of Cai's and Shalaev's: "A metamaterial is an artificially structured material which attains its properties from the unit structure rather than the

constituent materials. A metamaterial has an inhomogeneity scale that is much smaller than the wavelength of interest, and its electromagnetic response is expressed in terms of homogenized material parameters." Examples of these structures are shown in Figure 2.6.

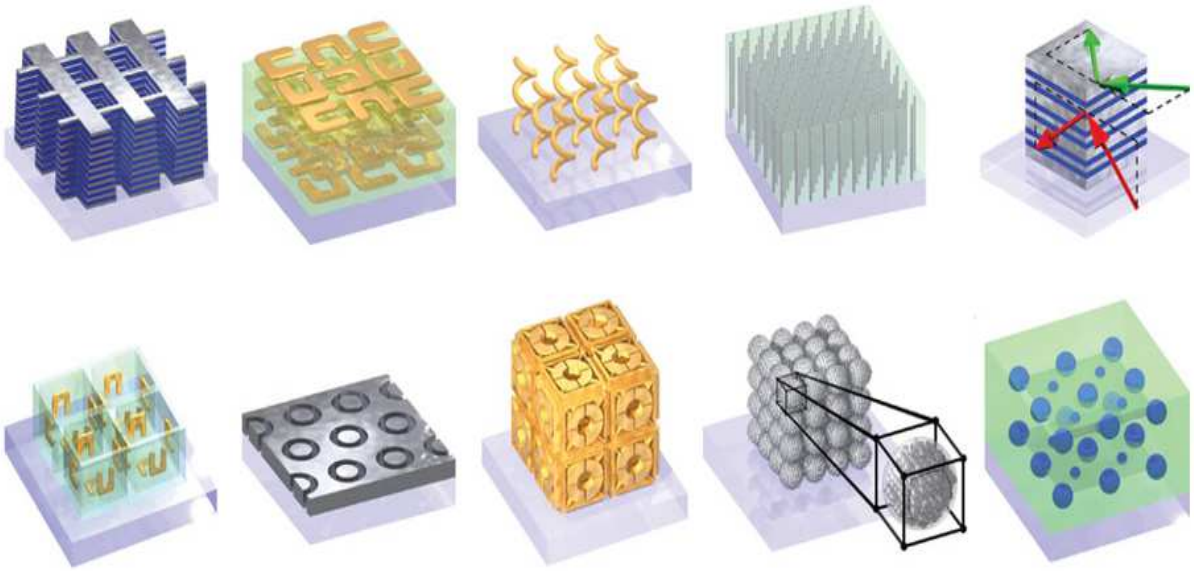

Figure 2.6: A variety of meta-atoms, which form the basis of their respective metamaterials. Taken from [39].

Much in the same way that atoms form the basis of a crystal structure, we refer to the basis of these metamaterials as meta-atoms. While metamaterials have applications within, among others, acoustic [40] and structural physics [41], the focus of this thesis is on optical metamaterials. These optical metamaterials are materials that have been designed in order to interact with electromagnetic waves to produce new electromagnetic phenomena, some examples of which are described below. In order to achieve this goal, the unit cell of the metamaterial must be smaller than the wavelength of the incoming light for the sake of anisotropy. This means that from the light's 'point-of-view', the materials are uniform, and are hence something wholly different from their subsequent parts. The lack of inhomogeneities separates the behaviour of these structures from others, such as photonic crystals and Bragg gratings, which usually rely on processes such as diffraction and interference. It is crucial for the reader to constantly bear in mind throughout this work that combining the different materials into a metamaterial causes the entire composite to become something macroscopically different.

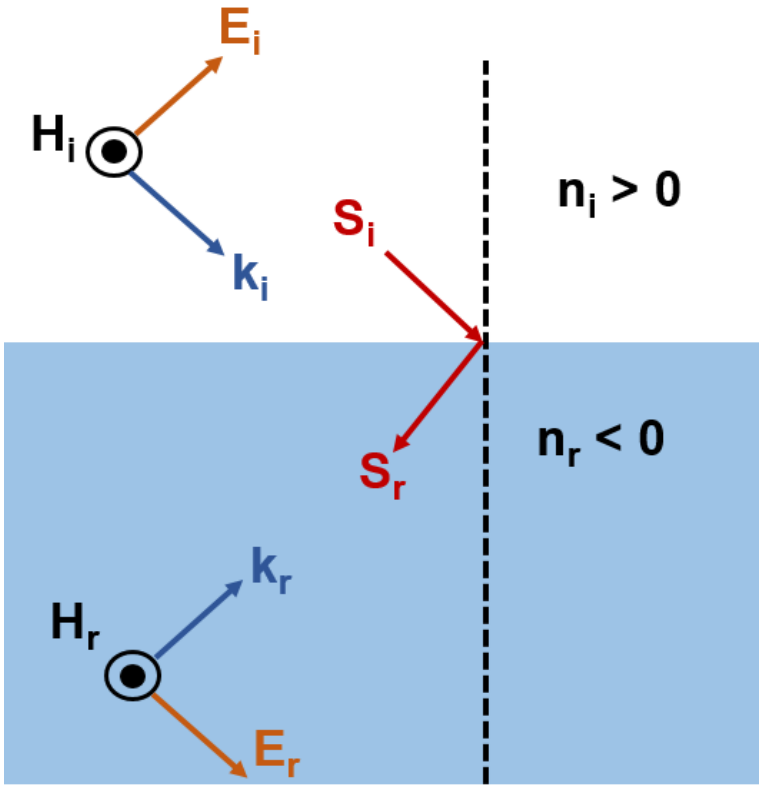

Figure 2.7: The physics of negative refraction. An electromagnetic wave impinges on a material with a negative refractive index, causing it to be refracted to the same side of the normal. Taken from [42]

2.5.2 Negative Refraction

The advent of metamaterials lies in Sir John Pendry's considerations about Veselago's idea: in 1968 Veselago stated [43] that if an incoming electromagnetic wave is greeted by a medium that has simultaneously negative values for the real parts of the permittivity and permeability, this wave will be refracted to the *same* side of the normal, as opposed to the opposite side of the normal which is observed in 'every-day' refraction, as depicted in Figure 2.7. Starting from Equation 2.12, it can be shown that for a negative refractive index, the following conditions must hold [44]:

$$n' = -\frac{1}{\sqrt{2}}(|\epsilon||\mu| + \mu'\epsilon' - \mu''\epsilon'')^{\frac{1}{2}} \tag{2.38a}$$

$$k'' = -\frac{1}{\sqrt{2}}\frac{\mu''\epsilon' + \mu'\epsilon''}{(|\epsilon||\mu| + \mu'\epsilon' - \mu''\epsilon'')^{\frac{1}{2}}} \tag{2.38b}$$

The above relations can be simplified into one equation:

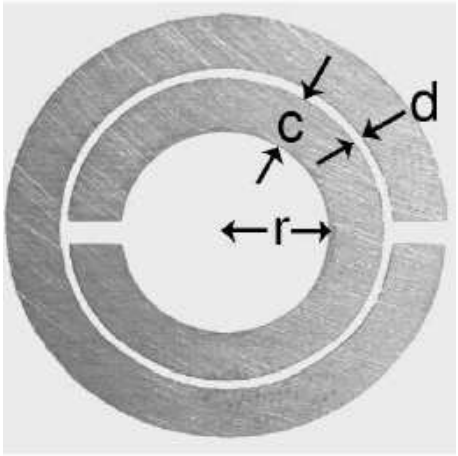

Figure 2.8: The first physical Split Ring Resonator, fabricated by Smith et al. [46]. The dimensions of this copper structure are: $c = 0.8mm$, $d = 0.2mm$, $r = 1.5mm$, with a resonance at 4.845 GHz.

$$\epsilon'|\mu| + \mu'|\epsilon| < 0 \tag{2.39}$$

Achieving a negative value for the electric permittivity of a material is simple: the electrons of noble metals oscillate out of phase with the incoming electric field, giving rise to a negative value for the noble metals' permittivity, as we saw in Figure 2.2. The challenge is being able to manipulate a material's *magnetic* response: as has already been stated, the deviation from unity for almost all material's permeabilities is negligible. In solving this problem, Pendry's idea gave rise to the entire field.

In 1999 Pendry showed [45] in a ground-breaking theoretical paper that a split ring resonator (SRR) has a magnetic response that is dependent upon the capacitance of the rings:

$$\mu_{eff} = 1 - \frac{\frac{\pi r^2}{a^2}}{1 + \frac{2l\sigma_1}{\omega r \mu_0} i - \frac{3lc_0^2}{\pi\omega^2 \ln\frac{2c}{d} r^3}} \tag{2.40}$$

where σ_1 and i are the resistance per unit length and current flowing through the SRR respectively, while c, l and r are the dimension parameters of the SRR shown in Figure 2.8. Note that the physical SRR was fabricated by Smith et al. [46]. Therefore, by tuning the structural parameters of the unit cell, it is possible to pick where in frequency space a magnetic resonance is desired. Figure 2.9 shows a plot of this effective permeability for typical structural dimensions, taken from [37].

An understanding of the SRR meta-atom is crucial for understanding the entire field of metamaterials. The incoming light excites a current within the rings of the meta-atom. Without the gap in the rings, a circular current would be generated. This would

produce a magnetic response, but the deviation from unity for the permeability would be small [5]. With the gaps, a capacitance is introduced. With both an inductance and capacitance, the SRR meta-atom becomes a resonant LC-circuit, with a large potential for permeability manipulation. The utilization of two rings with their gaps on either side of the meta-atom is a convenient method of suppressing the electric dipole generated by the structure: the electric dipole moment generated by one ring interacts destructively with the other.

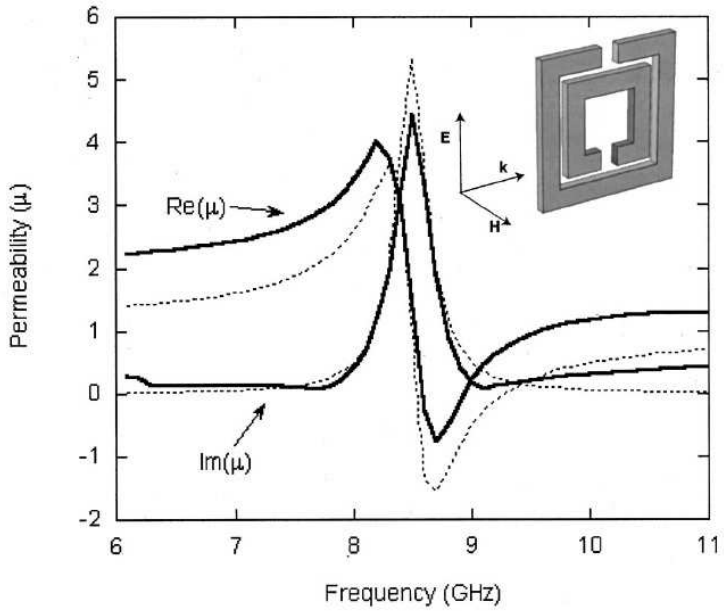

Figure 2.9: A plot of the calculated relative permeability - i.e. the magnetic response - of the SRR meta-atom shown in the inset. A resonance near 8GHz can clearly be seen. Taken from [37].

This theoretical idea became a physical reality two years later, when Shelby et al. [47] fabricated a unit cell consisting of SRRs and a straight metallic wire, shown in Figure 2.10. This design had been fabricated in 2000 by Smith et al. [46], but the refractive index had not been measured. The SRR is responsible for the negative magnetic response, while the metallic wire has a negative value for the relative permittivity. Across the entire frequency range where both μ and ϵ are negative, a left-handed medium with inverted Snell's Law and Cherenkov radiation [46] is created.

As stated above, the wavelength of the probing light source must be larger than the unit cell of the metamaterial. In order to experimentally confirm a theoretical metamaterial idea, it is therefore ideal to pick a light source with a large wavelength, as this enables the construction of large unit cells, simplifying the fabrication process. Most metamaterial ideas are therefore experimentally confirmed in the GHz-range. For example, a probing frequency of 10GHz allows the unit-cell size to reach 3cm.

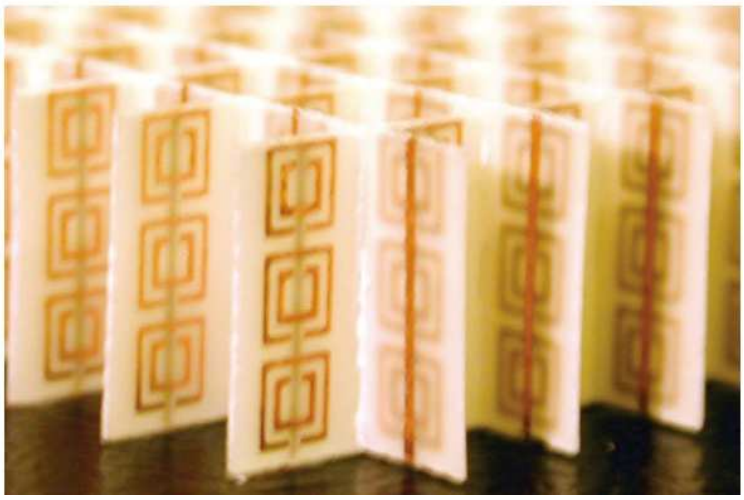

Figure 2.10: The first metamaterial fabricated with a negative refractive index. This left-handed material consists of SRRs combined with a metallic wire, two units which control the relative permeability and permittivity respectively. Taken from [47].

Since the aforementioned pioneering works were published, SRRs have become the bread-and-butter meta-atom, with successful fabrication for use, among others, at THz frequencies [48–50]; optical frequencies [51, 52]; being used to steer electromagnetic waves for use as invisibility cloaks [53]; perfect lens production [54]; engendering Fano resonances [55, 56], and flexible metamaterials [57–59].

While discussing the index of refraction, above, we saw that the electric dipoles of a system which absorb the incoming light are responsible for the refractive index of the structure. Even as the light source enters the regime of optical frequencies, the electric dipoles are still able to respond to the probing signal. Hence, the relative permittivity can easily differ from unity for a wide range of structures. On the other hand, the magnetic dipoles of a system cannot respond quickly enough to magnetic fields generated at optical frequencies. As has been described in this section, the relative permeability of a meta-atom is dependent upon the current generated within the metal. This current arises physically from the traveling free electrons of the metal, whose motion can be triggered even at optical frequencies. Combining this motion with an SRR allows a metamaterial to be constructed that can have a magnetic response at optical frequencies. In the most common metamaterial designs, the meta-atoms of which the structure is composed are placed far enough away from one another such that they don't interact, as this would have consequences on the intended physics. However, some metamaterial designs have been proposed that deliberately go against the grain of this rule, producing interesting physical effects. In analogy to the electronic or molecular energy theory, when electric or magnetic meta-atoms interact, the energy levels of the coupled system will split from the initial

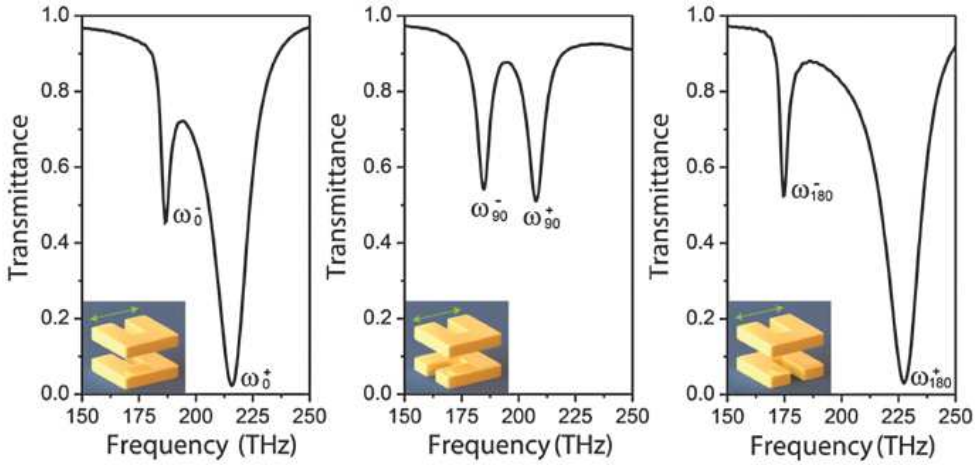

Figure 2.11: The effects of hybridization in a metamaterial, taken from [42]. The individual meta-atoms, in this case SRRs, are placed near enough to one another such that they interact, leading to electromagnetic modes (excitations) that are sensitive to the orientation of the coupling. As can be seen, as the lower SRR is rotated on its axis with the upper SRR held fixed, the modes change in their relative strength.

isolated state [42]. This hybridization approach was first introduced in electric plasmon structures [60]. In an analogous way to the plasma modes splitting into symmetric and antisymmetric, as we saw in Section 2.3.4, magnetic meta-atoms, such as SRRs, can be hybridized [61–63]. In fact, due to the SRRs' abilities to generate strong electric and magnetic dipoles and even higher-order terms, these structures offer great potential for hybridization to be utilized. Figure 2.11, taken from [64], shows one such example of hybridized SRR modes.

2.5.3 Invisibility Cloaks

Since the dawn of metamaterials, one idea that has garnered attention like no other is the idea of producing an invisiblity cloak. While this exciting idea was usually confined to the realm of science fiction, the advent of metamaterials now meant that more sophisticated ways of controlling light were possible. Not surprisingly, then, a paper that documents the ability of a metamaterial based on a split ring resonator to completely cloak an object [53] at GHz frequencies is at the time of writing the third most-cited paper in the history of metamaterial literature [65].

The structure in question can be seen in Figure 2.12. The layout consists of 10 concentric cylinders, each of which was three units cells tall. Through the mathematics contained in [53], it can be shown that the permeability of the structure must vary radially, the very feature we saw with the split ring resonators, above. Hence, these split ring resonators were placed such that their axes were along the radial direction, fulfilling

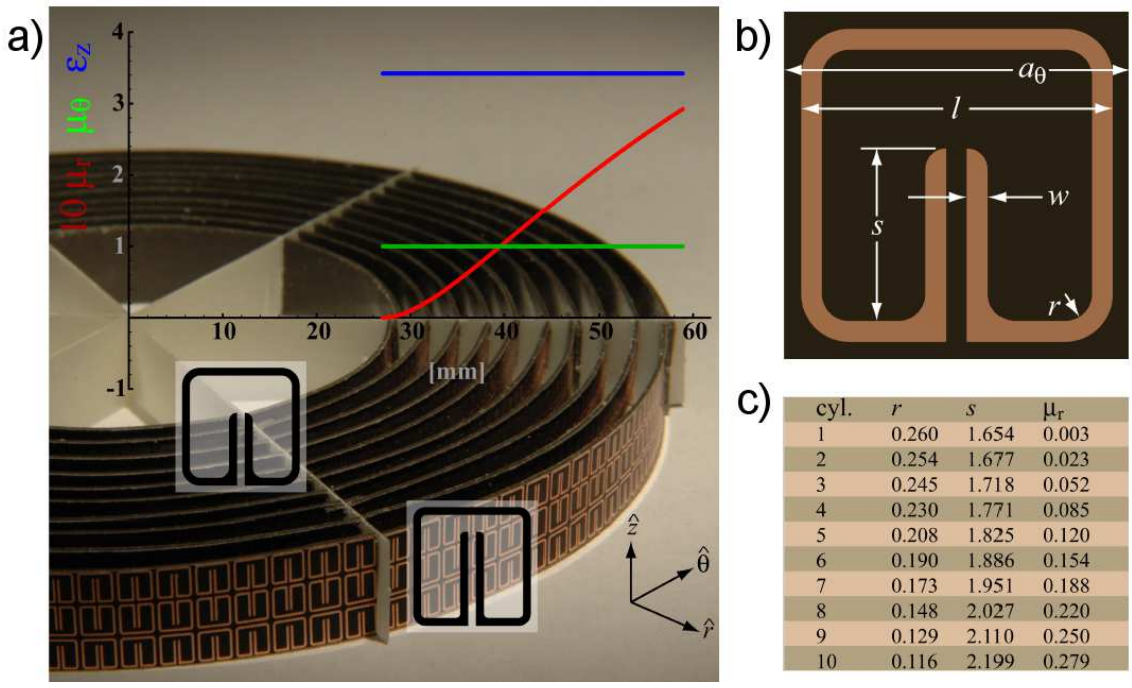

cyl.	r	s	μ_r
1	0.260	1.654	0.003
2	0.254	1.677	0.023
3	0.245	1.718	0.052
4	0.230	1.771	0.085
5	0.208	1.825	0.120
6	0.190	1.886	0.154
7	0.173	1.951	0.188
8	0.148	2.027	0.220
9	0.129	2.110	0.250
10	0.116	2.199	0.279

Figure 2.12: A metamaterial designed to cloak any object placed in the centre, taken from one of the most cited papers in metamaterial literature [53]. a) The metamaterial consists of ten layers of SRRs that vary in their structural parameters, engineered such that the radial component of the permittivity varies throughout the structure. b) and c) The structural parameters of the SRRs.

the required condition.

2.5.4 Optical Coefficients Generated by Metamaterials

One of the most frequent considerations for my work is to determine how much light is reflected, transmitted, and absorbed by the designed metamaterials. A wave incident on a metamaterial can only undergo one of these three interactions, meaning that this relationship boils down simply to the expression:

$$T(\omega) + R(\omega) + A(\omega) = 1 \tag{2.41}$$

Where T, R, A are the absolute values of the transmission, reflection and absorption coefficients respectively. These three coefficients comprise the *optical coefficients*. As we have seen previously, the metamaterial's electromagnetic response is frequency-dependent, so it is no surprise that the above optical coefficients must also contain this dependency.

The reflection of a material is dependent upon its complex impedance, Z:

$$Z = \sqrt{\frac{\mu(\omega)}{\epsilon(\omega)}} \tag{2.42}$$

The impedance of a vacuum is 376.7Ω. If the impedance of the metamaterial of interest is equal to this value, then naturally there will be no reflection, as from the light's 'point-of-view' there is no physical difference between the metamaterial and the vacuum. A strong mismatch between the impedances gives rise to a strong reflective character.

The transmissivity of a metamaterial is dependent upon the imaginary part of the refractive index. This parameter, referred to as k'' in the equations above, corresponds to the optical losses that occur in the metamaterial's interaction with the electromagnetic wave. The imaginary part of the refractive index is directly related to both the absorption coefficient, α, and conductivity, σ, of the metamaterial, as shown in the following two equations:

$$k'' = \frac{\sigma}{\omega} \tag{2.43}$$

$$\alpha = \frac{4\pi k''}{\lambda} \tag{2.44}$$

Therefore, the greater the imaginary part of the refractive index, the greater the conductivity of the material, corresponding to a larger reduction of the transmission of the light source through this material.

Theoretical retrieval equations [37, 66] enable a metamaterial's relative permittivity and permeability to be calculated from the optical coefficients:

$$t^{-1} = [\cos(nkd) - i(z + \frac{1}{z})\sin(nkd)]e^{ikd} \tag{2.45a}$$

$$\frac{r}{t'} = -\frac{1}{2}i(z - \frac{1}{z})\sin(nkd) \tag{2.45b}$$

Where d is the thickness of the metamaterial, n is its refractive index and z its impedance. k is the wavelength of the external light source and $\mathrm{t}' = e^{ikd}$. These equations can naturally be inverted. For brevity:

$$n = \frac{1}{kd}[[Im(\ln(e^{inkd})) + 2m\pi] - iRe(\ln(e^{inkd}))] \tag{2.46}$$

Where m is an integer which must be correctly determined. It arises from the fact that the logarithm functions here have multiple branches. An incorrect value for m returns a discontinuous refractive index function, a result which has no basis in reality.

Since the revelation that metamaterials seem to have the potential of having both electric and magnetic responses at almost any frequency (fabrication issues aside), metamaterials have been widely applied as absorbers. Such absorber designs include polarisation-indepedent [67, 68]; incident angle independent [69–71]; broadband [72–74]; multiband [75–78], perfect absorbers [79–82], and, less commonly, narrow-band [83]. The advantage of metamaterials for absorption purposes allow many of these features to be incorporated into one small and light product.

2.6 Multilayer Composites

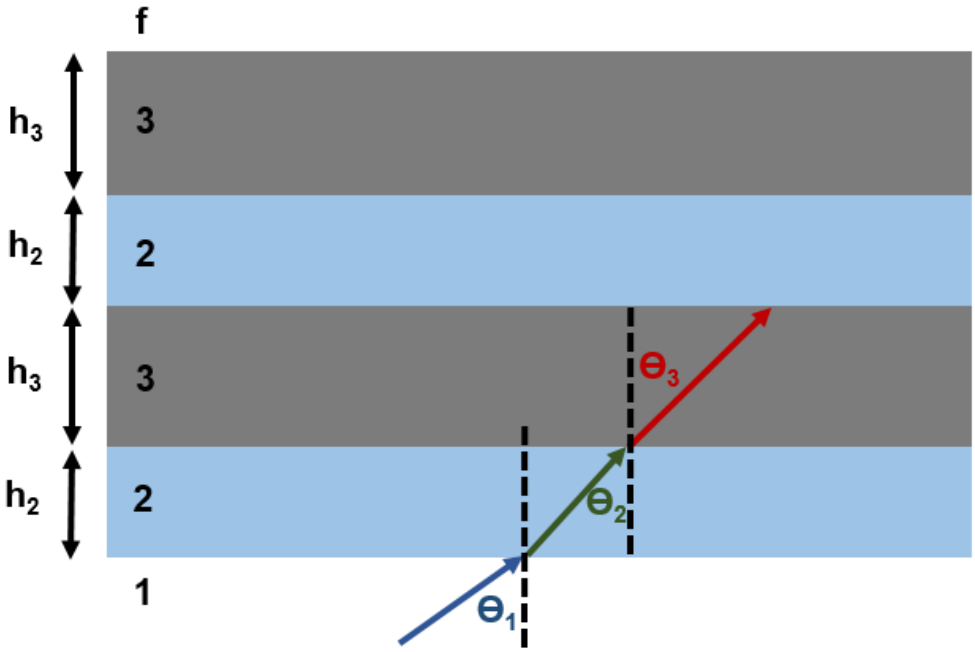

Figure 2.13: The physical setup of a stratified composite. The incident light wave, originally traveling through a medium with refractive index n_1 impinges on an interface of a composite. This composite is composed of two alternating layers with different refractive indices and heights. The electromagnetic wave finally exits the composite into the final medium with refractive index n_f. Adapted from [4].

A medium whose properties are constant throughout each plane perpendicular to a fixed direction is called a stratified medium [4]. A stratified medium with height h is characterised by an electric permittivity function ϵ and magnetic permeability function μ, a fact that should by now be unsurprising to the reader given the discussions in the previous chapters. Assuming that our multilayer composite is periodic in the z-direction, then our defined functions are dependent upon z such that:

$$\epsilon(z + jh) = \epsilon(z) \tag{2.47a}$$

$$\mu(z + jh) = \mu(z) \tag{2.47b}$$

where j is an integer in some fixed range $1 \leq j \leq N$, as N is the total number of layers. The physics of this problem is depicted in Figure 2.13.

Before continuing, it is important to introduce a characteristic matrix, $\mathbf{M}$, that is essentially a convenient piece of mathematics that enables the following equations to be simplified. While a full characterisation of this matrix is given in [4], it would be confusing to the reader not to elucidate its significance. Namely, it relates the x- and y-components of the electric or magnetic vectors in the plane z=0, i.e. *outside* of the stratified medium to the components in an arbitrary plane z=constant. This allows us to determine the propagation of a plane monochromatic wave through our stratified medium by only considering an appropriate two-by-two unimodular matrix $\mathbf{M}$. The mathematical underpinnings of $\mathbf{M}$ are such that:

$$\mathbf{M}(z_N) = \mathbf{M}_1(z_1)\mathbf{M}_2(z_2 - z_1)...\mathbf{M}_N(z_N - z_{N-1}) \tag{2.48}$$

The characteristic matrix that corresponds to one period is:

$$\mathbf{M}(h) = \begin{bmatrix} m_{11} & m_{12} \\ m_{21} & m_{22} \end{bmatrix}$$

By invoking the periodicity conditions from above, the characteristic matrix of the full setup, i.e. including all periods becomes:

$$\mathbf{M}(Nh) = \mathbf{M}(h) \cdot \mathbf{M}(h)...\mathbf{M}(h) = [\mathbf{M}(h)]^N \tag{2.50}$$

The solution to Nth-power unimodular matrices [84] allows the equation to take the form:

$$[\mathbf{M}(h)] = \begin{bmatrix} m_{11}U_{N-1}(a) - U_{N-2}(a) & m_{12}U_{N-1}(a) \\ m_{21}U_{N-1}(a) & m_{22}U_{N-1}(a) - U_{N-1}(a) - U_{N-2}(a) \end{bmatrix}$$

where:

$$a = \frac{1}{2}(m_{11} + m_{22}) \tag{2.52}$$

and U_N are the Chebyshev polynomials of the second kind [84]:

$$U_N(x) = \frac{\sin[(N+1])\cos^{-1}(x)}{\sqrt{1-x^2}} \tag{2.53}$$

So far we have considered a periodically stratified medium of uniform heights, permittivities, and permeabilities. The most typical Bragg filters, as we shall see in Chapter 3, consist of two layers that alternate. Naturally, we therefore want to generalise the above equations to allow for layers of different heights and refractive indices. We refer to the layers as n_2 and n_3 with respective heights of h_2 and h_3, as shown in Figure 2.13. As again we do not play with the permeabilities in this thesis, we set μ=1. The characteristic matrix of a single period is then [4]:

$$\mathbf{M}_2(h) = \begin{bmatrix} \cos\beta_2 & -\frac{i}{p_2}\sin\beta_2 \\ -ip_2\sin\beta_2 & \cos\beta_2 \end{bmatrix} \begin{bmatrix} \cos\beta_3 & -\frac{i}{p_3}\sin\beta_3 \\ -ip_3\sin\beta_3 & \cos\beta_3 \end{bmatrix}$$

$$= \begin{bmatrix} \cos\beta_2\cos\beta_3 - \frac{p_3}{p_2}\sin\beta_2\sin\beta_3 & -\frac{i}{p_3}\cos\beta_2\sin\beta_3 - \frac{i}{p_2}\sin\beta_2\cos\beta_3 \\ -ip_2\sin\beta_2\cos\beta_3 - ip_3\cos\beta_2\sin\beta_3 & \cos\beta_2\cos\beta_3 - \frac{p_2}{p_3}\sin\beta_2\sin\beta_3 \end{bmatrix}$$

where:

$$\beta_2 = \frac{2\pi}{\lambda_0} n_2 h_2 \cos\theta_2 \tag{2.55a}$$

$$\beta_3 = \frac{2\pi}{\lambda_0} n_3 h_3 \cos\theta_3 \tag{2.55b}$$

$$p_2 = n_2\cos\theta_2 \tag{2.55c}$$

$$p_3 = n_3\cos\theta_3 \tag{2.55d}$$

$$h = h_2 + h_3 \tag{2.55e}$$

With the above equation, in combination with Equation 2.50, the characteristic matrix $\mathbf{M}_{2N}(Nh)$ of the multilayer, which now has $2N$ layers in total is given by:

$$\mathbf{M}_{2N}(Nh) = \begin{bmatrix} M_{11} & M_{12} \\ M_{21} & M_{22} \end{bmatrix}$$

where:

$$M_{11} = (\cos\beta_2 \cos\beta_3 - \frac{p_3}{p_2} \sin\beta_2 \sin\beta_3) U_{N-1}(a) - U_{N-2}(a) \tag{2.57a}$$

$$M_{12} = -i(\frac{1}{p_3} \cos\beta_2 \sin\beta_3 + \frac{1}{p_2} \sin\beta_2 \cos\beta_3) U_{N-1}(a) \tag{2.57b}$$

$$M_{21} = -i(p_2 \sin\beta_2 \cos\beta_3 + p_3 \cos\beta_2 \sin\beta_3) U_{N-1}(a) \tag{2.57c}$$

$$M_{22} = (\cos\beta_2 \cos\beta_3 - \frac{p_2}{p_3} \sin\beta_2 \sin\beta_3) U_{N-1}(a) - U_{N-2}(a) \tag{2.57d}$$

$$a = \cos\beta_2 \cos\beta_3 - \frac{1}{2}(\frac{p_2}{p_3} + \frac{p_3}{p_2}) \sin\beta_2 \sin\beta_3 \tag{2.57e}$$

Finally, this allows the transmission and reflection coefficients to be obtained:

$$r = \frac{(M_{11} + M_{12}p_f)p_1 - (M_{21} + M_{22}p_f)}{(M_{11} + M_{12}p_f)p_1 + (M_{21} + M_{22}p_f)} \tag{2.58}$$

$$t = \frac{2p_f}{(M_{11} + M_{12}p_f)p_1 + (M_{21} + M_{22}p_f)} \tag{2.59}$$

where:

$$p_1 = \sqrt{\frac{\epsilon_1}{\mu_1}} \cos\theta_1 \tag{2.60a}$$

$$p_f = \sqrt{\frac{\epsilon_f}{\mu_f}} \cos\theta_f \tag{2.60b}$$

2.6.1 Nonlinear Optics with Metamaterials

As a large portion of my work involves analysing the nonlinear signal arising from metamaterials in the framework of second harmonic generation, it is important to discuss the impact of metamaterials on the world of nonlinear physics. Given the impact of metamaterials on linear optics, might we expect to see unusual and useful behaviour arising from the nonlinearities of these structures?

Observation of nonlinear optical activity due to the fast electronic mechanism of nonlinearity became possible in 1979 [85], using a high-intensity single-mode nanosecond-pulsed laser and the natural crystal of lithium iodate that is simultaneously a highly nonlinear and strongly optically active medium [86]. Thermal nonlinear optical activity was seen in optically active crystals [87–89]. Since then nonlinear optical activity has been observed in a number of chiral liquids [90–93]. Nevertheless, the effect remained challenging to detect, making it unsuitable for routine practical applications, even in spectroscopy [85]. Due to the difficulties of performing nonlinear measurements on metamaterials, the focus of nonlinear research in this area is mostly limited to the

theoretical. Negative index metamaterials have been especially popular in analysing nonlinear signals, with research including general treatments for nonlinear wave propagation and nonlinear Schrödinger equations in nonlinear index materials [94, 95], as well as specific nonlinear processes such as second-harmonic generation (SHG) and parametric amplification [96–99]. However, that is not to say that experimental research has not been undertaken. Indeed, metamaterial nonlinearities have been experimentally verified for a variety of structures, including meta-surfaces producing third-harmonic Fano resonances [100], giant nonlinear optical activity in a plasmonic metamaterial [85] and nonlinearities through structures combined with graphene [101]. By exciting a structure that has both strong field enhancement and strong nonlinear properties, large nonlinear signals can be produced at relatively low optical powers. In particular, nonlinear optical processes in plasmonic structures have been studied extensively [102, 103], including surface-enhanced Raman scattering [104–106], second-order optical interactions [107–118], and Kerr interactions [119, 120]. In circumventing the losses present due to the metals, the nonlinearities of dielectrics are also becoming increasingly more researched [121, 122].

2.6.2 Metals *vs.* Dielectrics

The strong field enhancement that accompanies the excitation of surface-plasmon polaritons (SPPs) on metallic nanoparticles [6, 123] makes these nanostructures ideal candidates for many applications, including nanoscale antennae, single-molecule detection *via* surface-enhanced Raman scattering, metallic nanotips for near-field optical microscopy, and optically-active guiding nanostructures [104, 106, 124–128]. However, the generation of large optical fields comes at a price of significant optical losses present in metals - the γ parameter that we saw in Eq. 2.13. In fact, these losses are viewed as the main factor that still precludes a widespread use of plasmonic devices in practical applications [129]. Methods that attempt to overcome this restriction include using doped semiconductors [130] and gain media [131]. We will see the difficulties that arise when attempting to engineer a transmission notch filter based on trenches in gold in Chapter 6.

An alternative to plasmonic materials, which aims to circumvent optical losses, consists of using all-dielectric resonant structures [132, 133]. Unlike the excitation of the metallic plasma that engenders the plasmonic resonances, it is the resonances of displacement currents, known as *Mie resonances* [134], that enable these all-dielectric components to be used for optical field manipulation. While the field enhancement of these dielectric structures is typically weaker than that of their metallic counterparts, their high quality factors enable intriguing optical phenomena to be produced, including magnetic mirrors [135], reflectionless ultrathin sheets mimicking highly directional Huygens sources [136, 137], and toroidal dipole sources [138, 140]. These dielectric nanostructures

have shown great promise in biosensing, optoelectronics, and energy applications [141]. Hence, the trade-off is clear: the selection of metal or dielectric is dependent upon the requirements of particular applications, namely whether one desires strong field enhancement or low optical losses.

This dichotomy extends to *nonlinear nanoscale photonics*. By exciting a structure that has both strong field enhancement and strong nonlinear properties, large nonlinear signals can be produced at relatively low optical powers. As in the linear case, these strong nonlinear optical effects in plasmonic structures are accompanied by large optical losses, which restrict the range of applications to which nonlinear optical interactions can be employed. It is therefore of particular interest to understand, in the context of nonlinear nanophotonics, the limitations and advantages provided by plasmonic structures, as compared to those characteristic to all-dielectric resonant subwavelength structures.

2.6.3 The Electromagnetic Multipole Family

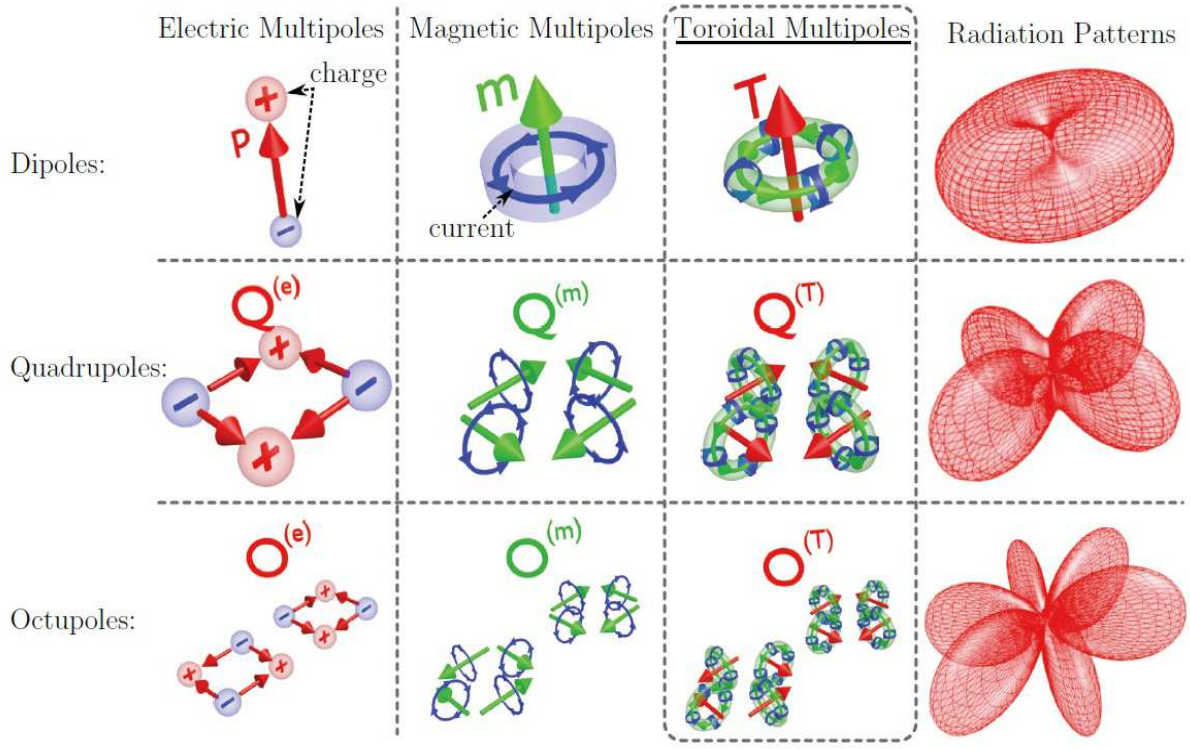

Figure 2.14: The dipole, quadrupole, and octupole moments for the electric, magnetic, and toroidal family, taken from [142]. Higher-order configurations naturally also exist, but are not shown. These three families complete the entire electromagnetic group - all electromagnetic sources are composed from these moments. The radiation patterns of these moments are also given.

Up to this point, the electromagnetic properties of the media have been described

in terms of the macroscopic material parameters of electric permittivity and magnetic permeability, which dictate the extent to which the media respond to external electromagnetic sources. These parameters are a convenient representation, which describe the underlying microscopic features of charge and current excitations. These excitations, however, can be decomposed into terms of the multipolar expansion. For full details of this expansion, the reader is encouraged to study Appendix A, where the origins and consequences of the multipoles are pursued mathematically. Here, we will simply state the key point: it is possible to consider electromagnetic waves as generated by an infinite series of excitations of varying significance.

Through consideration of the first terms of the multipolar expansion, we arrive at the equations for the electric dipole ($\mathbf{p}$), magnetic dipole ($\mathbf{m}$), and toroidal dipole ($\mathbf{T}$) alongside the electric quadrupole ($\mathrm{Q}_\alpha\beta$) and magnetic quadrupole ($\mathrm{M}_\alpha\beta$):

$$\mathbf{p} = \frac{1}{i\omega}\int \mathbf{J} d^3\mathbf{r} \tag{2.61a}$$

$$\mathbf{m} = \frac{1}{2c}\int (\mathbf{r}\times\mathbf{J}) d^3\mathbf{r} \tag{2.61b}$$

$$\mathbf{T} = \frac{1}{10c}\int [(\mathbf{r}\cdot\mathbf{J})\mathbf{r} - 2\mathbf{r}^2\mathbf{J}] d^3\mathbf{r} \tag{2.61c}$$

$$Q_{\alpha\beta} = \frac{1}{i\omega}\int [r_\alpha J_\beta + r_\beta j_\alpha - \frac{2}{3}(\mathbf{r}\cdot\mathbf{J})] d^3\mathbf{r} \tag{2.61d}$$

$$M_{\alpha\beta} = \frac{1}{3c}\int [(\mathbf{r}\times\mathbf{J})_\alpha r_\beta + (\mathbf{r}\times\mathbf{J})_\beta r_\alpha] d^3\mathbf{r} \tag{2.61e}$$

The three dipoles - the first three subequations shown above - are the most primitive building blocks of all electromagnetic sources of radiation, each belonging to a separate class of excitations. By 'separate', the following fundamental principle is meant: it is impossible to mathematically express the dipoles in terms of one another [143], and hence each family must be individually studied for a full understanding of the underlying physics.

These five excitations are the most important terms of the multipolar expansion with regards to my work. The higher-order terms are often negligible within the framework of my studies, and hence are not shown, an appropriate ansatz, as these higher-order terms are excited with increasingly higher frequencies [144], which are not considered within this work.

The electric dipole is a configuration of two charges, one negative and one positive, with the direction of the electric dipole vector pointing towards the positive charge. As can be seen in Figure 2.14, higher-order terms - such as the electric quadrupole and octupole - can be formed by combining electric dipoles for more complex arrangements.

A current oriented in a closed loop forms a magnetic dipole. The convention is that a current traveling in an anti-clockwise direction gives rise to a positive-valued magnetic moment. Again, higher-order terms in the magnetic family can be created.

While the magnetic moment is formed from a current traveling toroidally, the toroidal dipole arises from a current traveling poloidally. This is equivalent to having magnetic moments forming a closed loop. Like the magnetic moments, an anti-clockwise-traveling current engenders a positive-valued toroidal response. Once again, there is no theoretical limit on having higher-order toroidal terms.

The toroidal dipole is often overlooked in a full electromagnetic decomposition due to its comparative weakness with its siblings [144]. The power radiated by the electric and magnetic moments often drown out the toroidal moment's electromagnetic contribution. It must be noted that Radescu and Vaman are authors of two excellently in-depth papers detailing the precise formulations of the electromagnetic fields produced by the toroidal moments [143, 185].

It is possible to produce an electromagnetic configuration known as an anapole moment, whereby the radiation emitted by the toroidal moments cancels with the electric moment radiation. Upon the condition:

$$\mathbf{P} = ik\mathbf{T} \tag{2.62}$$

the electric and magnetic fields of the system vanish, but a non-zero vector potential remains. This unusual arrangement has been put forward as an explanation for dark matter [145]. Usually, if the wavelength of the field is large compared to the size of the object, the scattering is described mainly by the lowest- order multipole, the electric dipole, while the contributions from all higher-order multipoles are considered as mere perturbations [146]. However, it has been shown that in specifically designed optical metamaterials, the contribution of the magnetic dipole [147] and the electric quadrupole [148] can be generated to be significant role-players in the material's interaction with a light source. As we shall shortly see, deliberately creating strong toroidal dipoles that are in fact *stronger* than their electric and magnetic counterparts in metamaterials has been one of the main focuses of my work. To do this, the other electromagnetic moments must also be carefully analysed; the structures designed to house prevalent toroidal dipoles are engineered so as to suppress the electric and magnetic moments, often through creating antisymmetric excitations that cancel with one another. Taking care to plot the strengths of the relevant dipoles and corroborating the results through plotting the fields and current distributions at the relevant wavelengths is therefore of paramount importance.

2.6.4 Toroidal Metamaterials

One of the main focuses of my work has been to analyse the different ways in which metamaterials can be used to host toroidal dipoles, particularly at the second harmonic. This section will detail how this is achievable. While the toroidal moment that we saw in Section 2.6.3 was introduced by Zel'dovich in 1957, toroidal ordering in the solid state was first investigated theoretically in 1946 by Charles Kittel [149] in his work on ferromagnetic domains of small particles [150] and experimentally in 1974 [151] followed by a series of observations in 1984 and 1985, which confirmed the existence of static toroidal moments [152, 153].

Analogous to the electric polarization and magnetization that we observed at the start of this Chapter in Equation 2.2, a toroidal parameter, namely, toroidization, can be introduced. While the electric polarization effectively describes the electric dipole density and the magnetization describes the magnetic dipole density, the toroidization refers to the density of the toroidal dipoles. Materials that exhibit macroscopic toroidization are referred to as ferrotoroids, again analogous to ferroelectrics and ferromagnetics. Ferrotoroids, due to their make-up, will exhibit electric polarization (magnetization) in

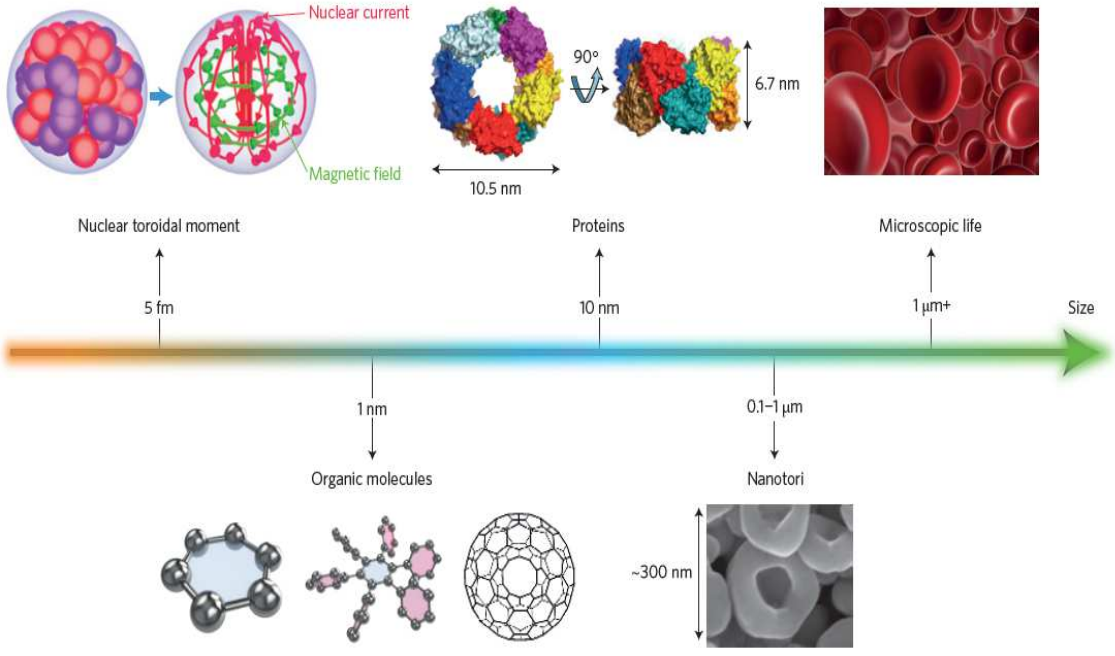

Figure 2.15: The prevalence of toroidal structures in the natural world. Taken from [149].

response to an external magnetic (electric) field [149]. This magnetoelectric response could well have an influence in applications in technological areas, such as data storage, where for example an electric field can read or write information in the magnetic state of a medium [154, 155]. In addition, ferrotoroids are expected to exhibit unique forms of

magnetic response [156–158] and nonreciprocal reflection and dichroism [159].

Since the above toroidal introductions, static toroidal dipoles have been found to exist in many natural media, including enzymes [160], DNA condensates [161], proteins [162], borocites [163], pyroxenes [164],olivines [165], metals [166], glasses [167], and hydrocarbons [168]. The toroidal activities of these substances, however, have always been weak. The prevalence of toroidal moments is described wonderfully by a figure taken from [149], shown in Figure 2.15.

In 2008, a pioneering theoretical work by Marinov et al. [169] showed that a 3D-array of toroidal solenoids would produce a significant *dynamic* toroidal response. The first toroidal metamaterial was fabricated and analysed two years later by Kaelberer et al. [170], with a strong toroidal dipole being prevalent. Since this work, which was aimed at the microwave regime, a variety of toroidal metamaterials have been produced for both microwaves [171–173] and optical frequencies [174–177] in order to further explore this new field. Peculiar effects pertaining to toroidal metamaterials include strong circular dichroism [178], electromagnetic-induced transparency [179], non-reciprocal refractive indices [180], parity nonconservation in atomic spectra [181–183], and violations of Newton's Third Law [184]. It must be added that energy conservation is not broken here once the energy and momentum of the electric field is taken into account.

As the far-field radiated by this moment is indistinguishable from the electric dipole far-field [139], it is possible to construct a system whereby the electric and toroidal fields destructively interfere with one another, leading to a non-radiating system known as an anapole moment [140], the discovery of which has been put forth as an explanation for dark matter [145]. While the behaviour of the toroidal dipole is clearly rich with curious activity, this moment is often overlooked in full electromagnetic expansions [144,185,186] due its comparative weakness with its siblings, an approach that has shown to be often dubious to the neglection of some pertinent physics [185].

The applications of toroidal moments include, among others, nanolaser [187] and plasmonic sensors [188].

Figure 2.16, taken from [170], shows the basic premise of toroidal metamaterials. In order to obtain a toroidal dipole, a closed loop of magnetic dipoles must be formed. To this end, Kaelberer et al. employed the use of split ring resonators. The light, oriented at a 45-degree angle with respect to the structure so as to ensure maximal interaction, excites a current within each loop. From the discussion of toroidal dipoles, it has been shown that a looped current produces a magnetic moment. Therefore, each split ring resonator produces their own magnetic moment, and these in turn form a closed loop, engendering a toroidal dipole. The orientation of the gaps in the rings is to ensure a minimal electric dipole excitation.

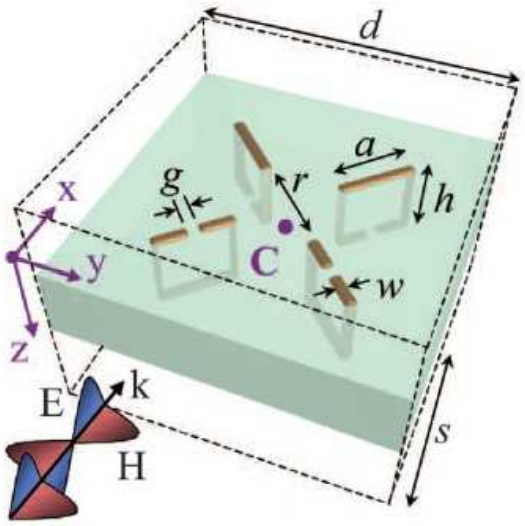

Figure 2.16: A metamaterial taken from [170], designed to host a toroidal dipole moment. Each metallic SRR is excited by the incoming electromagnetic wave. The induced currents give rise to magnetic moments, which in turn form a loop. A toroidal dipole is therefore generated.

Recently, an innovative work has shown that metal is not a required composite for a meta-atom [138] to produce dynamic toroidal dipoles. In this cited work, the structure in question consists of four parallel $LiTaO_3$ cylinders, shown in Figure 2.17. The incoming light induces Mie resonances, generating magnetic moments in each sub-unit of the structure, giving rise to a toroidal dipole. As is often the case with fabricating a structure designed to host a strong toroidal moment, achieving a 'perfect' loop (i.e. a total magnetic moment equal to zero) is a theoretical impossibility; the desired circle is 'chopped' into a number of segments that approximate a loop. In the depicted examples of Figure 2.16 and 2.17, if more units were incorporated, it would naturally more resemble a circular structure.

As we saw from the previous discussion, the use of all-dielectric metamaterial structures allows the dissipation loss of metals to be overcome [189, 190]. It is therefore no surprise that all-dielectric structures have shown promising results for biosensing and energy applications [141]. All-dielectric structures have since been theoretically [190] and experimentally [191, 192] shown to host strong toroidal dipoles.

2.7 Conclusions

We have analysed the underlying physics of metamaterials, showing how some novel phenomena can arise from metallic and all-dielectric meta-atoms. In particular, focus was

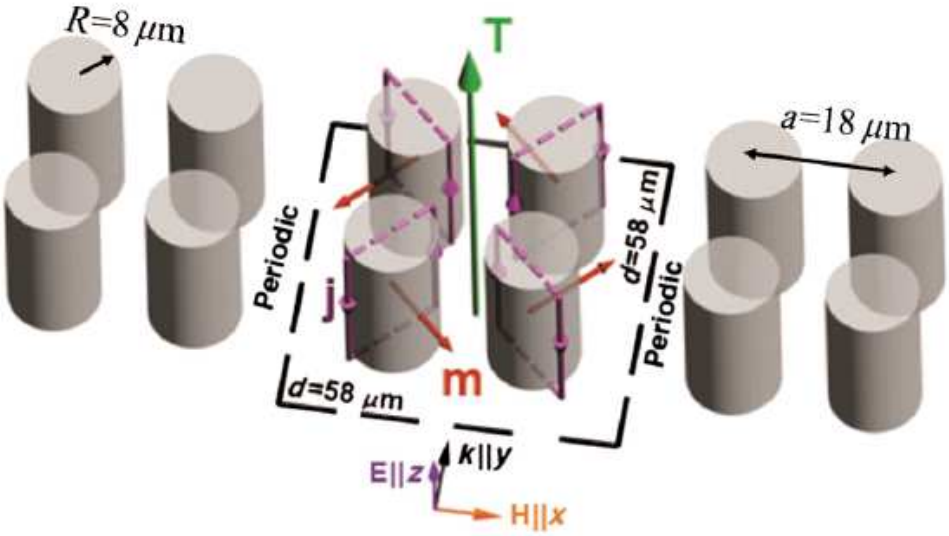

Figure 2.17: A metamaterial taken from [138], designed to host a toroidal dipole moment. The external light excites displacement currents within each cylinder, which in turn form a magnetic moment. The four magnetic moments interact with one another in a way that creates a closed loop, forming a toroidal dipole without the use of metal.

given to the electric permittivity functions of the materials, as these are in effect responsible for the macroscopic electromagnetic responses. Due to the fact that a large body of my work relies on engendering nonlinear signals from meta-atoms, the physics of second-harmonic generation of both plasmonic and all-dielectric meta-atoms was delineated in order to familiarise the reader with the applications and ideas of this field. The multipole expansion, with specific attention being given on the more exotic toroidal dipole, was also presented. These electromagnetic excitations provide detailed explanations of the workings of the meta-atoms. The curious phenomena and applications of these moments were also specified.

Bibliography

[1] P. J. Nahin, *The Life, Work, and Times of an Electrical Genius of the Victorian Age*, (John Hopkins University Press, 2002).

[2] http://www.metamorphose-eu.org/

[3] J. A. Stratton, *Electromagnetic Theory* (John Wiley and Sons, 1941).

[4] M. Born and E. Wolf *Principle of Optics*, 7th Edition, (Cambridge University Press, 1999).

[5] W. Cai and V. Shalaev, *Optical Metamaterials. Fundamentals and Applications* (Springer US, 2009).

[6] S. Maier, *Plasmonics: Fundamentals and Applications* (Springer US, 2007).

[7] P. Drude, "Zur Elektronentheorie der Metalle", Annalen der Physik **306**, 566-613 (1900).

[8] H. S. Nalwa, *Handbook of Advanced Electronic and Photonic Materials and Devices* (Academic Press, 2000).

[9] K. Murata, and H. Tanaka, "Surface-wetting effects on the liquid-liquid transition of a single-component molecular liquid", Nat. Comm. **1**, 16 (2010).

[10] N. Laman, and D. Grischkowsky, "Redued conductivity in the terahertz skin-depth layer of metals", Appl. Phys. Lett. **90**, 122115 (2007).

[11] J. M. Pitarke, V. M. Silkin, E. V. Chulkov, and P. M. Echenique, "Theory of surface plasmons and surface-plasmon polaritons", Rep. Prog. Phys. **70**, 1-87 (2007).

[12] W. Nomura, M. Ohtsu, and T. Yatsui, "Nanodot Coupler with a Surface Plasmon Polariton Condenser for Optical Far/Near-Field Conversion", Appl. Phys. Lett. **86**, 181108 (2005).

[13] N. C. Panoiu, and R. M. Osgood, "Subwavelength Nonlinear Plasmonic Nanowire", Nano Lett. **4**, 24272430 (2004).

[14] J. L. West, and N. J. Halas, "Engineered Nanomaterials for Biophotonics Applications: Improving Sensing, Imaging and Therapeutics", Annu. Rev. Biomed. Eng **5**, 285-92 (2003).

[15] C. J. Chen, R. M. Osgood, "Direct Observation of the Local-Field-Enhanced Surface Photochemical Reactions", Phys. Rev. Lett. **50**, 1705-1708 (1983).

[16] R. H. Ritchie, "Surface plasmons in solids", Surf. Sci. **34**, 1-19 (1973).

[17] P. J. Friebelman, "Electronic Screening at Metal Surfaces and the Connection with Physical Phenomena", Prog. Surf. Sci. **12**, 354-364 (1982).

[18] A. Liebsch *Electronic Excitations at Metal Surfaces* (Springer US, 1997).

[19] D. Ye, Z. Wang, K. Xu, H. Li, J. Huangfu, Z. Wang, and L. Ran, "Ultrawideband Dispersion Control of a Metamaterial Surface for Perfectly-Matched-Layer-Like Absorption", Phys. Rev. Lett. **111**, 187402 (2013).

[20] D. Ye, C. Cao, T. Zhou, J. Huangfu, G. Zheng, and L. Ran, "Observation of reflectionless absorption due to spatial KramersKronig profile", Nat. Comm., **8**, 51 (2017).

[21] W. Jiang, Y. Ma, J. Yuan, G. Yin, W. Wu, and S. He, "Deformable broadband metamaterial absorbers engineered with an analytical spatial KramersKronig permittivity profile", Laser and Phot. Rev. **11**, 1600253 (2017).

[22] P. A. Franken, A. E. Hill, C. W. Peters, and G. Weinreich, "Generation of Optical Harmonics", Phys. Rev. Lett. **7**, 118-120 (1961).

[23] G. H. C. New, and J. F. Ward, "Optical Third-harmonic Generation in Gases", Phys. Rev. Lett. **19**, 556-559 (1967).

[24] R. W. Terhune, P. D. Maker, and C. M. Savage, "Optical Harmonic Generation in Calcite", Phys. Rev. Lett. **8**, 404-406 (1962).

[25] R. W. Boyd, *Nonlinear Optics* (Academic Press, 2008).

[26] L. Cao, N. C. Panoiu, and R. M. Osgood, "J. Surface Second-Harmonic Generation from Surface Plasmon Waves Scattered by Metallic Nanostructures", Phys. Rev. B **75**, 205401 (2007).

[27] P. Guyot-Sionnest, and Y. R. Shen "Bulk Contribution in Surface Second-Harmonic Generation", Phys. Rev. B **38**, 7985-7989 (1988).

[28] J. E. Sipe, V. C. Y. So, M. Fukui, and G. I. Stegeman, "Analysis of second-harmonic generation at metal surfaces", Phys. Rev. B **21**, 4389-4402 (1980).

[29] F. Wang, F. J. Rodriguez, W. M. Albers, R. Ahorinta, J. E. Sipe, and M. Kauranen, "Surface and bulk contributions to the second-order nonlinear optical response of a gold film", Phys. Rev. B **80**, 233402 (2009).

[30] A. Taflove, and S. C. Hagness, *Computational Electrodynamics: The Finite Difference Time Domain Method*, Chapter 8, (Artech House, 2005).

[31] S. T. Cundiff, W. H. Knox, F. H. Baumann, K. W. Evans-Lutterodt, and M. L. Green, "Second-harmonic generation at the interface between Si(100) and thin SiO_2 layers", Journal of Vacuum Science & Technology A **16**, 1730-1734 (1998).

[32] H. W. K. Tom, T. F. Heinz, and Y. R. Shen, "Second-harmonic reflection from silicon surfaces and its relation to structural symmetry", Phys. Rev. Lett. **51**, 1983-1986 (1983).

[33] G. Lüpke, D. J. Bottomley, and H. M. van Driel, "SiO_2/Si interfacial structure on vicinal Si(100) studied with second-harmonic generation", Phys. Rev. B **47**, 10389 (1993).

[34] C. K. Chen, A. B. de Castro, and Y. B. Shen, "Surface-enchanced second-harmonic generation", Phys. Rev. Lett. **46**, 1555-1564 (1981).

[35] G. Erley, and W. Daum, "Silicon interband transitions observed at Si(100)-SiO_2 interfaces", Phys. Rev. B **58**, R1734(R) (1998).

[36] R. C. Miller, "Optical second harmonic generation in piezoelectric crystals", Appl. Phys. Lett. **5**, 17-18 (1964).

[37] D. R. Smith, S. Schultz, P. Markoš, and C. M. Soukoulis, "Determination of effective permittivity and permeability of metamaterials from reflection and transmission coefficients", Phys. Rev. B **65**, 195104 (2002).

[38] Conférence Générale des Poids et Mesures, XV, Pairs, 1975, Comptes Rendus des Séances (Paris, Bureau International des Poids et Mesures, 1976).

[39] C. M. Soukoulis, and M. Wegener, "Past achievements and future challenges in the development of three-dimensional photonic metamaterials", Nat. Phot. **5**, 523-530 (2011).

[40] N. Fang, D. Xi, J. Xu, M. Ambati, W. Srituravanich, C. Sun, and X. Zhang, "Ultrasonic metamaterials with negative modulus", Nat. Mat. **5**, 452456 (2006).

[41] X. Zheng, H. Lee, T. H. Weisgraber, M. Shusteff, J. DeOtte, E. B. Duoss, J. D. Kuntz, M. M. Biener, Q. Ge, J. A. Jackson, S. O. Kucheyev, N. X. Fang, and C. M. Spadaccini, "Ultralight, ultrastiff mechanical metamaterials", Science **344**, 1373-1377 (2014).

[42] Y. Liu, and X. Zhang, "Metamaterials: a new frontier of science and technology", Chem. Soc. Rev. **40**, 2494-2507 (2011).

[43] V. G. Veselago, "The electrodynamics of substances with simulataneously negative values of ϵ and μ Sov. Phys. Usp. **10**, 509-514 (1968).

[44] R. A. Depine, and A. A. Lakhtakia, "New condition to identify isotropic dielectric-magnetic materials displaying negative phase velocity", Microw. Opt. Technol. Lett. **41**, 315-316 (2004).

[45] J. B. Pendry, A. J. Holden, D. J. Robbins, and W. J. Stewart, "Magnetism from conductors and enhanced nonlinear phenomena", IEEE Transactions on Microwave Theory and Techniques, **47**, 2075-2084 (1990).

[46] D. R. Smith, W. J. Padilla, D. C. Vier, S. C. Nemat-Nasser, and S. Schultz, "Composite medium with simultaneously negative permeability and permittivity", Phys. Rev. Lett. **84**, 4184-4187 (2000).

[47] R. A. Shelby, D. R. Smith, and S. Schultz, "Experimental verification of a negative index of refraction", Science **292**, 77-79 (2001).

[48] H. Chen, W. J. Padilla, J. M. O. Zide, A. C. Gossard, A. J. Taylor, and R. D. Averitt, "Active terahertz metamaterial devices", Nature **444**, 597600 (2006).

[49] W. J. Padilla, M. T. Aronsson, C. Highstrete, M. Lee, A. J. Taylor, and R. D. Averitt, "Electrically resonant terahertz metamaterials: theoretical and experimental investigations", Phys. Rev. B **75**, 041102(R) (2007).

[50] A. K. Azad, A. J. Taylor, E. Smirnova, and J. F. O'Hara, "Characterization and analysis of terahertz metamaterials based on rectangular split-ring resonators", Appl. Phys. Lett. **92**, 011119 (2008).

[51] M. W. Klein, C. Enkrich, M. Wegener, C. M. Soukoulis, and S. Linden, "Single-slit split-ring resonators at optical frequencies: limits of size scaling", Opt. Lett. **31**, 1259-1261 (2006).

[52] T. D. Corrigan, P. W. Kolb, A. B. Sushkov, H. D. Drew, D. C. Schmadel, and R. J. Phaneuf, "Optical plasmonic resonances in split-ring resonator structures: an improved LC model", Opt. Exp. **16**, 19850-19864 (2008).

[53] J. B. Pendry, D. Schurig, and D. R. Smith, "Controlling electromagnetic fields", Science **312**, 1780-1782 (2006).

[54] J. B. Pendry, "Negative refraction makes a perfect lens" Phys. Rev. Lett. **85**, 3966-3969 (2000).

[55] B. Wang, Z. Xie, S. Feng, B. Zhang, and Y. Zhang, "Ultrahigh Q-factor and figure of merit Fano metamaterial based on dark ring magnetic mode", Opt. Commun. **335**, 60-64 (2015).

[56] I. Al-Naib, R. Singh, C. Rockstuhl, F. Lederer, S. Delprat, D. Rocheleau, M. Chaker, T. Ozaki, and R. Morandotti, "Excitation of a high-Q subradiant resonance mode in mirrored single-gap asymmetric split ring resonator terahertz metamaterials", Appl. Phys. Lett. **101**, 071108 (2012).

[57] H. Tao, A. C. Strikwerda, K. Fan, C. M. Bingham, W. J. Padilla, X. Zhang, and R. D. Averitt, "Terahertz metamaterials on free-standing highly-flexible polyimide substrates", J. Phys. D: Appl. Phys. **41**, 232004 (2008).

[58] K. Fan, A. C. Strikwerda, H. Tao, X. Zhang, and R. D. Averitt, "Stand-up magnetic metamaterials at terahertz frequencies", Opt. Exp. **19**, 12619-12627 (2011).

[59] H. Tao, J. J. Amsden, A. C. Strikwerda, K. Fan, D. L. Kaplan, X. Zhang, R. D. Averitt, F. G. Omenetto, "Metamaterial silk composites at terahertz frequencies", Adv. Mat. **22**, 3527-31 (2010).

[60] E. Prodan, C. Radloff, N. J. Halas, and P. Nordlander, "A hybridization model for the plasmon response of complex nanostructures", Science **302**, 419-422 (2003).

[61] H. Liu, Y. M. Liu, T. Li, S. M. Wang, S. N. Zhu, and X. Zhang, "Coupled magnetic plasmons in metamaterials", Phys. Status. Solidi B **246**, 1347-1406, (2009).

[62] H. Liu, D. A. Genov, D. M. Wu, Y. M. Liu, Z. W. Liu, C. Sun, S. N. Zhu, and X. Zhang, "Magnetic plasmon hybridization and optical activity at optical frequencies in metallic nanostructures", Phys. Rev. B **76**, 073101 (2007).

[63] D. A. Powell, M. Lapine, M. V. Gorkunov, I. V. Shadrivov, and Y. S. Kivshar, "Metamaterial tuning by manipulation of near-field interaction", Phys. Rev. B **86**, 155128 (2010).

[64] N. Liu, H. Liu, S. N. Zhu, and H. Giessen, "Lagrange model for the chiral optical properties of stereometamaterials", Nat. Photonics. **3**, 157-162 (2009).

[65] http://wok.mimas.ac.uk/

[66] X. Chen, T. M. Grzegorczyk, B.-I. Wu, J. Pacheco, Jr. and J. A. Kong, "Robust method to retrieve the constitutive effective parameters of metamaterials", Phys. Rev. E **70**, 016608 (2004).

[67] N. I. Landy, C. M. Bingham, T. Tyler, N. Jokerst, D. R. Smith, and W. J. Padilla, "Design, theory, and measurement of a polarization-insensitive absorber for terahertz imaging", Phys. Rev. B **79**, 207402 (2009).

[68] N. Liu, M. Mesch, T. Weiss, M. Hentschel, and H. Giessen, "Infrared perfect absorber and its application as plasmonic sensor", Nano Lett. **10**, 23422348 (2010).

[69] L. Huang, D. R. Chowdhury, S. Ramani, M. T. Reiten, S. Luo, A. J. Taylor, and H. Chen, "Experimental demonstration of terahertz metamaterial absorbers with a broad and flat high absorption band", Opt. Lett. **37**, 154-156 (2012).

[70] H. Tao, C. M. Bingham, A. C. Strikwerda, D. Pilon, D. Shrekenhamer, N. I. Landy, K. Fan, X. Zhang, W. J. Padilla, and R. D. Averitt, "Highly flexible wide angle of incidence terahertz metamaterial absorber: design, fabrication, and characterization", Phys. Rev. B **78**, 241103(R) (2008).

[71] M. Diem, T. Koschny, and C. M. Soukoulis, "Wide-angle perfect absorber/thermal emitter in the terahertz regime", Phys. Rev. B **79**, 033101 (2009).

[72] D. Ye, Z. Wang, K. Xu, H. Li, J. Huangfu, Z. Wang, L. Ran, "Ultrawideband dispersion control of a metamaterial surface for perfectly-matched-layer-like absorption", Phys. Rev. Lett. **111**, 187402 (2013).

[73] T. Cao, C. Wei, R. E. Simpson, L. Zhang, and M. J. Cryan, "Broadband polarization-independent perfect absorber using a phase-change metamaterial at visible frequencies", Sci. Rep. **4**, 3955 (2014).

[74] S. Gu, J. P. Barrett, T. H. Hand, B. I. Popa, and S. A. Cummer, "A broadband low-reflection metamaterial absorber", J. Appl. Phys. **108**, 064913 (2010).

[75] H. Tao, C. M. Bingham, D. Pilon, K. Fan, A. C. Strikwerda, D. Shrekenhamer, W. J. Padilla, X. Zhang, R. D. Averitt, "A dual band terahertz metamaterial absorber", J. Phys. D: Appl. Phys. **43**, 225102 (2010).

[76] Q. Wen, H. Zhang, Y. Xie, Q. Yang, and Y. Liu, "Dual band terahertz metamaterial absorber: design, fabrication, and characterization", Appl. Phys. Lett. **95**, 241111 (2009).

[77] D. T. Vieta, N. T. Hiena, P. V. Tuonga, N. Q. Minha, P. T. Tranga, L. N. Lea, Y. P. Leeb, and V. D. Lama, "Perfect absorber metamaterials: peak, multi-peak and broadband absorption" Opt. Commun. **322**, 209-213 (2014).

[78] Z. Mao, S. Liu, B. Bian, B. Wang, B. Ma, L. Chen, and J. Xu, "Multi-band polarization-insensitive metamaterial absorber based on chinese ancient coin-shaped structures", J. Appl. Phys. **115**, 204505 (2014).

[79] N. I. Landy, S.; Sajuyigbe, J. J. Mock, D. R. Smith, and W. J. Padilla, "Perfect metamaterial absorber", Phys. Rev. Lett. **100**, 207402 (2008).

[80] X. Liu, T. Starr, A. F. Starr, and W. J. Padilla, "Infrared spatial and frequency selective metamaterial with near-unity absorbance", Phys. Rev. Lett. **104**, 207403 (2010).

[81] D. Y. Shchegolkov, A. K. Azad, J. F. O'Hara, and E. I. Simakov, "Perfect subwavelength fishnetlike metamaterial-based film terahertz absorbers", Phys. Rev. B **82**, 205117 (2010).

[82] J. Hao, J. Wang, X. Liu, W. J. Padilla, L. Zhou, and M. Qiu, "High performance optical absorber based on a plasmonic metamaterial", Appl. Phys. Lett. **96**, 251104 (2010).

[83] Z. Li, S. Butun, and K. Aydin, "Ultranarrow band absorbers based on surface lattice resonances in nanostructured metal surfaces" ACS Nano **8**, 82428248 (2014).

[84] F. Abeès, "Recherches thoriques sur les propriétés optiques des lames minces", Le Journal de Physique et le Radium **11**, 301-310 (1950).

[85] M. Ren, E. Plum, J. Xu, and N. I. Zheludev, "Giant nonlinear optical activity in a plasmonic metamaterial", Nat. Comm. **3**, 833 (2012).

[86] S. A. Akhmanov, B. V. Zhdanov, N. I. Zheludev, A. I. Kovrigin, and V. I. Kuznetsov, "Nonlinear optical activity in crystals", JETP Lett. **29**, 264-268 (1979).

[87] D. Vlasov, and V. Zaitsev, "Experimental observation of nonlinear optical activity", JETP Lett. **14**, 112-115 (1971).

[88] V. V. Borshch, M. P. Lisitsa, P. E. Mozol, and I. V. Fekeshgaz, "Self-induced rotation of the direction of polarization of light in crystals of 422 symmetry", Sov. J. Quantum Electron **8**, 393-395 (1978).

[89] N. I. Zheludev, I. S. Ruddock, and R. Illingworth, "Intensity dependence of thermal nonlinear optical activity in crystals", Appl. Phys. B **49**, 65-67 (1989).

[90] R. Cameron and G. Tabisz, "Observation of two-photon optical rotation by molecules", Mol. Phys. **90**, 159-164 (1997).

[91] H. Mesnil, F. Hache, "Experimental evidence of third-order nonlinear dichroism in a liquid of chiral molecules", Phys. Rev. Lett. **85**, 4257-4260 (2000).

[92] H. Mesnil, M. C. Schanne-Klein, F. Hache, M. Alexandre, G. Lemercier, and C. Andraud, "Experimental observation of nonlinear circular dichroism in a pump-probe experiment", Chem. Phys. Lett. **338**, 269-276 (2001).

[93] P. P. Markowicz, M. Samoc, J. Cerne, P. N. Prasad, A. Pucci, and G. Ruggeri, "Modified z-scan techniques for investigations of nonlinear chiroptical effects", Opt. Exp. **12**, 5209-5214 (2004).

[94] V. M. Agranovich, Y. R. Shen, R. H. Baughman, and A. A. Zakhidov, "Linear and nonlinear wave propagation in negative refraction metamaterials", Phys. Rev. B **69**, 165112 (2004).

[95] M. Scalora, M. S. Syrchin, N. Akozbek, E. Y. Poliakov, G. D'Aguanno, N. Mattiucci, M. J. Bloemer, and A. Zheltikov, "Generalized nonlinear Schrdinger equation for dispersive susceptibility and permeability: application to negative index materials", Phys. Rev. Lett. **95**, 013902 (2006).

[96] A. K. Popov, and V. M. Shalaev, "Negative-index metamaterials: second-harmonic generation, ManleyRowe relations and parametric amplification", Appl. Phys. B **84**, 131-137 (2006).

[97] I. V. Shadrivov, A. A. Zharov, and Y. S. Kivshar, "Second-harmonic generation in nonlinear lefthanded metamaterials", J Opt Soc Am B **23**, 529-534 (2006).

[98] M. Scalora, G. DAguanno, M. Bloemer, M. Centini, D. de Ceglia, N. Mattiucci, and Y. S. Kivshar, "Dynamics of short pulses and phase matched second harmonic generation in negative index materials", Opt. Exp. **14**, 4746-4756 (2006).

[99] A. K. Popov, and V. M. Shalaev, "Compensating losses in negative-index metamaterials by optical parametric amplification", Opt. Lett. **31**, 2169-2171 (2006).

[100] Y. Yang, W. Wang, A. Boulesbaa, I. I. Kravchenko, D. P. Briggs, A. Puretzky, D. Geohegan, and J. Valentine, "Nonlinear Fano-resonant dielectric metasurfaces" Nano Lett. **15**, 73887393 (2015).

[101] A. E. Nikolaenko, N. Papasimakis, E. Atmatzakis, Z. Luo, Z. X. Shen, F. D. Angelis, S. A. Boden, E. D. Fabrizio, and N. I. Zheludev, "Nonlinear graphene metamaterial" Appl. Phys. Lett. **100**, 181109 (2012).

[102] M. Kauranen, and A. V. Zayats, "Nonlinear Plasmonics", Nat. Photon. **6**, 737-748 (2012).

[103] J. Butet, P. F. Brevet, and O. J. F. Martin, "Optical second harmonic generation in plasmonic nanostructures: from fundamental principles to advanced applications", ACS Nano **9**, 10545-10562 (2015).

[104] K. Kneipp, Y. Wang, H. Kneipp, L. T. Perelman, I. Itzkan, R. R. Dasari, and M. S. Feld, "Single molecule detection using surface-enhanced Raman Scattering (SERS)", Phys. Rev. Lett. **78**, 1667-1670 (1997).

[105] S. M. Nie and S. R. Emory, "Probing single molecules and single nanoparticles by surface-enhanced Raman Scattering", Science **275**, 1102-1106 (1997).

[106] R. M. Roth, N. C. Panoiu, M. M. Adams, R. M. Osgood, C. C. Neacsu, and M. B. Raschke, "Resonant-plasmon field enhancement from asymmetrically illuminated conical metallic-probe tips", Opt. Exp. **14**, 2921-2931 (2006).

[107] N. Bloembergen, R. K. Chang, S. S. Jha, and C. H. Lee, "Optical second-harmonic generation in reflection from media with inversion symmetry", Phys. Rev. **178**, 1528-1528 (1969).

[108] S. I. Bozhevolnyi, J. Beermann, and V. Coello, "Direct observation of localized second-harmonic enhancement in random metal nanostructures", Phys. Rev. Lett. **90**, 7403-7406 (2003).

[109] J. A. H. van Nieuwstadt, M. Sandtke, R. H. Harmsen, F. B. Segerink, J. C. Prangsma, S. Enoch, and L. Kuipers, "Strong modification of the nonlinear optical response of metallic subwavelength hole arrays", Phys. Rev. Lett. **97**, 146102 (2006).

[110] W. Fan, S. Zhang, N. C. Panoiu, A. Abdenour, S. Krishna, R. M. Osgood, K. J. Malloy, and S. R. J. Brueck, "Second harmonic generation from a nanopatterned isotropic nonlinear material", Nano Lett. **6**, 1027-1030 (2006).

[111] L. Cao, N. C. Panoiu, and R. M. Osgood, "Surface second-harmonic generation from surface plasmon waves scattered by metallic nanostructures", Phys. Rev. B **75**, 5401-5407 (2007).

[112] G. Bachelier, I. Russier-Antoine, E. Benichou, C. Jonin, and P. F. Brevet, "Multipolar second-harmonic generation in noble metal nanoparticles", J. Opt. Soc. Am. B **25**, 955-960 (2008).

[113] V. K. Valev, A. V. Silhanek, N. Verellen, W. Gillijns, P. V. Dorpe, O. A. Aktsipetrov, G. A. E. Vandenbosch, V. V. Moshchalkov, and T. Verbiest, "Asymmetric optical second-harmonic generation from chiral G-shaped gold nanostructures", Phys. Rev. Lett. **104**, 7401-7404 (2010).

[114] C. G. Biris, and N. C. Panoiu, "Second harmonic generation in metamaterials based on homogeneous centrosymmetric nanowires", Phys. Rev. B **81**, 5102-5117 (2010).

[115] L. H. Haber, S. J. J. Kwok, M. Semeraro, and K. B. Eisenthal, "Probing the colloidal gold nanoparticle/aqueous interface with second harmonic generation", Chem. Phys. Lett. **507**, 11-14 (2011).

[116] A. Capretti, E. F. Pecora, C. Forestiere, L. D. Negro, and G. Miano, "Size-dependent second-harmonic generation from gold nanoparticles", Phys. Rev. B **89**, 5414-5418 (2014).

[117] R. Czaplicki, J. Makitalo, R. Siikanen, H. Husu, J. Lehtolahti, M. Kuittinen, and M. Kauranen, "Second-harmonic generation from metal nanoparticles: resonance enhancement versus particle geometry", Nano Lett. **15**, 530-534 (2015).

[118] G. Sartorello, N. Olivier, J. Zhang, W. Yue, D. J. Gosztola, G. P. Wiederrecht, G. Wurtz, and A. V. Zayats, "Ultrafast optical modulation of second- and third-harmonic generation from cut-disk-based metasurfaces" ACS Photon. **3**, 1517-1522 (2016).

[119] I. I. Smolyaninov, A. V. Zayats, A. Gungor, and C. C. Davis, "Single-photon tunneling via localized surface plasmons", Phys. Rev. Lett. **88**, 7402-7405 (2002).

[120] X. W. Wang, G. C. Schatz, and S. K. Gray, "Ultrafast pulse excitation of a metallic nanosystem containing a Kerr nonlinear material", Phys. Rev. B **74**, 5439 (2006).

[121] J. Zhang, K. F. MacDonald, and N. I. Zheludev, "Nonlinear dielectric optomechanical metamaterials", Light: Science and Applications **2**, 1-5 (2013).

[122] C. Wu, N. Arju, G. Kelp, J. A. Fan, J. Dominguez, E. Gonzales, E. Tutuc, I. Brener, and G. Shvets, "Spectrally selective chiral silicon metasurfaces based on infrared Fano resonances", Nat. Comm. **5**, 3892 (2014).

[123] A. V. Zayats, I. I. Smolyaninov, A. A. Maradudin, "Nano-optics of surface plasmon polaritons", Phys. Rep. **408**, 131-314 (2005).

[124] B. Knoll, B. and F. Keilmann, "Near-field probing of vibrational absorption for chemical microscopy", Nature (London) **399**, 134-137(1999).

[125] N. C. Panoiu, and R. M. Osgood, "Subwavelength nonlinear plasmonic nanowire", Nano Lett. **4**, 24272430 (2004).

[126] G. Veronis, and S. Fan, "Bends and splitters in metal-dielectric-metal subwavelength plasmonic waveguides", Appl. Phys. Lett. **87**, 1102-1104 (2005).

[127] T. H. Taminiau, R. J. Moerland, F. B. Segerink, L. Kuipers, and N. F. van Hulst, "$\lambda/4$ resonance of an optical monopole antenna probed by single molecule fluorescence", Nano Lett. **7**, 28-33 (2007).

[128] F. Ye, D. Mihalache, B. Hu, and N. C. Panoiu, "Subwavelength plasmonic lattice solitons in arrays of metallic nanowires", Phys. Rev. Lett. **104**, 106802 (2010).

[129] J. B. Khurgin, "How to deal with the loss in plasmonics and metamaterials", Nat. Nanotechnol. **10**, 2-6 (2015).

[130] A. J. Hoffman, L. Alekseyev, S. S. Howard, K. J. Franz, D. Wasserman, V. A. Podolskiy, E. E. Narimanov, D. L. Sivco, and C. Gmachl, "Negative refraction in semiconductor metamaterials", Nat. Mater. **6**, 946-950 (2007).

[131] S. Xiao, V. P. Drachev, A. V. Kildishev, X. Ni, U. K. Chettiar, H. K. Yuan, and V. M. Shalaev, "Loss-free and active optical negative-index metamaterials", Nature (London) **466**, 735-738 (2010).

[132] A. Garcia-Etxarri, R. Gomez-Medina, L. S. Froufe-Perez, C. Lopez, L. Chantada, F. Scheffold, J. Aizpurua, M. Nieto-Vesperinas, and J. J. Saenz, "Strong magnetic response of submicron Silicon particles in the infrared", Opt. Exp. **19**, 4815-4826 (2011).

[133] A. I. Kuznetsov, A. E. Miroshnichenko, Y. H. Fu, J. Zhang, and B. Luk'yanchuk, "Magnetic light", Sci. Rep. **2**, 492 (2012).

[134] C. F. Bohren, and D. R. Huffman, *Absorption and Scattering of Light by Small Particles* (Wiley-Interscience, 1983).

[135] S. Liu, M. B. Sinclair, T. S. Mahony, Y. C. Jun, S. Campione, J. Ginn, D. A. Bender, J. R. Wendt, J. F. Ihlefeld, P. G. Clem, J. B. Wright, and I. Brener, "Optical magnetic mirrors without metals", Optica **1**, 250-256 (2014).

[136] C. Pfeiffer, and A. Grbic, "Metamaterial Huygens' surfaces: tailoring wave fronts with reflectionless sheets", Phys. Rev. Lett. **110**, 7401-7105 (2013).

[137] M. Decker, I. Staude, M. Falkner, J. Dominguez, D. N. Neshev, I. Brener, T. Pertsch, and Y. S. Kivshar, "High-efficiency dielectric Huygens' surfaces", Adv. Opt. Mater. **3**, 813-820 (2015).

[138] A. A. Basharin, M. Kafesaki, E. N. Economou, C. M. Soukoulis, V. A. Fedotov, V. Savinov, and N. I. Zheludev, "Dielectric metamaterials with toroidal dipolar response", Phys. Rev. X **5**, 1036-1046 (2015).

[139] G. N. Afanasiev and Y. P. Stepanovsky, "The electromagnetic field of elementary time-dependent toroidal sources", J. Phys. A **28**, 4565-4581 (1995).

[140] A. E. Miroshnichenko, A. B. Evlyukhin, Y. F. Yu, R. M. Bakker, A. Chipouline, A. I. Kuznetsov, B. Luk'yanchuk, B. N. Chichkov, and Y. S. Kivshar, "Nonradiating anapole modes in dielectric nanoparticles", Nat. Commun. **6**, 8069-8076 (2015).

[141] Y. S. Kivshar and A. Miroshnichenko, "Meta-Optics with Mie resonances", Optics and Photonics News **28**, 26-33 (2017).

[142] V. Savinov, V. A. Fedotov, and N. I. Zheludev, "Toroidal dipolar excitation and macroscopic electromagnetic properties of metamaterials", Phys. Rev. B **89**, 205112 (2014).

[143] E. E. Radescu, and G. Vaman, "Toroid moments in the momentum and angular momentum loss by a radiating arbitrary source", Phys. Rev. E **65**, 035601(R) (2002).

[144] J. D. Jackson, *Classical Electrodynamics* (John Wiley and Sons, 1962).

[145] C. M. Ho, and R. J. Scherrer, "Anapole dark matter", Phys. Lett. B, **722**, 341-346 (2013).

[146] P. Grahn, A. Shevchenko, and M. Kaivola, "Electromagnetic multipole theory for optical nanomaterials" New J. Phys. **14**, 093033 (2012).

[147] T. J. Yen, W. J. Padilla, N. Fang. D. C. Vier, D. R. Smith, J. B. Pendry, D. N. Basov, and X. Zhang, "Terahertz magnetic response from artificial materials", Science **303**, 1494-1496 (2004).

[148] D. J. Cho, F. Wang, X. Zhang, and Y. R. Shen, "Contribution of the electric quadrupole resonance in optical metamaterials", Phys. Rev. B **78**, 121101 (2008).

[149] N. Papasimakis, V. A. Fedotov, V. Savinov, T. A. Raybould, and N. I. Zheludev, "Electromagnetic toroidal excitations in matter and free space" Nat. Mater. **15**, 263271 (2016).

[150] C. Kittel, "Theory of the structure of ferromagnetic domains in films and small particles" Phys. Rev. **70**, 965-971 (1946).

[151] I. S. Zheludev, T. M. Perekalina, E. M.; Smirnovskaya, S. S. Fonton, and Y. N. Yarmukhamedov, "Magnetic properties of nickel-boracite iodide", JETP Lett. **20**, 129-130 (1974).

[152] V. L. Ginzburg, A. A. Gorbatsevich, Y. V. Kopayev, and B. A. Volkov, "On the problem of superdiamagnetism", Solid State Commun **50**, 339-343 (1984).

[153] D. G. Sannikov and I. S. Zheludev, "On the possibility of phase transitions with spontaneous toroidal moment formation in nickel boracites", Sov. Phys. Solid State **27**, 826828 (1985).

[154] D. Khomskii, "Classifying multiferroics: mechanisms and effects", Physics **2**, 20 (2009).

[155] A. P. Pyatakov, and A. K. Zvezdin, "Magnetoelectric and multiferroic media", Phys. Usp **55**, 557581 (2012).

[156] N. A. Tolstoi and A. A. Spartakov, "Aromagnetism: a new type of magnetism", JETP Lett, **52**, 161-164 (1990).

[157] V. A. Fedotov, K. Marinov, A. D. Boardman, and N. I. Zheludev, "On the aromagnetism and anapole moment of anthracene nanocrystals", New J. Phys. **9**, 95 (2007).

[158] M. A. Martsenyuk and N. M. Martsenyuk, "Origin of aromagnetism", JETP Lett. **53**, 243-246 (1991).

[159] N. A. Spaldin, M. Fiebig, and M. Mostovoy, "The toroidal moment in condensed-matter physics and its relation to the magnetoelectric effect", J. Phys. Condens. Matter **20**, 434203 (2008).

[160] R. Kovall and B. W. Matthews, "Toroidal structure of lambda-exonuclease", Science, **277**, 1824-1827 (1997).

[161] N. V. Hud and I. D. Vilfan, "Toroidal DNA condensates: unraveling the fine structure and the role of nucleation in determining size", Annu. Rev. Biophys. Biomol. Struct. **34**, 295-318 (2005).

[162] M. M. Hingorani and M. O'Donnell, "A tale of toroids in DNA metabolism", Nat. Rev. Mol. Cell Biol. textbf1, 2230 (2000).

[163] D. G. Sannikov, "Phenomenological theory of the magnetoelectric effect in some boracites", Zh. Eksp. Teor. Fiz. **111**, 536546 (1997); (English translation in J. Exp. Theor. Phys. **84**, 293299),

[164] B. Mettout, P. Tolédano, and M. Fiebig, "Symmetry replication and toroidic effects in the multiferroic pyroxene $NaFeSi_2O_6$", Phys. Rev. B **81**, 214417 (2010).

[165] H.-J. Feng and F.-M. Liu, "Ab initio prediction on ferrotoroidic and electronic properties of olivine Li_4 $MnFeCoNiP_4O_{16}$", Chinese Phys. B **18**, 24812486 (2009).

[166] S. Hayami, H. Kusunose, and Y. Motome, "Toroidal order in metals without local inversion symmetry", Phys. Rev. B **90**, 024432 (2014).

[167] Y. Yamaguchi and T. Kimura, "Magnetoelectric control of frozen state in a toroidal glass", Nat. Comm, **4**, 2063 (2013).

[168] V. A. Fedotov, K. Marinov, A. D. Boardman, and N. I. Zheludev, "On the aromagnetism and anapole moment of athracene nanocrystals", New Journal of Physics, **9**, 2967 (2007).

[169] K. Marinov, A. D. Boardman, V. A. Fedotov, and N. I. Zheludev, "Toroidal Metamaterial", New Journal of Physics, **9**, 324-202 (2007).

[170] T. Kaelberer, V. A. Fedotov, N. Papasimakis, D. P. Tsai, N. I. Zheludev, "Toroidal dipolar response in a metamaterial", Science, **330**, 1510-1512 (2010).

[171] Y. Fan, Z. Wei, H. Li, H. Chen, and C. M. Soukoulis, "Low-loss and high-Q planar metamaterial with toroidal moment", Phys. Rev. B **87**, 115417 (2013).

[172] Z. Dong, P. Ni, J. Zhu, X. Yin, and X. Zhang, "Toroidal dipole response in a multifold double-ring metamaterial", Opt. Exp. **20**, 13065-13070 (2012).

[173] V. A. Fedotov, A. V. Rogacheva, V. Savinov, D. P. Tsai, and N. I. Zheludev, "Resonant transparency and non-trivial non-radiating excitations in toroidal metamaterials", Sci. Rep. **3**, 2967 (2013).

[174] B. Ögüt, N. Talebi, R. Vogelgesang, W. Sigle, and P. A. van Aken, "Toroidal plasmonic eigenmodes in oligomer nanocavities for the visible", Nano Lett. **12**, 52395244 (2012).

[175] Y. Huang, W. T. Chen, P. C. Wu, V. A. Fedotov, V. Savinov, Y. Z. Ho, Y. Chau, N. I. Zheludev, and D. P. Tsai, "Design of plasmonic toroidal metamaterials at optical frequencies", Opt. Exp. **20**, 1760-1768 (2012).

[176] Z. Dong, J. Zhu, J. Rho, J. Li, C. Lu, X. Yin, and X. Zhang, "Optical toroidal dipolar response by an asymmetric double-bar metamaterial", Appl. Phys. Lett. **101**, 144105 (2012).

[177] Z. Dong, J. Zhu, X. Yin, J. Li, C. Lu, and X. Zhang, "All-optical Hall effect by the dynamic toroidal moment in a cavity-based metamaterial", Phys. Rev. B **87**, 245429 (2013).

[178] N. Papasimakis, V. A. Fedotov, K. Marinov, and N. I. Zheludev, "Gyrotropy of a metamolecule: wire on a torus", Phys. Rev. Lett. **103**, 093901 (2009).

[179] V. A. Fedotov, A. V. Rogacheva, V. Savinov, D. P. Tsai, and N. I. Zheludev, "Resonant transparency and Non-trivial nonradiating excitations in toroidal metamaterials", Sci. Rep. **3**, 2967 (2013).

[180] K. Sawada and N. Nagaosa, "Optical magnetoelectric effect in multiferroic materials: evidence for a Lorentz force acting on a ray of light", Phys. Rev. Lett. **95**, 237402 (2005).

[181] C. S. Wood, S. C. Bennett, D. Cho, B. P. Masterson, J. L. Roberts, C. E. Tanner, and C. E. Wieman, "Measurement of parity nonconservation and an anapole moment in cesium", Science, **275**, 1759-1763 (1997).

[182] W. C. Haxton and C. E. Wieman, "Atomic parity nonconservation and nuclear anapole moments", Annu. Rev. Nucl. Part. Sci. **51**, 261-293 (2001).

[183] J. S. M. Ginges and V. V. Flambaum, "Violations of fundamental symmetries in atoms and tests of unification theories of elementary particles" Phys. Rep. **397**, 63-154 (2004).

[184] G. N. Afanasiev, "Simplest sources of electromagnetic fields as a tool for testing the reciprocity-like theorems", Sci. Rep. **3**, 539-559 (2013).

[185] E. E. Radescu and G. Vaman, "Exact calculation of the angular momentum loss, recoil force, and radiation intensity for an arbitrary source in terms of electric, magnetic, and toroid multipoles", Phys. Rev. E **65**, 046609 (2002).

[186] V. M. Dubovik and V. V. Tugushev, "Toroid moments in electrodynamics and solid-state physics", Phys. Rep. **187**, 145-202 (1990).

[187] M. A. Noginov, G. Zhu, A. M. Belgrave, R. Bakker, V. M. Shalaev, E. E. Narimanov, S. Stout, E. Herz, T. Suteewong, and U. Wiesner, "Demonstration of a spaser-based nanolaser", Nature **460**, 11101112 (2009).

[188] S. Lal, S. Link, and N. J. Halas, "Nano-optics from sensing to waveguiding", Nat. Photon. **1**, 641648 (2007).

[189] T. Lepetit, É Akmansoy, and J.-P. Ganne, "Experimental measurement of negative index in an all-dielectric metamaterial", Appl. Phys. Lett. **95**, 121101 (2009).

[190] A. E. Miroshnichenko, A. B. Evlyukhin, Y. F. Yu, R. M. Bakker, A. Chipouline, A. I. Kuznetsov, B. Luk'yanchuk, B. N. Chichkov, and Y. S. Kivshar, "Nonradiating anapole modes in dielectric nanoparticles", Nat. Commun. **6**, 8069-8076 (2015).

[191] I. V. Stenishche and A. A. Basharin, "Toroidal response in all-dielectric metamaterials based on water", Sci. Rep. **7**, 9468 (2017).

[192] Z. Liu, S. Du, A. Cui, Z. Li, Y. Fan, S. Chen, W. Li, J. Li, and C. Gu, "High-quality-factor mid-infrared toroidal excitation in folded 3D metamaterials", Adv. Mater. **29**, 1606298 (2017).

Chapter 3

Computational Tools: Software and Scripts

This chapter will document all simulation packages that were utilized in the creation of any computational results seen within this thesis. The first section begins by discussing the framework of RSoft's DiffractMOD, the software implemented for studying all of the fabricated metamaterials within this thesis. Both the dual crosses and crosses with reduced metal of Chapter 6 will be analysed in order to highlight why these structures were selected to be fabricated and how the structural parameters came to be chosen by discussing the framework of RSoft's DiffractMOD.

Secondly, the workings of CST Studio Suite, which will be used to calculate the results in Chapters 4 and 5 are subsequently detailed. The attention here will be focused on purely computational work: generating toroidal dipoles in a plasmonic metamaterial to study both the fundamental field and second harmonic fields. A script that was heavily utilized for all the major linear and nonlinear results relied on a Near-to-Far-Field Transformation, an analysis of which is therefore subsequently given. Finally, this chapter concludes with a discussion on Bragg filters, showing how these filters and a composite involving metamaterials were simulated.

3.1 DiffractMOD

Unit cells depicted in the following sections, such as Figure 6.17, were drawn with RSoft's DiffractMOD, a rigorous coupled-wave analysis (RCWA) package designed to calculate a variety of electromagnetic properties that are engendered by the chosen unit cell. RCWA is a process used to calculate scattering plane waves by deconstructing the electromagnetic field into a finite set of terms [2], often referred to as 'harmonics'. This can be understood by considering a Fourier series; it is known that a periodic function can be represented

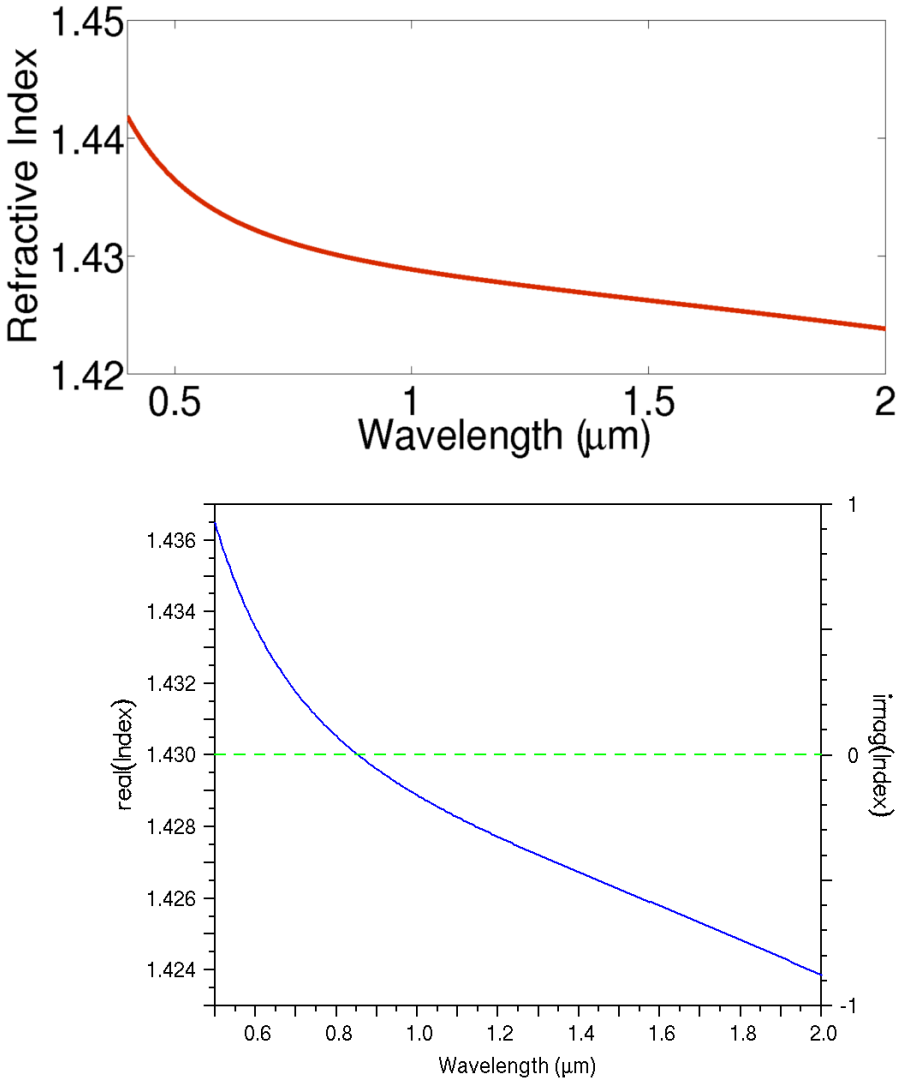

Figure 3.1: Top - The refractive index of CaF_2, taken from [3], where the Sellmeier coefficients from [1] were taken. Bottom - The same Sellmeier coefficients implemented in RSoft's DiffractMOD, the definition of which is utilized in all simulations using this material.

as an infinite sum of terms of varying significance. RCWA allows the number of terms (harmonics) to be selected, whereby an increase leads to more accurate results at the cost of computational time.

It must be noted that RCWA is a mathematical tool that is only applicable for periodic structures. Hence, it is not possible to simulate a single unit cell within DiffractMOD's framework and other software packages must therefore be used for this purpose. The input angle for the light source and its corresponding polarization, however, are quite flexible; it is also possible to utilize circularly-polarized light.

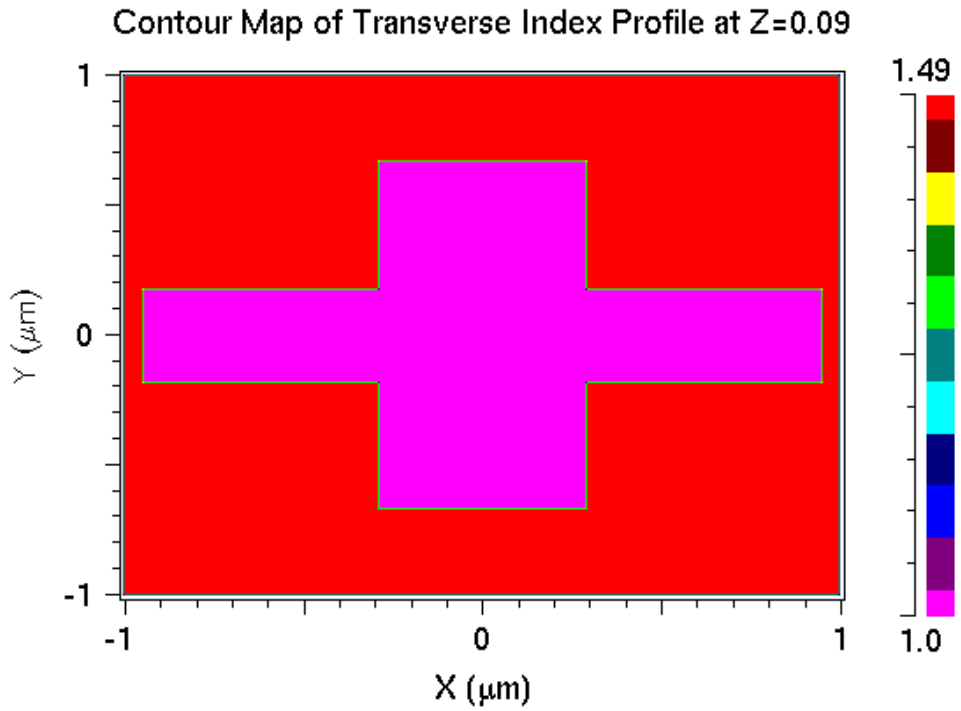

Figure 3.2: The output of DiffractMOD's Material Profile, where the real part of the refractive index is calculated for a cross trench for the plane z=0.09μm.

Examples of material characteristics that are able to be calculated within DiffractMOD include thermal conductivity, doping concentration and stress-optic coefficients.

A handy tool available in most software packages is the ability to define variables that can be used to build our structures. Rather than specifically defining a length of a structure, it is possible to define this length as a variable, which can then be altered later. DiffractMOD is no different in this regard. As we shall see with regards to a metamaterial structure utilized to create a strong toroidal dipole, often the electric fields are required for every wavelength for further calculations. DiffractMOD is again very flexible in this regard, allowing every component of the electric and magnetic fields to be exported for a selected grid size in each direction. Furthermore, each diffraction order and the three optical coefficients (transmission, reflection and absorption coefficients) can also be output into a file.

Each electromagnetic calculation does not have to be in terms of a wavelength scan; within the confines of the software, it is instead possible to calculate parameters in terms of the incident angle for both planes, i.e. θ and ϕ.

During this software package discussion, there are two types of metamaterial designs we are going to consider: a unit cell consisting of cross-shapes for a double resonance in the optical spectra; and split ring resonators (SRRs) employed to create a toroidal

resonance at the second harmonic. We will first analyse the cross-shapes.

3.1.1 Swiss Crosses

DiffractMOD contains a material library, with the permittivity and permeability functions being available for a wide range of wavelengths for common metals and dielectrics, including a few semiconductors. In simulating the cross-shape structures, the gold, titanium and PMMA material properties could simply be selected from the list in DiffractMOD. This library, however, is not overly extensive. It was therefore necessary to define calcium fluoride manually by inputting the material's Sellmeier coefficients, which describe how a dielectric's refractive index is dependent on the wavelength. Explicitly:

$$n^2(\lambda) - 1 = \sum_j \frac{B_j \lambda^2}{\lambda^2 - C_j} \tag{3.1}$$

Where B_j and C_j are the Sellmeier coefficients, which detail where in frequency-space the material experiences a resonance. Calcium fluoride is explicitly described [3] by:

$$n^2(\lambda) - 1 = 0.33973 + \frac{0.69913\lambda^2}{\lambda^2 - 0.09374^2} + \frac{0.11994\lambda^2}{\lambda^2 - 21.18^2} + \frac{4.35181\lambda^2}{\lambda^2 - 38.46^2} \tag{3.2}$$

where the first term on the right-hand side of the equation is an equivalent to the ϵ_∞ term we saw in Equation 2.22. It is these Sellmeier coefficients which DiffractMOD allows to be input for a new material to be added to the library. Before this can be done, however, it is necessary to select an option that allows material dispersion. DiffractMOD allows many different types of manual material definitions: while the default is a single value of the refractive index for all wavelengths, examples include the definition of anisotropy through input of each element of the electric susceptibility tensor; the same applies for all magnetic permeabilities; stress can be defined through the Young's Modulus. It is therefore highly important to visualise the resulting refractive index with the desired results. Figure 3.1 shows an example comparison.

When defining more complex structures such as the dual cross that we will see in Figure 6.37, care must be taken when writing components of the structure that overlap. As all the structures that we see in this section are composed of rectangles of varying shape, defining the cross-shaped air trenches meant that cross-shaped rectangles had to overwrite the underlying metal. This is achieved within DiffractMOD's framework by assigning priority to each element. By assigning the trenches a higher priority than the metal beneath, it is ensured that the trenches 'really do exist' from the software's point of view. Naturally, if this step is neglected, the software will only see uniform metal films

with no metamaterial patterns.

There is no need to draw the substrates to scale within the software, as it is simple to command the software to consider a substrate of infinite thickness by ending the bounding box of the CAD within the substrate. On a similar theme, care must be taken to ensure the bounding box allows a gap between the top of the designed meta-atom and the incident light source. Not doing so can lead to awkward unwanted scattering of the light due to the fact that the software is not sure where the light source ends and the structure begins.

A handy tool for allowing us to see that the simulation is setup correctly is DiffractMOD's 'Material Profile' section. Within this part of the software an image can be output containing information about certain calculated parameters, including the real and imaginary parts of the permittivity and permeability functions; the stress properties; and doping concentration. This is applied for any chosen slice through the structure. To highlight the use of this function, the real part of the refractive index for the original cross trench that will be fabricated in Chapter 6 is plotted in Figure 3.2 for a slice where z=0.09μm, i.e. through the cross trenches. It must be noted that for this simulation, the PMMA of the original cross is kept. Figure 3.3 shows the simulated reflection and transmission coefficients calculated by DiffractMOD for the original cross trench structure, excited by a plane wave, to be compared with the results taken from the source [4], shown in Figure 6.43. The PMMA of the original cross is again kept, but it must be noted that the physics describing the small resonance stemming from the carbonyl bond is not taken into account, and hence we do not expect to see this small Lorentzian. We see a clear agreement between the results of the original paper and our simulations.

As mentioned, one important parameter in electromagnetic wave calculation that must be selected before computation is the number of harmonics which are used. It is vital to realise that it is not mandatory to include as many harmonics as the Random Access Memory will allow. Rather, the results must start to show convergence when a larger number of terms are included: it is a fruitless venture to base the results of a calculation on 12 harmonics if the results diverge when 13 harmonics are invoked. If, on the other hand, the results begin to converge to a particular value, the results can be considered much more valuable. Figure 3.4 shows the importance of using an appropriate number of harmonics.

Moving towards the goal of having two different resonant units within the meta-atom, the effect of the periodicity on the transmission of the original cross structure is depicted in Figure 3.5. As is immediately clear, an increase in the periodicity leads to a decrease in the overall transmission of the incident light, a result that is exactly as we would expect; an increase in periodicity means that there are less metamaterial elements

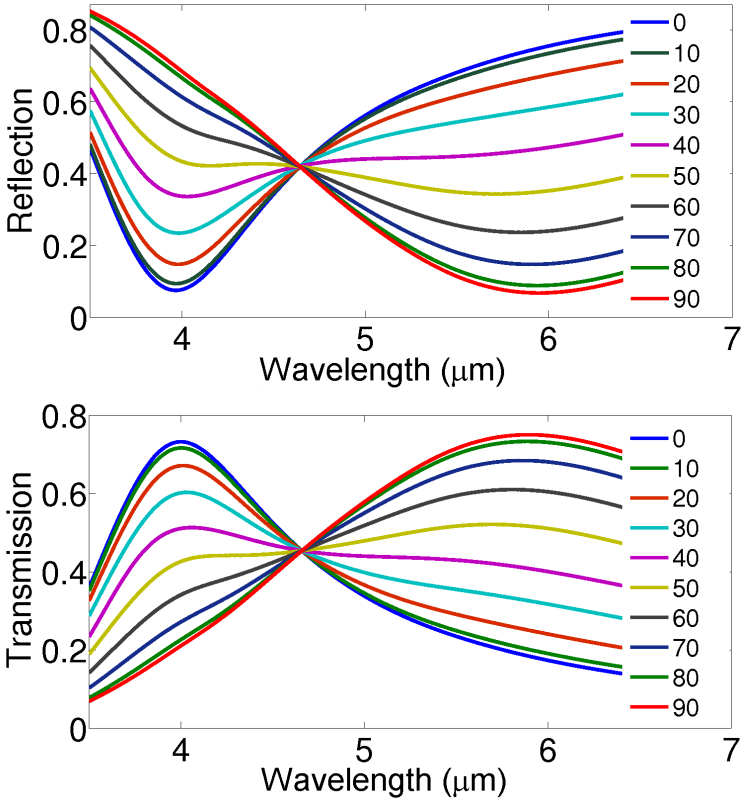

Figure 3.3: The reflection (top) and transmission (bottom) coefficients simulated *via* DiffractMOD for the structure that will be analysed in Figure 6.11, with each line corresponding to a different angle of polarization. The plots clearly match those in Figure 6.43.

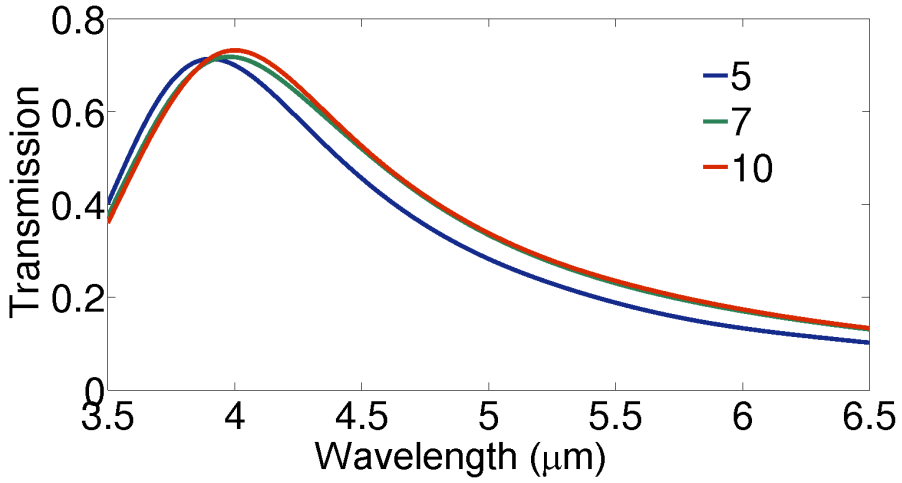

Figure 3.4: The effect of harmonics of the incident plane wave on the performance of the DiffractMOD simulations. Each line in this figure corresponds to a different number of Fourier terms used by the software to calculate the optical response. Clearly, as the number of harmonics increases, the results begin to converge. It is of primary importance to ensure that the output converges with each investigation.

per unit area. Hence, upon when maximally excited with the corresponding incident wavelength, there is overall less activation. This wavelength also naturally shifts to larger wavelengths with increasing periodicity, as the wavelength of maximum excitation is intrinsically linked with the periodicity of the structure. Also plotted in Figure 3.5 is the simulated transmission spectra of a unit cell that was a first experimentation in creating a multi-resonant meta-atom. This meta-atom consists of four original cross-trenches separated by a distance 2.5μm. However, two of these crosses are scaled by a factor of 10%, thus shifting their resonant wavelength slightly. We see the effects of this in the transmission spectra; the similar structural sizes, however, means that there is not enough 'space' to form two complete, separate resonances. It is possible to keep continuing the size of the periodicity until the peaks are distinct, but again this will reduce the strength of the overall transmission.

Here, the idea of deconstruction came into play: we see that the asymmetric nature of the original cross means that there are two resonances, as seen in Figure 3.3, where each one corresponds to the excitation of an arm. Furthermore, these resonances are far enough apart in wavelength space that the first assumption was thus: as the resonances corresponding to the original arms are far enough apart, surely a two-unit meta-atom could be designed, such that one unit consists of just the thinner arm, while the other is composed just of the thicker arm. Theoretically, the resulting structure should replicate the two resonances that we saw in Figure 3.3, but within the one structure *regardless of polarization*. The new structure does not have a polarization dependence due to its

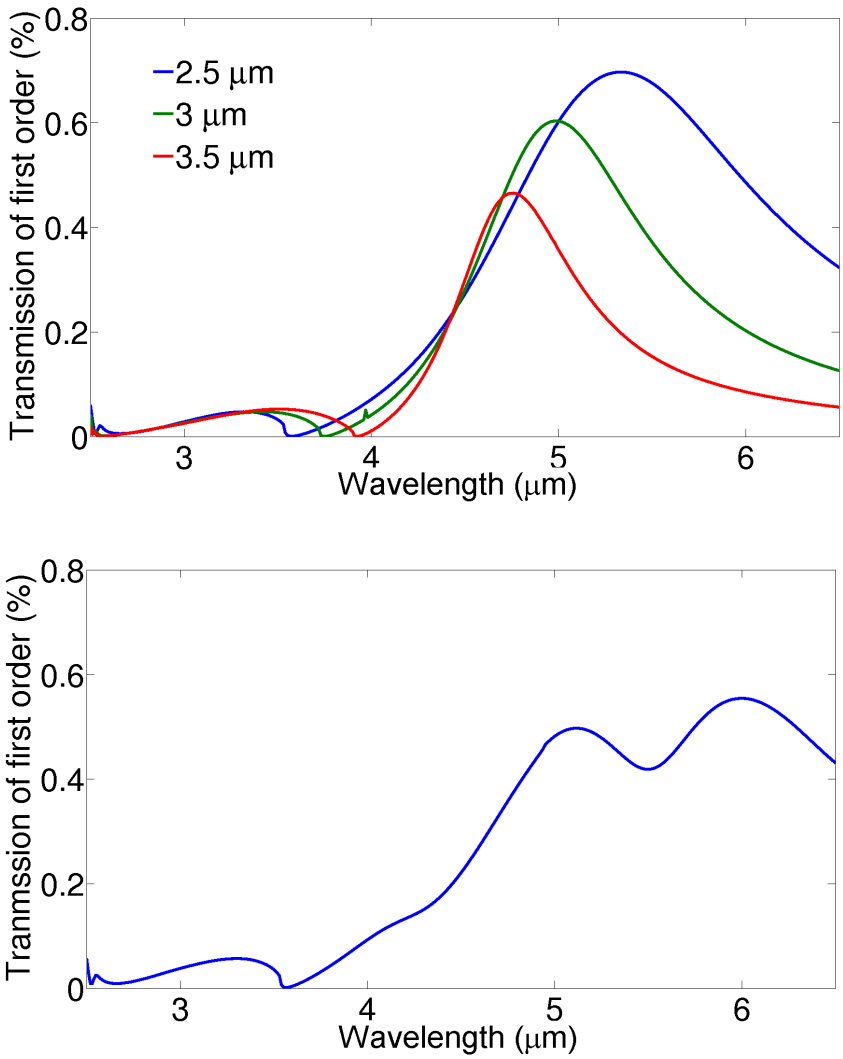

Figure 3.5: Top - The effect of periodicity on the optical response of the cross shown in Figure 6.11. It is clear that as the periodicity increases, the resonance simultaneously weakens and shifts in wavelength space. Bottom - The transmission coefficients of a hybridized meta-atom containing two different units, the first being the cross-shape of Figure 6.11, the second being this same cross shape multiplied by a scaling factor of 1.1. The periodicity is 2.5μm. A double resonance begins to emerge, but they are not distinct.

symmetric properties.

The deconstruction of the original cross was simulated with 14 harmonics to calculate the reflection and transmission spectra. This output is shown in Figure 3.6, where - as shall be seen in Chapter 6 - there is a clear agreement with the fabricated crosses. To reiterate, the strength differences of the peaks between experiment and computation is attributed to an insufficient milling time. We started with the idea of having two resonances from one meta-atom. Through deconstructing a polarization-dependent cross into two symmetric crosses, this has been achieved. We now turn to analysing the gold

SRR metamaterial.

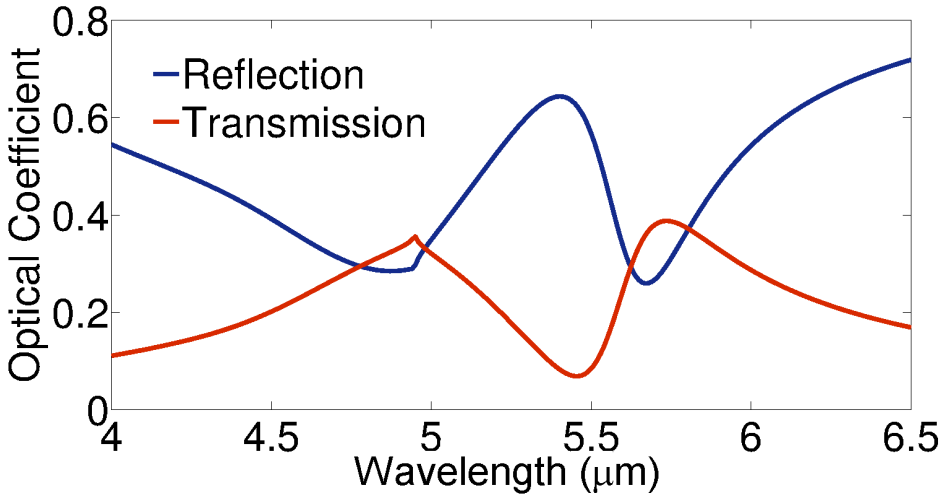

Figure 3.6: A dual resonance, formed by the structure in Figure 6.37, simulated by DiffractMOD. Each cross in the meta-atom causes a separate resonance to be located in wavelength space.

3.1.2 The MOST Optimizer

The framework for creating multiple resonances within a meta-atom has now been laid down. The focus for this section is on increasing the quality factor of the resonances. The quality factor is essentially the inverse of the full-width half-maximum (FWHM) value, as we see through the relation:

$$Q = \frac{\Delta\lambda}{\lambda_0} \tag{3.3}$$

where $\Delta\lambda$ is the FWHM of the resonance located at wavelength λ_0.

Achieving the maximum quality factor manually would be a pain-staking process. Slight changes to structural parameters would have to be made, recorded and simulated one-by-one in a brute force manner. Thankfully, there is no need for this hardship as RSoft comes with its own optimizing tool, called the MOST optimizer. A quote from the creators of this tool succinctly summarises its intentions and potential [5]:

"MOST, RSoft's Multi-Variable Optimization and Scanning Tool, is an exciting solution to the critical problem of design optimization for photonic devices. During the research or design cycle, it becomes vital to understand the full parameter space of the system. Acting as an automated driver for RSoft's physics-based simulators, MOST takes the drudgery out of these important operations by streamlining the definition, calculation and analysis of scans and optimizations."

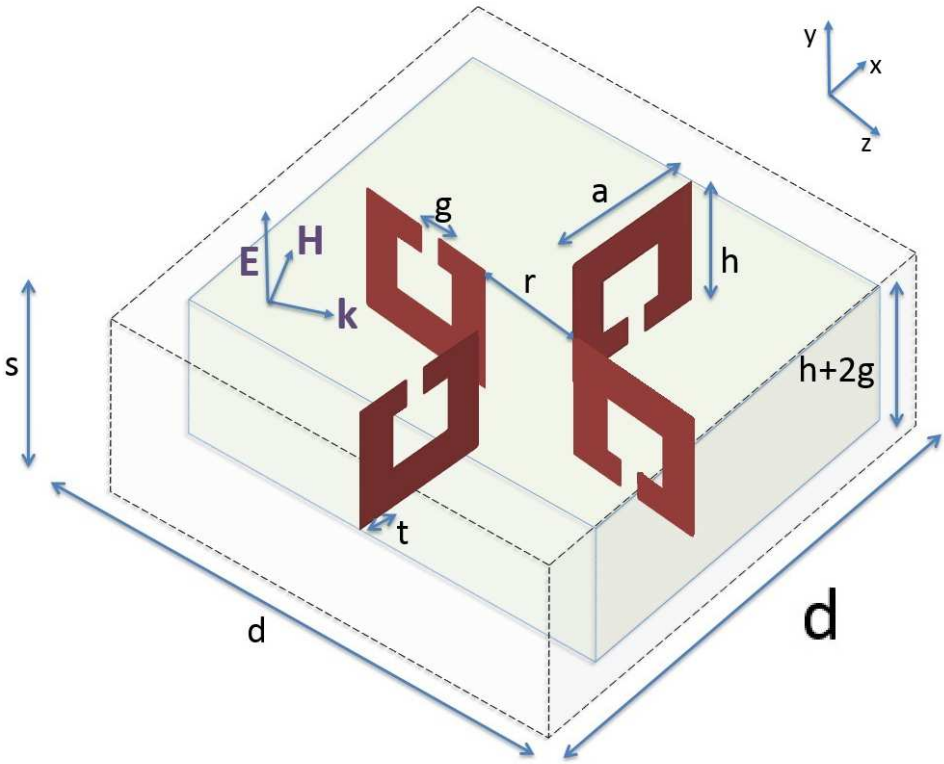

Figure 3.7: A gold SRR structure designed to induce a strong toroidal resonance [14]. At an incident wavelength of 2.5μm each SRR produces a magnetic moment, which in turn form a loop. A toroidal dipole is hence produced.

Before scans are performed, it is important to think of the goal as a function of parameters. Our goal was to simulate (and ultimately fabricate) a device that acts as a sharp transmission filter. We therefore want to minimise our transmission, T, which is a function of the structural parameters: T=$f(t_{au}$, a, w, l), where t_{au}, a, w, l are, respectively, the thickness of the gold, the width of the entire structure, the width of the arms, the length of the arms.

One of the most important steps before running the optimizer is to implement their scanning feature. As the output is a multi-dimensional function, there could easily be plenty of local minima that the software wrongly converges on if a full scan is initially ignored. These incorrect peaks can often lead to unphysical results, such as negative transmission, or structural parameters that are impossible to fabricate. Scanning first and foremost allows the user to get a feel for the results and physical underpinnings of the system. This step is achieved by selecting the parameters on which the user's function is dependent, and thence inputting the minimum and maximum values along with the step size.

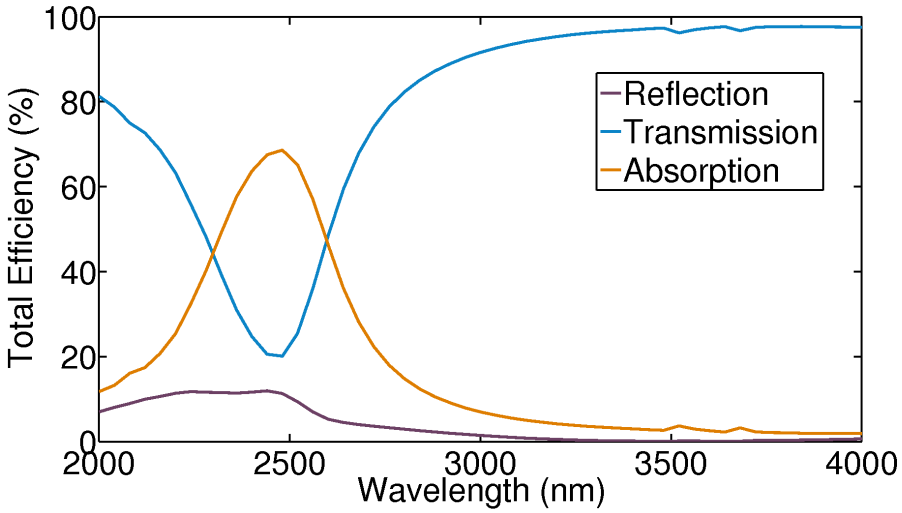

Figure 3.8: The transmission, reflection and absorption spectra for the SRR structure of Figure 3.7. A resonance is clearly seen for an incident wavelength of 2.5μm.

Once the scan is completed and observed to ensure all results are both physical and reasonable, the optimizer can be used. The optimizer works by minimising a so-called metric. This is where the above function can expressed in a more complex mathematical formula (metric) for the software to minimise. However, for our purposes, the required metric is the function, i.e. the transmission for a wavelength at 2.7μm.

The optimizer comes with several algorithms, one of which the user must select. Some of these algorithms are for specific cases, such as if the function to minimise is a function of one variable only. The algorithm selected for the cross was Powell's n-dimensional minimiser, which can take 0 or 1 initial values for each parameter on which the function depends. Once this solver was selected and the metric was defined, the optimizer was run, leading the software to output the structural parameters that will be seen in Figure 6.17.

3.1.3 Toroidal Moments within Metamaterials

The work presented in this section was the genesis of my nonlinear analysis. The goal here was to analyse the nonlinear signal arising from a metamaterial designed to host a strong toroidal dipole. Specifically, the nonlinear regime that is analysed is second harmonic generation (SHG). While a much more rigorous description of SHG is given in Chapters 4 and 5, it is important to bear in mind that this is a nonlinear optical interaction whereby an incident ray of light with frequency ω, interacts with and excites the structure to produce its own electromagnetic field at a frequency of 2ω, from here referenced to as Ω.

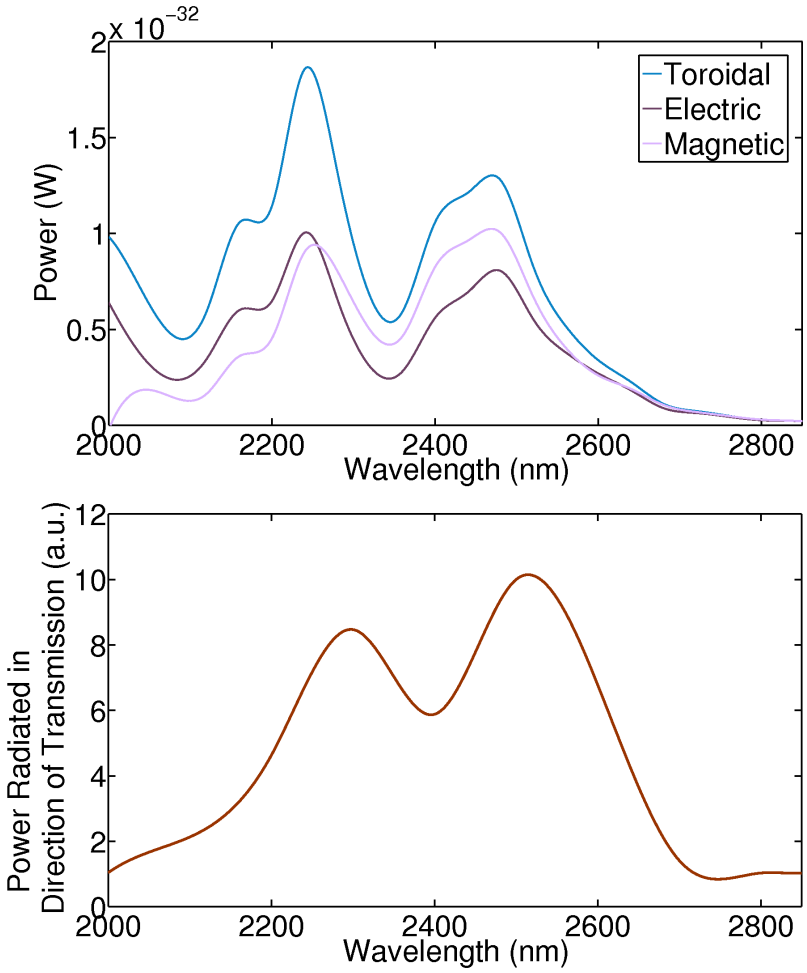

Figure 3.9: Top - The calculated radiated power for the SRR structure at the second harmonic by the electric, magnetic and toroidal dipoles. The toroidal dipole is clearly the strongest member of the family. Bottom - The calculated power in direction of transmission for *every* nonlinear moment based on a nonlinear generalised source method [17].

In a work by Savinov et al. [6], a metamaterial was designed such that its emission was primarily due to its toroidal dipole at the fundamental frequency. Toroidal moments have been analysed in a wide range of metamaterials [7–13], but the subsequent analysis always focuses solely on the linear regime. One of my aims, therefore, has been to build upon this analysis by extending it into the world of nonlinear physics.

In order to engender a strong nonlinear response, a metamaterial similar to Kaelberer's [15] was designed, as can be seen in Figure 3.7 [14]. Four gold split ring resonators are embedded in a dielectric with permittivity function $\epsilon = 3 + 0.0039i$. The SRRs are embedded with fabrication conditions in mind; while it is computationally simpler to consider just 4 SRRs suspended in air, we wished to bring these results away from the purely theoretical. The incoming light is oriented at a 45 degree angle in the x-y plane so

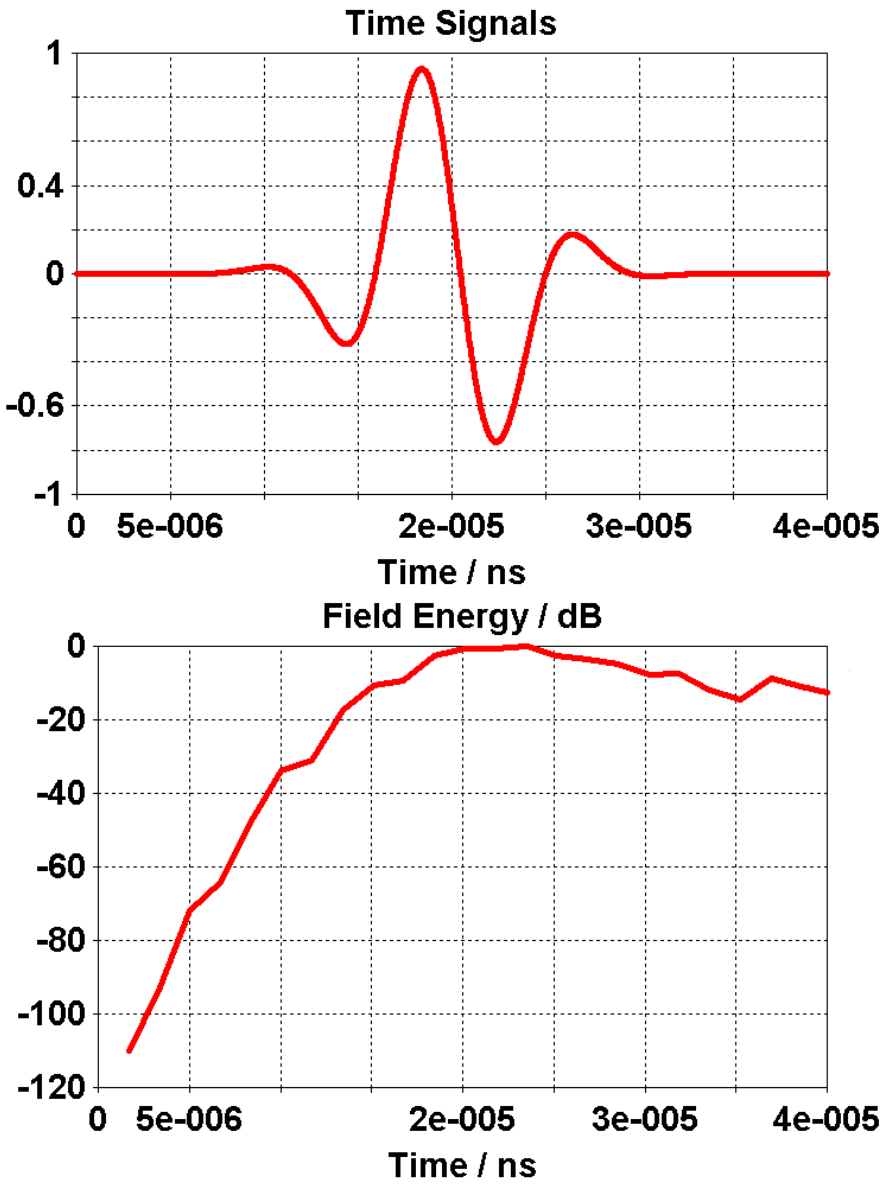

Figure 3.10: Top - The default power of the input signal used by the time-domain solver in CST Studio Suite. Bottom - an example of the energy decay in the simulation system. The maximum energy present naturally corresponds to the peak of the time signal.

as to ensure maximum interaction with the SRRs. At a particular frequency, the current is maximally generated within the rings, forming four loops of current. These current loops in turn form four independent magnetic moments, which themselves in turn form the toroidal dipole of the structure. Periodic boundary conditions were imposed along the x- and z- directions. The dimensions of the metamaterial are also given in Figure 3.7.

Before diving into the nonlinear results, it is always important to see what is happening in the linear regime; the linear results give plenty of pertinent information, such as the location and strength of any resonances, and which multipoles are responsible for them.

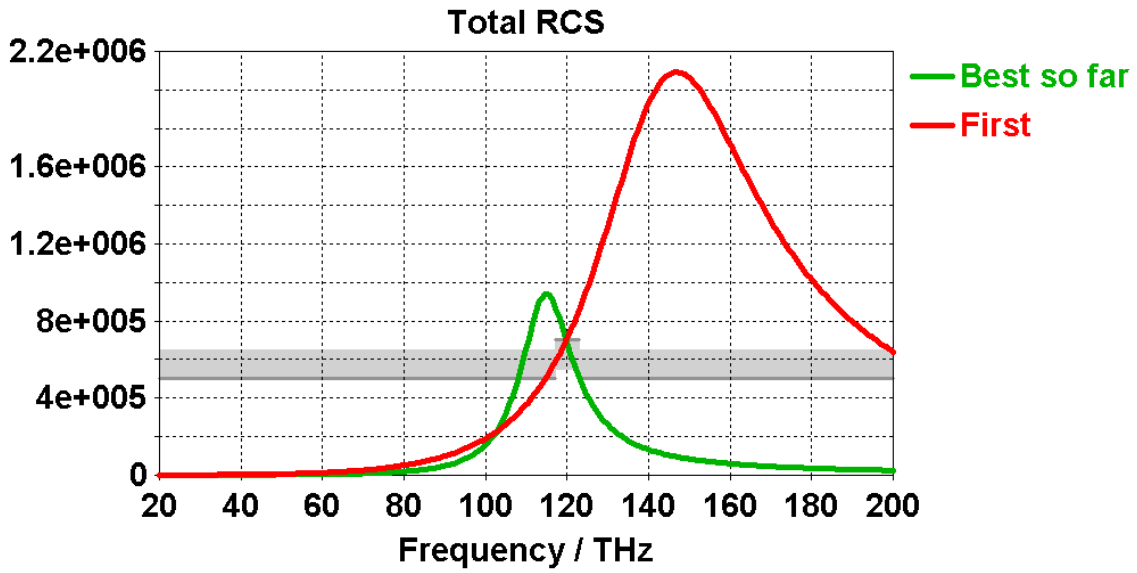

Figure 3.11: An example of an implementation of CST's optimizer. The grey shading shows the goals given to the optimizer: maximise the scattering cross section in the region 117THz - 123THz while minimising the signal elsewhere through changing the structural parameters. The first and best-so-far cross sections are displayed.

The most important linear result with regards to this work is the calculation of the optical coefficients, plotted here in Figure 3.8. It is clear that there is a strong resonance corresponding to an incident wavelength of 2.5μm. While most of the light is usually transmitted through the slab, it is blocked around this resonance, and hence the slab acts as quite a narrow transmission filter.

Figure 3.8 tells us a key piece of information: to see the most relevant SH results, we should look to a wavelength corresponding to half that of the resonance, as Ω=2ω, implying Λ=λ/2. Hence, we expect to see SH results that are resonant at a wavelength of 1.25μm.

A nonlinear optical interaction means that nonlinear currents must be calculated. In fact, the nonlinear polarizations were first calculated, with the useful relation of Equation 2.9 being utilised to shift the physics into the realm of currents. As we saw in the previous section, the flavour of nonlinear physics that must be considered all stems from the symmetry properties of the crystals in question. The primary material in question here is gold, forcing the physical framework into centrosymmetric physics.

The nonlinear currents generated by the gold are due to the fundamental frequency electric fields emitted at the surface of the metal. Although the bulk of the gold does have a nonlinear moment, it is assumed that the surface interactions are larger by several orders of magnitude. This assumption, incidentally, is more rigorously addressed in Chapter 4. For this section, it is sufficient to say that the stated assumption is accurate.

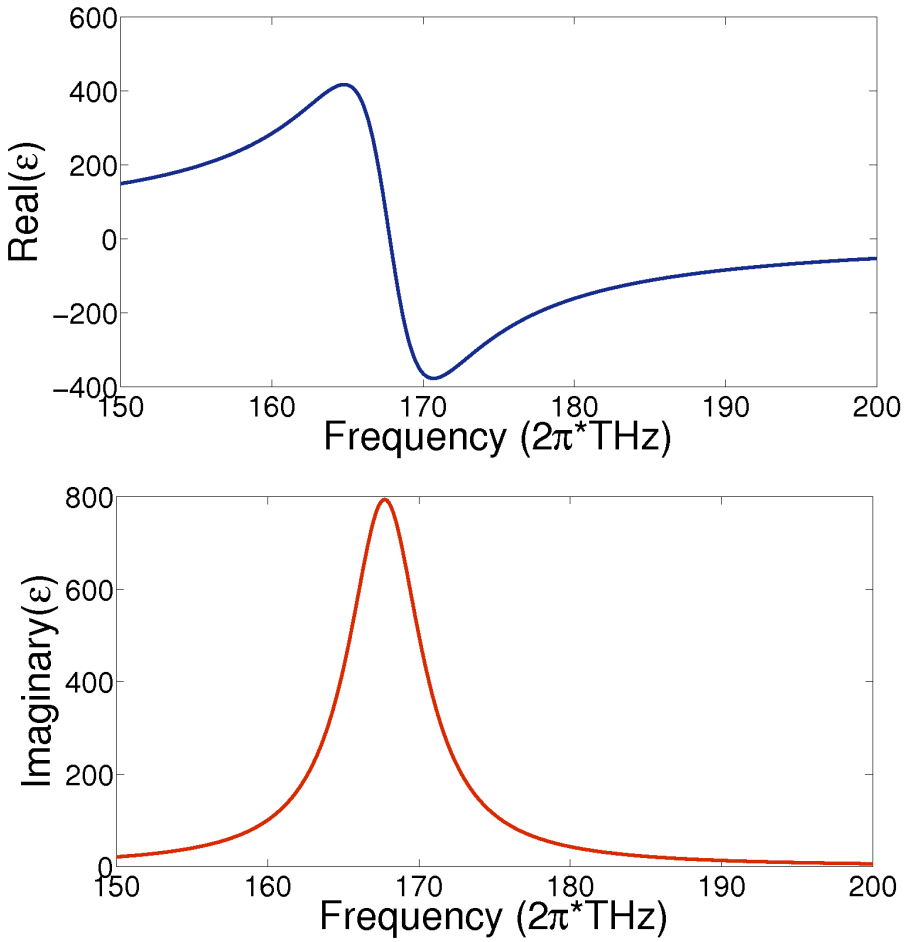

Figure 3.12: The real part (top) and the imaginary part (bottom) of the $LiTaO_3$ permittivity function, taken from [19]. There is a clear strong resonance due to the material's polaritonic properties.

Hence, in order to fully scrutinise the nonlinear currents generated by the gold, it is necessary to split the structure into two domains: surface and non-surface. To this end, a 129x33x129 grid was fitted to the structure, which is enabled in DiffractMOD's electric field calculations. Care was taken to ensure that the grid step-size was smaller than the smallest feature of the structure, namely the gaps in the rings, ensuring that we do indeed isolate all the surfaces, no matter how small. The three electric field components - E_x, E_y and E_z - were calculated for each grid point and output into a basic *.txt* file. This same grid was applied to the structure a second time, with the purpose of calculating the relative permittivity of each grid point. By analysing the grid points pertaining to the permittivity, it is possible to discard any non-surface grid point: any grid point belonging to the surrounding dielectric naturally has a permittivity value whose real part is equal to 3. The bulk of the gold can be similarly be located: by picking a known element pertaining to the bulk and making a note of its permittivity value, all bulk fields could

be similarly discarded. The remaining points therefore belong to the surfaces of the gold. However, it is necessary to know exactly which surface each point denotes, as there are two nonlinear vectorial polarizations to calculate [16]. Explicitly:

$$\mathbf{P}_{\perp}^{(2)}(\mathbf{r};\Omega) = \epsilon_0 \chi_{\perp\perp\perp}^{(2)} \mathbf{E}_{\perp}(\mathbf{r};\omega)\mathbf{E}_{\perp}(\mathbf{r};\omega) \tag{3.4a}$$

$$\mathbf{P}_{\parallel}^{(2)}(\mathbf{r};\Omega) = \epsilon_0 \chi_{\parallel\perp\parallel}^{(2)} \mathbf{E}_{\perp}(\mathbf{r};\omega)\mathbf{E}_{\parallel}(\mathbf{r};\omega) \tag{3.4b}$$

A script was therefore implemented to sort through the electric field arrays plane by plane, comparing each slice with the previous slice to assign the correct surface to the grid points. For example, if, moving in the positive x-direction, the previous slice has a permittivity belonging to the bulk, then it is clear that the slice to be determined belongs to the surface *on the positive x-side*. Performing this operation for each of the 6 sides - corresponding to the three Cartesian coordinates for both the positive and negative directions - the second harmonic currents can now be calculated. By repeating the previous steps for 50 wavelengths for an incident wavelength range of 2μm - 4μm, the second harmonic polarizations could be calculated. With these nonlinear polarizations, the power emitted *via* the nonlinear dipoles can be ascertained through the following equations:

$$\mathbf{p} = \frac{1}{i\omega}\int \mathbf{j} d^3\mathbf{r} \tag{3.5a}$$

$$\mathbf{m} = \frac{1}{2c}\int (\mathbf{r}\times\mathbf{j}) d^3\mathbf{r} \tag{3.5b}$$

$$\mathbf{T} = \frac{1}{10c}\int [(\mathbf{r}\cdot\mathbf{j})\mathbf{r} - 2\mathbf{r}^2\mathbf{j}] d^3\mathbf{r} \tag{3.5c}$$

$$\tag{3.5d}$$

where $\mathbf{p}$, $\mathbf{m}$ and $\mathbf{T}$ are the electric, magnetic and toroidal dipoles, respectively. $\mathbf{j}$ is the current density of the mesh element, which is located a distance $\mathbf{r}$ from the centre of the unit cell. It must be noted that these dipole equations are not nonlinear in themselves; they apply for all regimes, linear and nonlinear alike. It is the current density on which they depend that determines the order of linearity.

The power of the multipoles follows the equation [15]:

$$P = \frac{2\omega^4}{3c^3}|\mathbf{p}|^2 + \frac{2\omega^4}{3c^3}|\mathbf{m}|^2 + \frac{2\omega^6}{3c^5}|\mathbf{T}|^2 \tag{3.6}$$

The resulting calculated power radiated by the nonlinear dipoles is shown in the

top panel of Figure 3.9. It is clear that the toroidal dipole is the strongest dipole This is compared with the power radiated in the direction of transmission by *all* nonlinear dipoles obtained by an in-house software based on the non-linear generalized source method, the details of which can be found in [17].

In conclusion, we have shown a plasmonic metamaterial whose nonlinear toroidal response outweights that of the electric and magnetic dipoles.

3.2 CST Studio Suite

Computer Simulation Technology Studio Suite (CST) is a three-dimensional electromagnetic simulation software with both frequency-domain and time-domain solvers. While the full extent of the software reaches, among others, charged particle dynamics, thermal and mechanical stress solutions, it is CST's 'high-frequency' package that will be employed for this section.

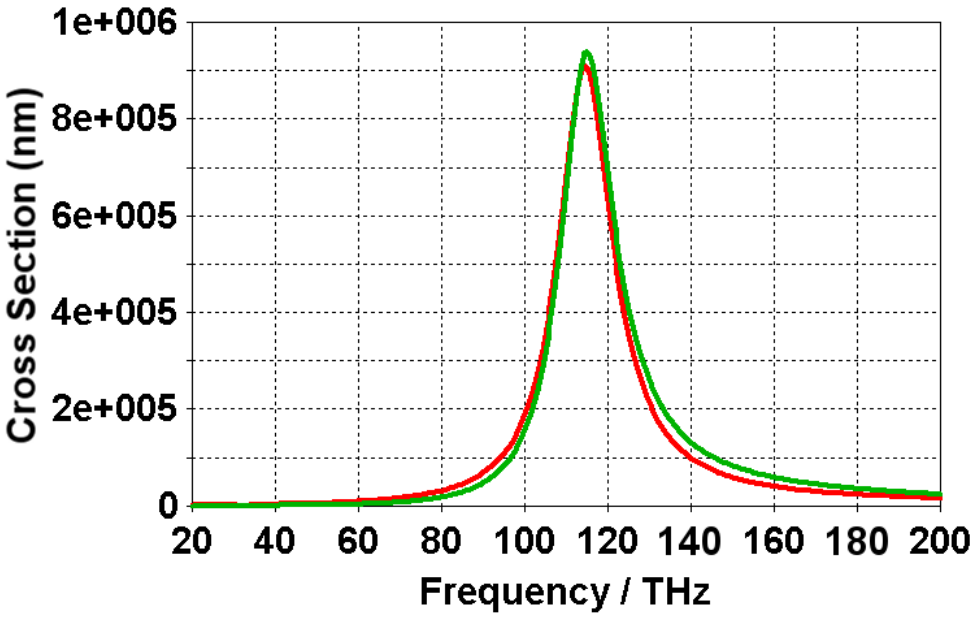

Figure 3.13: The absorption cross section (ACS), red, and scattering cross section (RCS), green, calculated for an example cross shape.

For our simulations, the time-domain solver was implemented. A time domain solver calculates the development of fields through time at discrete locations and at discrete time samples. It calculates the transmission of energy between various ports or other excitation sources and/or open space of the investigated structure. Consequently a time domain solver is remarkably efficient for most high frequency applications such as connectors, transmission lines, filters, antennas etc. and can obtain the entire broadband frequency

behavior of the simulated device from a single calculation run. The time-domain solver is based on the Finite Integration Technique (FIT), first proposed by Weiland in 1976/1977 [18]. FIT applies, as the CST documentation tells us, 'some highly advanced numerical techniques like the Perfect Boundary Approximation (PBA) in combination with the Thin Sheet Technique (TST) to allow accurate modeling of small and curved structures without the need for an extreme refinement of the mesh at these locations. This allows a very memory efficient computation together with a robust hexahedral meshing to successfully simulate extremely complex structures.' FIT discretizes and solves the integral form of Maxwells equations that we saw at the beginning of Chapter 2 for each mesh point. It is worth understanding the flexibility of CST's meshing abilities, as it allows a dynamic range of structures to be modeled with great accuracy. After the model has been set up geometrically and assigned the appropriate power sources and boundary conditions, the model has to be translated into a computer accessible format. For general purpose electromagnetic simulation methods, the calculation domain has to be subdivided into small cells, on which Maxwells Equations are to be solved.

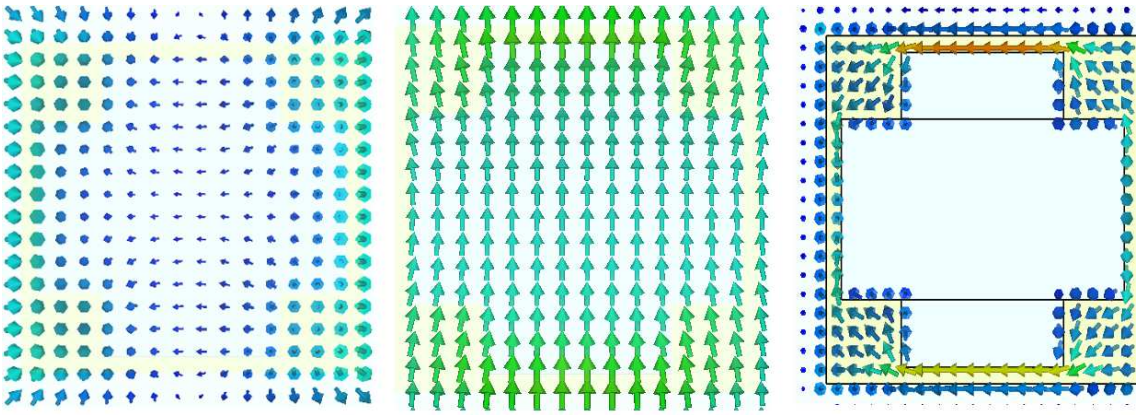

Figure 3.14: The electric field (left), magnetic field (centre), and current density (right) profiles of a cross-shaped structure simulated in CST Studio Suite. The colours of the arrows are a reference to field strength, where the bluer arrows refer to weaker parts of the field.

CST offers a variety of meshes and algorithms, which also enables an easy possibility of cross-verification of methods and meshes in the same GUI. The mesh influences the accuracy and speed of the simulation, so it is worth spending some time on understanding the meshing process. Which of these methods is best suited to the particular application depends on various aspects. In order to make the choice of the best-fitting solver and mesh easy for the user, CST has compiled a lot of experience in the so-called 'Project Wizard'. This wizard helps you to find the best solver and the best meshing technique by asking a few application-relevant questions in a short interview. After having finished this

interview for a certain application class, a template is saved, which can be directly used when studying the 2nd, 3rd, etc. geometry of the same application class. Throughout our simulations, it was found that the default mesh type (a hexagonal mesh) was suitable. The number of mesh points across all metal structures was greatly increased in every case to ensure high-quality results. The convergence of every structure was also tested for.

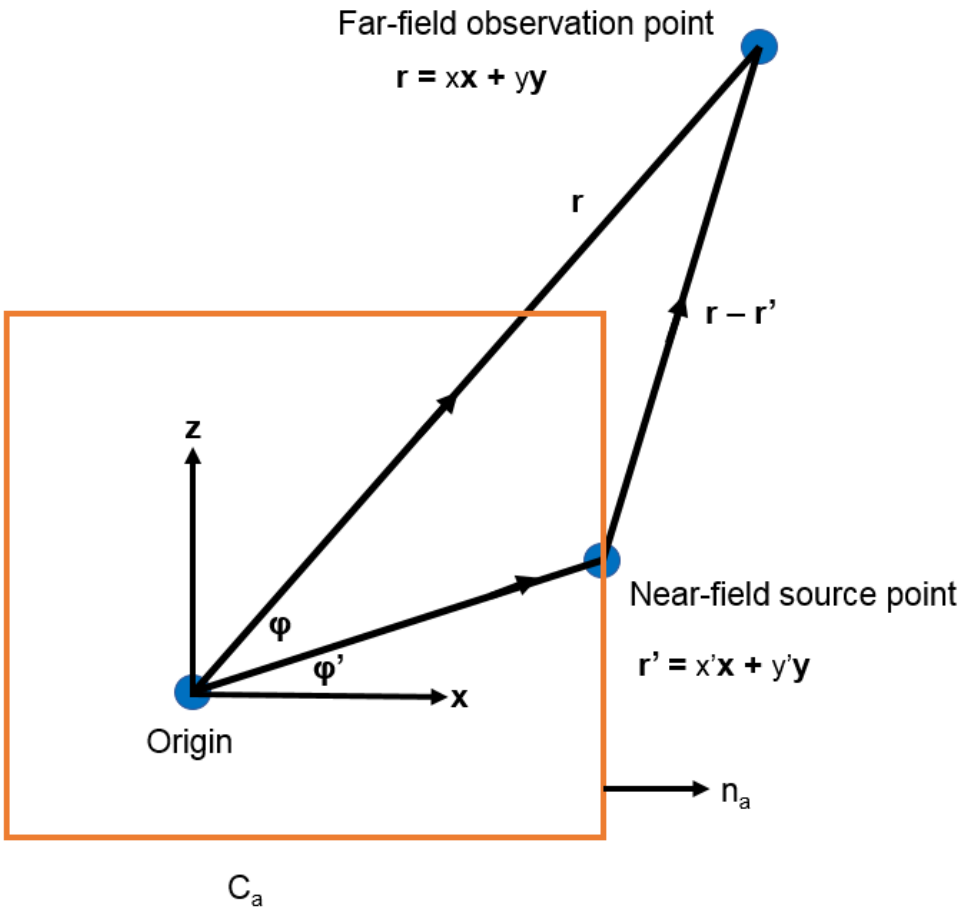

Figure 3.15: Geometry of the far-field observation point relative to the near-field integration contour, C_a.

To achieve convergence with high-quality results, a challenge when simulating metals, a few additional parameters within the solver's settings had to be adjusted before it could be used. Firstly, the accuracy of the simulations was increased to its maximum setting. This has the effect of increasing the computational time but ensures a more accurate Fourier transform from the input time signal to the required frequency space. Secondly, the number of pulses was increased to 500. This again has the effect of lengthening the simulation time, but increases the accuracy of the results. An example check of input signal quality and energy dissipation throughout the simulation is shown in Figure 3.10. A default transient analysis uses a single signal as stimulating excitation. This signal is called the 'Reference Signal'. One 'default' signal is always pre-defined as a Gaussian

signal type and refers to the globally defined frequency range. The context menu allows the choice of one of the existing signals as reference. The port mode excitation selection option in the solver menu allows the simultaneous excitation of the selected ports, each stimulated by a different excitation signal with it's own phase or time shift and different amplitude. In Figure 3.10 this signal is matched up with its energy dissipation. As can be observed, most energy contained within the simulation coincides with the peak of the wave.

A powerful concept within CST is its ability to model both periodic and single structures, with a quick method for switching between these regimes. Naturally, the type of simulation that we wish to undertake must be selected beforehand, by opening up CST's 'Boundaries' button. For the $LiTaO_3$ structure, 'open boundaries with air' was selected, i.e. the simulation only considers the single structure encapsulated in an air box. If no 'with air' option was chosen, CST would assume that the structure is encapsulated in the glass in which the parallelepipeds are embedded. For the cross structures of Chapter 4, however, it was necessary to select periodic boundary conditions with a period large enough to effectively have a single unit cell. The options for creating a mesh for the solver are also rigorous; the number of mesh cells for each part of the structure can be tailored accordingly.

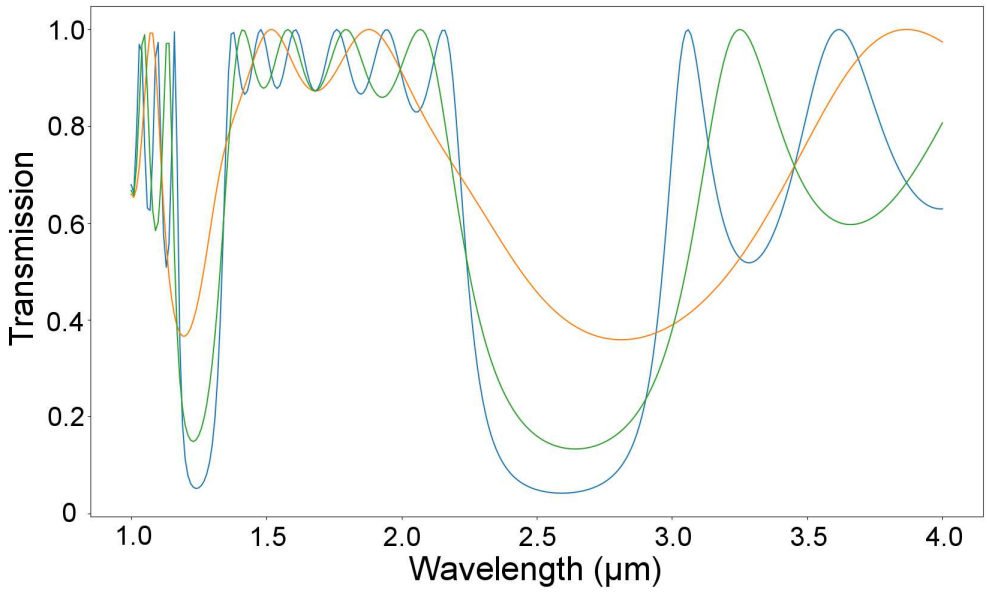

Figure 3.16: The optical response of a stratified medium dependent upon the number of layers. Orange, green, and blue, correspond to 6, 10, and 14 individual layers, respectively. Clearly, the Bragg filter acts as a notch filter much more convincingly with an increased number of layers. The layers consist of alternating widths of 300nm and 400nm, while the refractive indices were 1.38 and 2.32, respectively. It must be stressed that these parameters do not correspond to particular materials, but were used to showcase the working code.

While the material library of CST is more extensive than that of DiffractMOD, it was nevertheless still necessary to define key materials manually, such as the $LiTaO_3$ that will be seen Chapter 5. CST, like DiffractMOD, allows multiple ways of material definition to be input into the software, including thermal and mechanical definitions. However, a more flexible method is also applicable; CST allows the user to upload a file containing the permittivity values at specific wavelengths. For out $LiTaO_3$ definition, a file was created containing its real and imaginary permittivity values for every frequency between 1THz-5THz in 0.001THz increments, and subsequently uploaded into CST's software. Part of this calculated spectrum is shown in Figure 3.12

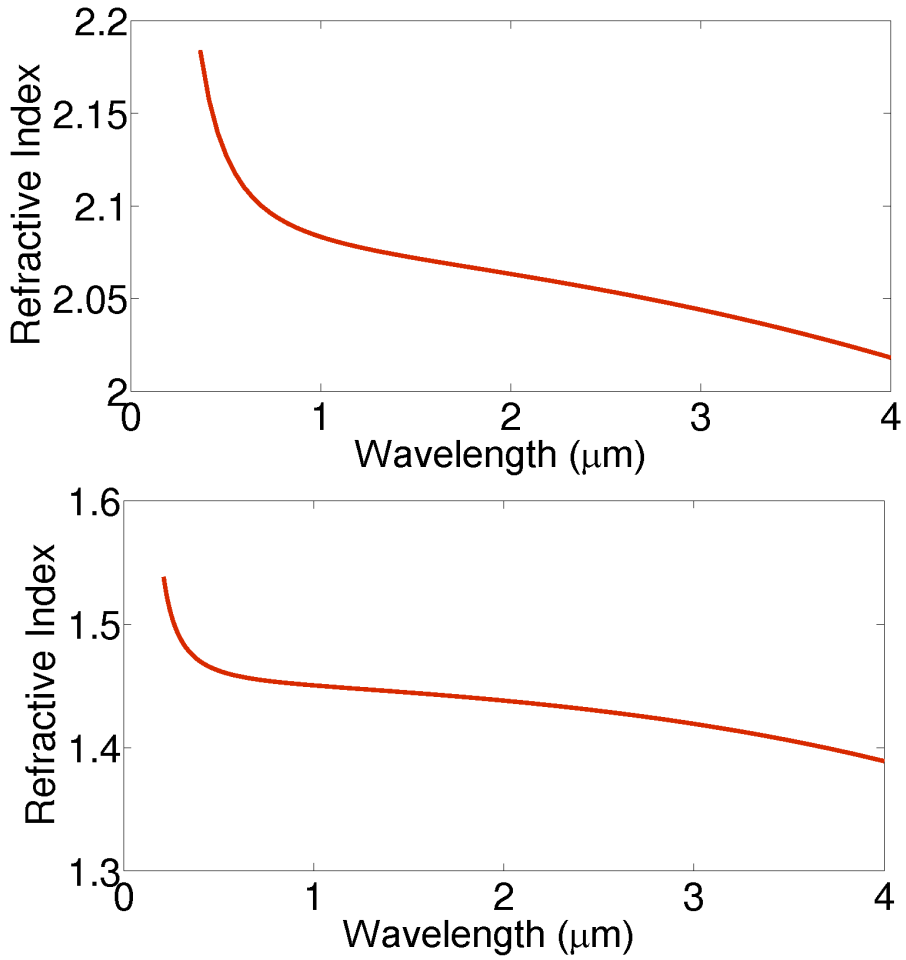

Figure 3.17: The refractive indices of HfO_2 (top) and SiO_2 (bottom). The definitions of these materials are taken from [21] and [22], respectively.

The visualisation abilities of CST are superior to DiffractMOD's: while simulating the required results, the solver can also simultaneously store the resulting electromagnetic fields alongside the current densities for any desired frequency in any desired region of the simulated space. This immediately allows the user to get a feel for the underlying

physics, a feature that is especially relevant for my projects, as often it was the study of electromagnetic multipoles that was being undertaken. To be able to view the current density patterns gives the user a large clue as to which multipole is being excited. As an example, we the electric and magnetic fields along with the current density profile of a standard cross-shape calculated with CST in Figure 3.14.

Useful parameters that CST calculates that enable the user to understand which frequencies are responsible for the resonances and how strongly the structures resonate at these frequencies are the cross-sections, specifically the absorption cross section (ACS) and radar cross section (RCS), which is also known as the scattering cross section. An example of these cross sections is plotted in Figure 3.13 for the $LiTaO_3$ structures that will be analysed in Chapter 5.

3.2.1 CST Optimizer

CST comes with its own optimizer, which can be used to optimize the quality factor of resonances more rigorously than DiffractMOD. It's possible to incorporate three goals into one optimization program; Figure 3.11 depicts an example of this. In the same style as the cross with reduced metal, Figure 3.11 shows the results of telling the optimizer to maximise the resonance between 117-123THz, and to minimise the signal outside of this range through freely manipulating the width of the gold and length and width of the arms of the cross. The resulting structure with its updated parameters is shown in Figure 6.17.

3.3 Near-To-Far-Field Transformation *via* Green's Function

In order to analyse the multipoles and their respective far-fields, a MATLAB script was implemented that utilizes a near-to-far-field transformation *via* implementation of Green's functions. While this process is fully described in [20], an overview of its processes is given here to aid the reader's understanding as to how the full power of the interacting multipoles is calculated from the simulated near-fields.

The problem of interest is shown in Figure 3.15. The top-right point denotes the location where the far-field, arising from the near-field, is experienced. The location of the near-field's genesis is shown relative to the origin. The problem, then, is clear: given this near-field, what exactly does the observer at the far-field experience?

In answering this pertinent question, it can be shown [20] that a key physical quantity that arises is:

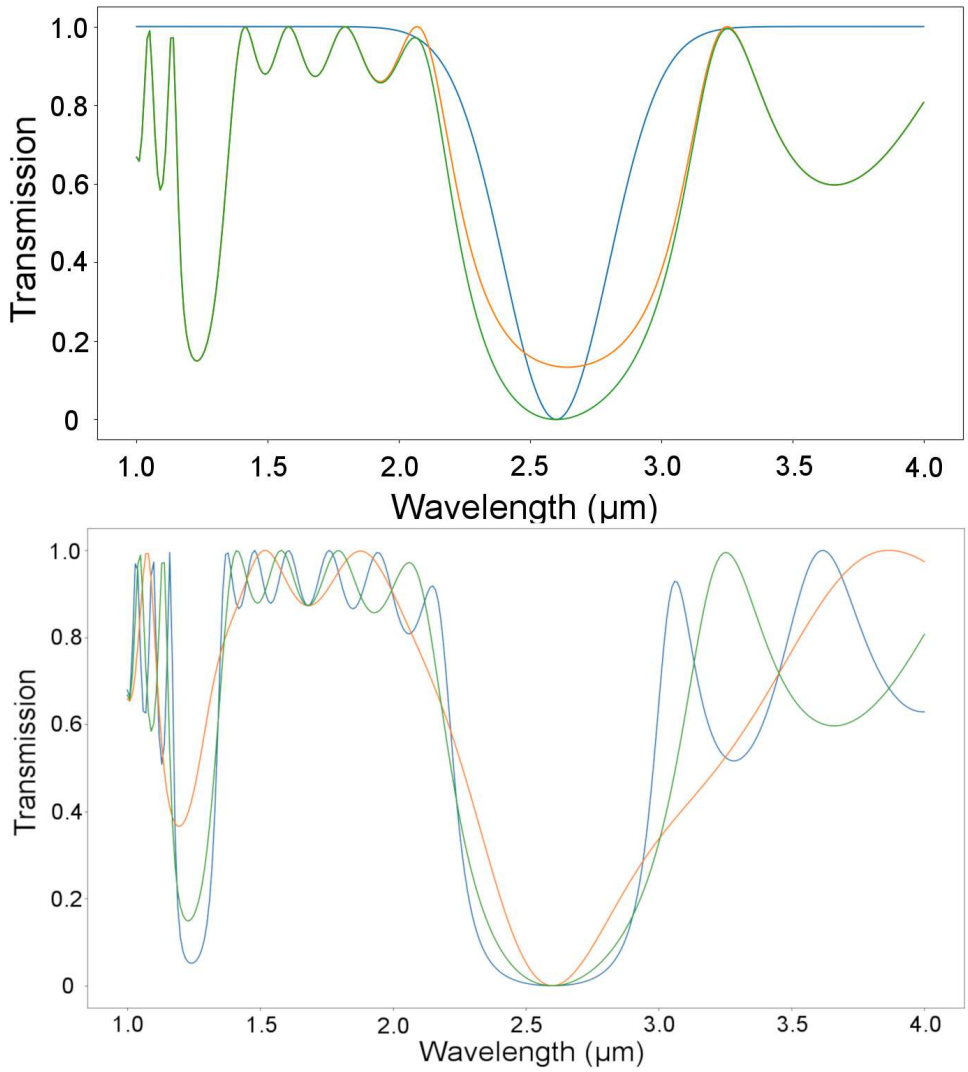

Figure 3.18: Top - Incorporating a Gaussian input into the Bragg gratings. The orange curve depicts a Bragg grating consisting of 10 layers for a uniform input. The blue curve is a Gaussian input, designed to reflect the notch-like characteristics of the metamaterial filter to be later placed on the Bragg filter. The green curve is a culmination of the Bragg grating accepting the Gaussian signal. The corresponding transmission acts more notch-like with the Gaussian inclusion. Bottom - The effect of increasing the number of layers of the Bragg filter that takes a Gaussian input. The orange, green, and blue curves correspond to 6, 10, and 14 individual layers, respectively. The composite acts as a notch filter with an increasing number of layers.

$$F(\phi) \equiv \frac{e^{j(\pi/4)}}{\sqrt{8\pi k}} \oint_{C_a} [\omega\mu_0 \hat{\mathbf{z}}' \cdot \mathbf{J}_{eq}(\mathbf{r}') - k\hat{\mathbf{z}}' \times \mathbf{M}_{eq}(\mathbf{r}') \cdot \hat{\mathbf{r}}] e^{jk\hat{\mathbf{r}}\cdot\mathbf{r}'} dC' \tag{3.7}$$

where $\mathbf{J}_{eq} \equiv \hat{n_a} \times \mathbf{H}$ and $\mathbf{M}_{eq} \equiv -\hat{n_a} \times \mathbf{E}$ are defined as the tangential equivalent electric and magnetic currents observed at C_a, respectively. The above definition of $F(\phi)$ is crucial for acquiring the near-to-far-field transformation, as the radar cross section (RCS) can

be defined:

$$RCS(\phi) \equiv 2\pi \frac{\text{power scattered per unit angle in direction}}{\text{incident power per unit length}} \equiv 2\pi \frac{|F(\phi)|^2}{|\mathbf{E}_{inc}|^2} \tag{3.8}$$

A quote from [20] helps elucidate why the above equations are so powerful: 'It should be emphasised that C_a is *not* a physical surface. It is a *virtual surface* that is the locus of points in space where E- and H-field data are being compiled and integrated. Because C_a can have an arbitrary shape, we can conveniently assign it to lie along a rectangle in the scattered-field zone of the FDTD [Finite Difference Time Domain] grid.'

The use of the term 'FDTD' is a reference to the popular computational technique that can calculate the electromagnetic fields at multiple frequencies in one run. Hence, the above method can be utilized to swiftly apply NTFF transformations for a wide range of frequencies.

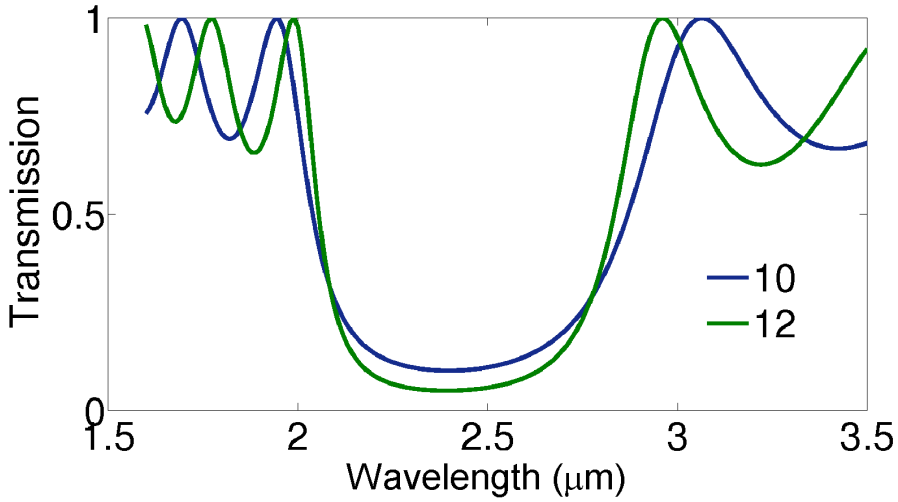

Figure 3.19: The response of the Bragg filter with a varying number of layers, composed of SiO_2 and HfO_2, simulated by DiffractMOD. Both 10 and 12 individual layers are depicted.

3.4 Conclusions

The software package DiffractMOD was introduced. The effects of periodicity upon the optical response of a metamaterial were simulated alongside with the role of the number of harmonics. Simulations that exhibit a double resonance from one metamaterial were also presented. A gold split ring resonator embedded in a dielectric was shown to exhibit a strong nonlinear toroidal resonance when excited by an impinging electromagnetic wave.

The important parameters of CST Studio Suite were also displayed, including the absorption cross section and time signals. The method of incorporating new materials was documented, an important feature for the following chapters of this thesis.

In both cases, the relevant optimizers were discussed in detail. These optimizers allow certain goals to be specified, which the optimizer then aims towards. As shall be seen later on, a large segment of this thesis deals with the fabrication of a cross-shaped trench structure, which is a direct result from the MOST optimizer.

Finally, this chapter finished with a brief discussion on combining metamaterials with Bragg filters. Due to its filtering effects, it is intuitive to think that a metamaterial can essentially act as a replacement for a number of layers in a Bragg filter. The plotted graphs do indeed show that several layers of a Bragg filter can be replaced by instead placing a metamaterial notch filter on top of the filter.

Bibliography

[1] H. H. Li, "Refractive index of alkaline earth halides and its wavelength and temperature derivatives", J. Phys. Chem. Ref. Data. **9**, 161-289 (1980) and references therein.

[2] S. Peng and G. M. Morris, "Efficient implementation of rigorous coupled-wave analysis for surface-relief gratings", JOSA A **12**, 1087-1096 (1995).

[3] www.refractiveindex.info

[4] E. J. Osley, C. G. Biris, P. G. Thompson, R. R. F. Jahromi, P. A. Warburton, and N. C. Panoiu, "Fano resonance resulting from a tunable interaction between molecular vibrational modes and a double continuum of a plasmonic metamolecule", Phys. Rev. Lett, **110**, 087402 (2013).

[5] Synopsys, [Accessed September 16th 2018], Available from: https://www.synopsys.com/optical-solutions/rsoft/most.html

[6] V. Savinov, V. A. Fedotov, and N. I. Zheludev, "Toroidal dipolar excitation and macroscopic electromagnetic properties of metamaterials", Phys. Rev. B **89**, 205112 (2014).

[7] B. Ögüt, N. Talebi, R. Vogelgesang, W. Sigle, and P. A. van Aken, "Toroidal plasmonic eigenmodes in oligomer nanocavities for the visible", Nano Lett. **12**, 52395244 (2012).

[8] Y. Huang, W. T. Chen, P. C. Wu, V. Fedotov, V. Savinov, Y. Z. Ho, Y. Chau, N. I. Zheludev, and D. P. Tsai, "Design of plasmonic toroidal metamaterials at optical frequencies", Opt. Exp. **20**, 1760-1768 (2012).

[9] Z. Dong, J. Zhu, J. Rho, J. Li, C. Lu, X. Yin, X. Zhang, "Optical toroidal dipolar response by an asymmetric double-bar metamaterial", Appl. Phys. Lett. **101**, 144105 (2012).

[10] Z. Dong, J. Zhu, X. Yin, J. Li, C. Lu, and X. Zhang, "All-optical Hall effect by the dynamic toroidal moment in a cavity-based metamaterial", Phys. Rev. B **87**, 245429 (2013).

[11] Y. Fan, Z. Wei, H. Li, H. Chen, and C. M. Soukoulis, "Low-loss and high-Q planar metamaterial with toroidal moment", Phys. Rev. B **87**, 115417 (2013).

[12] Z. Dong, P. Ni, J. Zhu, X. Yin, and X. Zhang, "Toroidal dipole response in a multifold double-ring metamaterial", Opt. Exp. **20**, 13065-13070 (2012).

[13] V. A. Fedotov, A. V. Rogacheva, V. Savinov, D. P. Tsai, and N. I. Zheludev, "Resonant transparency and non-trivial non-radiating excitations in toroidal metamaterials", Sci. Rep. **3**, 2967 (2013).

[14] D. Timbrell, M. Weismann, N. V. S. Braz, P. A. Warburton, and N. C. Panoiu, "Toroidal dipoles generated in nonlinear plasmonic metamaterials", Metamaterials 2015, (2015).

[15] T. Kaelberer, V. A. Fedotov, N. Papasimakis, D. P. Tsai, and N. I. Zheludev, "Toroidal dipolar response in a metamaterial", Science, **330**, 1510-1512 (2010).

[16] L. Cao, N. C. Panoiu, and R. M. Osgood, "Surface second-harmonic generation from surface plasmon waves scattered by metallic nanostructures", Phys. Rev. B **75**, 205401 (2007).

[17] M. Weismann, D. F. G. Gallagher, and N. C. Panoiu, "Nonlinear generalized source method for modelling second harmonic generation in diffraction gratings", J. Opt. Soc. Am. B, **32**, 523-533 (2015).

[18] T. Weiland, "A discretization method for the solution of Maxwell's equations for six-component fields: Electronics and communication", Archiv für Elektronik und Übertragungstechnik, **31**, 116-120, (1977).

[19] A. A. Basharin, M. Kafesaki, E. N. Economou, C. M. Soukoulis, V. A. Fedotov, V. Savinov, and N. I. Zheludev, "Dielectric metamaterials with toroidal dipolar response", Phys. Rev. X **5**, 011036 (2015).

[20] A. Taflove and S. C. Hagness, *Computational Electrodynamics: The Finite Difference Time Domain Method*, Chapter 8 (Artech House, 2005).

[21] D. L. Wood, K. Nassau, T. Y. Kometani, and D. L. Nash, "Optical properties of cubic hafnia stabilized with yttria", Appl. Opt. **29**, 604-607 (1990).

[22] C. Z. Tan, "Determination of refractive index of silica glass for infrared wavelengths by IR spectroscopy", J. Non-Cryst. Solids **223**, 158-163 (1998).

Chapter 4

Analysis of surface and bulk second-harmonic generation in centrosymmetric nanoparticles

4.1 Introduction

In this chapter a cross-shaped meta-atom is introduced and both a plasmonic and an all-dielectric case is considered. In both scenarios, the material from which the cross is constructed is centrosymmetric; gold and silicon are analysed for the plasmonic and all-dielectric case, respectively. The scattering configuration is first introduced, followed by the physics governing the linear optical interactions. The most important terms of the multipole expansion are also introduced. The linear results arising from both cases are then analysed in detail, with pertinent focus being concentrated on the important resonances.

The nonlinear regime for both the surface and bulk interactions are in each case considered, whereby the underlying physics is introduced and the nonlinear results delineated in detail. The nonlinear results highlight that a surface neglection in the bulk case most show itself to be valid, due to the strong possibility of the presence of salient physics.

4.2 Background

The strong field enhancement that accompanies the excitation of surface-plasmon polaritons (SPPs) on metallic nanoparticles [1, 2] makes these nanostructures ideal candidates for many applications, including nanoscale antennae, single-molecule detection *via* surface-enhanced Raman scattering, metallic nanotips for near-field optical microscopy,

and optically-active guiding nanostructures [3–9]. However, the generation of large optical fields comes at a price of significant optical losses present in metals. In fact, these losses are viewed as the main factor that still precludes a widespread use of plasmonic devices in practical applications [10]. Methods that attempt to overcome this restriction include using doped semiconductors [11] and gain media [12].

An alternative to plasmonic materials, which aims to circumvent optical losses, consists of using all-dielectric resonant structures [13,14]. Unlike the excitation of the metallic plasma that engenders the plasmonic resonances, it is the resonances of displacement currents, known as *Mie resonances* [15], that enable these all-dielectric components to be used for optical field manipulation. While the field enhancement of these dielectric structures is typically weaker than that of their metallic counterparts, their high quality factors enable intriguing optical phenomena to be produced, including magnetic mirrors [16], reflectionless ultrathin sheets mimicking highly directional Huygens sources [17, 18], and toroidal dipole sources [19, 20]. These dielectric nanostructures have shown great promise in biosensing, optoelectronics, and energy applications [21]. Hence, the trade-off is clear: the selection of metal or dielectric is dependent upon the requirements of particular applications, namely whether one desires strong field enhancement or low optical losses.

This dichotomy extends to *nonlinear nanoscale photonics*. By exciting a structure that has both strong field enhancement and strong nonlinear properties, large nonlinear signals can be produced at relatively low optical powers. In particular, nonlinear optical processes in plasmonic structures have been studied extensively [22, 23], including surface-enhanced Raman scattering [3,7,24], second-order optical interactions [25–36], and Kerr interactions [37,38]. As in the linear case, these strong nonlinear optical effects in plasmonic structures are accompanied by large optical losses, which restrict the range of applications to which nonlinear optical interactions can be employed. It is therefore of particular interest to understand, in the context of nonlinear nanophotonics, the limitations and advantages provided by plasmonic structures, as compared to those characteristic to all-dielectric resonant subwavelength structures.

In order to address this important problem, in this chapter we focus on second-harmonic generation (SHG), perhaps the most widely studied nonlinear optical interaction. Since most plasmonic materials are centrosymmetric, i.e. the crystal lattice is invariant upon inversion symmetry transformations, we consider for comparison dielectric materials that are also centrosymmetric. More specifically, we assume that the plasmonic and dielectric materials are *gold* (Au) and *silicon* (Si), respectively. Under these circumstances, the second-harmonic (SH) field has two principal components, namely the (local) surface and (nonlocal) bulk contributions of the medium to a nonlinear signal. From a physical point of view, as will become clear from the mathematical description

of these nonlinear optical effects, the main difference between the two contributions is that whereas the surface component is (quadratically) proportional to the optical field at the fundamental frequency (FF), the bulk component is proportional to the field and its derivatives.

It is a common assumption that the bulk nonlinear response to an applied electromagnetic field is negligible for plasmonic structures. The validity of this assumption, however, has hitherto been rigorously addressed only for plasmonic structures with simple configurations, such as metallic thin-films [39], spherical metallic particles [40], and split-ring resonators [41], *no attempts having been made to investigate this problem in the case of dielectric particles*. It should be noted that this problem does not have a simple, *a priori* answer. Thus, in plasmonic materials optical fields are highly inhomogeneous, so that the field derivatives can be rather large; however, these fields extend from the surface into the bulk no more than about a skin-depth, that is, the characteristic distance the electric field penetrates into a metal. By contrast, optical fields penetrate throughout a dielectric structure, yet they are much less inhomogeneous as compared to the plasmonic case. To elucidate this matter, in this chapter we study theoretically and computationally, the relative contribution to SHG of the surface and bulk effects in two generic structures made of centrosymmetric materials, one metallic and one dielectric, both exhibiting resonant field enhancement. In particular, we choose cruciform-shaped particles as they have pronounced electric dipole, magnetic dipole, and electric quadrupole resonances. However, more complex resonances, such as Fano resonances [42–45], or particle shapes can be considered.

The chapter is organized as follows. In the following section we describe the scattering configuration, the computational approach used in our study, and the physical model for SHG in nanoparticles made of centrosymmetric materials. In the third section we present the frequency dependence of the linear and nonlinear optical coefficients of gold and silicon. The main results of our analysis are presented in Results and Discussion, with the main conclusions being summarized in the final section.

4.3 Model and Scattering Configuration

The structure analyzed here is shown schematically in Fig. 4.1, with the dimensions given in the caption. This symmetric cross sits atop a glass substrate, with permittivity $\epsilon_s = 2.5$, which is assumed to occupy the region $z < 0$. The cross is illuminated with normal-incidence light ($-z$-direction), with the $\mathbf{E}$ and $\mathbf{H}$ fields polarized along the x- and $-y$-direction, respectively, the wave intensity being $1\,\mathrm{GW\,cm^{-2}}$. The optical response of this structure is, however, polarization-independent due to its symmetry.

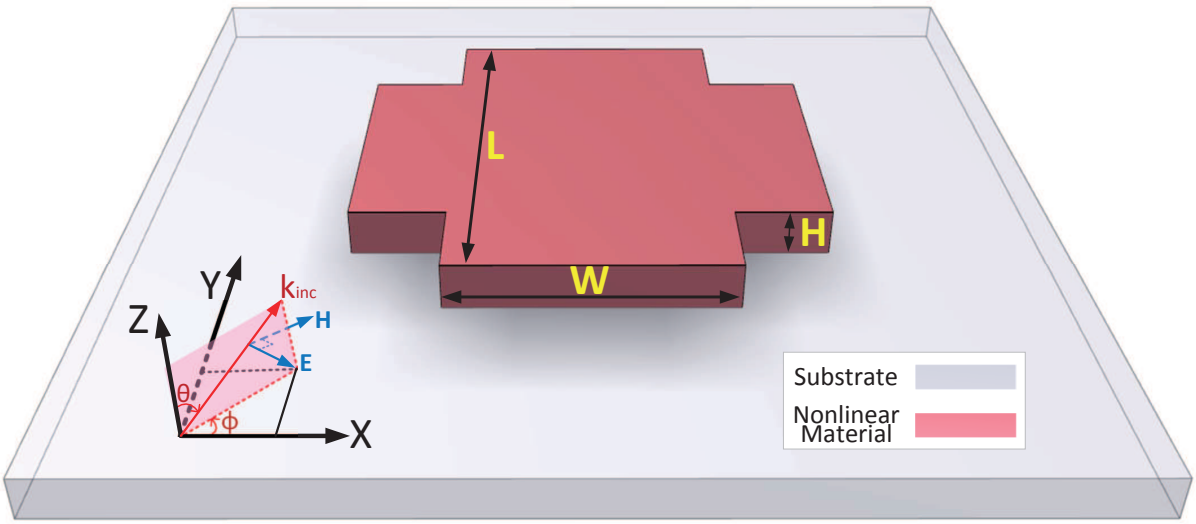

Figure 4.1: Schematics of the analyzed structure. A cruciform scatterer made of centrosymmetric materials (Au or Si) sits atop a glass substrate lying in the xy-plane. The gold cross has dimensions of $L = 100\,\text{nm}$, $W = 55\,\text{nm}$, and $H = 30\,\text{nm}$, whereas the silicon cross has dimensions of $L = 370\,\text{nm}$, $W = 220\,\text{nm}$, and $H = 220\,\text{nm}$. The cross is illuminated with a plane wave impinging normally onto the substrate, with the electric and magnetic fields being oriented along the arms of the cross. Hence, for the purposes of our calculations, we set $\theta = \pi$ and $\phi = \pi/2$.

The choice of dimensions of the particles was guided by general characteristics of common experimental set-ups. Thus, plasmonics experiments are usually performed in the visible spectrum, whereas most applications of silicon devices are in the IR spectral domain (1.3 µm and 1.55 µm for data centers and telecom applications, respectively). Therefore, we chose the dimensions of our particles such that they have resonances in the corresponding spectral domain of practical interest. In addition, we chose a thickness of the silicon cross of $H = 220\,\text{nm}$ because a common material platform employed in nonlinear optics experiments is silicon-on-insulator (SOI), the thickness of the silicon layer of commonly used SOI wafers being $H = 220\,\text{nm}$.

We select the cruciform shape of particles as they are an excellent middle-ground between analytically solvable structures such as spheres and specifically tailored structures, i.e. they are complex enough to provide generality to our conclusions yet not too complex to completely obscure the origin of the revealed physics. In addition, the cruciform particles support the most basic Mie-type resonances, i.e. electric dipole, magnetic dipole, and electric quadrupole resonances. Therefore, we expect that most of the new physics revealed by our study should apply to nanoparticles with other shapes, too, as there is nothing specific regarding the nature of the Mie resonances of the nanoparticles investigated in this work. Finally, one expects that the ratio between the contribution

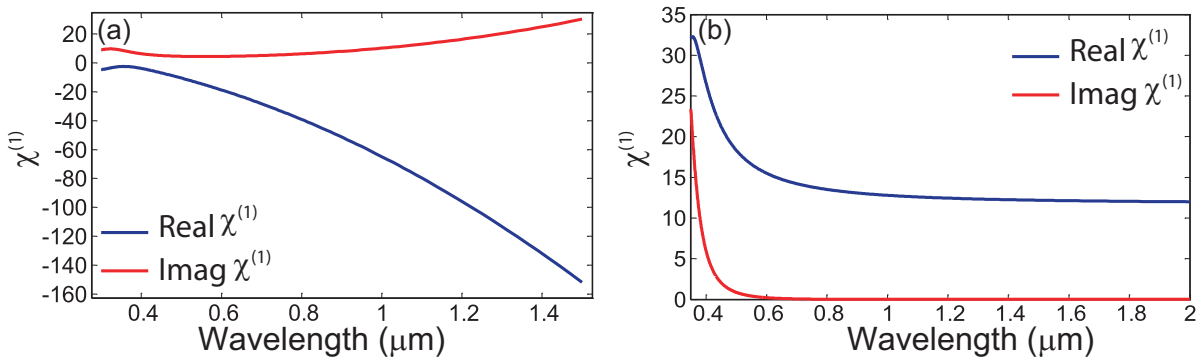

Figure 4.2: a), b) The wavelength dependence of the real and imaginary parts of the linear susceptibility of Au and Si, respectively. The dispersion of the metal is clearly stronger.

of bulk and surface effects to SHG is primarily determined by the inhomogeneity of the optical near-field at the FF. This inhomogeneity is the largest at the wavelengths of the resonances of the particle, and does not change significantly with the angle of incidence. Therefore, we employ a simple scattering configuration, which still captures the main physics of the problem investigated in our study.

The linear optical response of the cruciform structures has been calculated using the time-domain solver of CST Studio Suite [46]. Periodic boundary conditions are employed in the x- and y-direction, whereas in the z-direction we use perfectly absorbing boundary conditions. The period is chosen large enough so as in the spectral range considered here the optical coupling between the crosses is negligible and thus we can assume that we operate in the single-scatterer regime. Moreover, in order to study size dependence effects, we also consider crosses whose arm length and width are scaled by a factor α (the height is kept constant, as this choice better reflects standard experimental conditions), with $\alpha = 1, 1.25, 1.5, 1.75$, and 2.

In our calculations, a frequency scan from 200 THz to 1000 THz (150 THz to 500 THz) in 4 THz (0.5 THz) increments is performed for gold (silicon), for a sufficiently fine computational mesh. In both cases the frequency dispersion of the permittivity is fully taken into account by fitting the experimental data with a Drude function and a set of Lorentzians in the case of Au, and a set of Lorentzians in the case of Si (see the section Dispersion of Linear and Nonlinear Optical Coefficients for more details regarding the modeling of the frequency dispersion of Au and Si). Note that our models for the frequency dispersion of the permittivity of gold and silicon take into account both interband transitions effects in the case of gold and bandgap effects in the case of silicon.

A key property of optical materials is the frequency dispersion of their permittivity. This wavelength-dependent function describes the electromagnetic response of the ma-

terial in the linear regime. Figure 4.2 depicts both the real and imaginary parts of the susceptibility function, $\chi^{(1)}$, of Au and Si. As can be seen by comparing the data plotted in this Figure, the electric response of the metal is clearly more dispersive, a fact that was eluded to in the theoretical discussion in Chapter 2. These linear susceptibilities are taken from several references regarding linear optical properties of Au [47, 48] and Si [49–51].

As is well known, electromagnetic multipoles associated to a nanoparticle can reveal key physical insights into the optical properties of the subwavelength scatterer [52]. Therefore, for both types of crosses, we performed a multipole decomposition, whereby the radiated powers associated with the first three terms of the multipole expansion were calculated. These multipoles, the electric dipole, magnetic dipole, and electric quadrupole, were witnessed in detail in Chapter 2.

In order to describe the nonlinear optical signal generated by the scatterer, we employ a widely used model of SHG in centrosymmetric media [53]. Specifically, SHG has a surface component generated within a few atomic layers at the surface of the material and a bulk component generated inside the material, as given in Chapter 2.

Except for the case when the surface contains structural features with intrinsic chirality, the surface of centrosymmetric media possesses an isotropic mirror-symmetry plane perpendicular to the interface. Then, the surface nonlinear susceptibility $\hat{\chi}_s^{(2)}$ has only three independent components, that is, $\hat{\chi}_{s,\perp\perp\perp}^{(2)}$, $\hat{\chi}_{s,\perp\parallel\parallel}^{(2)}$, and $\hat{\chi}_{s,\parallel\perp\parallel}^{(2)} = \hat{\chi}_{s,\parallel\parallel\perp}^{(2)}$, where the symbols $\perp$ and $\parallel$ refer to the directions normal and tangent to the surface, respectively. As most theoretical models predict that $\hat{\chi}_{s,\perp\parallel\parallel}^{(2)} = 0$ [54, 55], we make this assumption in our calculations, too. The susceptibility components of Au, measured at $\lambda = 810\,\mathrm{nm}$, are $\hat{\chi}_{s,\perp\perp\perp}^{(2)} = -(0.86 + 1.34i) \times 10^{-18}\,\mathrm{m^2\,V^{-1}}$ and $\hat{\chi}_{s,\parallel\parallel\perp}^{(2)} = \hat{\chi}_{s,\parallel\perp\parallel}^{(2)} = -(4.61 + 0.43i) \times 10^{-20}\,\mathrm{m^2\,V^{-1}}$ [56], whereas in the case of Si, their measured values at $\lambda = 800\,\mathrm{nm}$ are $\hat{\chi}_{s,\perp\perp\perp}^{(2)} = 65 \times 10^{-19}\,\mathrm{m^2\,V^{-1}}$ and $\hat{\chi}_{s,\parallel\parallel\perp}^{(2)} = \hat{\chi}_{s,\parallel\perp\parallel}^{(2)} = 3.5 \times 10^{-19}\,\mathrm{m^2\,V^{-1}}$ [57].

The nonlinear polarizations that are generated can be used to calculate the nonlinear multipoles, which can be viewed as multipolar sources for the nonlinear field. However, this approach is less accurate when applied to the SH calculations, as in this case the ratio between the nanoparticle size and wavelength is larger than it is at the FF and therefore the multipole expansion converges more slowly. As a result, we use an alternative method to calculate the nonlinear optical response of the crosses. Thus, these same polarizations define nonlinear currents, *via* $\mathbf{J}_\Omega^{s,b}(\mathbf{r}) = -i\Omega\mathbf{P}_\Omega^{s,b}(\mathbf{r})$ (an $e^{-i\omega t}$ dependence of all harmonic fields is assumed throughout this study). These nonlinear currents can subsequently be used to calculate the nonlinear optical far-field by employing a near-field/far-field transformation [59], thus enabling a complete characterization of the nonlinear scattering

process.

4.4 Dispersion of Nonlinear Optical Coefficients

As discussed in the preceding section, our calculations incorporate the frequency dispersion of the linear optical susceptibility function. More specifically, the permittivity for gold is taken from Refs. [47, 48], and it is valid for the wavelength range of 0.15 µm to 24.93 µm, whereas the permittivity of silicon, valid in the wavelength range of 0.25 µm to 25 µm, is taken from Refs. [49–51].

In order to describe the nonlinear optical response of the nanoparticles, one can incorporate in the computational analysis the frequency dependence of the surface and bulk nonlinear susceptibilities, too. This frequency dispersion can be described using the Miller rule [60]. Explicitly, this rule states that the ratio

$$\frac{\chi^{(2)}(\omega_1+\omega_2;\omega_1,\omega_2)}{\chi^{(1)}(\omega_1+\omega_2)\chi^{(1)}(\omega_1)\chi^{(1)}(\omega_2)}=\mathcal{C} \tag{4.1}$$

is nearly constant. In Eq. (4.1), $\chi^{(1)}$ is the linear susceptibility, $\chi^{(2)}$ is any of the surface or bulk nonlinear susceptibilities, $\hat{\chi}^{(2)}_{s,\perp\perp\perp}$, $\hat{\chi}^{(2)}_{s,\parallel\parallel\perp}=\hat{\chi}^{(2)}_{s,\parallel\perp\parallel}$, γ, and ζ, whereas ω_1 and ω_2 are the frequencies of the interacting beams.

As our chapter concerns SHG, we put $\omega_1=\omega_2\equiv\omega$. The constant $\mathcal{C}$ can be calculated using the corresponding experimental data at an arbitrary reference frequency, ω_r, and thence subsequently used to calculate the full nonlinear dispersions of our materials. In particular, $\mathcal{C}$ is given by

$$\mathcal{C}=\frac{\chi^{(2)}(\Omega_r,\omega_r)}{\chi^{(1)}(\Omega_r)[\chi^{(1)}(\omega_r)]^2}, \tag{4.2}$$

where $\Omega_r=2\omega_r$.

The real and imaginary parts of the main bulk nonlinear susceptibility, γ, are presented for Au and Si in Figs. 4.3(a) and 4.3(b), respectively. Due to the nature of the Miller rule, the shape of the dispersion curves corresponding to the other nonlinear susceptibilities will remain the same; only the scaling constant $\mathcal{C}$ will change. A comparison of the data plotted in Figure 4.2 reveals that for Au the magnitude of the nonlinear susceptibilities increases when the wavelength increases, whereas it decreases in the case of Si. It is also clear that the variance of the susceptibility values is greater for Au, which is not a surprising fact considering that the nonlinear dispersion is dependent upon the square of the linear dispersion.

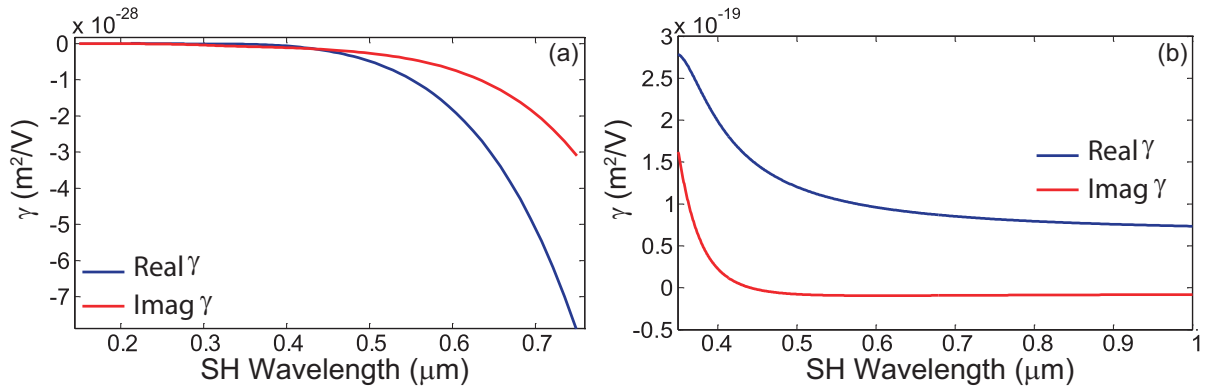

Figure 4.3: Frequency dispersion of the second-order surface and bulk susceptibilities of Au and Si. (a), (b) The wavelength dependence of the bulk nonlinear susceptibility, γ, of Au and Si, respectively. All nonlinear susceptibilities will follow the same wavelength dependence, but multiplied by a different scaling constant.

4.5 Results and Discussion

The nonlinear polarization, and implicitly the sources of the SH field, is primarily determined by the field at the FF, and therefore we have started our analysis with the calculation of the linear optical field. The spectra of the linear scattering cross-section of the metallic crosses, determined for several values of the scaling parameter α, are plotted in Fig. 4.4(a). They show a prominent resonance, which for the cross with $\alpha = 1$ is located at 0.63 µm. Unsurprisingly, as seen from our discussion in Chapter 3, as the cross is scaled to larger sizes, the resonance peak shifts to increasing wavelengths. The field distribution calculated at the resonance wavelength of the cross with $\alpha = 1$ and shown in the inset of Fig. 4.4(b), suggests that this is an electric dipole resonance. To confirm this, we performed a multipole decomposition. The results of these calculations, summarized in Fig. 4.4(b) for $\alpha = 1$, clearly prove that the electric dipole has the dominant contribution to the total radiated power, in the entire wavelength range. The peak of this electric dipole spectrum is located at 0.63 µm, thus further validating our conclusion.

We compare these fundamental field results to those corresponding to a cross made of Si. The spectra of the linear scattering cross-section of this structure, determined for the same five values of α, are shown in Fig. 4.5(a). Due to the dielectric nature of the cross, more spectral resonances exist within the scanned wavelength range. In particular, as the wavelength of the incoming light decreases, higher-order (Mie) resonances of the cross can be excited within the structure. Figure 4.5(b) shows the spectra of the total radiated power as well as the spectra corresponding to the electric dipole and magnetic dipole, all calculated for the cross with $\alpha = 1$, whereas the resulting electric field distributions within the Si structure, calculated at the wavelengths of the first three resonances, namely

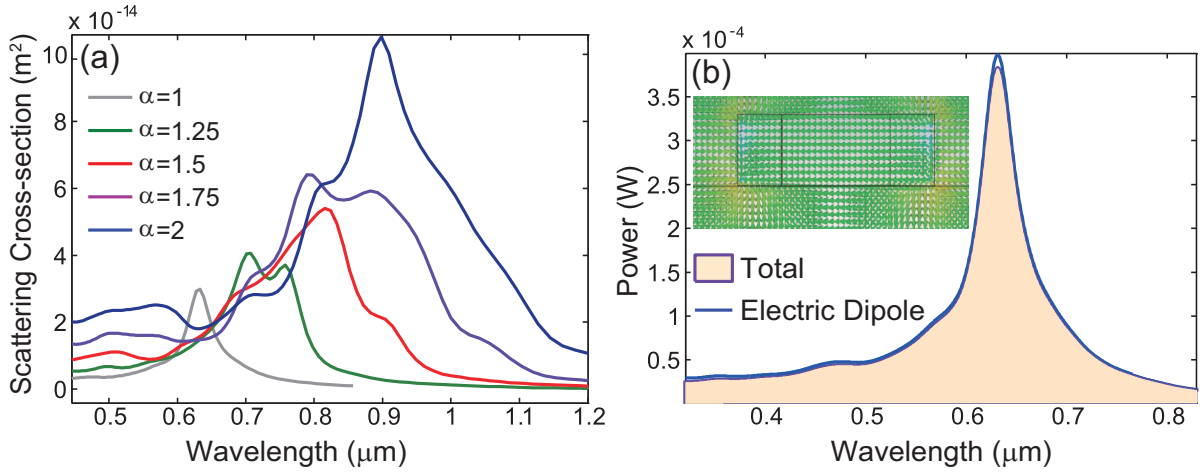

Figure 4.4: a) The spectra of the linear scattering cross-section of a cross made of gold, determined for different scaling values, α. b) A more detailed understanding of the linear regime for the case $\alpha = 1$ is provided by the spectra of the total radiated power and the power radiated by the electric dipole of the cross. The inset shows the electric field distribution calculated at the resonance wavelength in the xz-plane passing through the center of the cross.

at 0.73 µm, 0.81 µm, and 1.2 µm, are presented in Fig. 4.5(c). As these figures illustrate, the multipole expansion is less accurate when applied to the Si cross, chiefly because in this case the ratio between the cross size and wavelength is larger than that for the Au cross and thus the long-wavelength approximation, in which the multipole expansion holds, becomes inaccurate.

Inspecting the spectrum of the total radiated power, one can observe three distinct peaks within the wavelength range. The spectra in Fig. 4.5b and the field profiles shown in Fig. 4.5c suggest that peaks A and C correspond to an electric dipole mode and a superposition of a strong magnetic dipole mode and a weaker, higher-order magnetic mode, respectively, whereas the spectral peak B is the result of a mixture of multipole resonances. Note also that both the scattering spectra and field distributions suggest that at peak A there is an additional contribution from a magnetic dipole mode. Moreover, one can clearly see in Fig. 4.5(b) spectral regions where the light radiated by different multipoles interfere destructively or constructively, thus suppressing or enhancing the total radiated power, respectively. This interference among optical fields emitted by different multipoles has been observed experimentally [61], both in the linear and nonlinear regimes.

It must be noted that, as expected, the quality factor of the resonances of the gold cross is smaller than that of the silicon cross. This is due to the optical losses in the metal, which add to the radiative ones. Moreover, the total power radiated by the silicon cross naturally outweighs the total power scattered by the gold cross, as the ratio of the

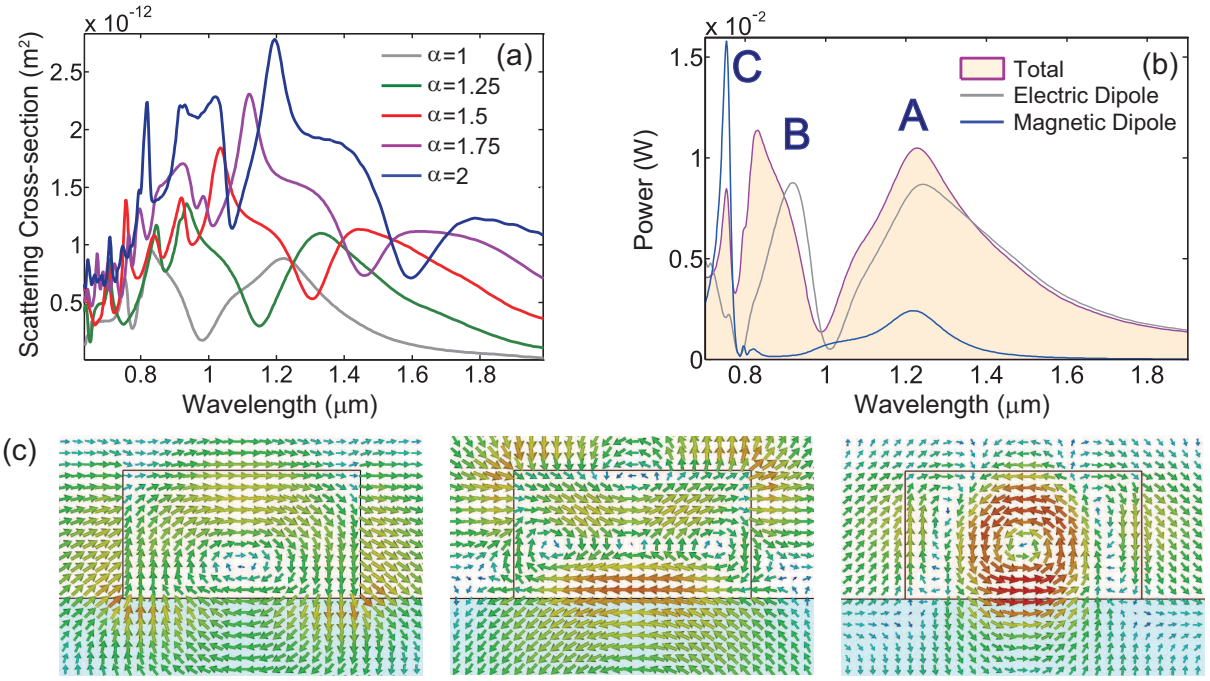

Figure 4.5: a) The spectra of the linear scattering cross-section of a silicon cross, determined for different scaling values, α. b) A more detailed understanding of the linear regime for the case $\alpha = 1$ is provided by the spectra of the total radiated power and the power radiated by the electric dipole and magnetic dipole of the cross. Resonances A and C are primarily of electric dipole and magnetic dipole type, respectively, whereas additional terms must be considered to accurately describe resonance B. Note also that there is a small contribution to resonance A from a magnetic dipole. c) From left to right, bottom panels show the electric field distribution at the resonances A, B, and C, in the xz-plane passing through the center of the cross.

structural volumes is $V_{Si}/V_{Au} = 108.5$.

An insightful picture of the nature of resonances of nanoparticles is provided by the differential scattering cross-section, as well as the differential cross-sections of the electromagnetic multipoles associated to these resonances. Using a multipolar decomposition of the linear polarization associated to the Au and Si crosses, we have calculated the differential scattering cross-sections corresponding to these resonances. The results of this computational analysis, summarized in Figure 4.6, clearly demonstrate the specific nature of the main resonances of the two crosses: the Au cross has an electric dipole resonance, whereas the Si cross has an electric dipole resonance, a magnetic dipole resonance, and a mixture between an electric dipole resonance and higher-order resonances.

For resonances corresponding to a wavelength closer to the size of the structure, we expect to see higher-order multipoles. This is clearly shown in Figure 4.7. While the individually-considered multipoles suggest the dominance of a dipole in the metallic case, the full interaction shows that higher-orders must indeed be considered, as the shapes do

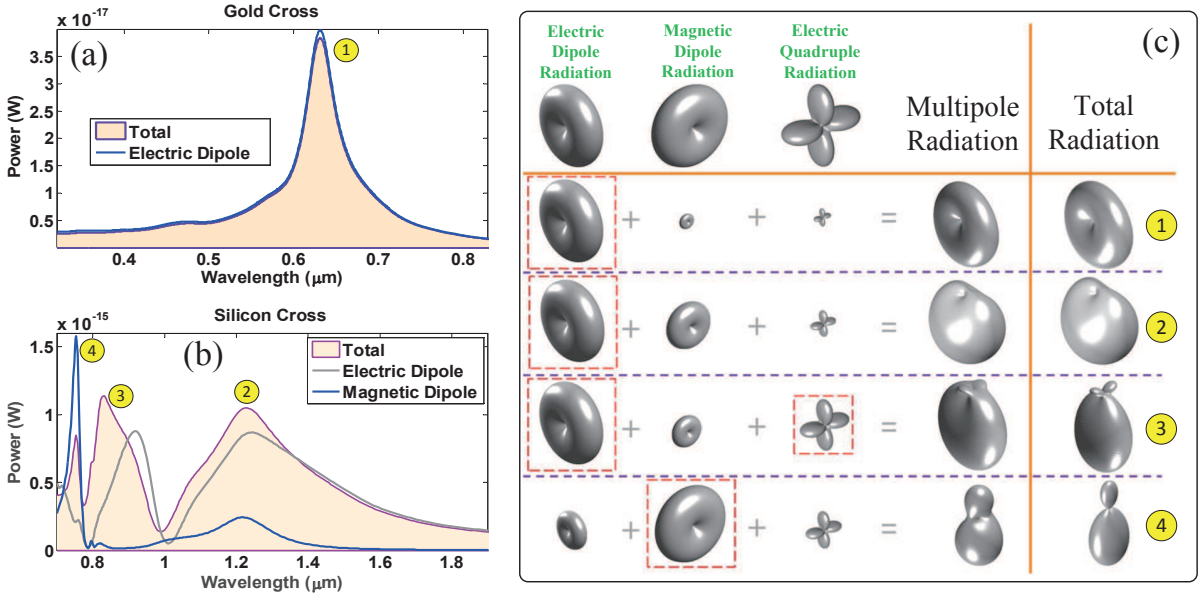

Figure 4.6: Spectra of the radiated power at fundamental frequency and differential scattering cross section. (a) Spectra of the total radiated power and the power radiated by the electric dipole of the Au cross with α=1. (b) Spectra of the total radiated power and the power radiated by the electric dipole and magnetic dipole of the Si cross with α=1. Resonances 2 and 4 are primarily of electric dipole and magnetic dipole type, respectively, whereas additional terms must be considered to accurately describes resonance 3. (c) Differential scattering cross sections corresponding to the main resonance of the Au and Si crosses with α=1, as well as those associated to the electric dipole, magnetic dipole, electric quadrupole, and their sum, calculated at the same resonance wavelengths.

mot match for either Si or Au.

Additional information about the specific nature of various resonances of the nanoparticles investigated in our chapter is provided by the near-field distribution. In order to facilitate a better understanding of the characteristics of the near-field distribution corresponding to the main resonances of the silicon cross, denoted above as resonances A, B and C, we present in Figure 4.8 these distributions computed in the main symmetry planes of the cross. As discussed above, resonances A and C correspond to an electric dipole mode and a superposition of a strong magnetic dipole mode and a weaker, higher-order magnetic mode, respectively, whereas the resonance B is the result of a mixture of multipole resonances. At resonance A, an additional contribution from a magnetic dipole mode can be observed, too. The SHG is primarily determined by the characteristics of the near-field distribution at the fundamental frequency. In particular, it is expected that the larger the enhancement of the near-field is, the stronger the SHG is. In order to illustrate this idea, we plot in Figure 4.9 the spatial distribution of the amplitude of the electric field determined at the resonance wavelength for gold crosses with different size.

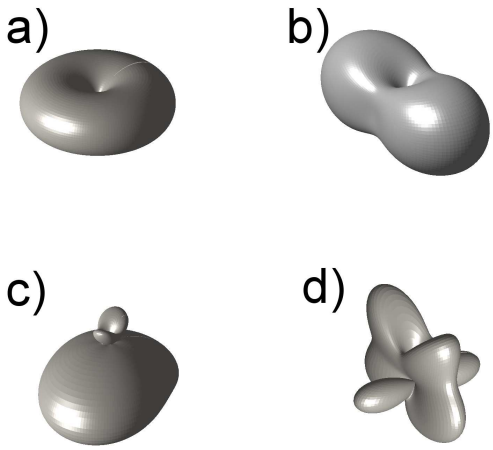

Figure 4.7: Differential scattering cross section at the second harmonic. (a) Differential scattering cross section corresponding to the main nonlinear resonance for a scaling factor of α=1.5 for Au, arrived at by summing the first three multipoles. (b) The same as in (a), but including every multipole and their interferences with one another. The two cases are clearly not in agreement, and hence a rigorous multipole analysis would require more multipoles to be calculated. (c) The differential scattering cross section corresponding to the electric dipole resonance for the case α=1.5. (d) The same as in (c), but including every multipole and their interferences with one another.

As discussed above, it can be seen that as the size of the cross decreases, the maximum enhancement of the near-field increases, which explains why in the case when the surface and bulk nonlinear susceptibilities are frequency-independent the SHG increases, too (see also Figures 4.4 and 4.5). We move now on to the nonlinear optical response of the two types of crosses and start with a brief discussion of the key ideas pertaining to the basic nonlinear physics. The external field of frequency, ω, impinges on the "meta-atom", exciting an electromagnetic field at frequency, $\Omega = 2\omega$. Hence, we expect to see a strong SH signal when optical resonances are excited at the FF. Generally, this nonlinear optical process can occur both at the surface and in the bulk of the scatterer, with different physics governing each component.

In order to calculate the surface and bulk nonlinear polarizations we used Eqs. 2.33 and 2.35 in conjunction with the fields at the FF. These nonlinear polarizations are then employed to calculate the corresponding surface and bulk optical powers and the total power emitted at the SH, as explained in the preceding section. Since these calculations

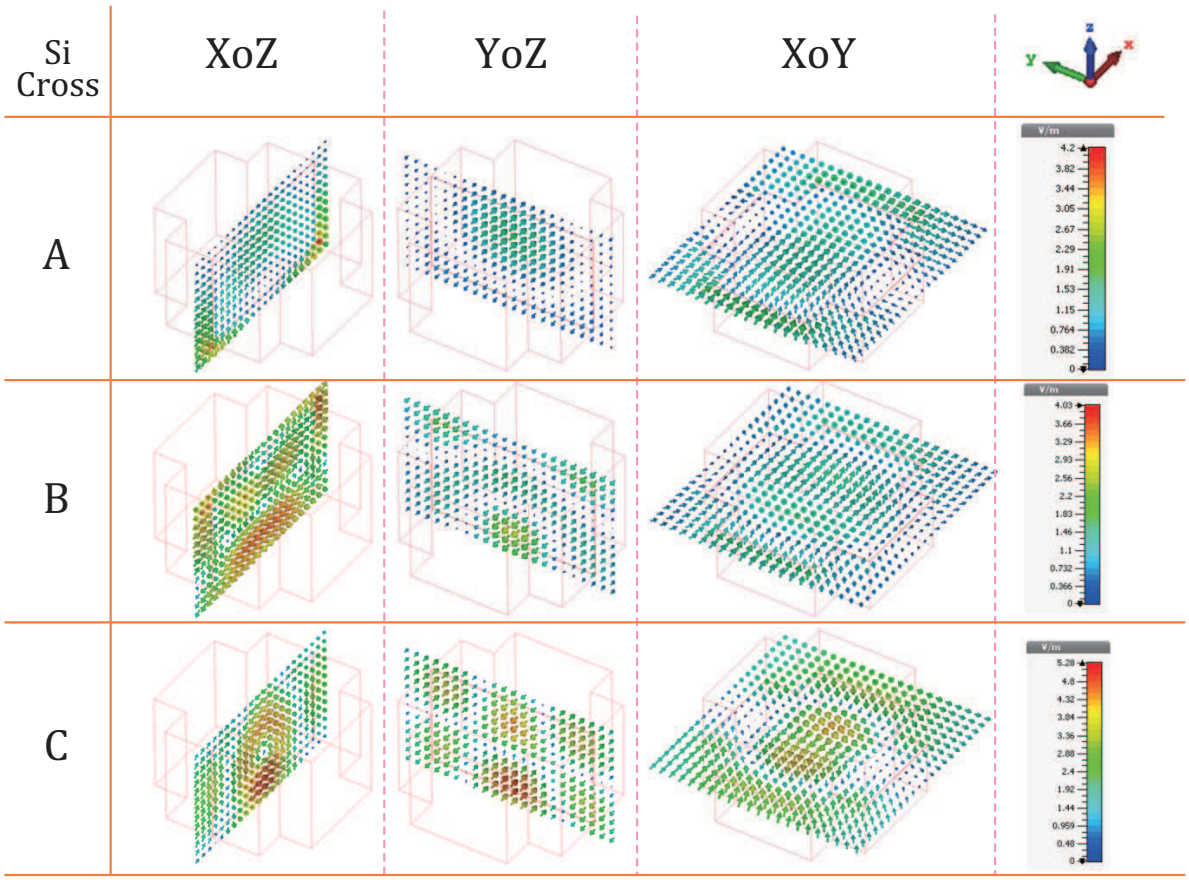

Figure 4.8: Optical near-field. Near-field distributions computed in the main symmetry planes of the silicon cross, corresponding to the main resonances denoted in this Chapter as resonances *A*, *B*, and *C*.

are performed in the frequency domain, this approach can be readily applied both in the case when the nonlinear coefficients are frequency dependent, as well as in the dispersionless case. These calculations were performed both for Au and for Si. The values of the surface and bulk nonlinear susceptibilities of Au and Si used in these calculations are given in the Model and Scattering Configuration section, and correspond to the reference wavelengths $\lambda_r = 810\,\text{nm}$ (Au) and $\lambda_r = 800\,\text{nm}$ (Si). Hence, the dispersionless case is based purely on experimental data, whereas the dispersive regime theoretically extrapolates this data using the Miller rule. The results of this analysis, determined under both the dispersive and non-dispersive regime for the surface component and for all of the Au and Si crosses, are plotted in Fig. 4.10. As is evident from this figure, the resonances observed at the SH are located at wavelengths $\Lambda_{res} = \lambda_{res}/2$, where λ_{res} are the corresponding resonance wavelengths at the FF.

A more careful examination of the power spectra depicted in Fig. 4.10 reveals several differences between the nonlinear optical response of Au and Si crosses. Thus, with

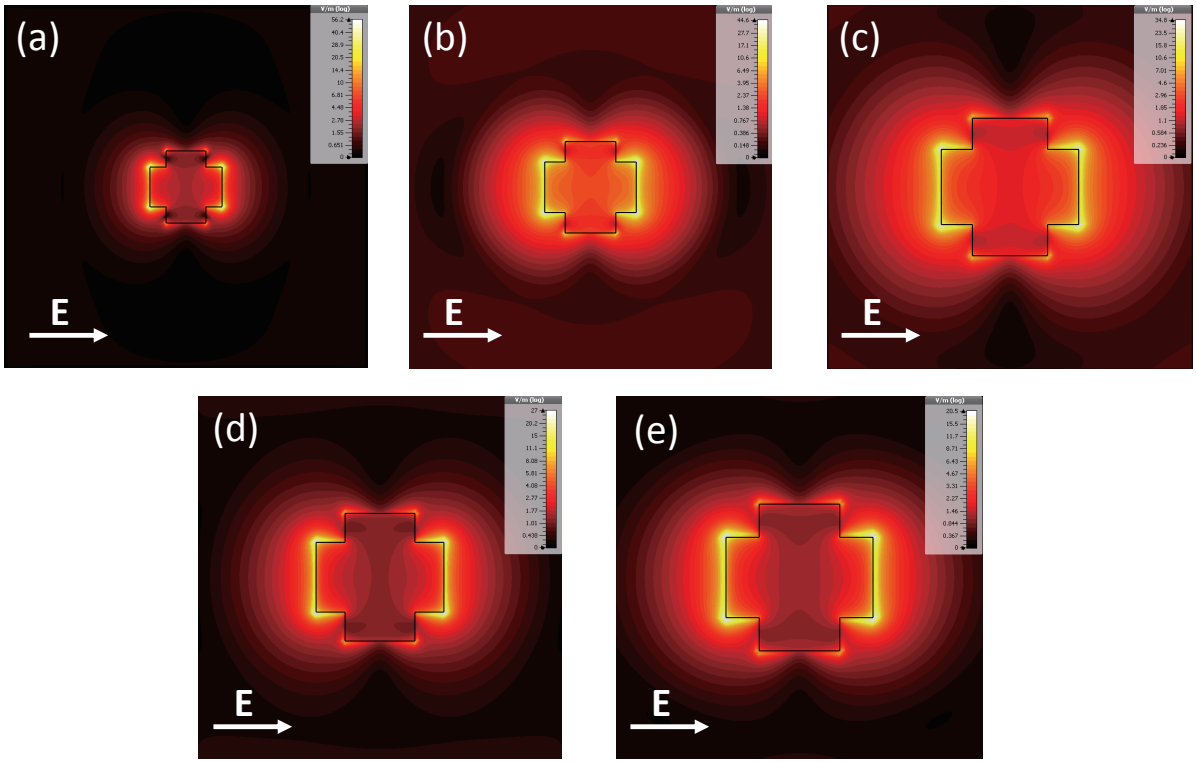

Figure 4.9: Optical near-field enhancement. (a), (b), (c), (d), (e) Spatial distribution of the amplitude of the electric field determined for metallic crosses with scaling parameter α=1,1.35,1.5,1.75,2, respectively. The arrow indicates the polarization of the incident wave and the amplitude of the incident field is 1V/m.

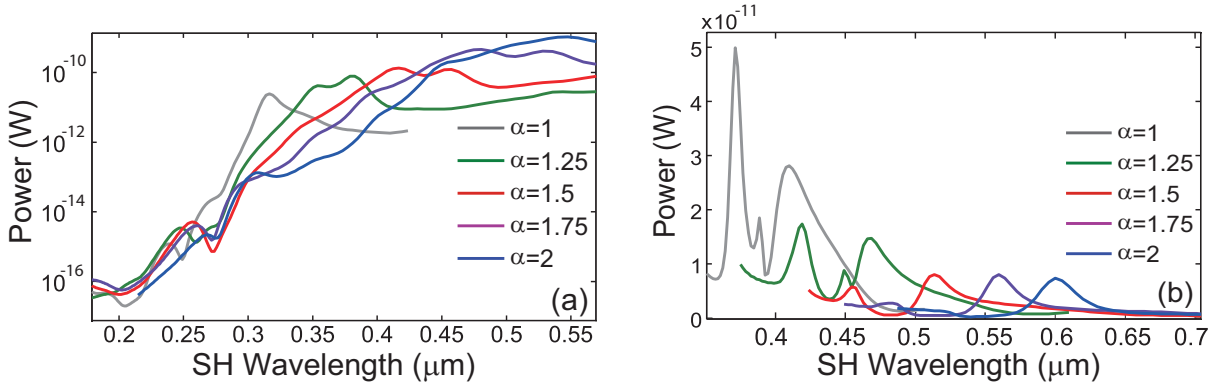

Figure 4.10: a) The spectra of the power radiated at the second-harmonic by the non-linear surface sources within the dispersive framework induced in a cross made of gold, determined for different scaling values, α. b) The same as in a) but calculated for crosses made of silicon. A log scale is chosen for the Au case to help highlight the resonances.

regards to the Au cross, the electric dipole generated at the FF is the main source of power radiated at the SH. Indeed, the wavelength of the maximum SH intensity coincides with half the wavelength of the dipole resonance at the FF (see Fig. 4.4). However, by

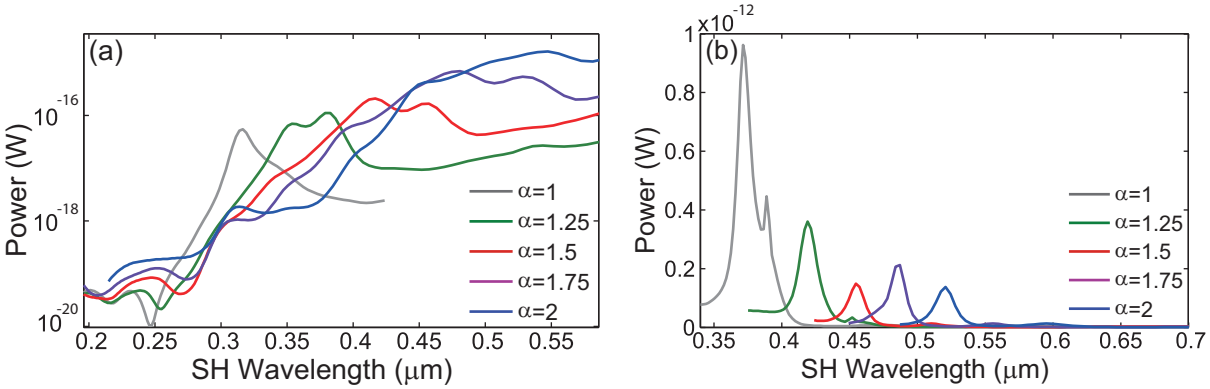

Figure 4.11: a) The spectra of the power radiated at the second-harmonic by the nonlinear bulk sources within the dispersive framework induced in a cross made of gold, determined for different scaling values, α. b) The same as in a) but calculated for crosses made of silicon. A log scale is chosen for the Au case to help highlight the resonances.

contrast, in the case of the Si cross the electric dipole resonance has the weakest signature in the nonlinear spectrum, the main signal at the SH originating from the resonances labeled in Fig. 4.5(b) with B and C (magnetic dipole resonance). This suggests that in the case of the electric dipole resonance of the Si cross, there is only a small overlap between the distribution of nonlinear surface currents and the plane waves of the radiation continuum, and therefore only a small amount of light is radiated.

An equally important but rather unexpected result is that in the case of the silicon cross the strongest nonlinear signal is generated by the smallest cross. This is explained by the fact that as the size of the cross increases the resonance wavelength is red-shifted to a spectral region of much weaker surface nonlinearity. This size dependence of the surface SHG becomes more complex in the case of the gold cross. Thus, Fig. 4.10(a) shows that in the dispersive case the SHG increases as the size of the cross increases, whereas if the dispersion of the surface nonlinearity is neglected the opposite dependence is observed, as plotted in Fig. 4.10(c). There are two concurrent effects that lead to these outcomes. When the size of the cross increases the resonance wavelength increases, too, so that it moves in a spectral region of much larger surface nonlinearity. On the other hand, the size dependence of the surface SHG observed in the dispersionless case is explained by the fact that, as our numerical simulations and previous works corroborate [62], the strongest field enhancement is achieved for the crosses with the smallest size, an effect that outweighs the fact that in this case the SH is generated on a smaller surface. More specifically, the maximum field enhancement computed for gold crosses in the dispersive case with $\alpha = 1$, 1.25, 1.5, 1.75, and 2 is 56.2, 44.6, 34.8, 27, and 20.5, respectively. Removing the dispersive behavior of the nonlinearity within the Si crosses also leads to observable differences. It is clear, as shown in Fig. 4.10(d), that the factor by which the field is

enhanced increases. More importantly, the radiative power becomes more comparable between all of the crosses.

In order to quantify the relative contributions of the surface and bulk nonlinear currents to the total radiated power at the SH, we show in Fig. 4.11 the radiation spectra corresponding to the bulk nonlinear polarization, calculated for the dispersive and non-dispersive cases, for both types of crosses and for all values of the scaling factor. These calculations show that generally the bulk effects are much weaker than the surface ones, by more than four orders of magnitude for gold crosses and by more than two orders of magnitude for crosses made of silicon. In addition, it can be seen that the relative strength of the spectral resonances varies from the surface to bulk spectra, which is particularly evident in the case of Si crosses. In comparison with the surface spectra, the non-dispersive regime leads to stronger field enhancement, especially in the case for larger scale sizes. Removing the dispersion of the nonlinear optical susceptibilities leads to the same phenomena shown in Fig. 4.10, namely, in the dispersionless case, the power radiated by the Au crosses decreases with increasing scale size. Furthermore, the power radiated by all Si crosses does not change much with the size of the cross.

Despite the fact that generally the nonlinear bulk effects are weaker than the surface ones, close to bulk resonances their contribution can become comparable. Here we call bulk (surface) resonances spectral peaks that are observed when only bulk (surface) nonlinear currents are included in the calculations. In order to illustrate this important idea, we plot in Figs. 4.12(a) and 4.12(b) the ratio, $\kappa = P_s/P_b$, between the SH powers generated by the surface and bulk nonlinear currents, P_s and P_b, respectively, determined for the gold and silicon crosses, and for all five scaling factors in the dispersive framework. The results corresponding to the non-dispersive case are depicted in Fig. 4.13. These figures clearly show that in the long-wavelength limit the bulk contribution to the total SHG is negligible. For wavelengths comparable to the size of the crosses, however, the bulk contribution can become commensurate to that of the surface, but only for silicon crosses. Equally important, even though the surface and bulk contributions to SHG are different in the dispersive and dispersionless cases, their ratio is almost the same (compare Fig. 4.12 and Fig. 4.13). This conclusion is explained by the fact that, due to the Miller rule, both contributions scale with frequency in the same way.

The surface and volume of the crosses increase at different rate with the cross size and therefore one expects that the relative contribution of the surface and bulk nonlinear currents varies with the size of the crosses. In order to verify this argument, we evaluated the ratio κ at the wavelength at which the bulk contribution is the largest and repeated these calculations for all values of the scaling factor, both for the gold and silicon crosses. The histograms corresponding to the dispersive gold and silicon crosses, presented in

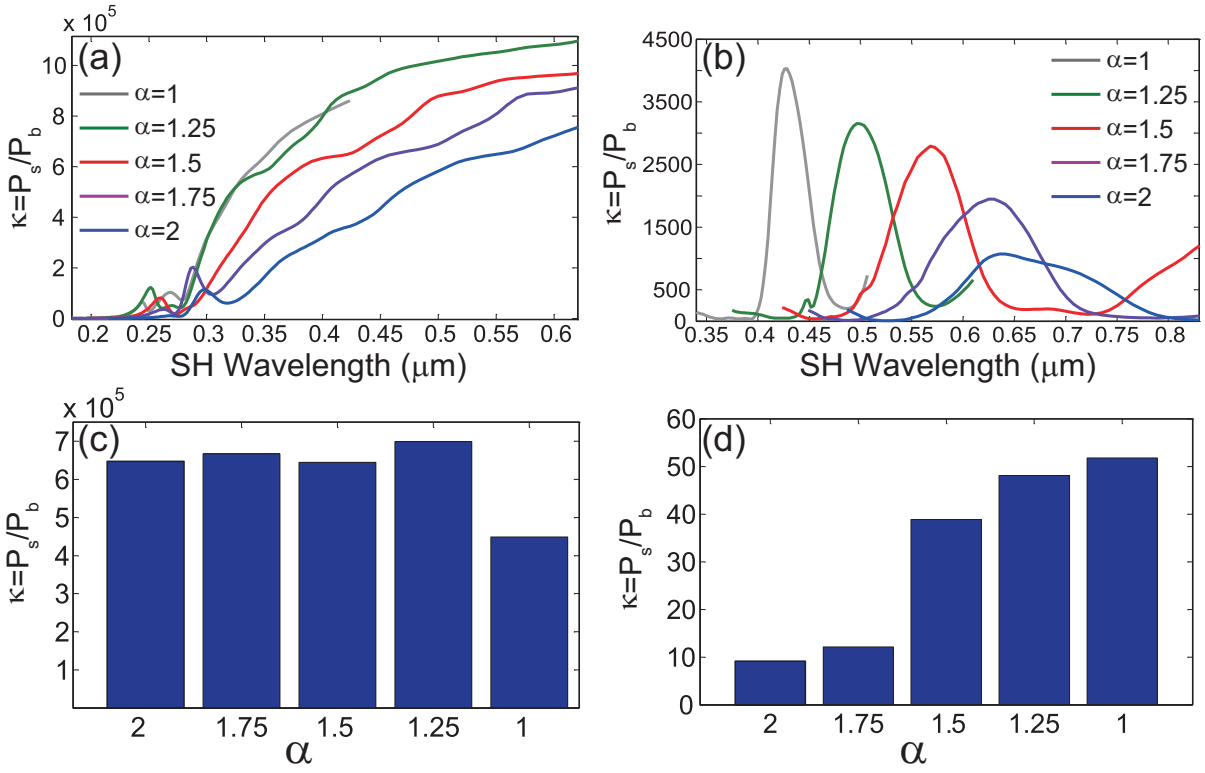

Figure 4.12: a) The dependence of the ratio $\kappa = P_s/P_b$ between the SH powers generated by the surface and bulk nonlinear sources induced in a cross made of gold within a dispersive framework, determined for different scaling values, α. b) The same as in a) but calculated for the crosses made of silicon. c) The value of the ratio κ evaluated at the wavelength at which the bulk contribution is maximum vs. the scaling parameter α, calculated for the crosses made of gold. d) The same as in c) but calculated for the crosses made of silicon.

Figs. 4.12(c) and 4.12(d), respectively, suggest that there are significant qualitative differences between the two cases. Thus, in the case of metallic crosses, κ does not vary much with α. This apparent paradox is explained by the fact that the effective region where nonlinear currents are induced in the bulk only extends about a skin-depth from the surface into the metal. As a result, the surface and bulk effects increase in fact at the same rate with the size of the gold cross, and therefore the ratio κ should only weakly depend on α. In the case of dielectrics, on the other hand, the field at the FF penetrates throughout the (nonlinear) medium and therefore nonlinear currents are induced in the entire bulk region. Consequently, the bulk part increases faster with the cross size as compared to the surface one, in complete agreement with the dependence of κ on α shown in Fig. 4.12(d). All these conclusions remain valid in the non-dispersive case, too, which can be inferred from Figs. 4.13(c) and 4.13(d).

We stress that we did not attempt to optimize our structures so as to maximize the contribution of the bulk effects to the SHG. Nevertheless, our analysis suggests that it

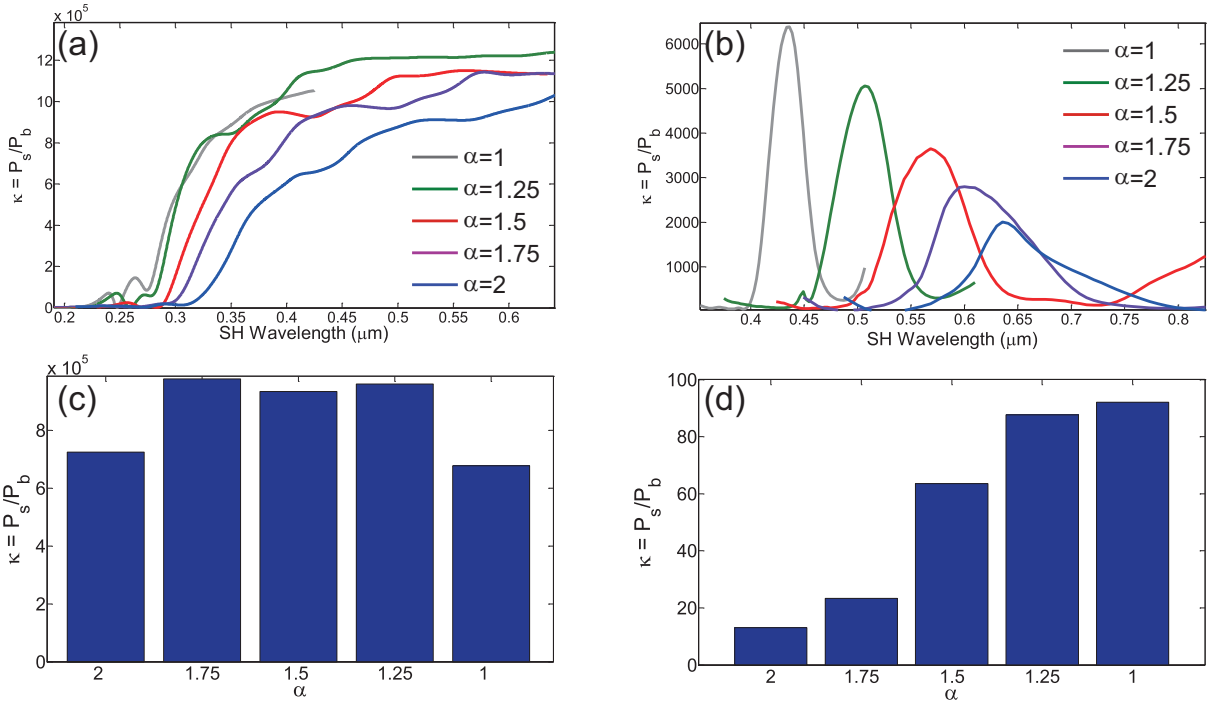

Figure 4.13: a) The dependence of the ratio $\kappa = P_s/P_b$ between the SH powers generated by the surface and bulk nonlinear sources induced in a cross made of gold under the assumption of dispersionless nonlinearity, determined for different scaling values, α. b) The same as in a) but calculated for the crosses made of silicon. c) The value of the ratio κ evaluated at the wavelength at which the bulk contribution is maximum vs. the scaling parameter α, calculated for the crosses made of gold. d) The same as in c) but calculated for the crosses made of silicon.

is conceivable that, at least in the case of all-dielectric nanoparticles, one can design structures for which the bulk effects are comparable or even larger than the surface ones. This means that care must be taken when experimental results pertaining to SHG in all-dielectric nanostructures made of centrosymmetric materials are theoretically interpreted, as our analysis suggests that the validity of the commonly used practice to neglect the bulk contribution to SHG might break down in this instance.

4.6 Dispersionless Nonlinearities

The results presented above correspond to the case in which the frequency dispersion of the surface and bulk nonlinear susceptibilities is taken into account. In order to gain a better understanding of the influence of the dispersion of surface and bulk nonlinear susceptibilities on the conclusions of our study, we have calculated the surface and bulk contributions to the total SHG, as well as the ratio between these two contributions, in the dispersionless case, namely when these nonlinear optical constants are frequency

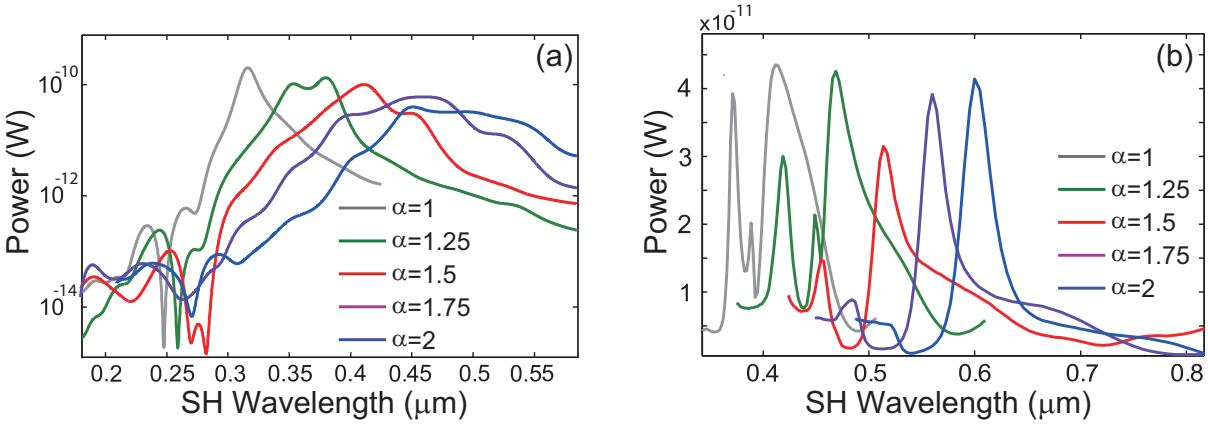

Figure 4.14: Surface SHG radiated power - dispersionless case. (a) The spectra of the power radiated at the second-harmonic by the nonlinear surface sources induced in a cross made of gold, determined for different scaling values, α. (b) The same as in (a) but calculated for crosses made of silicon. A log scale is chosen for the Au case to help highlight the resonances.

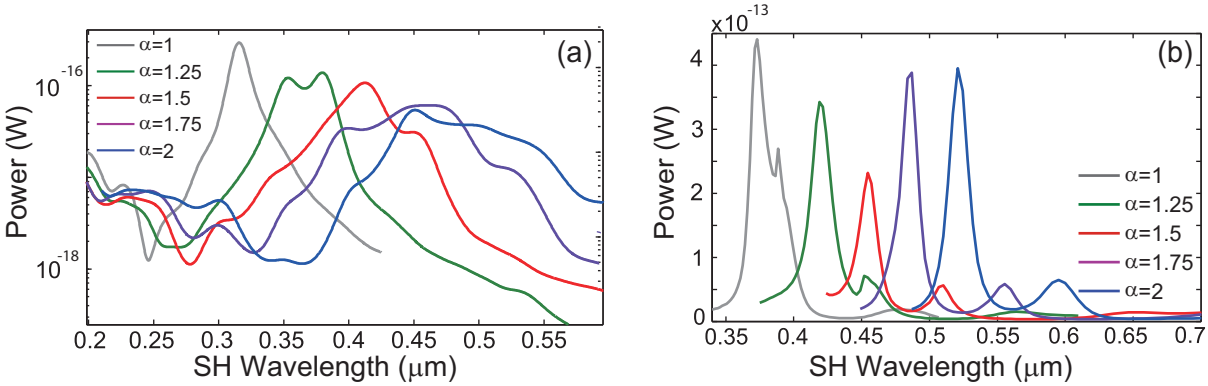

Figure 4.15: Bulk SHG radiated power - dispersionless case. (a) The spectra of the power radiated at the second-harmonic by the nonlinear bulk sources induced in a cross made of gold, determined for different scaling values, α. (b) The same as in (a) but calculated for crosses made of silicon. A log scale is chosen for the Au case to help highlight the resonances.

independent. These calculations were performed both for Au and for Si. The values of the surface and bulk nonlinear susceptibitilies of Au and Si used in these calculations are given in the preceding sections and correspond to the reference wavelengths $\lambda_r = 810$nm (Au) and $\lambda_r = 800$nm (Si).

For an easy comparison, the results are plotted in a manner similar to that of the dispersive case. More specifically, Figure 4.14 is the analogue version of Figure 4.11 (the dispersive case surface results) and contains scattering spectra pertaining to the surface contributions to the SHG; Figure 4.15 is the analogue version of Figure 4.11 (the dispersive case bulk results) and contains scattering spectra pertaining to the bulk contributions to

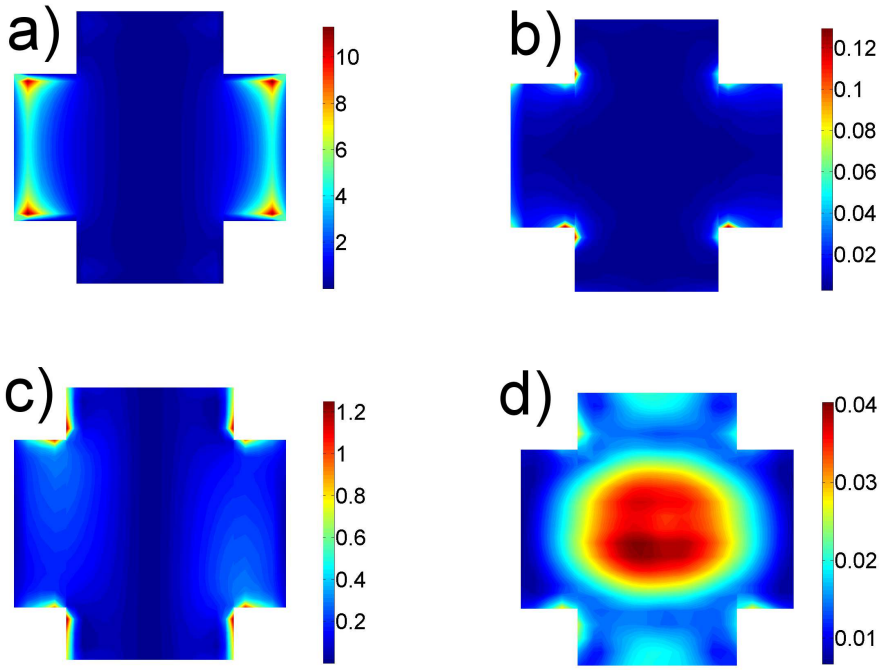

Figure 4.16: Nonlinear surface and bulk currents. (a), (b) The absolute value of the surface and bulk nonlinear current distributions, respectively, for the gold cross of scale factor α=1.5, multiplied by a factor of 10^5. The surface considered is the plane z=30nmm, whereas the bulk layer considered is the central layer, i.e. 15nm. The resonance in consideration is the main resonance present in Figure 4.10, i.e. for an incident wavelength of 0.82μm. (c), (d) The same as (a), (b), but for a cross made of silicon factor α=1.5. We consider here the resonance corresponding to the linear electric dipole, i.e. for an incident wavelength of 1.44μm.

the SHG. Finally, Figure 4.13 is the analogue version of Figure 4.12 (the dispersive case ratio results) and contains information pertaining to the ratio of the surface and bulk contributions. To further cast light on the SHG characteristics, we plot in Figure 4.16 the absolute value of the current density, decomposed into the surface and bulk contributions at a wavelength corresponding to a resonance. As discussed in the dispersive case, the surface contribution outweighs the bulk for both materials at the resonance in question, and this is indeed exemplified here.

4.7 Conclusions

We have studied the second-harmonic generation arising from cruciform structures made of centrosymmetric metallic and dielectric materials, the physical cornerstones of which

were described in Chapter 2. We have focused on the nonlinear optical response of such subwavelength scatterers, aiming to elucidate whether the surface or bulk contribution to the second-harmonic generation is dominant. Our analysis has provided a nuanced answer to this question, corresponding to one of the key achievements of this thesis, namely in the case of metallic structures the nonlinear power generated by surface interactions surpasses *by orders of magnitude* that due to bulk effects, whereas in dielectric structures, in certain circumstances, these two contributions can become comparable. This indeed adds to the discussion of Chapter 2, where it must now be mentioned that bulk and surface sources can become equal in magnitude. We have also discussed practical implications of these findings for subsequent experimental verifications. We will now explore nonlinear signal generation in metamaterials further by generating a nonlinear toroidal dipole in an all-dielectric meta-atom.

Bibliography

[1] A. V. Zayats, I. I. Smolyaninov, and A. A. Maradudin, "Nano-optics of surface plasmon polaritons", Phys. Rep. **408**, 131-314 (2005).

[2] S. A. Maier, *Plasmonics: Fundamentals and Applications* (Springer, New York, 2007).

[3] K. Kneipp, Y. Wang, H. Kneipp, L. T. Perelman, I. Itzkan, R. R. Dasari, and M. S. Feld, "Single molecule detection using surface-enhanced Raman Scattering (SERS)", Phys. Rev. Lett. **78**, 1667-1670 (1997).

[4] B. Knoll and F. Keilmann, "Near-field probing of vibrational absorption for chemical microscopy", Nature (London) **399**, 134-137 (1999).

[5] N. C. Panoiu and R. M. Osgood, "Subwavelength nonlinear plasmonic nanowire", Nano Lett. **4**, 2427–2430 (2004).

[6] G. Veronis and S. Fan, "Bends and splitters in metal-dielectric-metal subwavelength plasmonic waveguides", Appl. Phys. Lett. **87**, 1102–1104 (2005).

[7] R. M. Roth, N. C. Panoiu, M. M. Adams, R. M. Osgood, C. C. Neacsu, and M. B. Raschke, "Resonant-plasmon field enhancement from asymmetrically illuminated conical metallic-probe tips", Opt. Exp. **14**, 2921-2931 (2006).

[8] T. H. Taminiau, R. J. Moerland, F. B. Segerink, L. Kuipers, and N. F. van Hulst, "$\lambda/4$ resonance of an optical monopole antenna probed by single molecule fluorescence", Nano Lett. **7**, 28–33 (2007).

[9] F. Ye, D. Mihalache, B. Hu, and N. C. Panoiu, "Subwavelength plasmonic lattice solitons in arrays of metallic nanowires", Phys. Rev. Lett. **104**, 6802–6805 (2010).

[10] J. B. Khurgin, "How to deal with the loss in plasmonics and metamaterials", Nature Nanotechnol. **10**, 2–6 (2015).

[11] A. J. Hoffman, L. Alekseyev, S. S. Howard, K. J. Franz, D. Wasserman, V. A. Podolskiy, E. E. Narimanov, D. L. Sivco, and C. Gmachl, "Negative refraction in semiconductor metamaterials", Nat. Mater. **6**, 946-950 (2007).

[12] S. Xiao, V. P. Drachev, A. V. Kildishev, X. Ni, U. K. Chettiar, H. K. Yuan, and V. M. Shalaev, "Loss-free and active optical negative-index metamaterials", Nature (London) **466**, 735-738 (2010).

[13] A. Garcia-Etxarri, R. Gomez-Medina, L. S. Froufe-Perez, C. Lopez, L. Chantada, F. Scheffold, J. Aizpurua, M. Nieto-Vesperinas, and J. J. Saenz, "Strong magnetic response of submicron Silicon particles in the infrared", Opt. Exp. **19**, 4815-4826 (2011).

[14] A. I. Kuznetsov, A. E. Miroshnichenko, Y. H. Fu, J. Zhang, and B. Luk'yanchuk, "Magnetic light", Sci. Rep. **2**, 492 (2012).

[15] C. F. Bohren and D. R. Huffman, *Absorption and Scattering of Light by Small Particles* (Wiley-Interscience, New York, 1983).

[16] S. Liu, M. B. Sinclair, T. S. Mahony, Y. C. Jun, S. Campione, J. Ginn, D. A. Bender, J. R. Wendt, J. F. Ihlefeld, P. G. Clem, J. B. Wright, and I. Brener, "Optical magnetic mirrors without metals", Optica **1**, 250-256 (2014).

[17] C. Pfeiffer and A. Grbic, "Metamaterial Huygens' surfaces: Tailoring wave fronts with reflectionless sheets", Phys. Rev. Lett. **110**, 197401 (2013).

[18] M. Decker, I. Staude, M. Falkner, J. Dominguez, D. N. Neshev, I. Brener, T. Pertsch, and Y. S. Kivshar, "High-efficiency dielectric Huygens' surfaces", Adv. Opt. Mater. **3**, 813-820 (2015).

[19] A. A. Basharin, M. Kafesaki, E. N. Economou, C. M. Soukoulis, V. A. Fedotov, V. Savinov, and N. I. Zheludev, "Dielectric metamaterials with toroidal dipolar response", Phys. Rev. X **5**, 011036 (2015).

[20] A. E. Miroshnichenko, A. B. Evlyukhin, Y. F. Yu, R. M. Bakker, A. Chipouline, A. I. Kuznetsov, B. Luk'yanchuk, B. N. Chichkov, and Y. S. Kivshar, "Nonradiating anapole modes in dielectric nanoparticles", Nat. Commun. **6**, 8069-8076 (2015).

[21] Y. S. Kivshar and A. E. Miroshnichenko, "Meta-optics with Mie resonances", Opt. Photon. News **28**, 26–33 (2017).

[22] M. Kauranen and A. V. Zayats, "Nonlinear plasmonics", Nature Photon. **6**, 737–748 (2012).

[23] J. Butet, P. F. Brevet, and O. J. F. Martin, "Optical second harmonic generation in plasmonic nanostructures: From fundamental principles to advanced applications", ACS Nano **9**, 10545–10562 (2015).

[24] S. M. Nie and S. R. Emory, "Probing single molecules and single nanoparticles by surface-enhanced Raman scattering", Science **275**, 1102–1106 (1997).

[25] N. Bloembergen, R. K. Chang, S. S. Jha, and C. H. Lee, "Optical second-harmonic generation in reflection from media with inversion symmetry", Phys. Rev. **178**, 1528–1528 (1969).

[26] S. I. Bozhevolnyi, J. Beermann, and V. Coello, "Direct observation of localized second-harmonic enhancement in random metal nanostructures", Phys. Rev. Lett. **90**, 197403 (2003).

[27] J. A. H. van Nieuwstadt, M. Sandtke, R. H. Harmsen, F. B. Segerink, J. C. Prangsma, S. Enoch, and L. Kuipers, "Strong modification of the nonlinear optical response of metallic subwavelength hole arrays", Phys. Rev. Lett. **97**, 146102 (2006).

[28] W. Fan, S. Zhang, N. C. Panoiu, A. Abdenour, S. Krishna, R. M. Osgood, K. J. Malloy, and S. R. J. Brueck, "Second harmonic generation from a nanopatterned isotropic nonlinear material", Nano Lett. **6**, 1027-1030 (2006).

[29] L. Cao, N. C. Panoiu, and R. M. Osgood, "Surface second-harmonic generation from surface plasmon waves scattered by metallic nanostructures", Phys. Rev. B **75**, 205401 (2007).

[30] G. Bachelier, I. Russier-Antoine, E. Benichou, C. Jonin, and P. F. Brevet, "Multipolar second-harmonic generation in noble metal nanoparticles", J. Opt. Soc. Am. B **25**, 955–960 (2008).

[31] V. K. Valev, A. V. Silhanek, N. Verellen, W. Gillijns, P. V. Dorpe, O. A. Aktsipetrov, G. A. E. Vandenbosch, V. V. Moshchalkov, and T. Verbiest, "Asymmetric optical second-harmonic generation from chiral G-shaped gold nanostructures", Phys. Rev. Lett. **104**, 7401-7404 (2010).

[32] C. G. Biris and N. C. Panoiu, "Second harmonic generation in metamaterials based on homogeneous centrosymmetric nanowires", Phys. Rev. B **81**, 195102 (2010).

[33] L. H. Haber, S. J. J. Kwok, M. Semeraro, and K. B. Eisenthal, "Probing the colloidal gold nanoparticle/aqueous interface with second harmonic generation", Chem. Phys. Lett. **507**, 11–14 (2011).

[34] A. Capretti, E. F. Pecora, C. Forestiere, L. D. Negro, and G. Miano, "Size-dependent second-harmonic generation from gold nanoparticles", Phys. Rev. B **89**, 125414 (2014).

[35] R. Czaplicki, J. Makitalo, R. Siikanen, H. Husu, J. Lehtolahti, M. Kuittinen, and M. Kauranen, "Second-harmonic generation from metal nanoparticles: resonance enhancement versus particle geometry", Nano Lett. **15**, 530-534 (2015).

[36] G. Sartorello, N. Olivier, J. Zhang, W. Yue, D. J. Gosztola, G. P. Wiederrecht, G. Wurtz, and A. V. Zayats, "Ultrafast optical modulation of second- and third-harmonic generation from cut-disk-based metasurfaces" ACS Photon. **3**, 1517-1522 (2016).

[37] I. I. Smolyaninov, A. V. Zayats, A. Gungor, and C. C. Davis, "Single-photon tunneling via localized surface plasmons", Phys. Rev. Lett. **88**, 187402 (2002).

[38] X. W. Wang, G. C. Schatz, and S. K. Gray, "Ultrafast pulse excitation of a metallic nanosystem containing a Kerr nonlinear material", Phys. Rev. B **74**, 195439 (2006).

[39] F. Wang, F. J. Rodriguez, W. M. Albers, R. Ahorinta, J. E. Sipe, and M. Kauranen, "Surface and bulk contributions to the second-order nonlinear optical response of a gold film", Phys. Rev. B **80**, 233402 (2009).

[40] A. Capretti, C. Forestiere, L. D. Negro, and G. Miano, "Full-wave analytical solution of secondharmonic generation in metal nanospheres", Plasmonics **9**, 151–166 (2014).

[41] C. Ciraci, E. Poutrina, M. Scalora, and D. R. Smith, "Origin of second-harmonic generation enhancement in optical split-ring resonators", Phys. Rev. B **85**, 201403 (2012).

[42] B. Luk'yanchuk, N. I. Zheludev, S. A. Maier, N. J. Halas, P. Nordlander, H. Giessen, and C. T. Chong, "The Fano resonance in plasmonic nanostructures and metamaterials", Nature Mater. **9**, 707–714 (2010).

[43] S. Zhang, G.-C. Li, Y. Chen, X. Zhu, S.-D. Liu, D. Y. Lei, and H. Duan, "Pronounced Fano resonance in single gold split nanodisks with 15 nm split gaps for intensive second harmonic generation", ACS Nano **10**, 11105–11114 (2016).

[44] S.-D. Liu, E. S. P. Leong, G.-C. Li, Y. Hou, J. Deng, J. H. Teng, H. C. Ong, and D. Y. Lei, "Polarization-independent multiple Fano resonances in plasmonic nonamers for multimode-matching enhanced multiband second-harmonic generation", ACS Nano **10**, 1442–1453 (2016).

[45] M. F. Limonov, M. V. Rybin, A. N. Poddubny, and Y. S. Kivshar, "Fano resonances in photonics", Nature Photon. **11**, 543–554 (2017).

[46] CST Computer Simulation Technology GmbH. [Accessed 16th September 2018], Available from: https://www.cst.com

[47] W. S. M. Werner, K. Glantschnig, and C. Ambrosch-Draxl, "Optical constants and inelastic electronscattering data for 17 elemental metals", J. Phys. Chem. Ref. Data **38**, 10131092 (2009).

[48] R. L. Olmon, B. Slovick, T. W. Johnson, D. Shelton, S.-H. Oh, G. D. Boreman and M. B. Raschke, "Optical dielectric function of gold", Phys. Rev. B **86**, 235147 (2012).

[49] C. D. Salzberg and J. J. Villa, "Infrared refractive indexes of silicon germanium and modified selenium glass", J. Opt. Soc. Am. **47**, 244246 (1957).

[50] D. F. Edwards and E. Ochoa, "Infrared refractive index of silicon", Appl. Opt. **19**, 41304131 (1980).

[51] M. A. Green and M. J. Keevers, "Optical properties of intrinsic silicon at 300 K", Progr. Photovolt. **3**, 189192 (1995).

[52] A. I. Kuznetsov, A.E. Miroshnichenko, M. L. Brongersma, Y. S. Kivshar, and B. Luk'yanchuk, "Optically resonant dielectric nanostructures", Science **354**, aag2472 (2016).

[53] T. F. Heinz, *Nonlinear Surface Electromagnetic Phenomena* chap. 5, Second-Order Nonlinear Optical Effects at Surfaces and Interfaces, p. 353. (Elsevier, Amsterdam, 1991).

[54] M. Corvi and W. Schaich, "Hydrodynamic-model calculation of second-harmonic generation at a metal surface", Phys. Rev. B **33**, 3688–3695 (1986).

[55] P. Guyot-Sionnest, W. Chen, and Y. R. Shen, "General considerations on optical second-harmonic generation from surfaces and interfaces", *Phys. Rev. B* **33**, 8254–8263 (1986).

[56] D. Krause, C. W. Teplin, and C. T. Rogers, "Optical surface second harmonic measurements of isotropic thin-film metals: Gold, silver, copper, aluminum, and tantalum", J. Appl. Phys. **96**, 3626–3634 (2004).

[57] M. Falasconia, L. C. Andreania, A. M. Malvezzib, M. Patrinia, V. Mullonic, L. Pavesic, "Bulk and surface contributions to second-order susceptibility in crystalline and porous silicon by second-harmonic generation", Surf. Sci. **481**, 105–112 (2001).

[58] J. E. Sipe, V. C. Y. So, M. Fukui, and G. I. Stegeman, "Analysis of second-harmonic generation at metal surfaces", Phys. Rev. B **21**, 4389–4402 (1980).

[59] A. Taflove and S. C. Hagness, *Computational Electrodynamics: The Finite Difference Time Domain Method, 3rd ed.*, chap. 8 (Artech House, New York, 2005).

[60] R. W. Boyd, *Nonlinear Optics* (Academic Press, 2008).

[61] S. Kruk, M. Weismann, A. Yu. Bykov, E. A. Mamonov, I. A. Kolmychek, T. Murzina, N. C. Panoiu, D. N. Neshev, and Y. S. Kivshar, "Enhanced magnetic second-harmonic generation from resonant metasurfaces", ACS Photon. **2**, 1007–1012 (2015).

[62] P. I. Geshev, S. Klein, T. Witting, K. Dickmann, and M. Hietschold, "Calculation of the electric-field enhancement at nanoparticles of arbitrary shape in close proximity to a metallic surface", Phys. Rev. B **70**, 075402 (2004).

Chapter 5

Nonlinear Toroidal Dipoles generated from Linear Toroidal Dipoles

5.1 Introduction

In this chapter an all-dielectric meta-atom is shown to exhibit a strong linear toroidal dipole. After the configuration and set-up of the system is explained, the physics regarding the linear regime is detailed. The discussion then moves on to the nonlinear regime, whereby the physics of non-centrosymmetric second harmonic generation is analysed. The nonlinear results stemming from the linear regime show that this meta-atom also exhibits a nonlinear toroidal dipole.

5.2 Background

First predicted by Zel'dovich in 1957 [1], the toroidal dipole was subsequently added to the class of fundamental electromagnetic excitations. The history of this mode has hitherto been intertwined with curious physical phenomena, with the toroidal dipole playing a key role in parity nonconservation in atomic spectra [2–4], violations of Newton's Third Law [5] and the non-reciprocal refraction of light [6]. As the far-field radiated by this moment is indistinguishable from the electric dipole far-field [7], it is possible to construct a system whereby the electric and toroidal fields destructively interfere with one another, leading to a non-radiating system known as an anapole moment [8], the discovery of which has been put forth as an explanation for dark matter [9]. While the behaviour of the toroidal dipole is clearly rich with curious activity, this moment is often overlooked

in full electromagnetic expansions [10–12] due its comparative weakness with its siblings, an approach that has shown to be often dubious to the neglection of some pertinent physics [10].

Metamaterials have been shown to be excellent candidates for the generation of strong dynamic toroidal dipoles [13–17]. By tailoring these sub-wavelength structures to either suppress the remaining multipoles or enhance the toroidal dipole, in the past decade we have seen scenarios where the toroidal moment can be made to be the strongest electromagnetic excitation supported by these structures at both microwave [14, 15, 18] and optical [19, 20] frequencies. While this field is still in its infancy, the high quality factors associated with these resonances suggest that toroidal dipoles would be beneficial in applications with narrowband filters [21], radiationless objects [22, 23] and laser gain media [24]. The application of interest in this thesis, however, is the toroidal dipole's effect on the nonlinear physics, specifically the signal arising from the light-matter interaction second harmonic generation (SHG). While SHG is perhaps the most widely studied nonlinear optical phenomenon, to our knowledge the influence of the toroidal dipole on this nonlinearity has until now not been investigated.

Most of the metamaterial structures utilized to create toroidal dipoles have relied on metals, shaping the plasmonic currents to achieve the desired resonances. Recently however, an all-dielectric meta-atom has been shown to host a prevalent toroidal excitation [25] through displacement current resonances, known as Mie resonances [26]. As these excitations have higher quality factors than their metallic counterparts through bypassing the inherent plasmonic loss, all-dielectric structures have shown promising results for biosensing and energy applications [27].

All-dielectric structures have since been theoretically [8] and experimentally [28] shown to host strong toroidal dipoles. To this end, we utilise a modified version of the $LiTaO_3$ structure found in [25], designed in this chapter so as to be a manufacturable, experimentally-verifiable unit. We find the unusual result that the nonlinear signal produced by the linear toroidal dipole is also toroidal in nature.

5.3 Configuration

The meta-atom of interest is shown in Fig. 5.1, with the dimensions given in the caption. These $LiTaO_3$ parallelepipeds are embedded in a finite glass block with permittivity function $\epsilon = 1.96$, with the entire structure being surrounded by a vacuum. The incident light is a plane wave incident in the y-direction, with the $\mathbf{E}$ and $\mathbf{H}$ fields polarized along the z- and x-directions respectively. It must be noted that we consider in this chapter only the one structure as shown in Fig. 5.1, i.e. the meta-atom. Naturally, however,

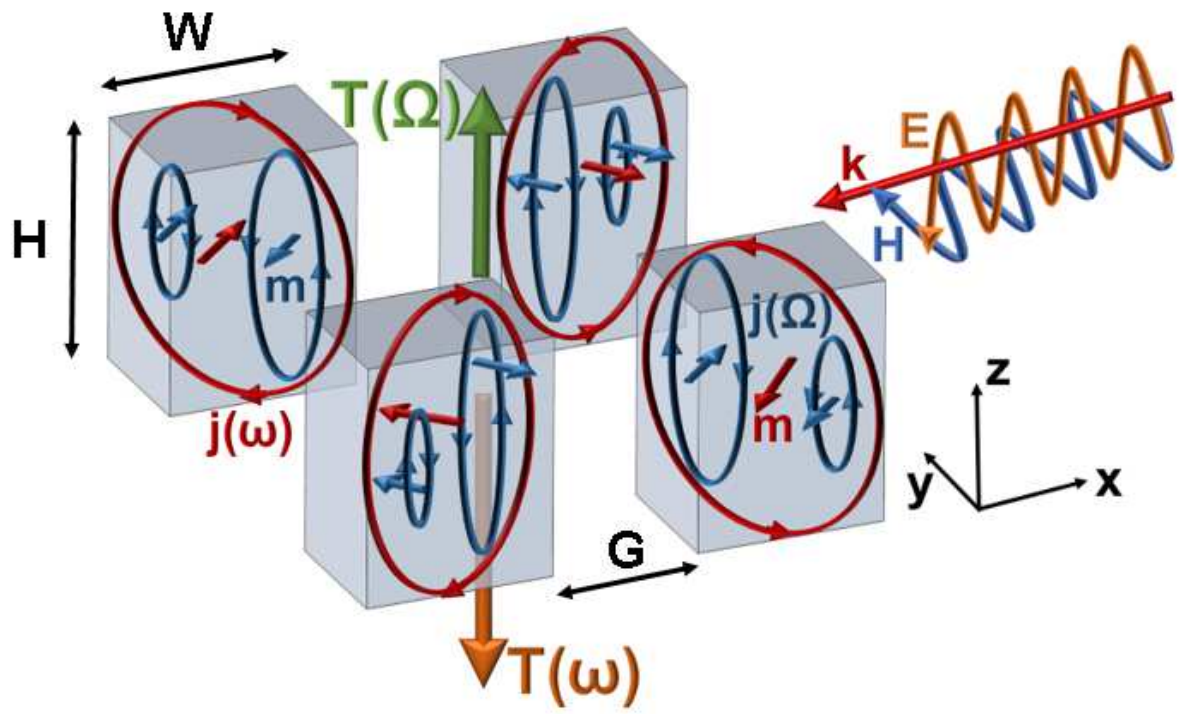

Figure 5.1: Schematics of the analyzed structure. Four cuboids made of non-centrosymmetric $LiTaO_3$ are embedded in a glass background with height H and width of 600μm. The structure has dimensions of $H = 270\mu$m, $W = 16\mu$m, and $G = 4\mu$m. The meta-atom is illuminated with a plane wave traveling in the y-direction, with the electric and magnetic fields being oriented along the z- and x-directions respectively.

the results can be extended to a fully periodic metamaterial array provided that the periodicity is sufficiently large that there is no crosstalk between the unit cells. The inclusion of the surrounding glass is made with experimental conditions in mind; due to the size of the structural parameters combined with the direction of the **k**-vector, this structure is experimentally verifiable.

The linear electromagnetic response of the cuboids was calculated using the time-domain solver of CST Studio Suite [29]. We implement open boundary conditions to ensure the subsequent results stem from one meta-atom. In our calculations, a frequency scan from 1.5THz to 1.8THz in 0.0005THz increments was performed for a sufficiently fine computational mesh.

$LiTaO_3$ was selected as the material for the parallelepipeds due to its ability to host a multipole excitation several wavelengths greater than its structural size. This phenomenon arises from the consideration that $\lambda_r \sim na$ where λ_r is the resonant wavelength, n is the effective refractive index of the implemented medium and a is the typical feature size of the structure. Due to its polaritonic properties, $LiTaO_3$ has a large refractive

index when interacting with THz-frequency light:

$$\epsilon = \epsilon_\infty \frac{\omega^2 - \omega_L^2 + i\omega\gamma}{\omega^2 - \omega_T^2 + i\omega\gamma} \tag{5.1}$$

where $\epsilon_\infty = 13.4$, the longitudinal and transverse optical phonon frequencies are $\omega_L/2\pi = 46.9$THz and $\omega_T/2\pi = 26.7$THz respectively, and the damping factor due to dipole relaxation is $\gamma/2\pi = 0.94$THz. Hence, the permittivity function for our calculations reached a maximum of ϵ_{max}=41.434. While the above permittivity function is indeed highly dispersive for frequencies close to the optical phonon frequencies, across our implemented frequencies, the variation of the $LiTaO_3$ permittivity is 0.118%.

To ensure the toroidal dipole as the majority power-emitter in the linear regime, the other relevant electromagnetic multipoles must be closely regarded. We therefore also calculated the electric dipole, magnetic dipole and electric quadrupole, the full set of which are given in Chapter 2:

In order to describe the nonlinear optical signal generated by the scatterer, we employ a widely used model of SHG in non-centrosymmetric media [30]. Specifically, SHG has just a bulk component determined by the nonlinear susceptibility. The surface elements of the cuboids hence play no role in the second harmonic (SH). This bulk component is given by:

$$\mathbf{P}_\Omega^b(\mathbf{r}) = \epsilon_0 \hat{\chi}_b^{(2)} : \mathbf{E}_\omega(\mathbf{r})\mathbf{E}_\omega(\mathbf{r}), \tag{5.2}$$

where $\Omega = 2\omega$ is the SH frequency and $\chi_b^{(2)}$ is the bulk second-order susceptibility tensor.

Due to the symmetry properties of the $LiTaO_3$ crystal, the non-zero susceptibility tensor values, measured with a laser of wavelength $\lambda = 1.058\mu m$ [31], are: $\chi_{b,xxy}^{(2)} = \chi_{b,xyx}^{(2)} = \chi_{b,yxx}^{(2)} = -\chi_{b,yyy}^{(2)} = 3.4 \times 10^{-12}\ m^2V^{-1}$; $\chi_{b,xxz}^{(2)} = \chi_{b,xzx}^{(2)} = \chi_{b,yyz}^{(2)} = \chi_{b,yzy}^{(2)} = \chi_{b,zxx}^{(2)} = \chi_{b,zyy}^{(2)} = 2.14 \times 10^{-12}\ m^2V^{-1}$; $\chi_{b,zzz}^{(2)} = 32.8 \times 10^{-12}\ m^2V^{-1}$ [32]. The meta-atom was aligned such that the above crystal symmetry matches the computational setup.

The nonlinear polarization above can be used to calculate the nonlinear multipoles, which can be viewed as multipolar sources for the nonlinear field. These same polarizations define nonlinear currents, *via* $\mathbf{J}_\Omega^{s,b}(\mathbf{r}) = -i\Omega\mathbf{P}_\Omega^{s,b}(\mathbf{r})$ (an $e^{-i\omega t}$ dependence of all harmonic fields is assumed throughout this study). These nonlinear currents can subsequently be used to calculate the nonlinear optical far-field by employing a near-field/far-field transformation [33], thus enabling a complete characterization of the nonlinear scattering process.

The necessity of having multiple cuboids within one meta-atom is due to the more complex nature of the toroidal dipole. As this moment is formed *via* a closed loop of magnetic moments (equivalently one can say poloidally-traveling currents), this loop is easier to achieve with more metamaterial elements. The impinging light hence excites a

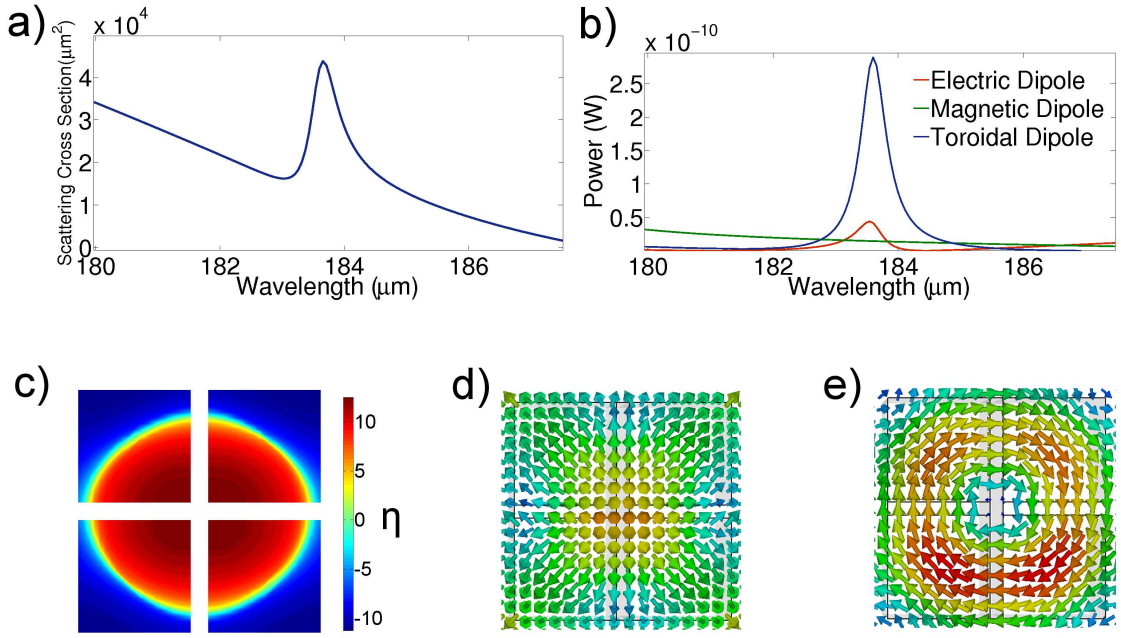

Figure 5.2: a) The scattering cross section of the meta-atom calculated with CST Studio Suite. The prominent resonance for an incident wavelength of 183.6μm is the resonance of interest for this chapter. b) The relevant multipoles calculated through utilization of the linear fields. The main resonance, corresponding to the resonance present in a), shows that this resonance is indeed toroidal in nature. c) The value $\eta = sign(J_z) \times |J_z|^{\frac{1}{4}}$ is plotted to highlight the current distribution at the surface of the cuboids in the xy-plane, making it easier to visualise the generated toroidal dipole. d) The electric field distribution at the surface. e) The same as in d) but for the magnetic field.

magnetic dipole in each cuboid, the close proximity of which means that the near-fields interact, leading to four oscillating magnetic dipoles oriented such that the displacement currents flow along the innermost vertex.

5.4 Results and Discussion

The nonlinear polarizations and subsequent SH are primarily determined through the linear response of the structure. We therefore begin by analysing the salient linear optical field before moving on to the nonlinear results. Finding the resonance that corresponds to the toroidal dipole is not a trivial process; as the wavelength decreases, larger-order multipoles are generated. This means that a strong toroidal dipole can be generated at several distinct wavelengths, but becomes mixed with the stronger quadrupoles and octupoles, etc. The resonance that we desire, therefore, is the resonance where the toroidal dipole is the highest-order multipole excited at that wavelength.

The structural parameters naturally play a vital role in the generation of the required

toroidal dipole. As we wish to study the SH signal arising from this excitation, it was required that the other multipoles were suppressed as maximally as possible at the resonant wavelength. It was therefore not the toroidal resonance that generated the most emitted power that was desired, but rather the resonance that was "most toroidal". The structural parameters in Fig. 5.1 were hence chosen to bring about this effect.

The full linear response of the meta-atom generated *via* CST Studio Suite is plotted in Fig. 5.2. A clear isolated resonance is depicted. Resonances created at larger wavelengths are naturally present but these correspond to lower-order multipoles, i.e. the electric and magnetic dipole. As well as plotting the full radiated cross section, we plot the relevant electromagnetic multipoles. A small magnetic moment accompanied with a large toroidal moment is indicative of having a symmetric loop of magnetic moments; these moments generate the toroidal dipole, but cancel with one another in a full summation on account of being vectors. To further illustrate the physics of the resonance, the quantity $\eta = sign(J_z) \times |J_z|^{\frac{1}{4}}$ is calculated. It must be noted that while this is not a physical quantity, it is useful to visualise the toroidal moment generated at the resonance wavelength, as it gives both the direction and magnitude of the current density, but scaled in a way that makes the results more accessible visually. The electric and magnetic fields are also plotted in the xy-plane. For our multipole equations the glass was neglected due to the negligible field enhancement within this dielectric. The main role played by the glass is a structural support for the cuboids in experimental circumstances; replacing the glass with a vacuum would simply shift the obtained spectra in wavelength-space.

We now move on to the nonlinear electromagnetic response of the meta-atom and begin with a brief description of the underlying physics. The external incident light of frequency ω interacts with the meta-atom, producing its own electromagnetic field at frequency $\Omega = 2\omega$. We hence expect to see a strong SH signal at a wavelength of 91.8μm, i.e. at a wavelength half that of the linear resonance. To model the nonlinear framework described previously, it was firstly necessary to discard the physics occurring at the surface of each cuboid due to its negligibility in non-centrosymmetric SHG. The nonlinear polarizations were subsequently calculated using the linear fields generated from our computational setup. From the discussion of the linear scattering process thus far it is clear that the nonlinear multipoles can be calculated through feeding the multipole equations with these nonlinear polarizations. We therefore implement this method, taking care to remove any mesh points that correspond to a surface element of our structure. Due to the values of the crystal nonlinear susceptibility tensor, it is clear that the z-component of the current density distribution will be the strongest.

The total nonlinear power is plotted alongside the most relevant multipoles in Fig. 5.3. This total is not merely a summation of the individual components, but rather also cal-

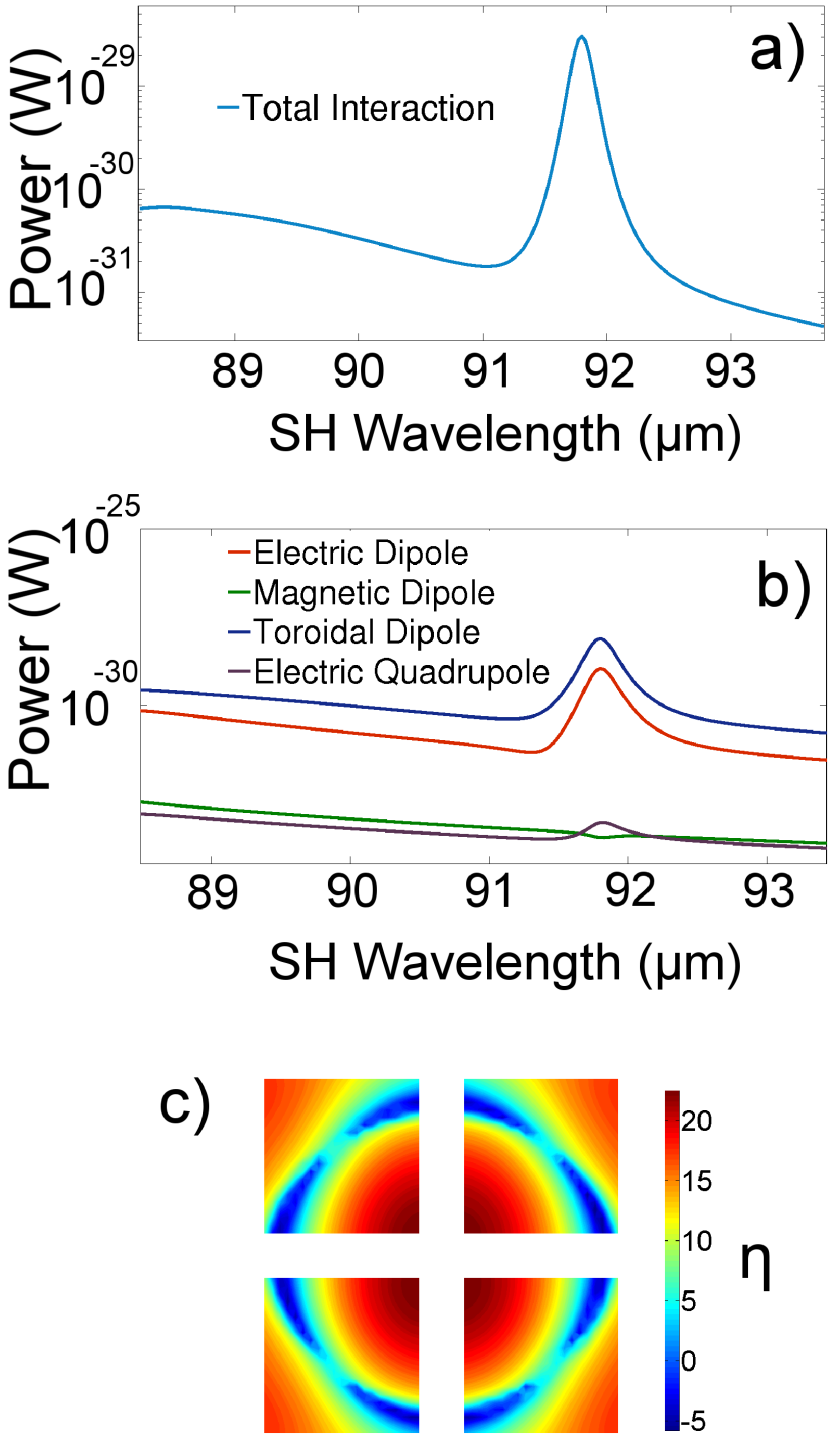

Figure 5.3: a) The total nonlinear signal calculated, which includes the interaction terms of the multipoles. The clear resonance is, as expected, at half the wavelength of the resonance in Fig.5.2. b) The nonlinear electromagnetic multipoles are calculated *via* the nonlinear polarizations. Note that a log plot is required to accurately compare these multipoles. Clearly the SH is primarily toroidal in nature. c) The quantity η is calculated. Two toroidal loops are squeezed into the cuboids at the SH.

culates the interaction of the multipoles. We do indeed observe a resonance at 91.8μm, as predicted from combining SHG theory with the linear results calculated previously. Moreover, the nature of this resonance is unexpected; the SH signals generated by nanostructures are most frequently due to nonlinear electric dipoles. Here, however, we observe a rare instance where a linear toroidal dipole generates a nonlinear toroidal dipole. This indicates that the nonlinear currents that are produced from the material's interaction with the external light source are rather more complicated than is typically observed. We hence plot again the quantity η. There is an interesting difference between the linear and nonlinear regimes: while the linear side has one loop present within each metamaterial component, the nonlinear current plot shows that two loops are squeezed into each cuboid.

5.5 Conclusions

We have studied the nonlinear signal arising from a meta-atom comprised of a non-centrosymmetric material, $LiTaO_3$. The first goal was to ensure that the linear signal generated by the external plane wave was primarily toroidal in nature, with the structural parameters being chosen in such a way as to maximize this resonance. The nonlinear currents were then calculated, plotted, and utilized so as to rigorously analyze the nonlinear electromagnetic moments arising from this structure. Surprisingly, this nonlinear signal was also toroidal in nature. The structure was also designed such that these results are experimentally verifiable.

Bibliography

[1] Y. B. Zel'dovich, Zh. Eksp. Teor. Fiz. **33**, 1531 (1957) [Sov. Phys.JETP 6, 1184 (1958)].

[2] C. S. Wood, S. C. Bennett, D. Cho, B. P. Masterson, J. L. Roberts, C. E. Tanner, and C. E. Wieman, "Measurement of parity nonconservation and an anapole moment in cesium", Science, **275**, 1759-1763 (1997).

[3] W. C. Haxton and C. E. Wieman, "Atomic parity nonconservation and nuclear anapole moments", Annu. Rev. Nucl. Part. Sci. **51**, 261-293 (2001).

[4] J. S. M. Ginges and V. V. Flambaum, "Violations of fundamental symmetries in atoms and tests of unification theories of elementary particles" Phys. Rep. **397**, 63-154 (2004).

[5] G. N. Afanasiev, "Simplest sources of electromagnetic fields as a tool for testing the reciprocity-like theorems", Sci. Rep. **3**, 539-559 (2013).

[6] K. Sawada and N. Nagaosa, "Optical magnetoelectric effect in multiferroic materials: evidence for a Lorentz force acting on a ray of light", Phys. Rev. Lett. **95**, 237402 (2005).

[7] G. N. Afanasiev and Y. P. Stepanovsky, "The electromagnetic field of elementary time-dependent toroidal sources", J. Phys. A **28**, 4565-4581 (1995).

[8] A. E. Miroshnichenko, A. B. Evlyukhin, Y. F. Yu, R. M. Bakker, A. Chipouline, A. I. Kuznetsov, B. Luk'yanchuk, B. N. Chichkov, and Y. S. Kivshar, "Nonradiating anapole modes in dielectric nanoparticles", Nat. Commun. **6**, 8069-8076 (2015).

[9] C. M. Ho, and R. J. Scherrer, "Anapole dark matter", Phys. Lett. B, **722**, 341-346 (2013).

[10] E. E. Radescu and G. Vaman, "Exact calculation of the angular momentum loss, recoil force, and radiation intensity for an arbitrary source in terms of electric, magnetic, and toroid multipoles", Phys. Rev. E **65**, 046609 (2002).

[11] J. D. Jackson, *Classical Electrodynamics* (John Wiley and Sons, 1962).

[12] V. M. Dubovik and V. V. Tugushev, "Toroid moments in electrodynamics and solid-state physics", Phys. Rep. **187**, 145-202 (1990).

[13] V. Savinov, V. A. Fedotov, and N. I. Zheludev, "Toroidal dipolar excitation and macroscopic electromagnetic properties of metamaterials", Phys. Rev. B **89**, 205112 (2014).

[14] T. Kaelberer, V. A. Fedotov, N. Papasimakis, D. P. Tsai, N. I. Zheludev, "Toroidal dipolar response in a metamaterial", Science, **330**, 1510-1512 (2010).

[15] V. A. Fedotov, A. V. Rogacheva, V. Savinov, D. P. Tsai, and N. I. Zheludev, "Resonant transparency and non-trivial non-radiating excitations in toroidal metamaterials", Sci. Rep. **3**, 2967 (2013).

[16] Y. Fan, Z. Wei, H. Li, H. Chen, and C. M. Soukoulis, "Low-loss and high-Q planar metamaterial with toroidal moment", Phys. Rev. B **87**, 115417 (2013).

[17] Y. Huang, W. T. Chen, P. C. Wu, V. A. Fedotov, V. Savinov, Y. Z. Ho, Y. Chau, N. I. Zheludev, and D. P. Tsai, "Design of plasmonic toroidal metamaterials at optical frequencies", Opt. Exp. **20**, 1760-1768 (2012).

[18] K. Marinov, A. D. Boardman, V. A. Fedotov, and N. I. Zheludev, "Toroidal Metamaterial", New Journal of Physics, **9**, 324-202 (2007).

[19] Z. Dong, J. Zhu, J. Rho, J. Li, C. Lu, X. Yin, and X. Zhang, "Optical toroidal dipolar response by an asymmetric double-bar metamaterial", Appl. Phys. Lett. **101**, 144105 (2012).

[20] B. Ögüt, N. Talebi, R. Vogelgesang, W. Sigle, and P. A. van Aken, "Toroidal plasmonic eigenmodes in oligomer nanocavities for the visible", Nano Lett. **12**, 52395244 (2012).

[21] N. Papasimakis, V. A. Fedotov, V. Savinov, T. A. Raybould, and N. I. Zheludev, "Electromagnetic toroidal excitations in matter and free space" Nat. Mater. **15**, 263271 (2016).

[22] Z. Dong, J. Zhu, X. Yin, J. Li, C. Lu, and X. Zhang, "All-optical Hall effect by the dynamic toroidal moment in a cavity-based metamaterial", Phys. Rev. B **87**, 245429 (2013).

[23] W. Liu, J. Zhang, and A. E. Miroshnichenko, "Toroidal dipole-induced transparency in coreshell nanoparticles", Laser Photonics Rev. **9**, 564-570 (2015).

[24] Y.-W. Huang, W. T. Chen, P. C. Wu, V. A. Fedotov, N. I. Zheludev, and D. P. Tsai, "Toroidal Lasing Spaser", Sci. Rep. **3**, 1237 (2013).

[25] A. A. Basharin, M. Kafesaki, E. N. Economou, C. M. Soukoulis, V. A. Fedotov, V. Savinov, and N. I. Zheludev, "Dielectric metamaterials with toroidal dipolar response", Phys. Rev. X **5**, 011036 (2015).

[26] C. F. Bohren, and D. R. Huffman, *Absorption and Scattering of Light by Small Particles* (Wiley-Interscience, 1983).

[27] Y. S. Kivshar and A. E. Miroshnichenko, "Meta-optics with Mie resonances", Opt. Photon. News **28**, 26–33 (2017).

[28] I. V. Stenishche and A. A. Basharin, "Toroidal response in all-dielectric metamaterials based on water", Sci. Rep. **7**, 9468 (2017).

[29] CST Computer Simulation Technology GmbH. [Accessed 16th September 2018], Available from: https://www.cst.com

[30] R. W. Boyd, *Nonlinear Optics* (Academic Press, 2008).

[31] M. J. Weber, *Handbook of Optical Materials* (CRC Press, 2002).

[32] S. Cabuk and S. Simsek, "First-principles calculation of the linear and nonlinear optical properties of $LiTaO_3$", Phys. Scr. **81**, 055703 (2010).

[33] A. Taflove and S. C. Hagness, *Computational Electrodynamics: The Finite Difference Time Domain Method, 3rd ed.*, chap. 8 (Artech House, New York, 2005).

Chapter 6

Metamaterial Fabrication, SEM Images, and FTIR Measurements

This section will firstly detail the fabrication process used to produce periodic arrays of U-shapes. The justifications behind the equipment used is given along with the optimal parameters. The source of the U-shapes is also given, with an explanation as to how these shapes are useful for future fabrication work. The workings of the Fourier Transform Infrared Spectrometer, along with its measurements of the optical coefficients of the U-shapes are presented.

Cross-shaped trenches are the second metamaterial considered in this chapter. Once again its origins and usefulness are delineated, with a slight modification being made to remove an extra layer of PMMA from the original structure. Different cross-shaped trenches are introduced and combined to formulate a multi-resonant meta-atom, the measurements of which are also introduced. Due to small alterations in the fabrication procedure, it is again necessary to fully expand the details of each fabrication step.

Finally, a third metamaterial is introduced that consists of a cross-shaped trench with a reduced quantity of surrounding metal. The fabrication procedure for this structure requires an additional substance, referred to as HSQ, which strongly alters the entire production process. The steps are hence given, and the measured responses are shown.

Throughout the fabrication of the above-mentioned metamaterials, there were many alternative approaches and ideas that ultimately had to be changed due to their lack of success. The most important of these are given here in detail.

6.1 Fabrication of U-Shape Structures

Before the process of production for our metamaterials can be discussed, it must be noted that there is no 'one size fits all' fabrication method for metamaterials: the choice

of substrate, metal(s), and desired patterns all dramatically affect the role that fabrication parameters play. Figure 6.1 helps elucidate this principle. In terms of fabrication, there are, broadly speaking, two main types of metamaterial: hill-type structures, where the pattern of interest is a metallic design on top of a substrate; and valley-type structures, where the pattern of interest is a gap within the metal which sits atop the substrate, also depicted in Figure 6.1.

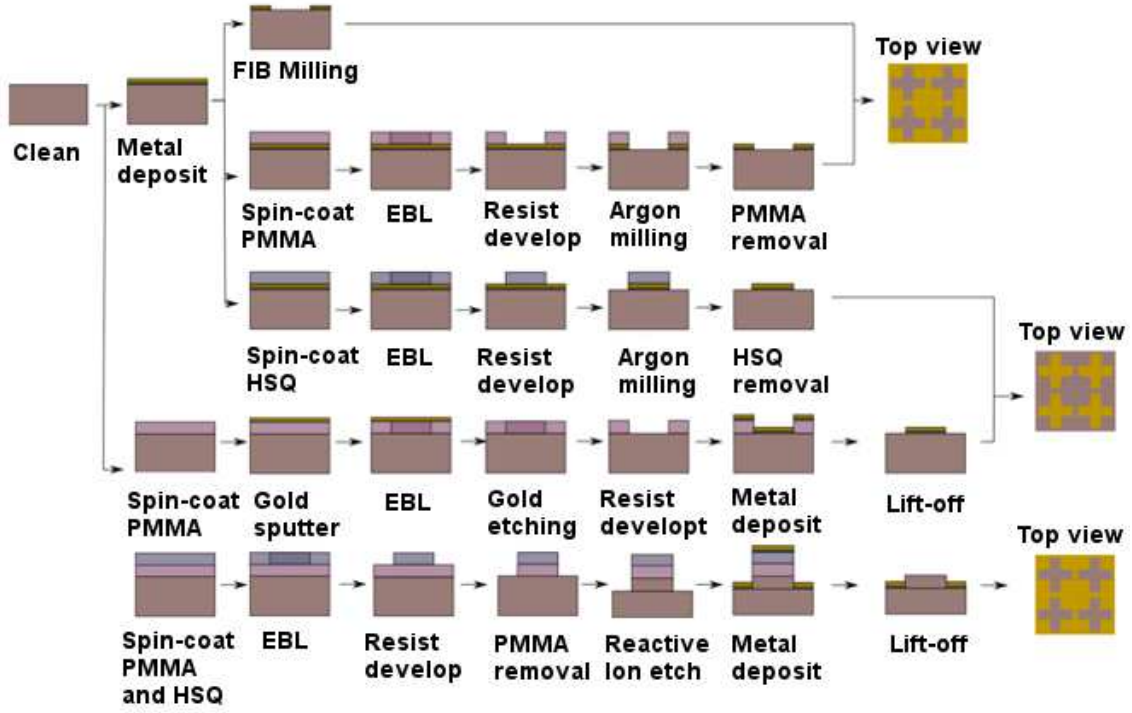

Figure 6.1: Examples of different fabrication procedures to produce hill- and valley-type metamaterials. The choice of procedure will be dependent upon the choice of materials that constitute the metamaterial.

The structure of interest for this section is a hill-type structure, as shown in Figure 6.2. These structures are closely related to split ring resonators (SRRs) [1, 2], but the small upper-arms of the SRR in this instance are removed to increase the resonance frequency at a given minimum feature size and to simplify the nanofabrication procedure [3]. These U-shapes are ideal for becoming acquainted with the equipment used for producing metamaterials, as the structure does not present too challenging a work: there are no tricky aspects such as small features or uncommon materials, and the structure has been extensively analysed within metamaterial literature [3–5]. This means that the manufactured metamaterial can be compared with the known optical response in order to determine whether its production was successful.

The unit cell consists of a Si substrate followed by a 5nm U-shaped layer of Ti,

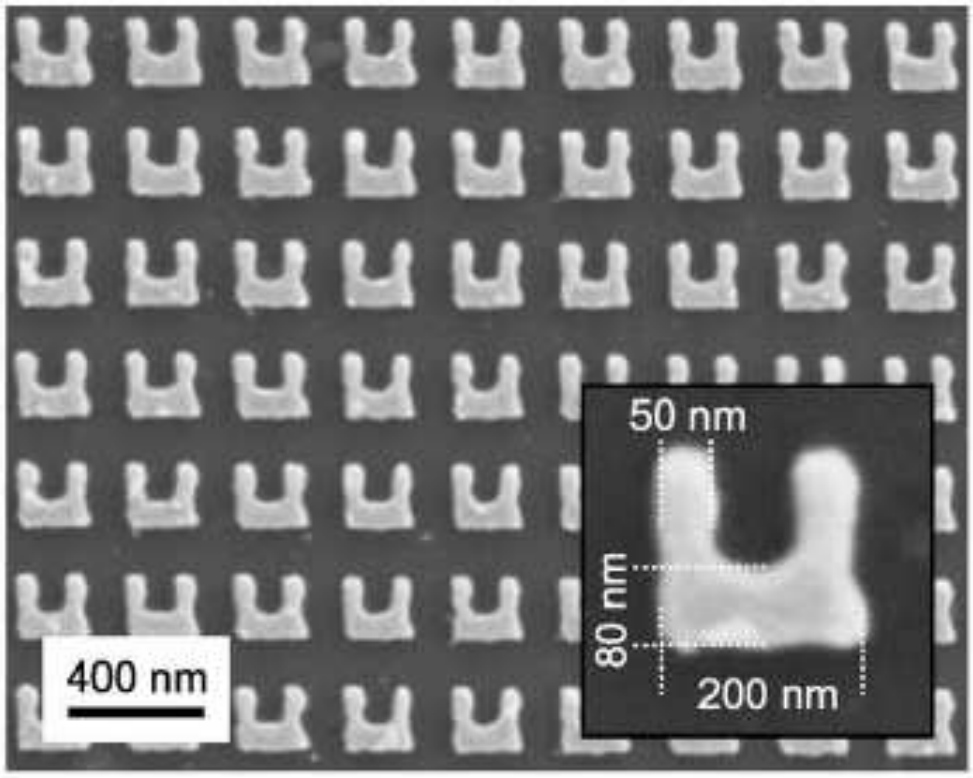

Figure 6.2: The U-shaped metamaterial that will first be analysed in order to become acquainted with metamaterial fabrication procedures. Taken from [4].

and a final 30nm U-shaped layer of Au. It is important to note that this structure is polarization-dependent: the orientation of the incoming electric field determines which part of the U-shape is excited. Figure 6.3, below, taken from [4], shows the optical response of this dependence.

6.1.1 Cleaning and Spin-coating

Surface impurities on a substrate can wreak havoc for the entire fabrication procedure. With the potential for creating uneven metallic surfaces and producing vast areas where patterning is impossible, the preliminary cleaning of a substrate is therefore always a necessity. To this end, the substrates were placed in a thermal bath of 50°C at 45KHz sweep mode for 10 minutes in Acetone, followed by 10 minutes in IPA and 5 minutes in DI-water at the same frequency and temperature. A plasma asher was then used to descum the substrates: an O_2 plasma buffeted the surfaces of the Si substrate for 5 minutes.

A critical layer which enables the structures to be patterned into the metamaterial is a masking polymer. Various masking polymers designed for varying functionalities exist, but in this instance a 100nm-layer of Poly(methyl methacrylate) (PMMA) is used. It is

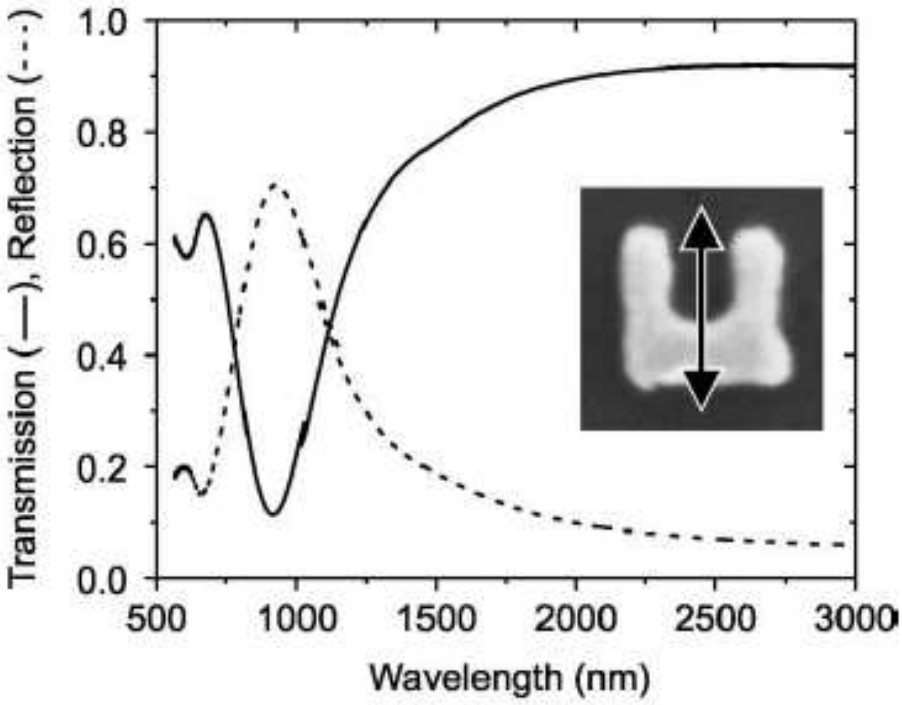

Figure 6.3: The polarization-dependence of the U-shape structure demonstrated through measurements of the normal-incidence transmission and reflection spectra. Taken from [4].

required, much like a stencil, for the design patterning, but must also be removed at the end of the fabrication process. Therefore, it is often referred to as a sacrificial layer.

In order to evenly distribute and solidify the initially liquefied PMMA, it must be spin-coated. This process involves placing the substrate centrally on a stage, which rotates with a selected angular frequency. The substrate is then covered with PMMA, while making sure no bubbles are present, as these interfere with how evenly the PMMA is distributed. A spin-recipe is then selected. The rapid rotation of the stage causes the PMMA to experience a centripetal force. This force, combined with the surface tension of the liquid, causes the PMMA to solidify in an even manner across the surface of the substrate [6].

Different PMMA products are dissolved in different amounts of anisole and are designed to also have different molecular weights. The selection of molecular weights, percentage solution, and rotation frequency creates a flexible choice of PMMA thickness. Figure 6.4 shows the dependence of the thickness of 950 PMMA-Ax (PMMA solutions of molecular weight 950,000 which are dissolved in x percent of anisole). To produce the required 100nm-layer of sacrificial layer, 950 PMMA-A2 was used for my experiments, spun at 500rpm for 2 seconds and subsequently at 2000rpm for 45 seconds. After spin-coating, the substrate was baked at 180°C for one minute to dry, ready to be placed into

Figure 6.4: The effect of spin rate upon the final thickness of the PMMA-layers depending upon the concentration of the PMMA. Taken from [6].

an Electron Beam Lithographer.

At the end of this step, the sample is built up as in Figure 6.5.

6.1.2 Electron Beam Lithography

Electron Beam Lithography is the step in the fabrication procedure which enables the patterns to be designed and implemented. By firing a beam of electrons into the PMMA resist, the solubility of the exposed resist is altered. This means that after fabrication there are effectively two different types of PMMA present on the substrate. By applying the right solvents, therefore, the exposed PMMA can be removed while leaving the unexposed PMMA in place as a mask for further processing. Before the designs can be implemented, however, the Electron Beam Lithographer (EBL) must be finely focused by tuning a multitude of parameters, including the aperture size and working distance of the gun; stigmation; electron beam voltage; stage height; and aperture alignment to ensure that the patterns are as accurate as possible. It is worth discussing the role these parameters play in the patterning process, as every slight change to an EBL function can

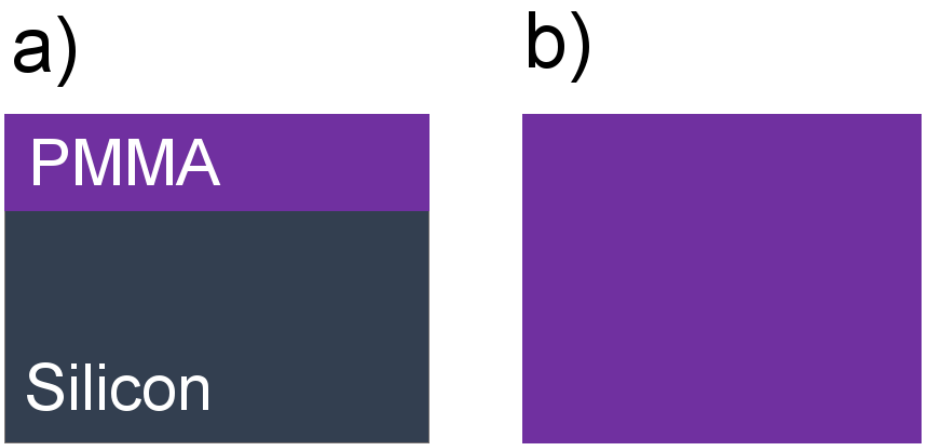

Figure 6.5: a) The state of the future U-shaped sample after the substrate has been cleaned and had a 100nm layer of PMMA spin-coated upon it. b) The bird's eye view is also presented for a visual aid to help the reader grasp each step in the fabrication process.

radically alter, and hence ruin, the desired outcome.

The aperture size controls the size of the beam. If we liken the EBL's firing of electrons to a hose squirting water, the aperture size alters the surface area of water flowing through the nozzle. This beam naturally spreads outwardly as it travels, and hence the working distance of the gun to the substrate decides the extent of this spreading. The stage height is a parameter that is utilized in conjunction with the working distance. While the stage height is simply how far above the default position the stage must be raised, the working distance determines the height from the sample to the EBL gun. The electron beam voltage dictates the power with which the electrons are fired. Not all resists have the same thickness, and hence to penetrate a more thickly coated resist it is often advisable to ramp up the EBL beam voltage. The stigmation and aperture alignment are often set in tandem while setting up the EBL. The stigmation is judged by eye, with the best stigmation setting being set by the user's sense of minimal astigmatism. The EBL can change the stigmation of the beam by applying a weak electromagnetic field, slightly altering the movements of the electrons. The aperture alignment simply ensures that the beam of electrons flows dead centre with respect to the sample.

The write-field alignment must also be executed: usually, the EBL only 'sees' an area of 100μm x 100μm. For areas larger than this, the stage is mechanically shifted by the EBL. Correcting the write-field alignment therefore makes certain that the second 100μm

x 100μm perfectly sits next to the first with no gaps or overlap. In EBL terminology this is often referred to as 'stitching', a correction that must be manually accounted for before the patterning can begin.

As mentioned, the aperture size controls the width of the beam. It is therefore no surprise that this parameter plays a crucial role in the magnitude of the current that flows from the electron beam. This value is of crucial significance when calculating the EBL's dwell time. The dwell time dictates how long the EBL should stay in a fixed position (dwell) while firing the beam to deliver the specified dose into the resist. If this dwell time is not recalculated for every EBL session it could easily ruin the entirety of the sample, as the EBL will dwell for an incorrect length of time, leading to over/under-exposed structures.

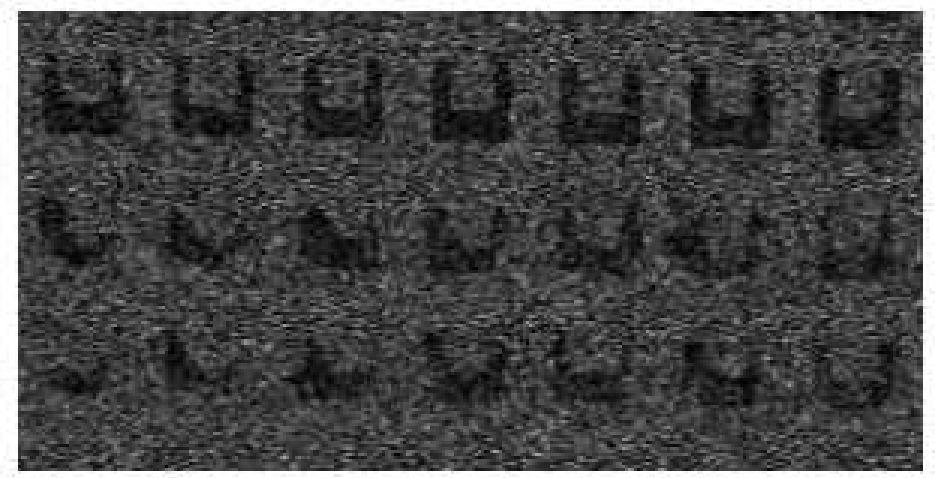

Figure 6.6: A scanning-electron microscope image of a portion of a dose test. The dose is gradually increased moving from left to right. Hence, the top-right U-shape has the highest dose. We can see that when the dose is very low, the U-shape's features are not visible.

A vital investigation when creating a new structure is to find through experimentation the optimum dose of the EBL for that particular structure. This dose is intrinsically linked to the intensity with which the EBL fires the beam of electrons. The EBL's perfect dose is hence the dose that produces the best patterns. If the dose is too small, this equivalently means that the beam of electrons is too weak, leading to poorly-defined features. If the dose is too strong, the required designs will have no sharp features, and any sharp corners will be transformed into rather rounded shapes. This difference between dose values is delineated in Figure 6.6. It is therefore a necessity to produce a full sample containing features of varying doses, in order to find this 'Goldilocks dose'. My usual method for locating this dose is to create a 2x2 array of the structure in question with an assigned dose of 0.01. This structure is then duplicated hundreds of times with an incremental increase

in dose of 0.01. This therefore produces an array, with the constituent components exhibiting a range from poorly defined features to overly defined features.

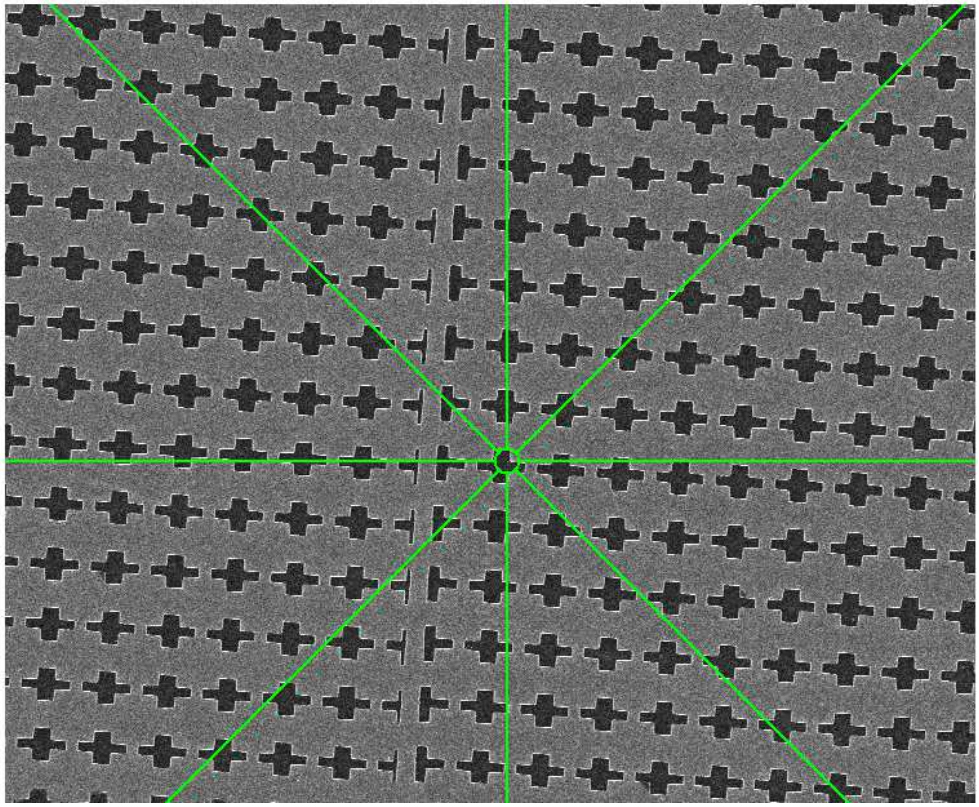

Figure 6.7: An example of an incorrectly aligned writefield. It is as if a column of crosses has been ripped apart. It is often advisable for a user to repeat writefield alignments within the EBL framework to ensure that they stitch together correctly.

An important image that highlights the importance of ensuring the writefield is correctly aligned is depicted in Figure 6.7. It is clear that one column of crosses actually belongs to two writefields that have not been correctly stitched, a mistake that is the fault of the user. This splitting of the crosses would naturally not be visible were the writefields correctly aligned. With a writefield area of 100μm x 100μm, a working distance of 8.9mm, and aperture size 20μm, a dose of 1.41 generated the highest-quality U-shapes, as depicted in Figure 6.8.

6.1.3 Development and Electron Beam Evaporation

Once the exposure is complete, the exposed PMMA resist can be removed by placing the sample in a solution of MIBK:IPA 1:3 for 60 seconds, followed by pure IPA for a further 60 seconds. After drying the sample with N_2 (placing the sample on a hot plate here can potentially damage the patterned features), the sample is ready to have the metals

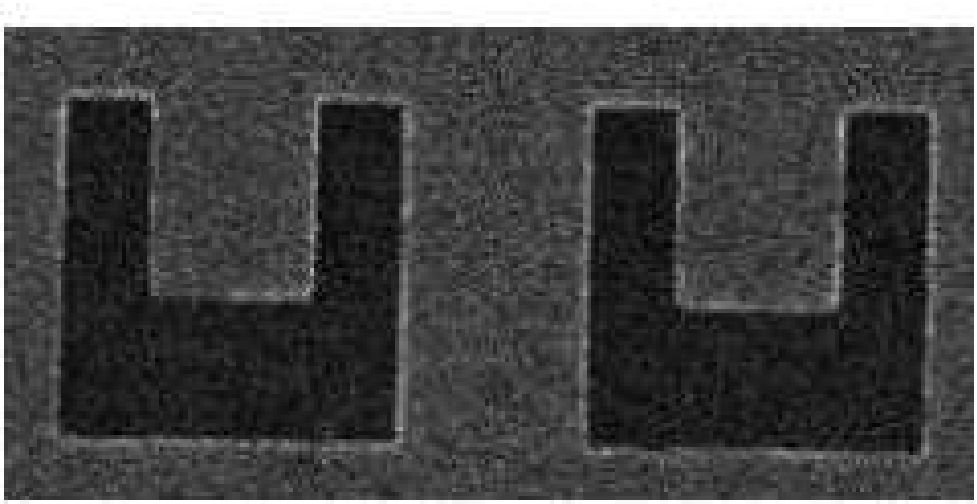

Figure 6.8: The best dose, 1.41, taken from the same array as Figure 6.6.

evaporated upon it. At this point, the structure appears as in Figure 6.9.

An electron beam evaporator is an efficient way of achieving this goal. The evaporator is able to fire electrons through a vacuum to irradiate the metal of choice. The metal heats and evaporates, depositing uniformly upon the substrates which rotate above the metal source. By tuning the current through the filament, one has the ability to finely tune the rate of evaporation. For the manufactured U-shapes, the rates of evaporation were, according to the crystal monitor present within the equipment, 0.043nm/s and 0.076nm/s for the titanium and gold respectively. The 5nm layer of titanium does not play a role in the optical characteristics of the metamaterial, but is required as a glue: gold is naturally not adhesive, and would not form a sustainable layer without the stickier titanium.

When fixing the samples to the rotating ceiling, the simplest method is to ensure the substrates are placed onto a glass slide enveloped in sticky-tape. This glass slide is then in turn stuck to the ceiling. It is useful to tape over a partial region of the substrates, as this will produce a region, once the tape has been removed, where no metals have been deposited. Having both regions allows the height of the gold to be accurately calculated using a DekTak Profilometer after evaporation is complete. This Profilometer consists of a diamond-tipped stylus that outputs its height as an analogue signal. By making this stylus run over both metallic and non-metallic regions, the height difference - i.e. height of the deposited metal - can be measured. Once again we provide the reader with a visual aid as to how the structure looks once this metallic evaporation is complete, depicted in Figure 6.10.

After the metallic evaporation, the remaining PMMA must be removed. This is

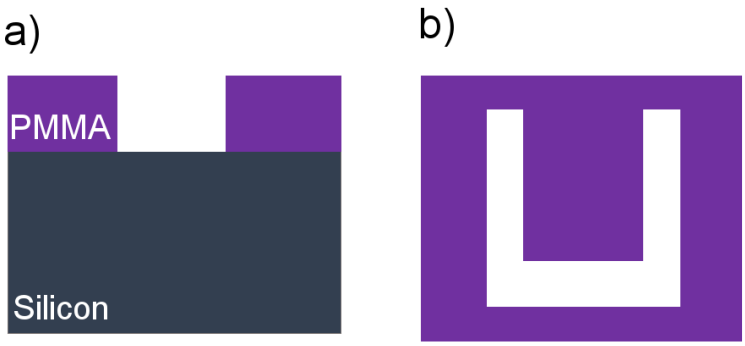

Figure 6.9: a) The sample has now been exposed to the EBL and has had the exposed PMMA removed through development in solvents. There are therefore now gaps present in the PMMA where the substrate can be seen from above. b) The top-down view enables the reader to see the gaps that have been formed *via* the EBL exposure.

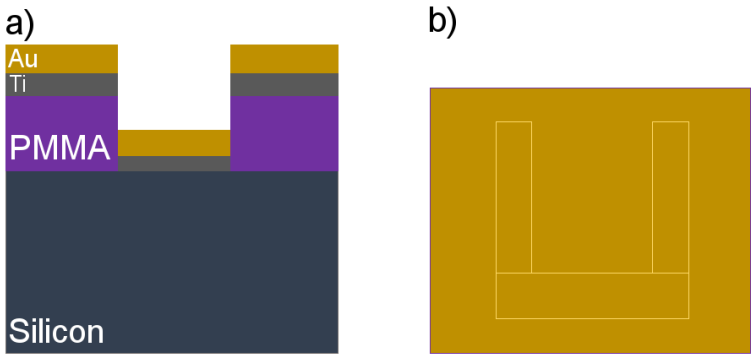

Figure 6.10: a) The metals titanium and gold are evaporated uniformly across the sample. This naturally includes the regions where the PMMA was removed. b) The gold U-shapes are now starting to become apparent. Once the PMMA is removed with solvents, the sample is complete.

achieved by placing the sample in acetone for 24 hours, followed by an ultrasonic bath in acetone for 30 seconds, then IPA for a further 30 seconds. Once the sample is N_2-dried, the metamaterial consists of titanium and gold-layered U-shapes.

This concludes the discussion of how to fabricate the U-shaped arrays. The optical spectra of this fabricated metamaterial is detailed in Section 6.6.1. We now turn to fabricating Swiss Crosses.

6.2 Swiss Cross Structures - Dual Crosses

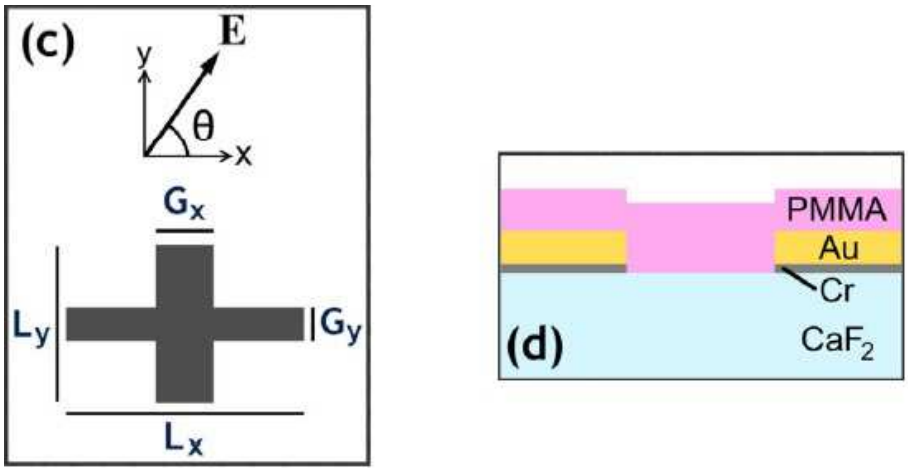

Figure 6.11: The unit cell upon which our structure is based, taken from [7]. Here, the dimensions, in nm, are: $G_x = 580$, $G_y = 390$, $L_x = 1900$ $L_y = 1340$. The thickness of the PMMA, gold and titanium are, in nm, 85, 35 and 5 respectively. The periodicity of the crosses is 2.5μm. Note the way the angle of polarisation is defined here.

There are two main structures that we need look at concerning Swiss Crosses: a meta-atom consisting of two different Swiss crosses, and a Swiss cross with a reduced amount of metal on the surface. As these structures require different fabrication procedures, we being with the former case.

The investigation that we wish to undertake here is the following: given two individual unit cells, M_1 and M_2, each with a corresponding resonance in frequency space at f_1 and f_2, is it possible to create a meta-atom $M = M_1 + M_2$ with resonances at both f_1 and f_2?

The structure of interest for this section is a valley-type metamaterial, with the unit cell based on the structure shown in Figure 6.11 and dimensions given in the caption. The unit cell consists of a CaF_2 substrate followed by a narrow layer of Ti, and a final thicker layer of Au, with the cross-shape gap cutting through everything but the substrate. This unit cell is from the work of Osley et al. [7]. In that particular paper, the aim was to study the Fano resonance which occurs due to the carbonyl bond of the PMMA deposited

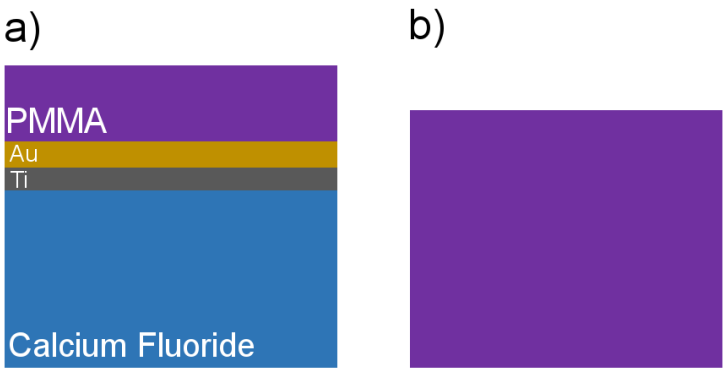

Figure 6.12: a) The experimental setup for the dual crosses. We must here evaporate the metals before spin-coating the PMMA, due to the insulating nature of the CaF_2. b) From above, the only surface that the EBL will subsequently see is the 100nm layer of PMMA.

on the unit cell [8–11]. As this Fano resonance is not required for this thesis, the PMMA layer can simply be removed from the unit cell. This removal simply blue-shifts the main resonance. Here, the interest lies in producing a unit cell with two distinct resonances.

The asymmetry of the above unit cell induces a polarisation-dependence of the metamaterial: we saw from Chapter 2 how the metamaterial's response depends upon the current induced within the metal. Depending on how the electric field is polarised, different arms of the cross will be excited. Hence, symmetric crosses are polarisation-independent. Asymmetric crosses have been studied extensively [12, 13]. As a unit cell exhibiting two distinct resonances is required, a sensible starting point is the deconstruction of the unit cell in Figure 6.11 into two crosses, where one component of the meta-atom, M_1, is created from the thinner arm of the original cross, with the thicker arm being used for the second cross, M_2.

6.2.1 Cleaning, Electron Beam Evaporation and Spin-Coating

The initial substrates were cleaned in the same way outlined above, but here the metals must be evaporated on the substrate *before* the PMMA is spin-coated. For the Swiss crosses manufactured below, the filament current was 27mA for titanium and 27.4mA for gold. The rates of evaporation were 0.153nm/s and 0.357nm/s for titanium and gold respectively. 100nm of PMMA A4 was spin coated on top of the metal. At this stage, the sample is configured as in Figure 6.12

6.2.2 Electron Beam Lithography

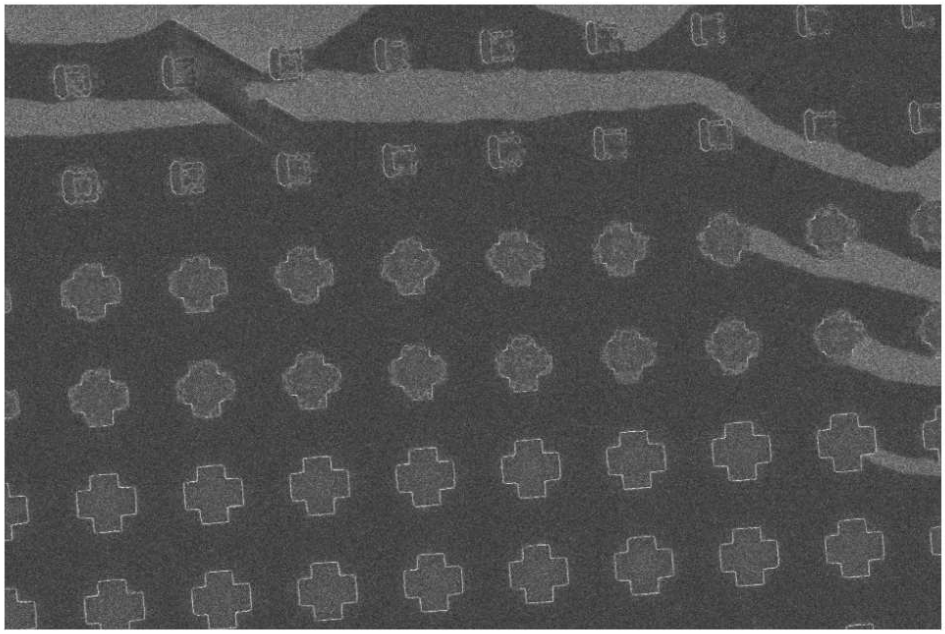

Figure 6.13: A scanning-electron microscope image of the dose-test undertaken for the thick-armed cross. In the upper-area of the picture, poorly-defined structures can be seen. The dose for these crosses was too small.

Once again, a dose test is mandatory for generating the highest-quality features. Here, with a writefield area of 100μm x 100μm, a working distance of 8.9mm, an aperture size 20μm, and a dose of 0.75 generated the highest-quality crosses. One example of a dose test for this structure is depicted in Figure 6.13, whereas the perfect dose is shown in Figure 6.14

6.2.3 Development and Argon Ion Milling

The exposed PMMA resist can now be removed in the same manner as for the U-shapes, by placing the sample in a solution of MIBK:IPA 1:3 for 60 seconds, followed by pure IPA for a further 60 seconds. After drying the sample with N_2, the sample is ready to be exposed to argon ion milling, the purpose of which is to remove cross-shaped portions of the gold and titanium. This step was not required when considering the U-shapes, due to the fact that there the metal was deposited upon the sacrificial layer, and hence could easily be removed with the PMMA. Before the argon milling takes place, the sample is depicted in Figure 6.15.

By bombarding the entire surface of the sample with argon ions, the gold and titanium atoms are ejected from their respective layers. The control over the voltage and current

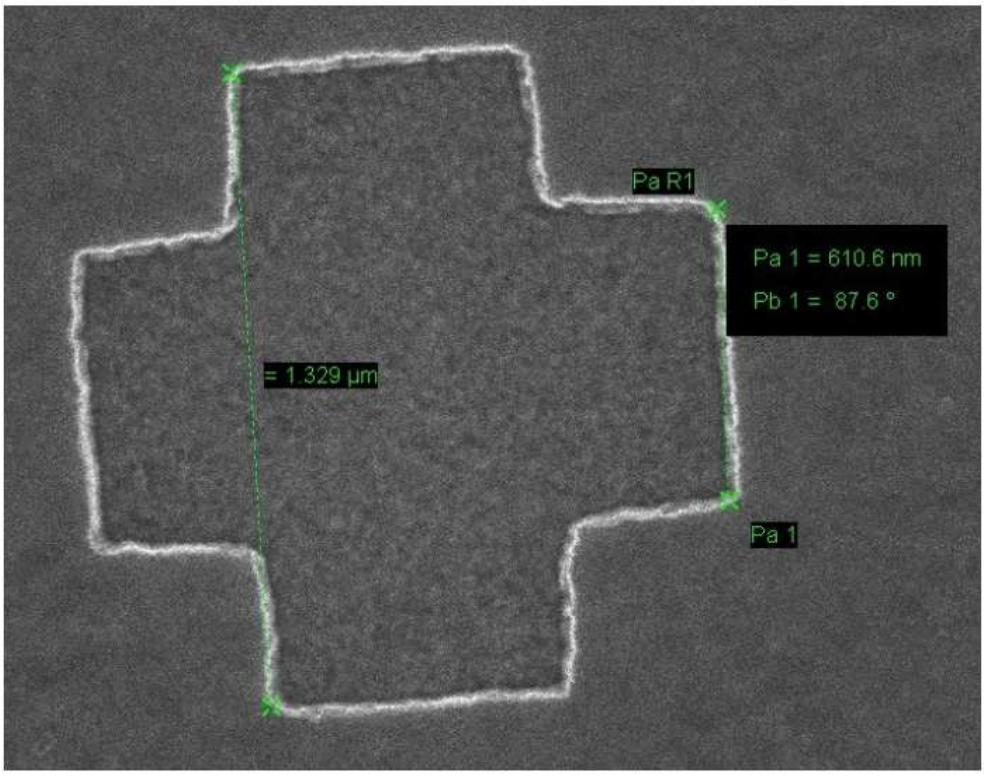

Figure 6.14: A dose of 0.75 yielded the highest-quality cross-shapes. Shown here is the cross made of the thick-armed cross.

allows precise milling rates to be achieved. For example, a standard recipe for the acceleration voltage, beam voltage and beam current of 390V, 200V and 10mA respectively leads to a milling rate of 5.5 nm/s for gold and 2.2nm/s for silicon. The PMMA, which is still present on the remainder of the sample, acts as a mask for these surfaces. The purpose of having a mask with a low milling rate (2.2nm/s for the above parameters) enables the surface under the PMMA to remain unaltered throughout the milling process.

After milling, the sample appears as in Figure 6.16. It was subsequently left in acetone for 24 hours, followed by an ultrasonic bath in acetone for 30 seconds, then IPA for a further 30 seconds. Once the sample is N_2-dried, the metamaterial consists of cross-shaped gaps within the deposited titanium and gold.

6.3 Swiss Cross Structures - Reduced Metal

This section arises from an investigation into metamaterial notch transmission filters using metal. The origins of the structure and its parameters, depicted in Figure 6.17, were dealt with in more detail in Chapter 3. The basic premise, however, is that the reduction of metal on the surface allows for greater transmission by removing the possible reflection

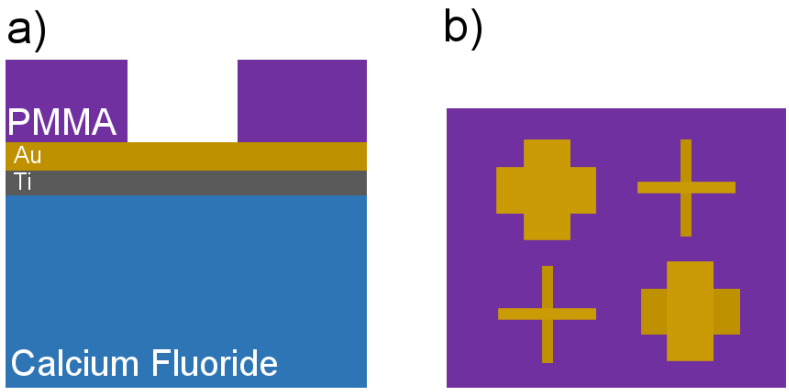

Figure 6.15: a) After the EBL exposure the sample has the exposed areas of the PMMA removed, and the metal shines through ready for milling. b) The metallic crosses are clearly visible. As the end goal is to have cross-shaped trenches, this sample must be milled with the PMMA acting as a mask.

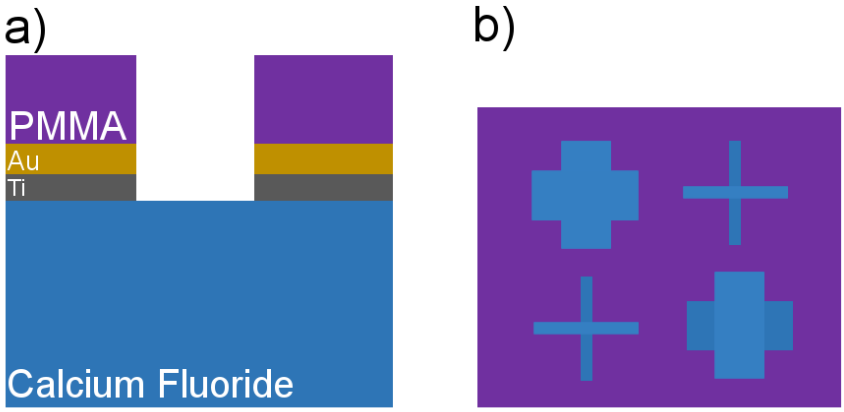

Figure 6.16: a) The trenches have now been made, and all that is left to complete is the removal of the PMMA. b) It is clearer from the top-down perspective that once the PMMA has been removed with acetone and IPA, cross-shaped trenches are present in the metals.

and/or absorption via the gold. There is, on the other hand, still enough gold present for a metamaterial to be present that can interact with the extraneous light source and block the desired wavelength(s). The desired wavelength we wish to block and hence upon which the structural parameters are based, is 2.7μm.

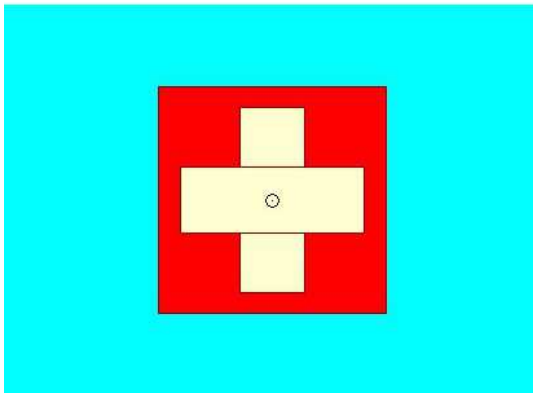

Figure 6.17: The new Swiss cross meta-atom optimized for improving transmission, i.e. generating sharper and deeper resonances in the transmission spectrum. The width and length of the cross is 174nm and 486nm respectively. The square made of gold (depicted as red) has a width of 600nm. The periodicity and thickness of the gold is 1620nm and 30nm respectively, as generated by RSoft's DiffractMOD MOST optimizer. The blue and cream colours refer to the surrounding dielectric and the cross-shaped gaps, respectively.

6.3.1 Cleaning, Electron Beam Evaporation and Spin-Coating

The substrates were cleaned in the same way as before. At this point in my fabrication career I was adding 2 more minutes to each solvent bath simply for good measure. As in the other Swiss Cross case, the metals have to be evaporated upon the substrate before any spin-coating takes place. At this stage, too, a small change was made; after experiencing less than desirable results, the amount of titanium was decreased from 5nm to 1nm. As mentioned previously, the role of the titanium plays no optical role, it is simply a glue used to keep the gold on the substrate. Due to the weak resonances being acquired, it was thought that the 5nm layer was potentially too thick and in actual fact interacting with the impinging light. The reduction could only have a positive effect, as a 1nm coat is still plenty for the Ti to act as cement.

During my time in the lab attempting to fabricate this sample successfully, the PMMA at one point had to be changed; the cleanroom was out of stock of PMMA A2 (950) and had no plans to continue its purchase. I subsequently had the selection of PMMA A4 (950) and PMMA A2 (495). Initially I opted for the latter, as it supposedly gave the same thickness as my original source. However, this radically altered the optimal dose, and hence all the EBL parameters. When using the 4% PMMA instead, although the

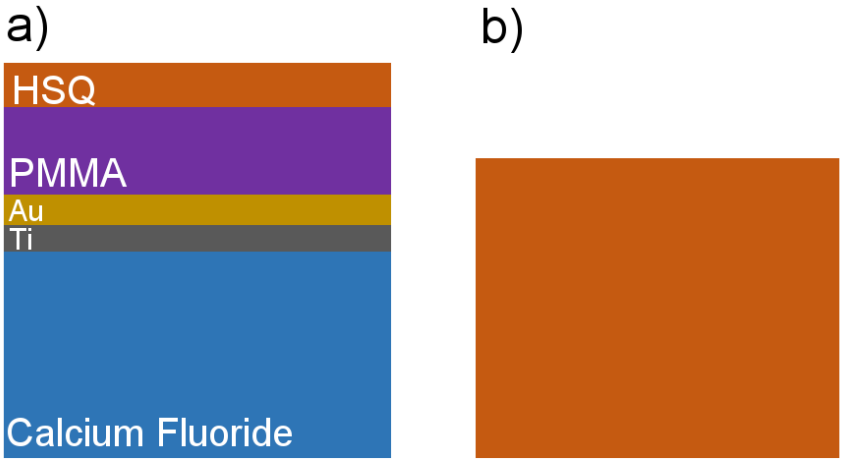

Figure 6.18: a) The setup for the notch filter to be manufactured. The substrate has had the metals evaporated upon it, with both PMMA and subsequent HSQ spin-coats. b) The bird's eye perspective. From the EBL's point of view it will only 'see' the HSQ.

thickness was now to be 200nm, it was substantially easier to achieve sharply defined structures using this brand of PMMA.

The change in structure from an all-gold background to a mostly-transparent background requires a rather dramatic way in fabricating this metamaterial. We cannot simply follow the method of the dual-crosses, as we need to be more selective about how our gold is removed. To this end, a second sacrificial layer is added on top of the PMMA; 6% hydrogen silsesquioxane (HSQ) is spin coated at 5000rpm for 45 seconds to give a layer of 85nm. It will shortly become clear why this is necessary. After these steps are implemented, Figure 6.18 represents how the structure appears.

One important factor to note here is that HSQ is a *negative* resist, while PMMA is a *positive* resist. This means that while it is the exposed area of PMMA that is usually removed, it is the *unexposed* region of HSQ that gets removed upon development.

6.3.2 Electron Beam Lithography

Through much trial and error, it was found that a change to the aperture size, from 20μm to 10μm, produced better results. The writefield area was kept at 100μm x 100μm. A working distance of 9.1mm was implemented. These parameters gave an optimal dose of 0.141 as depicted in Figure 6.19.

6.3.3 Development and Argon Milling

As can be immediately seen from viewing Figure 6.18, we cannot immediately jump to developing the PMMA like we did with the other structures. In fact, the PMMA

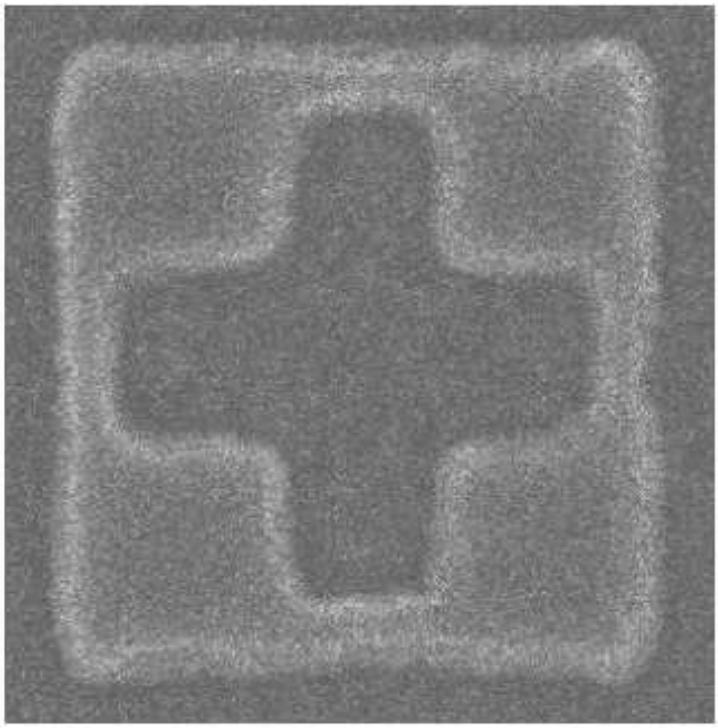

Figure 6.19: The optimum dose, 0.141, for the Swiss cross with reduced metal. The base dose was $500\mu\text{Ascm}^{-1}$.

cannot be developed, it is the HSQ that the EBL's electrons interfered with, changing the solubility of the HSQ. The PMMA is, under correct implementation of the EBL, untouched. The following question naturally arises: why is the PMMA necessary? If it is added, never touched or interfered with, only to be removed, is it not possible to skip a step and only use the HSQ? Here, however, we have a problem that is the exact opposite of the gold; the HSQ is too adhesive. Spin-coating HSQ directly onto the metal would simply ruin the sample, as removing the HSQ would not leave the metal intact. The addition of using PMMA allows us to sidestep this issue, as the HSQ is removed alongside the PMMA. To develop the HSQ, the sample is placed in solvent MF 26-A for 1 minute, followed by DI water for a further minute.

The PMMA layer is, naturally, still present. While we want to keep the PMMA that is under the unexposed HSQ, we must remove the PMMA that is now exposed to the air due to the HSQ removal. Once this is complete, the sample is ready to be placed in the argon miller. Figure 6.20 elucidates this principle.

Once again, the PMMA acts as a mask so that the desired gold is not milled away. The freely exposed metal is bombarded with argon ions, removing the metal. It is important to note here that for many trial runs, a thin metallic layer was deliberately left un-milled, so as to provide an easily conductive surface when the sample is later placed again in

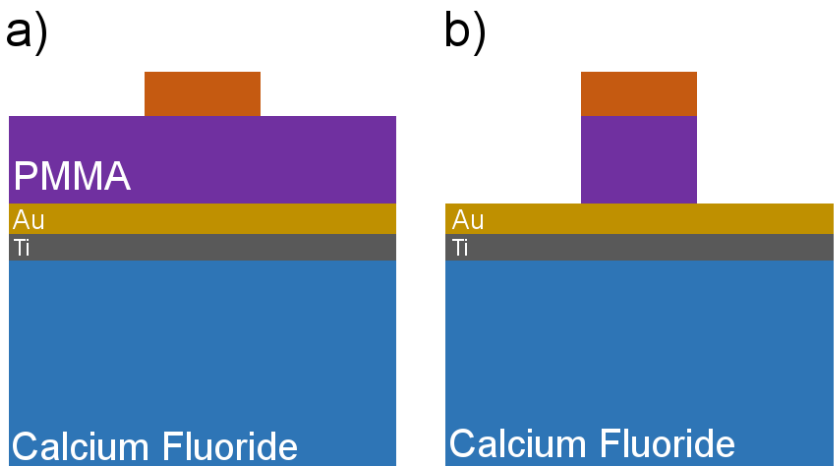

Figure 6.20: As both the unexposed HSQ and the PMMA underneath this region must be removed, there are two steps to the development process. a) Firstly, the unexposed HSQ is removed with MF 26-A and DI water. b) The underlying PMMA is then removed in an alternate fashion to the previous metamaterial cases as it has not been exposed to the EBL beam. It is removed through placing the sample in an O_2 plasma asher.

the EBL to record images with the scanning electron microscope. It is possible to use another method, whereby conducting tape joins the substrate to the EBL stage, but the method of reduced argon milling is simplest. This process is necessary due to the fact that CaF_2 is a natural insulator. For the EBL to successfully have a functioning beam of electrons, there must be some conduction on the receiving end of the beam. We illustrate the state of the sample at the end of this milling in Figure 6.21.

Afterwards, the remaining PMMA is removed as before by placing the sample in acetone for 24 hours, followed by an ultrasonic wash of acetone for 30 seconds and a further ultrasonic wash in IPA for 30 seconds. The sample is then dried with N_2.

6.3.4 Box Shapes

Alongside these crosses, I experimented with another shape that, according to simulations, should yield promising transmission results. This shape, a box shape, is depicted in Figure 6.22. It should not be surprising that there exist other structures that effectively give the same results as the crosses. The crosses are essentially a symmetric piece of metal on top of a substrate, and hence this box shape works in the same way; composed of a square, it is also polarization independent.

There is no need to thoroughly document how this box shape was made; the structural properties meant that it was fabricated in the same way as the crosses. The only parameter that needs to be changed is the dose of the EBL; yet again a dose test must be undertaken to find this value.

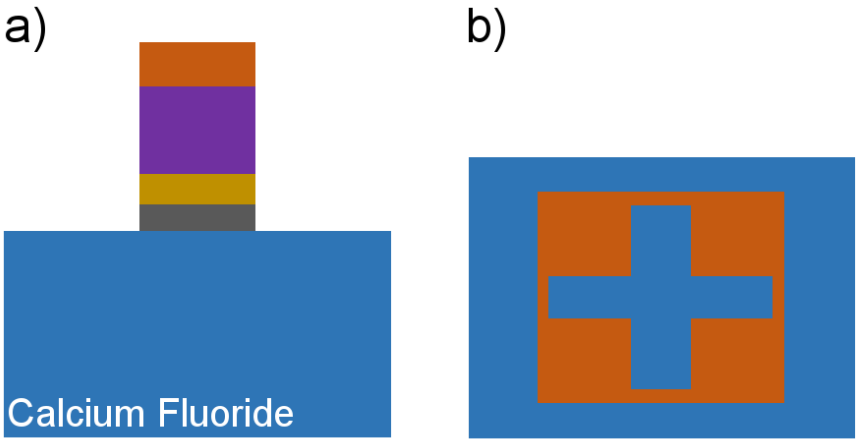

Figure 6.21: a) The state of the sample after the metal has been milled. The remaining stack of resists on the metals is simply removed with acetone. b) The bird's eye perspective helps show the cross-shapes that have now been formed.

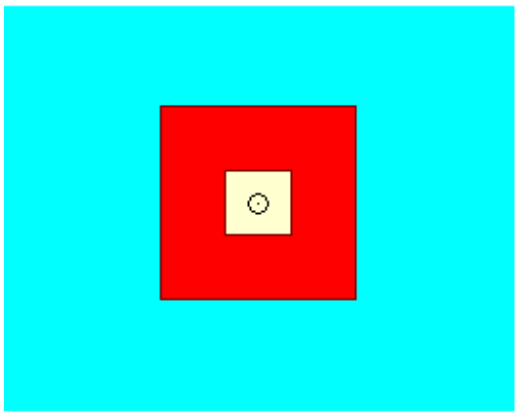

Figure 6.22: The origins of the box-shape. The width of the gold is 600nm, while the width of the air-gap is 200nm. The periodicity is 1.62μm.

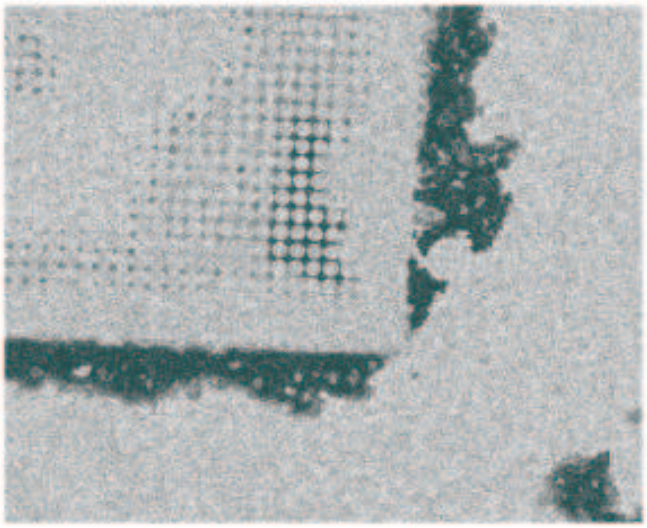

Figure 6.23: An example of HSQ that has started to degrade but has been spin-coated and exposed in the EBL. The layer is clearly not uniform, and causes scattered clumps of low-quality resist.

6.4 Scanning Electron Microscope Results - Incorrect Procedures

In this section a large quantity of images taken with the scanning electron microscope (SEM) are given whereby some parameters were not set correctly or a false assumption was made, to further cast light on the myriad of factors that govern the fabrication procedure.

6.4.1 The instability of HSQ

HSQ is rather more sensitive than PMMA. While a PMMA solution can be stored after opening for months at a time and still give the appropriate uniform thickness after spin-coating, there is no such guarantee with HSQ; the short shelf-life and the need to be stored in a fridge can often cause an unwanted low-quality coating to be applied to the sample, as can be seen in Figure 6.23. A work-around is to take small samples frequently from a large sample continuously stored in a freezer, an unfortunately more expensive process.

A further complication caused by adding HSQ to the PMMA is the stark difference in power that is required from the EBL to produce an array of well-defined features. The base power with which the EBL is utilized in conjunction with PMMA A2 is $180\mu\text{Ascm}^{-1}$. Upon adding the HSQ, it was recommended to increase this base dose to $330\mu\text{Ascm}^{-1}$.

However, as is shown in Figure 6.24, the dose tests that we apply shows significant sensitivity with each incremental increase in dose. With previous structures, the perfect dose sits between the poorly defined dose and the overly defined dose, with a wide range of adequate doses separating them. The reader may benefit by thinking of a bell curve, with the dose along the x-axis and the quality of the structure along the y-axis. While the perfect dose is the peak of the curve, that is not to say that all the other doses will not give good results. Indeed, any structure designed with a dose that is within a significant margin of this peak will engender a strong response when utilized for optical experiments. What we effectively see when using this HSQ in conjunction with a low base dose, however, is again a bell curve but with an extraordinarily low full-width half maximum (equivalently a high quality factor). This phenomenon was overcome by increasing the base dose further to $500\mu\text{Ascm}^{-1}$. The range of adequate doses was therefore increased to a more acceptable level.

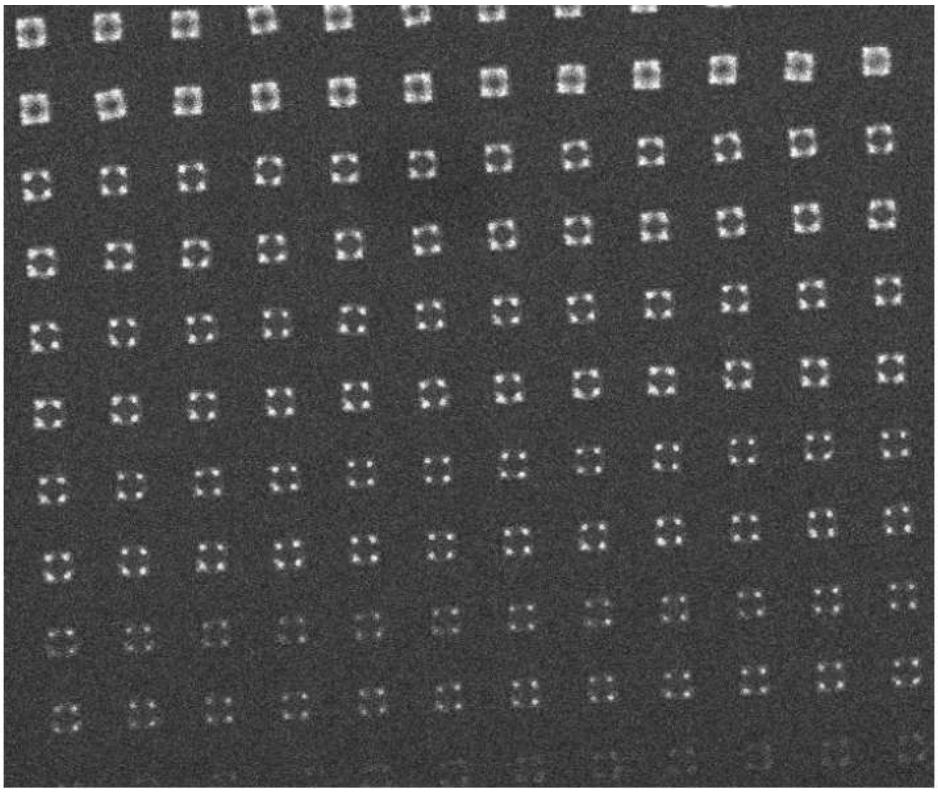

Figure 6.24: An example of how sensitive the dose tests can be if the base dose is not correctly set. With PMMA the usual base dose is $180\mu\text{Ascm}^{-1}$. The sample in this Figure is based on an HSQ resist of base dose $330\mu\text{Ascm}^{-1}$. However, this is still too small, evidenced by how quickly the shapes go from poorly defined to overly defined.

6.4.2 The Switching of PMMA

As noted earlier, there was a point in time at which the London Centre for Nanotechnology stopped stocking the PMMA that I was regularly using. At this point I was focused purely on fabricating the Swiss crosses with reduced metal. Due to the fact that the PMMA that I require lies underneath the HSQ, and hence does not get directly exposed, my assumption was that the PMMA played no great role in the EBL optimisation, i.e. that the PMMA is a sacrificial layer placed under the HSQ so as to avoid the HSQ adhering to the gold and could subsequently be removed, having caused no alterations in the actual patterning process.

This was not the case. Once the A2 PMMA was switched to A4, giving a thicker layer, it became immediately obvious that the optimum dose that I had before was no longer applicable. A new dose test had to be administered to find the new optimum dose, as this thicker underlayer had changed. Most likely this is due to the scattering of the electrons at the PMMA/HSQ interface.

6.4.3 Complex Polygons

Initially while trying to create the Swiss cross with reduced metal, as seen in Section 6.3, I created a single shape for the EBL to expose, i.e. the orange area that is depicted in Figure 6.21. This is not quite as simple as it first sounds due to the rudimentary nature of the EBL CAD. Instead, a two components must be input into the CAD - specifically a square and a cross - and a subsequent Boolean operation applied. These Boolean logical operators are present within the interface of the CAD, and Figure 6.25 is intended to help the reader understand how the EBL's logical operators function. From this Figure, it is clear that it is the XOR command, which stands for 'exclusively OR', that produces the desired structure.

This option - creating a polygon from a Boolean operation - caused a number of problems, as we shall now see. It was later suggested to me by a more experienced user to never use these operations; no matter how complex the structure to be designed, it should always essentially be composed of circles and rectangles. The software glitches that follow can thus be quite simply side-stepped.

The SUB operation (standing for subtract) also appears that it should create the Swiss cross with reduced metal. My first attempts at creating this structure focused on applying this Boolean operation. However, it quickly became apparent that this would not be a fruitful endeavour. Figure 6.26 gives a couple of examples where this operation was applied. Regardless of the dose, the resulting structure has no features. One possible reason for this is that the way the EBL attempted to subtract one logical operator

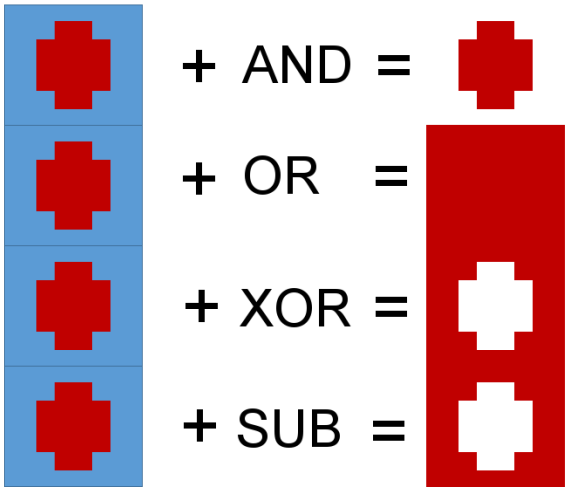

Figure 6.25: Four of the logical operators provided by the EBL CAD. Assuming that the blue square is element 1 and the red cross element 2, logical operators can be applied to these elements. As an OR function produces a positive result when even both structures are present, it will be the XOR (exclusively OR) function that shall interest us more in this section.

from the other; perhaps it attempted to subtract the smaller structure from the larger, confusing its internal logic process, or some other reason entirely. It is clear that more fruitful results will be found elsewhere.

Figure 6.27 documents a phenomenon that occurred while using the XOR operation. We see well-defined features for the cross, but it is apparent that a large portion of the crosses, while having been exposed, have not properly developed; the middle of the cross is still present. The panel on the left is the same structure but multiplied by a scale factor of 2. Another case was observed on more than one occasion while creating these structures: as seen in Figure 6.28, there were times when whole segments of an array simply were not fabricated, always in the centre of the array.

An effect similar to this was produced on another sample, where an array with uniform doses was fabricated. However, rather than producing an array of identical crosses, there is a clear variance of dose across the sample. This is demonstrated in Figure 6.29.

Results were immediately improved upon switching from a Boolean-designed cross to a cross made from a selection of rectangles. The dichotomy between these two regimes is strongly demonstrated in Figure 6.30. The left panel of this Figure shows a portion of a dose test from the newly conceived rectangle collection, whereas the right panel shows the Boolean operation. Both of these arrays were created on the same sample on the same day. The rectangle collection clearly provides a more stable, better defined meta-atom.

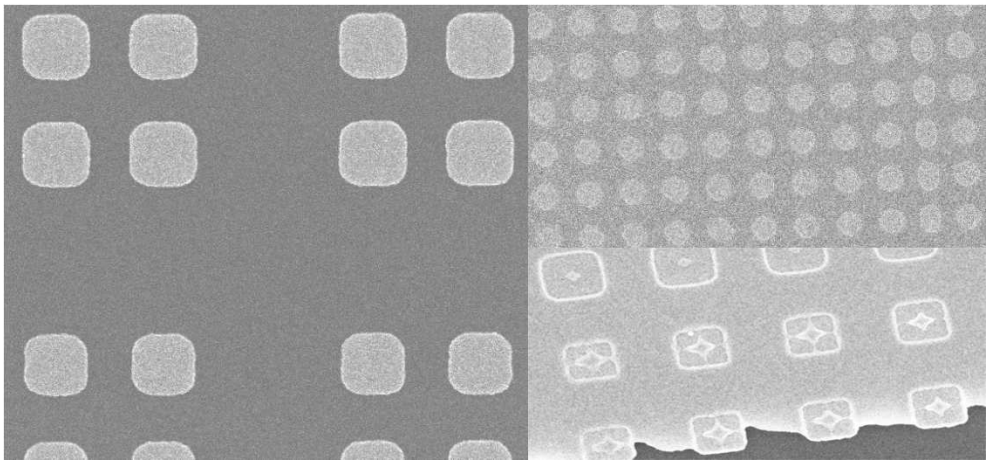

Figure 6.26: 3 separate examples of the SUB Boolean operation are given. It is clear that at best we get an incredibly poor representation of a cross shape. Rather than trying to further battle through the complications that the SUB operation creates, I thought the XOR Boolean operation would lead to better results.

6.4.4 Two-Tone Colouring

After viewing many different versions of the Swiss cross with reduced metal, I noticed a common pattern pertaining to many of my samples. While this phenomenon is quite glaring when looking for it, it is easily overlooked if the focus is on the shape and quality of the fabricated structures. This phenomenon is the colouring of the crosses, as shown in Figure 6.31. There seems to be two types of crosses in terms of the colouring; one is clearly brighter than the other. What causes this? The electrons flowing from the EBL beam are hitting the sample and traveling through the metal, effectively 'activating' the meta-atoms. The most plausible explanation is that the darker meta-atoms are not being activated, i.e. the metal of which they are comprised does not have a current flowing through it. A possible reason for this could be residual resists amongst some of the crosses, insulating them from electron flow, possibly combined with the heights of the crosses - a factor that we naturally cannot see due to the bird's eye view. It is very telling about the EBL that this problem went away as soon as the Boolean operations, which we saw above, were discontinued. The combination of errors so far is strong evidence that when using these Boolean operations, the crosses are no longer identical, but particular software glitches imbue many of the array elements with their own characteristic properties.

6.4.5 Rectangular Composites

While it may seem initially trivial, there are multiple ways to construct this cross from rectangles. As we shall quickly discover, this problem does not stay trivial when it is

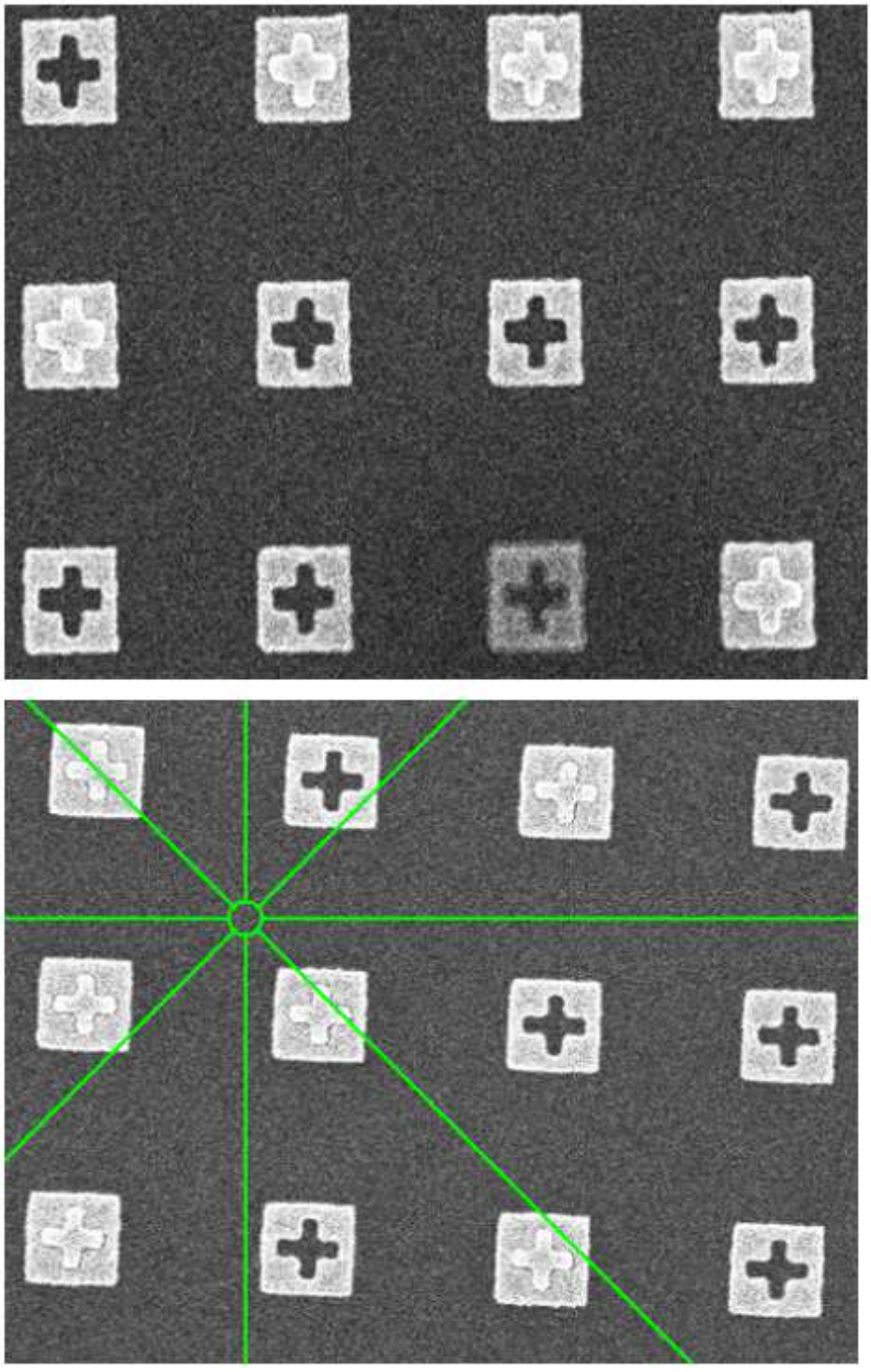

Figure 6.27: Two panels are shown. The size of the structure in the bottom panel is twice that of the structure in the top panel. In both cases we see a significant portion of the array is ruined; even though the features are sharply defined, the middles of many crosses have not been emptied.

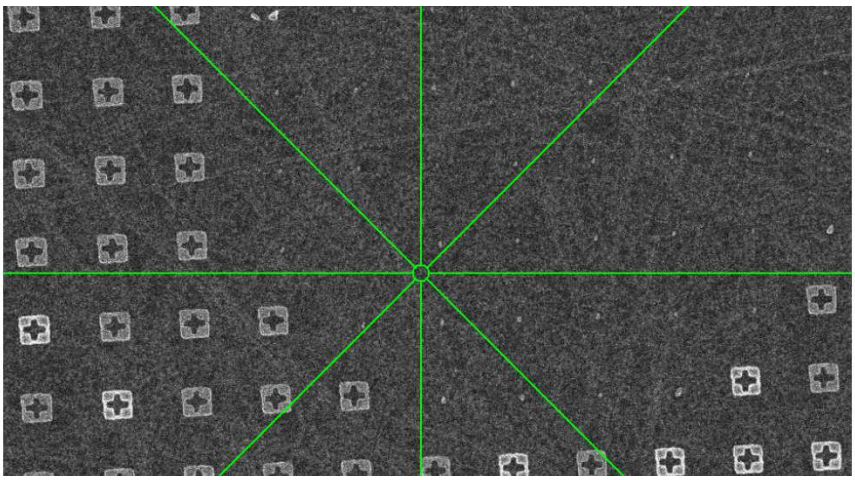

Figure 6.28: A phenomenon is observed whereby the centre of the array has not been correctly exposed.

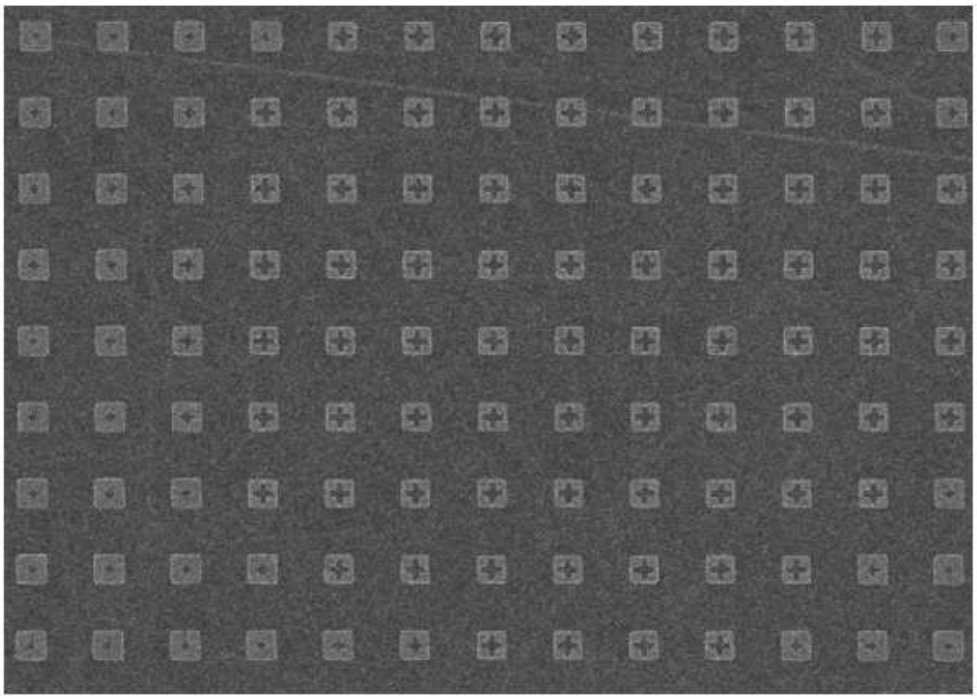

Figure 6.29: There is a clear variance of dose across this array of crosses, despite each member of the array being given the identical dose value.

viewed from the point of view of the electron beam of the EBL. There are two ways that I experimented with designing these structures, as shown in the upper portion of Figure 6.32. Initial fabrication efforts were geared towards the construction on the upper-left side of the Figure, i.e. a cross composed of four squares and four much smaller rectangles that joined these squares.

It did not take long before the second construction was invoked, due to the results

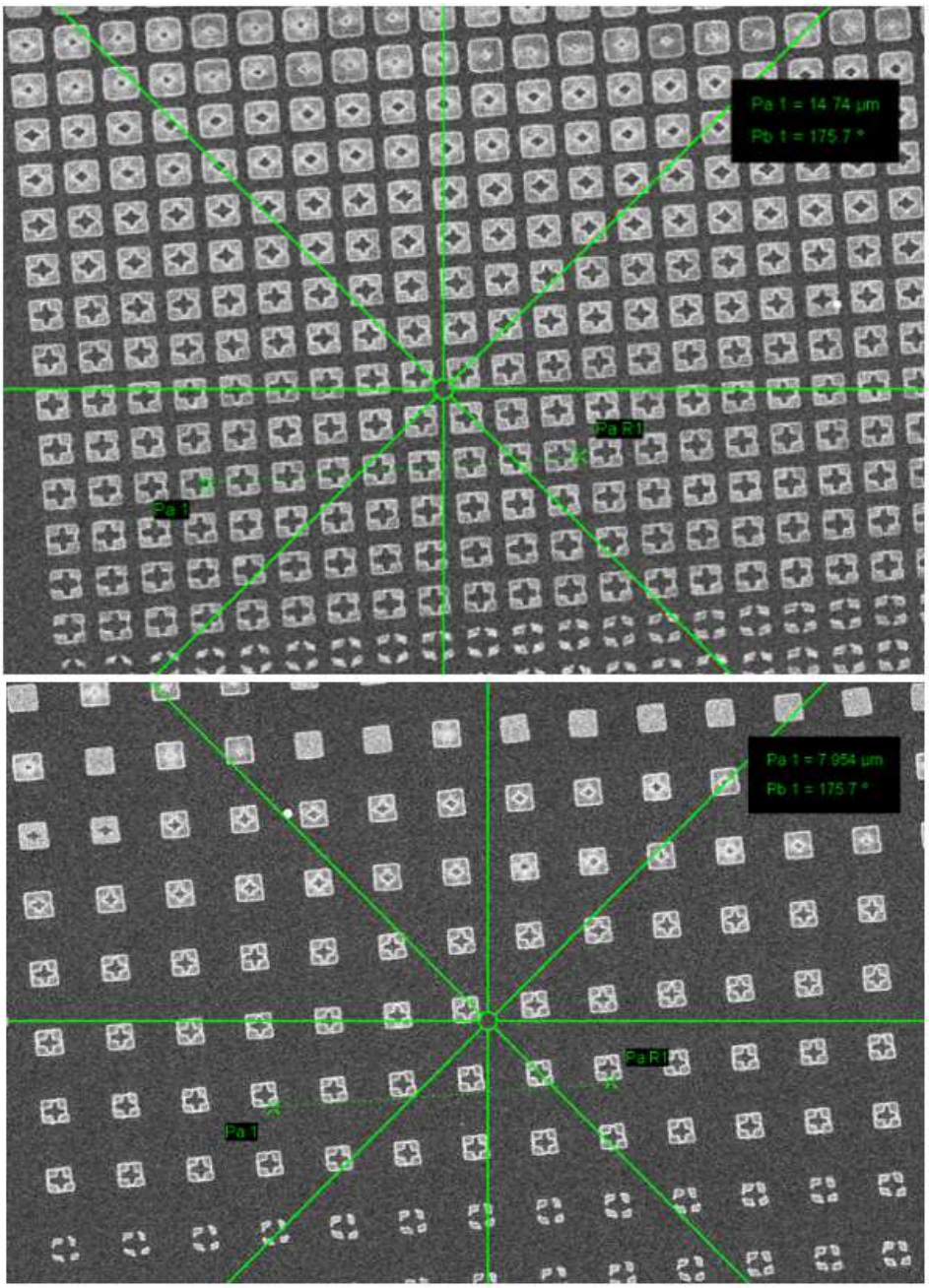

Figure 6.30: Two arrays fabricated on the same sample are shown. Top - the Swiss cross with reduced metal made by stitching rectangles together. Bottom - the Swiss cross made *via* a Boolean operation. The former clearly wins in a competition of quality.

attained through SEM imaging, as shown in Figure 6.33. This Figure contains a small segment of crosses created for a dose test. A comparison of the cross in the bottom-left corner with the cross in the top-right corner will help the reader to see the variance in dose across this image. There are two main problems with every cross in this picture. Firstly, there is an evident kink on the right-hand side of every cross, perturbing what

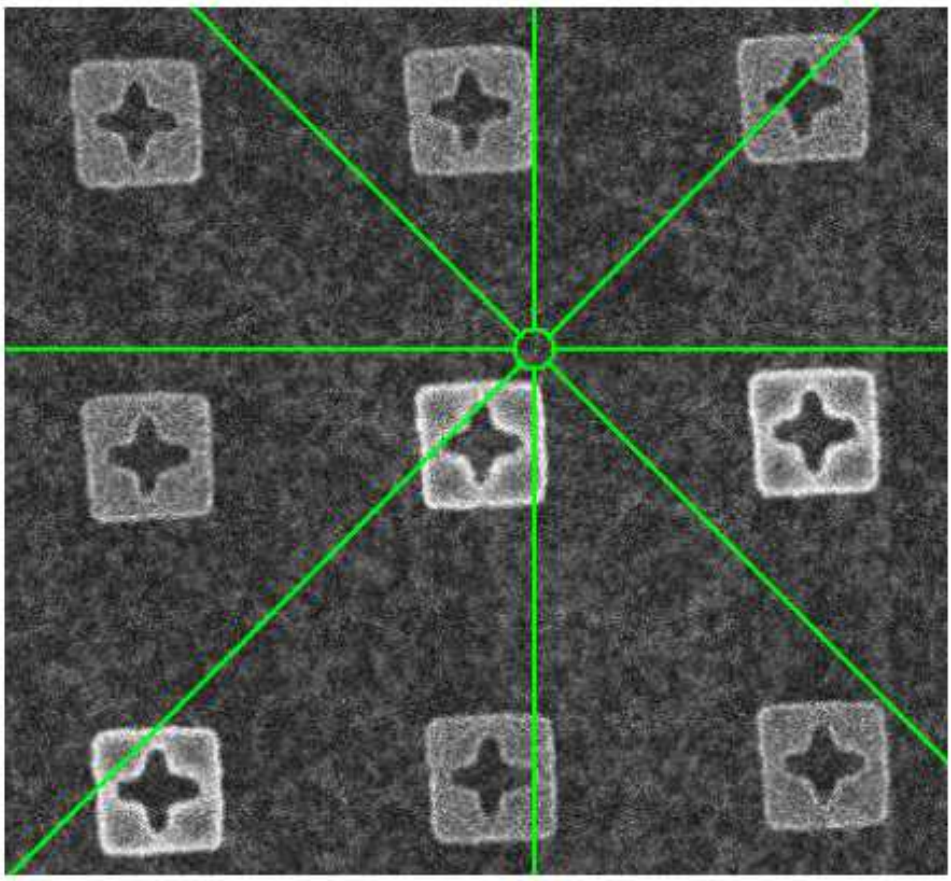

Figure 6.31: A phenomenon whereby some meta-atoms have a different colouring. The most plausible explanation is that some of these elements are not conducting as they should.

should be the square boundary that encloses the cross pattern. The second problem is the shape of the cross itself. While with a dose test we expect to see poor drawings of our shapes though either over exposure or under exposure, we see that the crosses are not *symmetrically ruined*. Observing the lower-end of the dose spectrum, it is clear that the left arm is longer and fatter than the right arm. However, even when we shift our attention to the upper-right corner of the image, the size of the top and bottom arms in comparison to the other two reveals an unequal distribution of beam exposure. It therefore seemed a sensible idea to opt for the second design in Figure 6.32.

This very same issue can be extended to the box-shapes mentioned briefly in Section 6.3.4. The inclusion of the small hole in the middle of the square turns an easily-fabricated square into a more subtly complex pattern. As before, while there exist multiple ways of constructing this box from individual rectangles, we will see that the first structure leads to unsuccessful SEM images, prompting a much-improved second attempt at patterning the structure. Alongside the different cross designs, Figure 6.32 also shows the

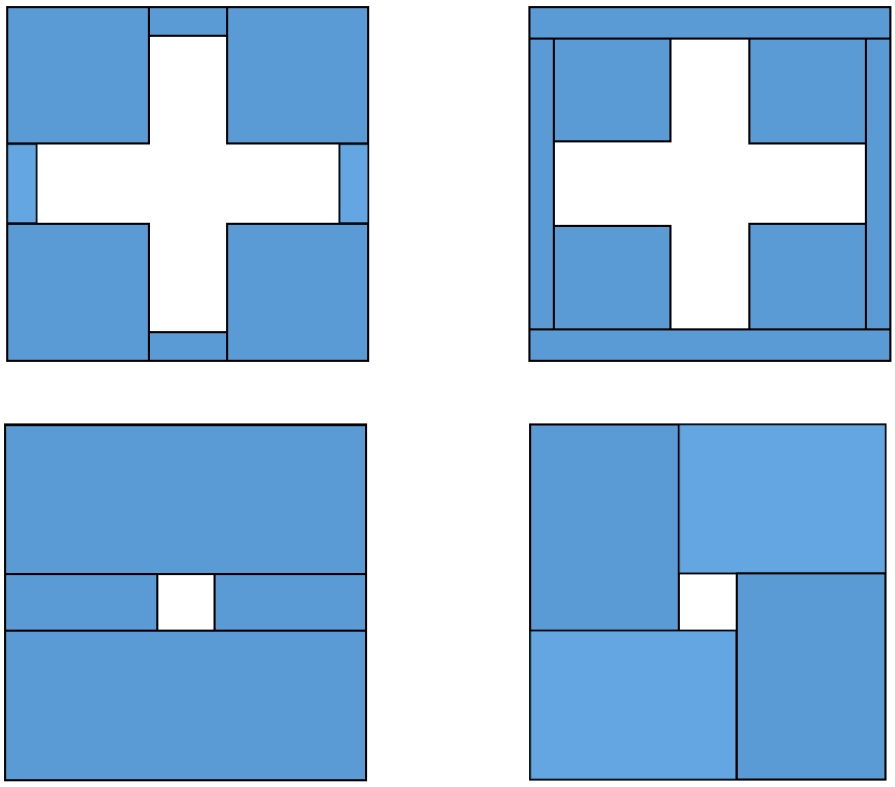

Figure 6.32: Two different ways of drawing the surroundings of crosses (top) and boxes (bottom). In both cases, the left-hand structures, when implemented in the EBL CAD, were not drawn sufficiently, as shall be seen in Figures 6.33 and 6.34. The right-hand side, in both cases, were the most acceptable, leading to well-drawn structures.

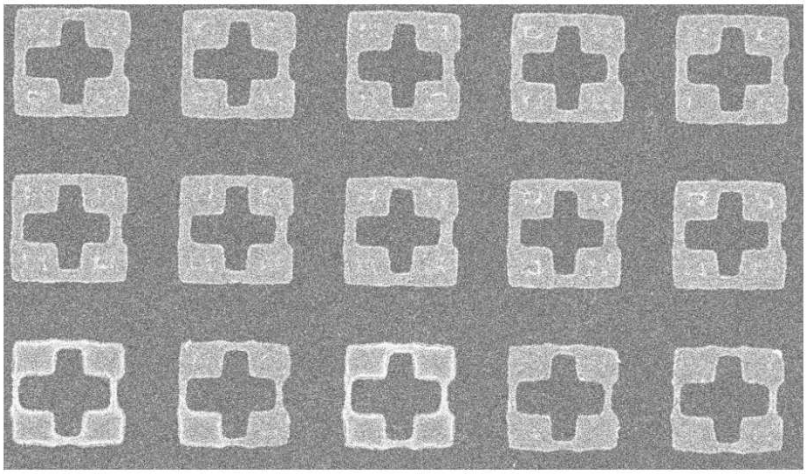

Figure 6.33: A portion of a dose test for the construction of a Swiss cross with reduced metal designed from the upper-left panel of Figure 6.32.

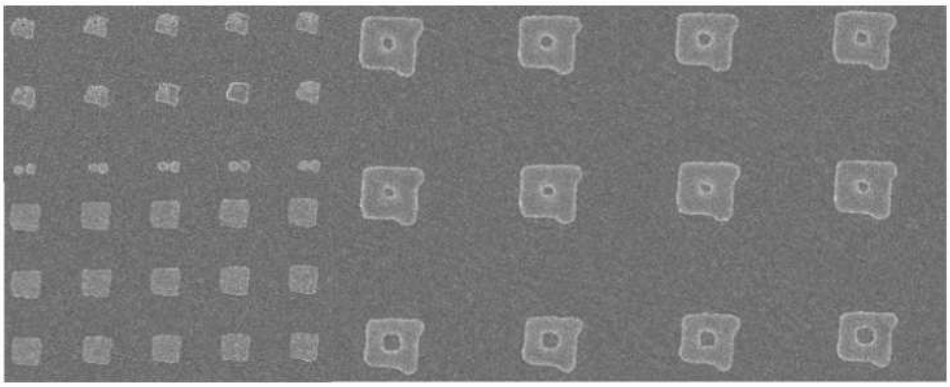

Figure 6.34: Upper-left - A segment containing the small doses of a dose test for a box-shape of size half that in Figure 6.22. The EBL clearly struggles to fabricate the desired structure designed according to the lower-left part of Figure 6.32. Lower-left - The same dose test as before, focused on the higher-end of the dose spectrum. We see that the dose is immaterial with respect to creating quality structures through the implemented design. Right - A dose test for a box-shape twice the size of the boxes in the left-hand panels. While we see the central hole start to emerge, the actual quality of the structures is no better than the previous dose test.

two box-shape designs implemented, with the first, unsuccessful attempt on the lower-left. With hindsight it is easy to see why the design on the right-hand side is naturally superior; composed of four equally-portioned segments, the EBL is not forced, as it is for the first design, to switch between patterning large and small segments that have been stitched together. In Figure 6.34 we plot portions of two dose tests, one fabricated for a structural size of half that in Figure 6.22, seen in the two left-hand panels, and one dose test consisting of a box-shape twice that structural size. On the upper-left picture, corresponding to the lower-end of the dose spectrum, we see that there is no discernible hole in the middle of the box. Furthermore, the boxes are not even square-shaped. The structures do indeed become more square-shaped as the dose is increased, as evidenced in the lower-left panel. However, there is still no requisite hole. The structures do not much improve once the structure is scaled by a factor of 2; the right-hand panel shows oddly-shaped polygons with a rather poor round hole.

6.4.6 Step Sizes in the EBL

This section is intended to highlight for the reader how the EBL 'sees' the patterns that we implement in the CAD. Within the software of the EBL a mesh is applied to the structure, which the user can alter from the default value to vary the density of the mesh. The default step size, which is 10nm, is perfect for creating structures such as the U-shapes we saw previously; each individual component of the array has, due to its

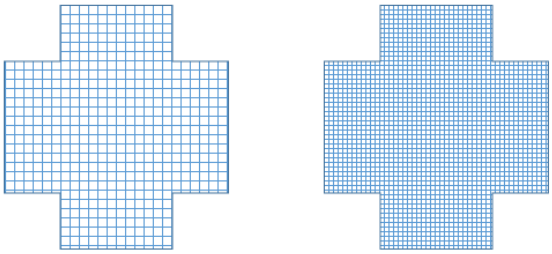

Figure 6.35: Two identical crosses are given that have different meshes applied to them *via* the EBL software. A denser mesh can often lead to refined structures when dealing with scales in the order of tens of nanometres. However, this increase in mesh points comes at the cost of computational time.

micron-sized width and length, has enough mesh points for the EBL to make an accurate representation of this structure in the resist. When dealing with smaller structures, it can however be beneficial to decrease the step size to a value such as 2nm for an attempt at increasing the definition of the structure. It is important to note that, for example, decreasing the step-size from 10nm to 2nm in both directions causes the fabrication time to increase by a factor of 25. Figure 6.35 showcases two identical crosses with different meshes applied in each case.

6.5 Scanning Electron Microscope Results - Success Stories

Thankfully the fabrication story told here is not all replete with doom and gloom; in this section we provide the reader with images of high-quality structures that were fabricated regarding the structures that we have hitherto discussed. The results that we later discuss are all based on the structures documented in this section.

6.5.1 U-shapes

There are, regrettably, no images of the high-quality U-shapes that generated the successful transmission and reflection measurements performed later on. These patterns were created at the very beginning of my fabrication adventures and it did not occur to me to take some SEM images of the final result. While I do have images of the dose tests and therefore the optimum dose of the structures, these images were taken before the titanium and gold were deposited on top of the U-shaped gaps. The contrast of these images, while useable on a computer monitor, do not lend themselves to printed versions, as I discovered after they were printed in my transfer thesis.

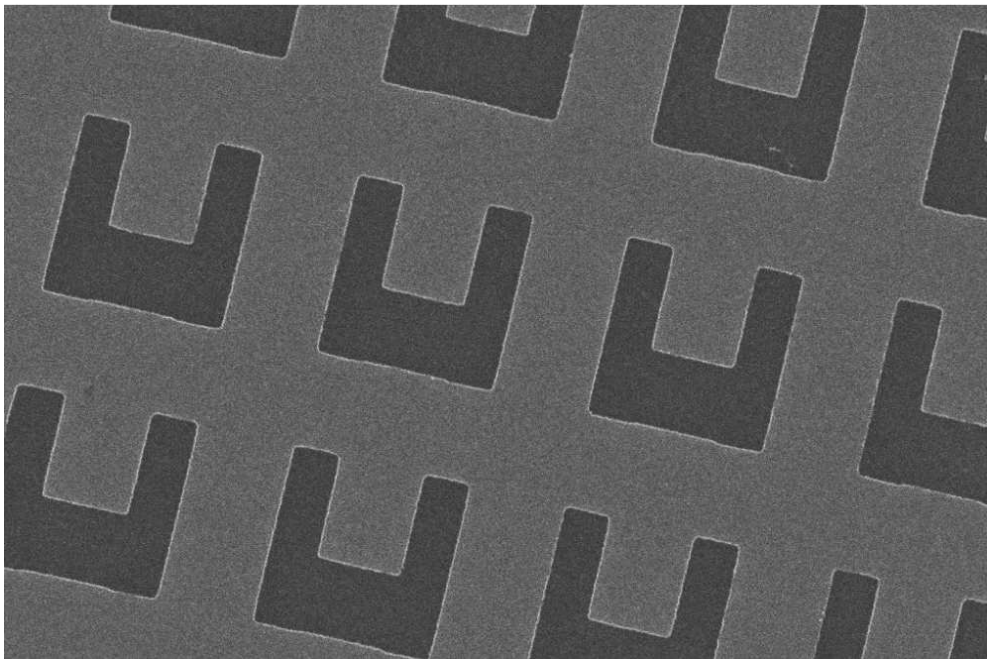

Figure 6.36: High quality U-shaped trenches, fabricated *via* the HSQ method in Section 6.3. The dose used here is 1.41.

I therefore offer the reader images of the inverse-structure, where U-shaped valleys are fabricated instead of the hills. The reason for their fabrication is due to the trials and tribulations experienced while attempting to manufacture a working Swiss cross with reduced metal. The sheer number of factors that I started to discover were thwarting my fabrication process caused me to return to the drawing board and fabricate a much simpler pattern that had already been designed, to see if these same factors were present. This U-shape implementation indeed helped me to discover that the HSQ base dose that I was utilizing in the EBL was far too low, while simultaneously forcing me to realise that a Boolean operation is not needed to fabricate the polygon. These high quality helpful U-shapes can be seen in Figure 6.36.

6.5.2 Swiss Crosses Deconstructed

There are three cross-shapes that are pertinent to this section. As we shall discover a little later on while analysing in detail the origins of these structures, these experiments began with a cross-shaped trench taken from [7]. My fabrication of this asymmetric cross is depicted in Figure 6.37. This cross-shape is clearly of high-quality. There are well-defined edges without any roundness to the structure. The dose used for this structure (after a base dose of $180\mu\text{Ascm}^{-1}$.) was 0.62. As mentioned previously, this structure lends itself to the creation of two symmetric crosses, each composed of one of the original's

arms. Both of these crosses are depicted alongside the original cross in Figure 6.37. The perfect dose for the thinner and thicker cross was also 0.62.

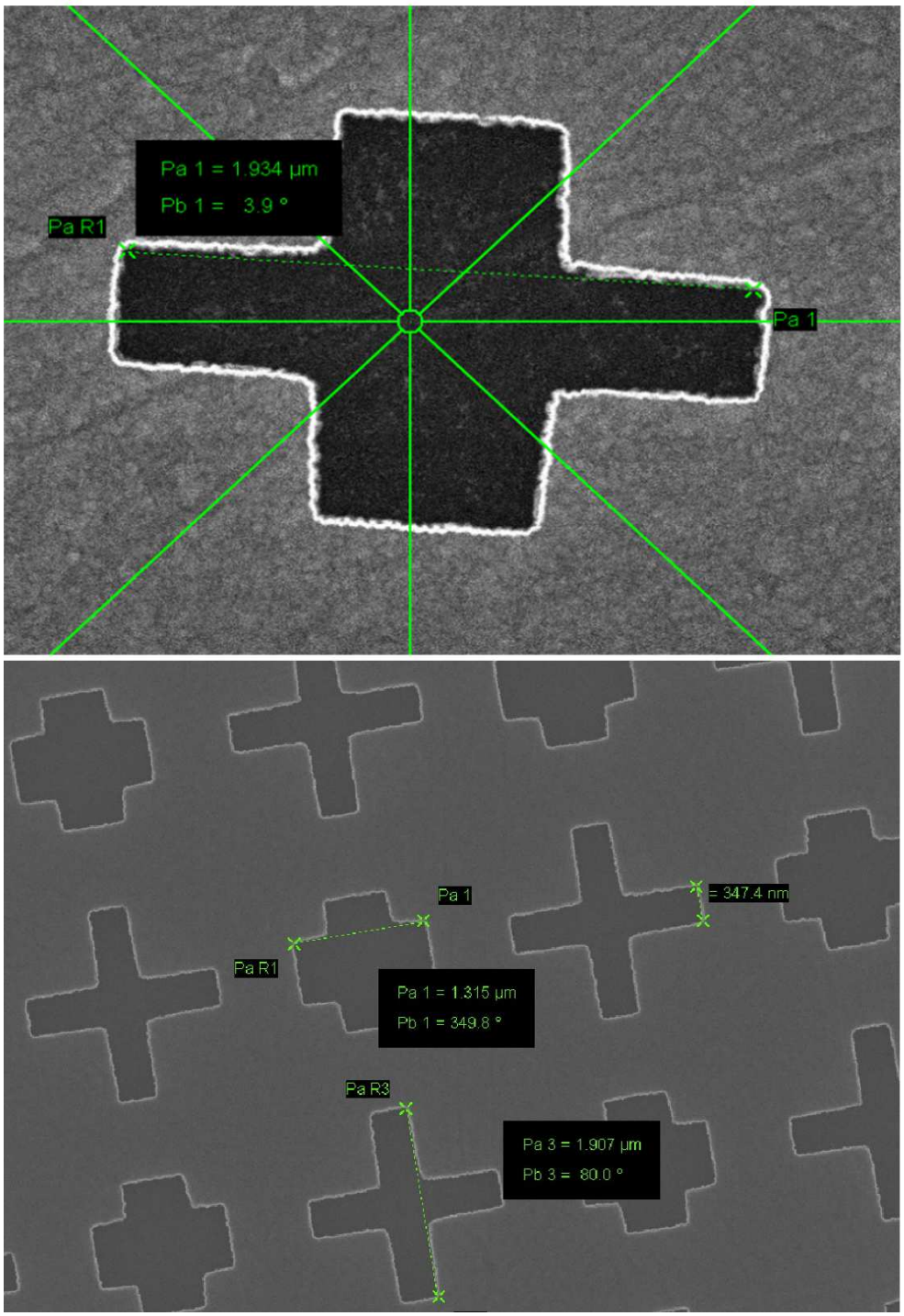

Figure 6.37: The three crosses fabricated *via* the method described in Section 6.2. Top - the original cross fabricated with dose 0.62. Bottom - The thin and thick armed crosses alternating in an array. The dose used is the same as the original cross, 0.62.

6.5.3 Swiss Crossed with Reduced Metal

Two cross structures of high quality are pictured here, one corresponding to the structure created with PMMA A2, with the other cross being produced after it became necessary to switch PMMA solutions to PMMA A4. The dose corresponding to the PMMA A2 cross is 0.141 and is displayed on the left-hand side of Figure 6.38. The cross corresponding to the implementation of A4, shown on the right-hand side of the same Figure, was fabricated with a dose of 0.277, all other parameters being equal. This is a stark shift and highlights the underlying sensitivity of every step in the fabrication procedure.

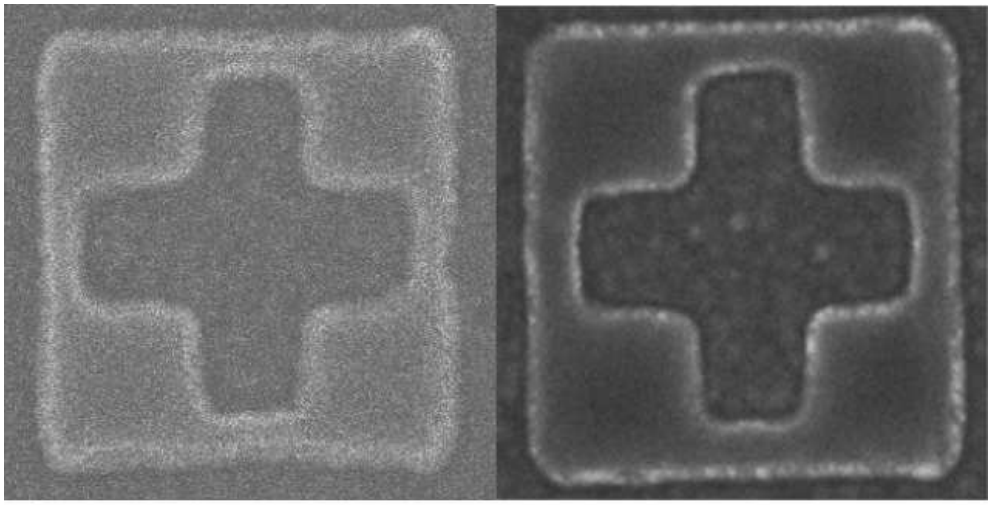

Figure 6.38: Left - A cross made through the use of PMMA A2, fabricated with a dose of 0.141. Right - A cross consisting of the same dimensions but fabricated with PMMA A4. This change in PMMA required a new dose; shown here is a dose of 0.277.

6.5.4 Box-Shapes

The boxes described above were, after correcting for the Boolean operations and tessellation of rectangles, produced with a dose of 0.145, as shown in Figure 6.39.

6.6 Fourier Transform Infrared Spectroscopy

The results presented here all stem from the high quality samples we saw in the previous section. The initial focus, when fabricating U-shapes, was to ensure that both the transmission and reflection measurements matched up to the literature, as a sure sign that every step I was doing in the cleanroom was correct. The focus subsequently started to shift to only transmission, as we shall shortly see. Before delving into the measurements obtained, it is important to explain the inner workings of Fourier Transform Infrared

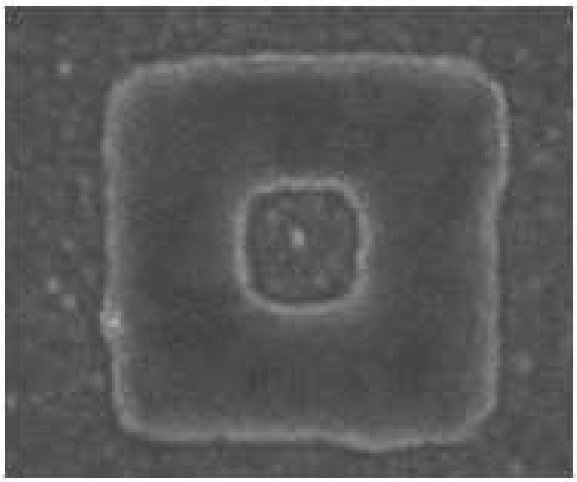

Figure 6.39: A box-shape fabricated *via* the HSQ method outlined in Section 6.3. The utilized dose was 0.145.

Spectroscopy, commonly abbreviated as FTIR. FTIR measurements have a wide-range of applications, including pharmaceutical and life science sectors, building materials and soil analysis [15].

As stated, the entire purpose of my FTIR measurements was to measure reflection and transmission coefficients for a wide range of wavelengths. To do this, the FTIR does not utilize one wavelength of light at a time. Rather, a polychromatic light source impinges upon a beam splitter, in our case composed of KBr. Once the beam is split, there are two possible pathways for the light to follow: one path leads to a stationary mirror, while the other leads to a crucial moveable mirror. Once the two beams of light recombine, they interfere with one another, producing an interference pattern that is recorded and analysed by the FTIR. The moveable mirror is not moved manually, but rather by the FTIR itself. The adjustment of this mirror enables the FTIR to alter the frequencies of light that are emitted through interference. The interference pattern that is produced measures two variables: the intensity of the light recorded as a function of the mirror position. After hundreds of such measurements, a Fourier transform is applied to the data, which gives rise to the optical spectra in terms of wavenumber. An understanding of these principles is aided by the diagram in Figure 6.40, which briefly highlights the pertinent physics and gives an example of an interferogram, which is the name given to the interference patterns produced by the FTIR.

When using the FTIR, it is first necessary to cool the detector down using liquid nitrogen. There is a small hole at the back of the machine that can be opened, where liquid nitrogen should be poured to ensure the detector operates as quickly, sensitively and accurately as possible. Once this action is performed, the FTIR can operate for a few

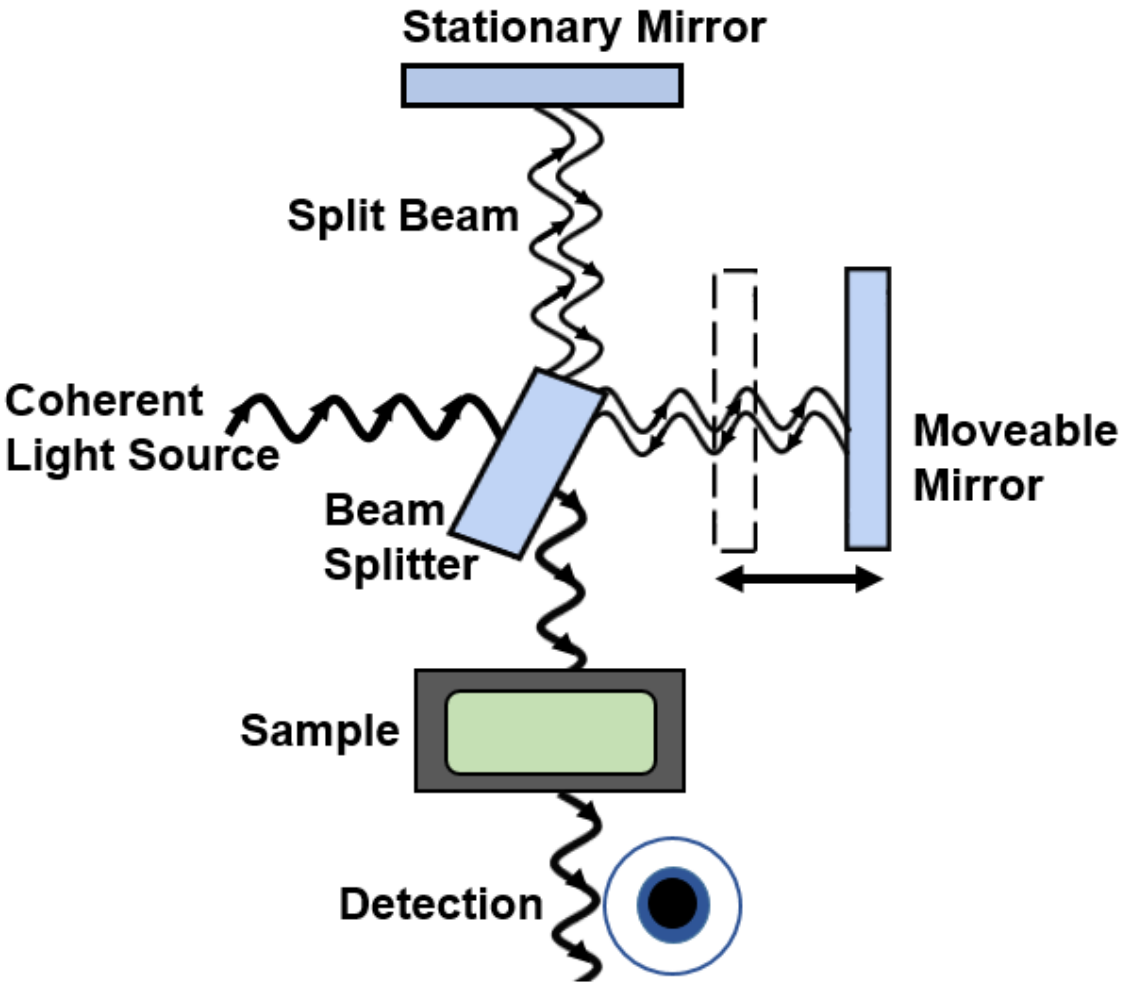

Figure 6.40: The setup of the FTIR. A polychromatic light source impinges upon a beam splitter, allowing two possible pathways for the light to follow: one path leads to a stationary mirror, while the other leads to a crucial moveable mirror. Once the two beams of light recombine, they interfere with one another, producing an interference pattern that is recorded and analysed by the FTIR. The moveable mirror is not moved manually, but rather by the FTIR itself. The adjustment of this mirror enables the FTIR to alter the frequencies of light that are emitted through interference. The interference pattern that is produced measures two variables: the intensity of the light recorded as a function of the mirror position. After hundreds of such measurements, a Fourier transform is applied to the data, which gives rise to the optical spectra in terms of wavenumber.

hours before the detector begins to lose its calibration. Thankfully, the FTIR itself will tell the user when this happens with its own built in detector, so there is no guesswork needed on the user's end.

Ensuring that the sample receives the maximum amount of light is of paramount importance before the measurements begin. To do this, the FTIR enables the user to minutely alter the stage height and outputs the intensity of the received signal. Infrared (IR) filters are then inserted into their place and the appropriate scanning settings are chosen. Typically, for the FTIR measurements depicted here, 800 scans were run per measurement with a resolution of 8cm^{-1}. The wavevector range varied depending upon the sample to be measured, but the total range across all samples was from $>10000\text{cm}^{-1}$ to 500cm^{-1}, corresponding to a wavelength range of $<1\mu$m to 20μm.

Before the main reflection/transmission measurements can be obtained, it is necessary to perform a background measurement. The FTIR then compares its interferogram with the background measure to give the true reflection/transmission coefficients. For a reflection background measurement, it is necessary to focus the incoming polychromatic source onto a region that is highly reflective and that does not contain any special features. When performing these measurements for the cross trenches, for example, this was simply done, as most of the sample is covered in gold, with the exception of the cross-shaped holes of the array. For a sample such as the U-shapes, obtaining a highly reflective non-metamaterial surface requires a little more engineering on the user's part. Throughout the fabrication process it is important to keep in mind the final goal, i.e. FTIR measurements. Hence, for samples such as the U-shapes, throughout the fabrication procedure sections on the sample were masked so that the gold was not removed at the end of the process with the acetone wash.

As one would expect, a highly transmissive section of the sample is required to perform a background measurement before transmission optical coefficients are calculated. While this naturally would be difficult to ensure with certain substrates, CaF_2 is highly transmissive in the wavelength regions of interest. It must also be noted that any change to the FTIR's parameters requires an immediate re-doing of the background measurement.

We are now in a position to analyse, in detail, the optical spectra gathered from the FTIR measurements.

6.6.1 U-shapes

We have hitherto seen the fabrication procedure and best dose utilized to create the U-shapes. Also shown were the measured transmission and reflection spectra taken from [4] for this structure. As these U-shapes were analysed in order to learn how to fabricate metamaterials, a true test of this is matching my reflection and transmission measure-

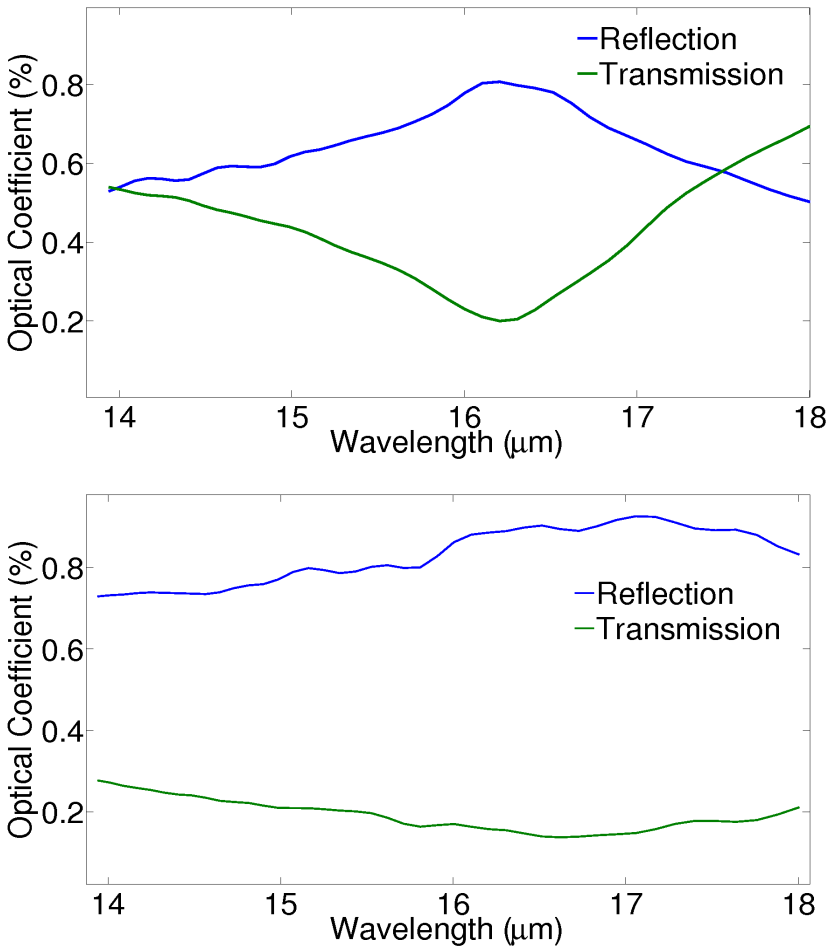

Figure 6.41: The optical coefficients (reflection and transmission) measured by the FTIR for two different polarizations. Top - 0° and bottom - 90° polarizations. Blue and green correspond to reflection and transmission results, respectively.

ments to those of the simulations.

Figure 6.41 shows the FTIR measurements collected by measuring the fabricated U-shapes that we saw in the fabrication section. For 0° polarization, we see a peak corresponding to an incident wavelength of 16μm, whereas 90° polarization has almost uniform reflection and transmission, i.e. there are no main peaks to speak of.

Figure 6.42, on the other hand, shows the transmission, reflection and absorption coefficient obtained through simulating the periodic U-shapes with DiffractMOD. We have seen how these structures are simulated in detail in Chapter 3. Here it is important to note the peak corresponding to a wavelength of approximately 16.4μm for an incident polarization of 0°, whereas there is a weak bump for a polarization of 90° for a wavelength of approximately 15.3μm.

As Figures 6.41 and 6.42 demonstrate, the fabricated structures do indeed strongly

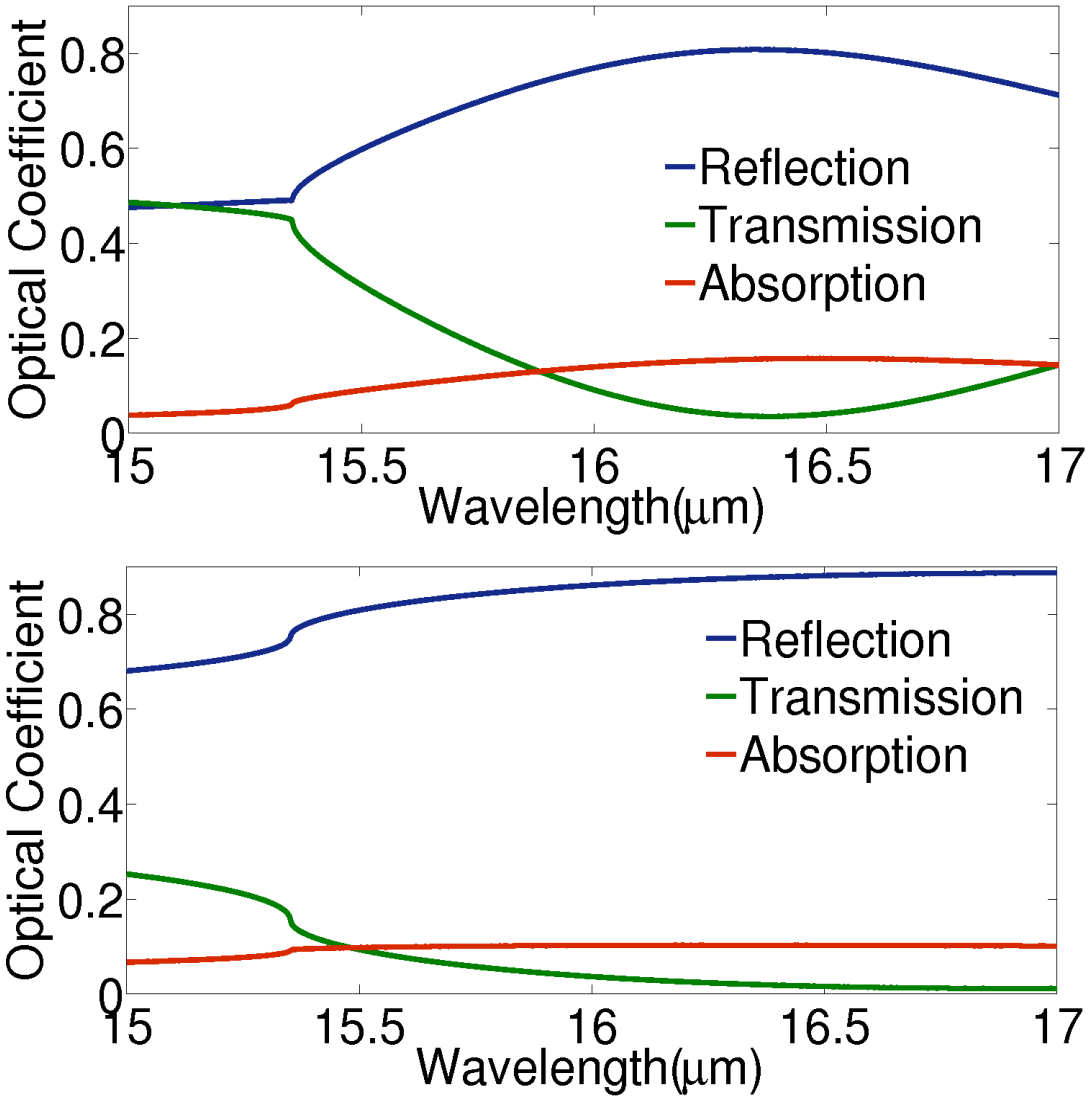

Figure 6.42: The optical coefficients (reflection and transmission) simulated by DiffractMOD for two different polarizations. Top - 0° and bottom - 90° polarizations. Blue, green and red correspond to reflection, transmission and absorption curves, respectively.

match the simulated predictions. The slight shift in wavelength space between the simulated and measured resonance for an incident polarization of 0° is easily explained: slight deviations in the structural sizes, a common theme for experimentalists, would shift the location at which the metamaterials would resonate. In simulations, the structural dimensions are perfect, whereas it is not unreasonable to observe a structural difference of 10% when these structures are made in a lab. From the above figures, therefore, the fabrication process can be regarded as a success.

6.6.2 Swiss Cross Trenches

This section documents a deconstruction of the cross seen in Figure 6.11, hereafter referred to as the original cross, into two symmetric crosses.

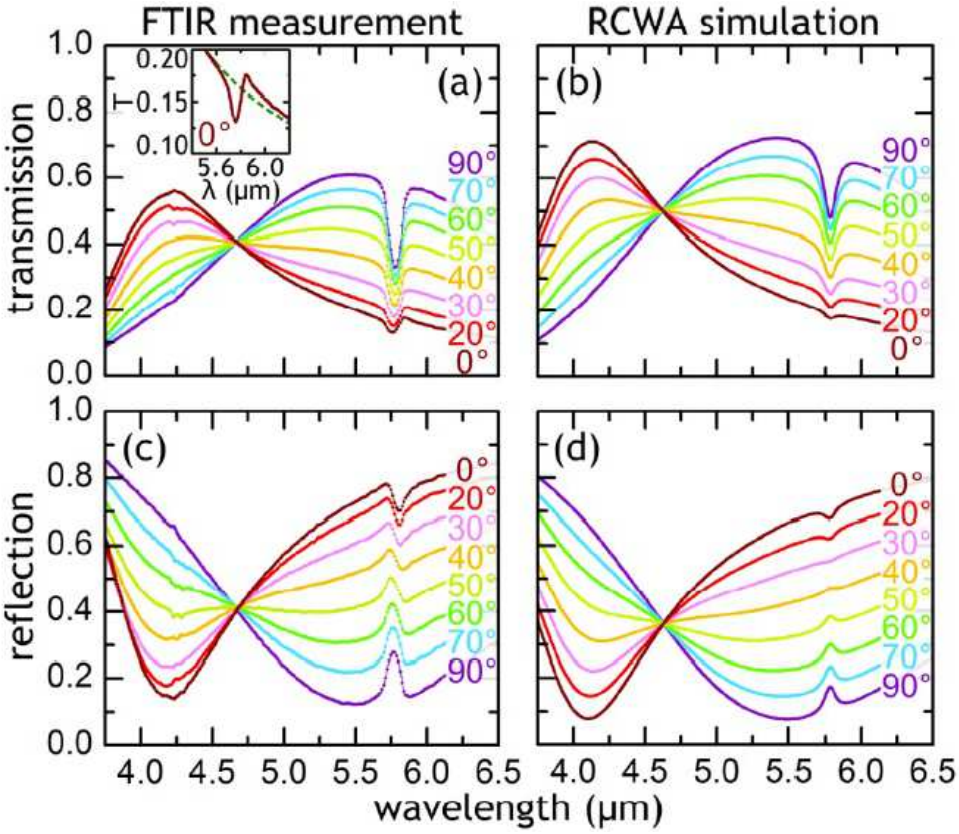

Figure 6.43: Simulated and measured reflection and transmission spectra of the original cross from [7]. The differently coloured lines refer to different values for incident polarization. This polarization-dependence is a by-product of utilising an asymmetric cross. The small resonance at 5.75μm is due to a carbonyl bind within the final layer of PMMA, a feature which we do not expect to see with our modifications. This phenomenon is an example of absorption-induced transparency [14].

Because the transmission spectrum calculations require a background measurement

focused on a highly transmittive part of the sample, during the fabrication process of these crosses, an area of CaF_2 was left untouched by the gold and titanium precisely for this purpose. This is easily achieved by simply covering a section of the sample with sticky tape, a commonly used implement in the cleanroom.

In the same manner as the U-shapes, above, for every following FTIR measurement, 800 scans were run with a resolution of 8cm^{-1} for a wavevector range of 10000cm^{-1} to 500cm^{-1} - corresponding to a wavelength scan of 1μm to 20μm.

The transmission and reflection spectra obtained by Osley et al. are shown in Figure 6.43. Within every panel of this Figure, a small resonance for an incident wavelength of 5.75μm can be seen. In the cited paper, Osley et al. were studying the effects of this resonance, produced by a carbonyl bond in the PMMA that was spin-coated on top of the sample *after all other fabrication steps*. Hence, in that paper, there is an extra layer of PMMA on top of the deposited metal. As the studying of this bond is not crucial for my work, no final layer of PMMA was added to my cross-shaped trenches. Two main consequences of this decision are expected: firstly, of course, the small carbonyl bond interaction should not appear in our FTIR results. Secondly, we expect the main resonances to shift in wavelength-space.

The FTIR measurements of the original crosses that I produced are shown in Figure 6.44 for P- and S-polarisations (0° and 90° respectively). The polarisation-dependence of these asymmetric crosses can be seen. While the resonances occur in almost the same frequency-space - a blue-shift due to lack of PMMA accounts for this - the resonances produced by my structures are not as strong. This can be attributed to not milling the structure for a long-enough time period, meaning that a thin layer of metal still lingers on top of the calcium fluoride substrate.

After the cross was deconstructed into the two symmetric crosses, as depicted in Figure 6.45, the reflection and transmission spectra were measured for arrays composed of each cross individually, i.e. I acquired the FTIR spectra for an array of thin-armed crosses and separate FTIR results for thick-armed crosses, as seen in Figure 6.46. Also in these figures are the spectra for arrays where both crosses are in one unit cell. We expect the combined unit cell to experience two resonances, one corresponding to the excitation of the thick-armed cross, and one corresponding to the excitation of the thin-armed cross. The results collected in Figure 6.46 agree reasonably well with this theory: the resonance at approximately 4.25μm corresponds to the electromagnetic excitation of the thin-armed cross. After this peak, the activity of the thick-armed cross takes over with a much broader resonance.

We have seen that a polarisation-dependent cross can be deconstructed into two polarisation-independent crosses exhibiting *both* resonances of the polarisation-dependent

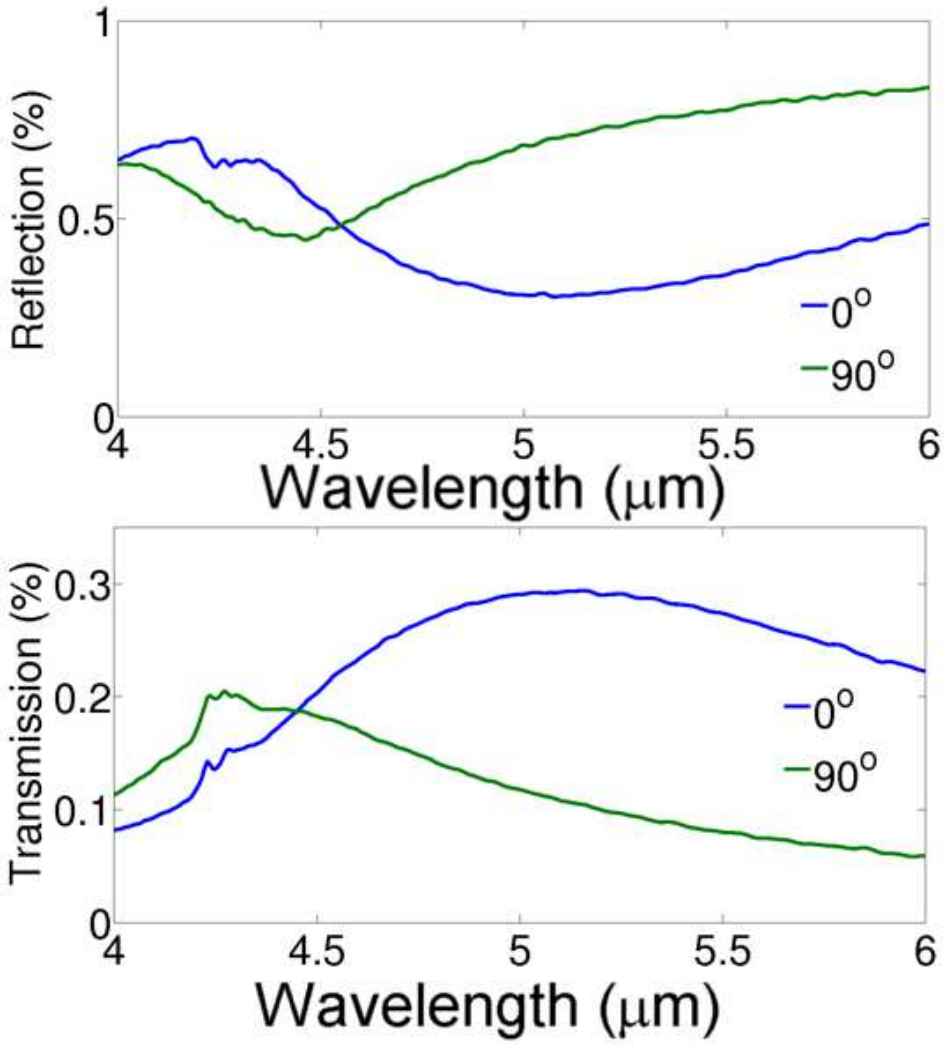

Figure 6.44: Top - the measured reflection spectra of my fabricated crosses for 0° (blue) and 90° (green). The same frequency dependence as Figure 6.43 can be seen. Bottom - the measured transmission spectra of the Swiss crosses for 0° (blue) and 90° (green).

cross.

6.6.3 Swiss Cross - Reduced Metal

The above cell created from the hybridisation of two Swiss crosses has rather broad resonances. With regards to transmission filters, where we only want to block a small range of frequencies, the transmission must naturally be large outside the frequency of interest, with a sharp, narrow drop occurring for the frequency we wish to block. Moving towards this goal, a Swiss cross structure similar to the design of above was utilised, but with the amount of gold covering the surface being reduced, as we saw previously in Figure 6.17. To understand why this structure is so intriguing, we plot here

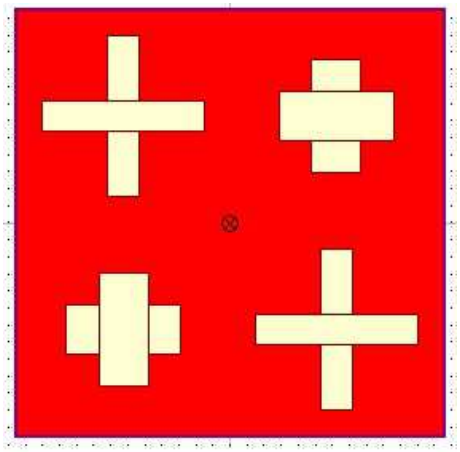

Figure 6.45: The deconstructed cross. A meta-atom with thick and thin arms is repeated periodically with a horizontal and vertical distance of 2.5μm between each cross.

the simulated transmission and reflection spectra obtained through implementation of RSoft's DiffractMOD, displayed in Figure 6.47.

The structural dimensions of this new meta-atom were arrived at by using DiffractMOD's MOST optimizer. By defining a function of multiple parameters, MOST attempts to minimise the defined function. Here, it was told to minimise the transmission at 2.7μm as a function of the height and width of the cross alongside the thickness of the deposited gold. Further details of how this optimizer is implemented and how exactly the software obtains the optical coefficients were given in Section 3.

This reduced quantity of gold enables the plasmonic features of the meta-atom to still apply, as the crucial cross-structure is present. It is outside of the resonance frequency, however, that this structure has a true advantage over a structure with more metal: the reflection will be greatly reduced due to the lack of reflective metal present.

Following successful fabrication of this metamaterial, as seen in Figure 6.38, the FTIR measurements were collected. Thanks must be given here to Professor Shuang Zhang at Birmingham University for allowing me to use his FTIR machine once UCL's became inoperable due to a laser fault. The Birmingham FTIR is superior to UCL's for two reasons: firstly, it was no longer necessary to run a recommended 800 scans per measurement for the FTIR to calculate the optical coefficients. Instead, only 32 runs were required for high-quality results, naturally saving plenty of time. Secondly, the range of wavelengths accessible to the FTIR was greater; while UCL's FTIR could not give any meaningful results for a wavelength below 2μm, the FTIR in Birmingham allowed wavelengths below 1μm to be measured. All other parameters were kept constant.

In Figure 6.48 the transmission coefficients are plotted for both 0° and 90° polarizations. Reflection measurements were not taken here, as the purpose is to manufacture

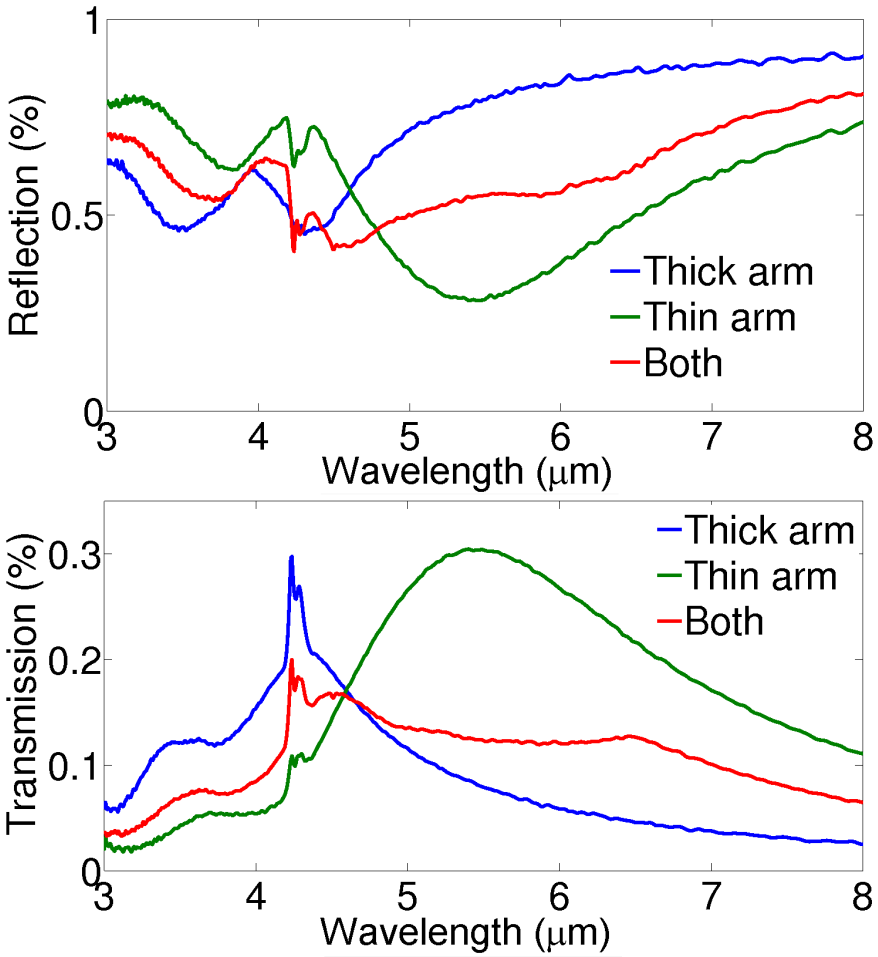

Figure 6.46: Top - the reflection spectra for the thick-armed cross (blue), thin-armed cross (green) and combined crosses as in Figure 6.45 (red). The resonances, particularly in regards to transmission, appear to agree with the theory that the cell should experience two resonances. Due to symmetry, the unit cell is now polarization-independent. Bottom - the transmission spectra for the same crosses. 0° polarization is used for all results in this Figure.

a transmission filter. How this light is blocked at the crucial wavelength, i.e. whether it is reflected or absorbed, is to us immaterial. We see in this Figure some interesting phenomena. It is immediately apparent that the metamaterial is strongly resistant to polarization change, but not immune; there is, outside of the main resonance, slightly reduced transmission for 90°-polarized light.

The main feature of interest, however, is the resonance itself. It is clear that there is reduced transmission at the point corresponding to maximum metamaterial excitation. The shift of wavelength from the simulated (shown in Figure 6.47) to the actual can be explained by considering the effects of slight alterations to the heights of the metal, as

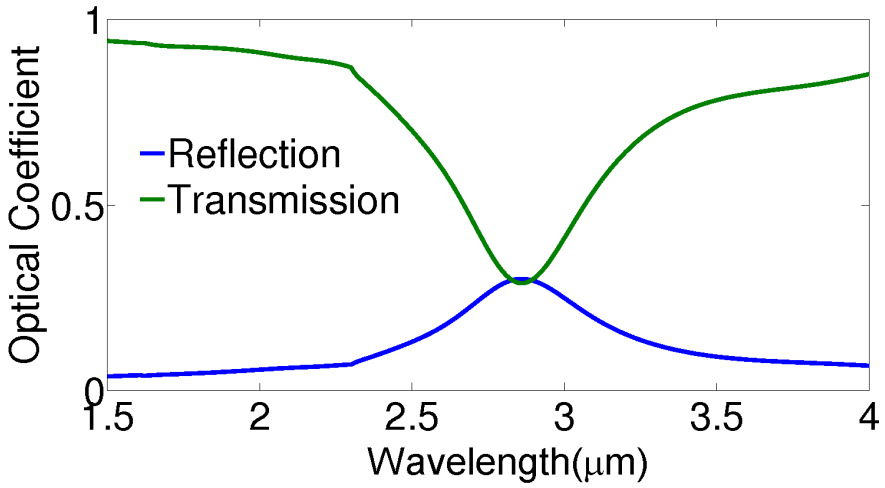

Figure 6.47: The reflection (blue) and transmission (green) spectra of the structure shown in Figure 6.17, calculated *via* RSoft's DiffractMOD.

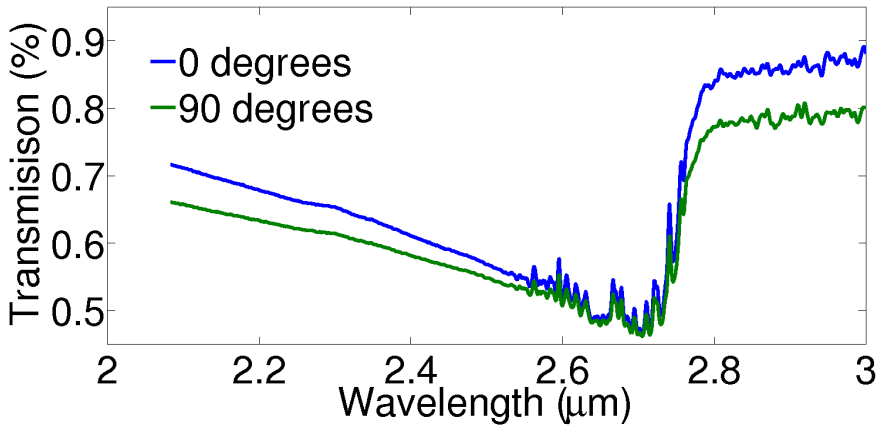

Figure 6.48: The transmission spectra of a fabricated array of crosses with reduced metal measured with the FTIR, shown in Figure 6.17. The incident polarization is 0° (blue) and 90° (green). There is clear activity at 2.7μm.

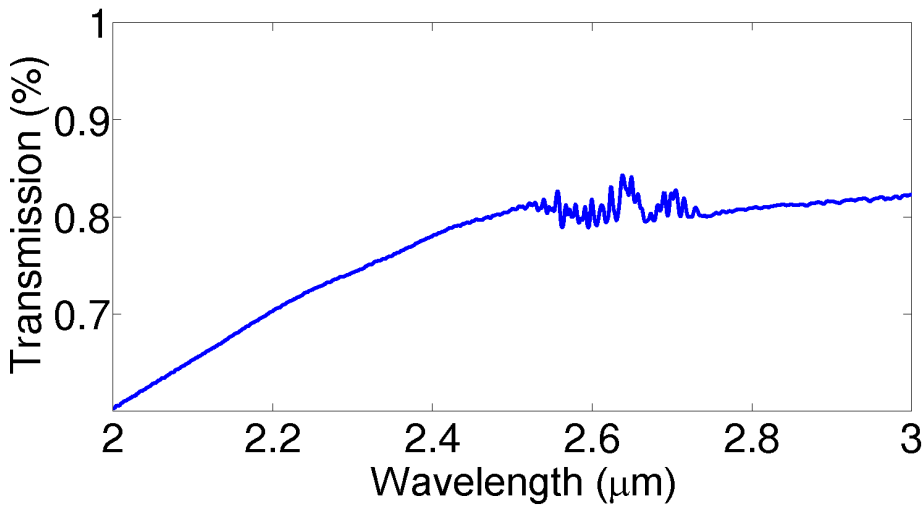

Figure 6.49: The transmission spectra of a fabricated array of box-shapes measured with the FTIR, shown in Figure 6.39. The incident polarization is 0°. While activity can be seen centered at 2.65μm, there is no clear resonance.

we discussed in Section 6.6.1. There are two main problems with the resonance, however. The first is that the 'exit' from the notch to the surrounding wavelengths is far too shallow on one side when compared with the other. If the steep jump to approximately 85% transmission at a wavelength of 2.8μm could be replicated on the other side of the resonance, the fabricated metamaterial would be much more satisfactory. Secondly, the resonance is not deep enough, i.e. not enough light is blocked at the resonance. Possible distortions from the 'perfect' cross to the real may be the cause of this.

6.6.4 Box-Shapes

The box-shapes fabricated in the same manner as the above crosses were shown previously in Figure 6.39. Both the simulated and obtained transmission spectra are depicted in Figure 6.49. While DiffractMOD predicts a sharp resonance for a wavelength of 2.7μm, we see no such activity in the fabricated patterns. There is a glimmer of activity in this region, and hence the metamaterial appears to be activated, but the match between the simulations and actuality cannot be considered a success.

6.7 Conclusion

This chapter began with a discussion about a U-shape metamaterial. The simplicity of the structure combined with its strong optical response made it a perfect metamaterial to first fabricate in the laboratory while becoming acquainted with the different equipment.

Each fabrication step for the manufacture of this structure was broken down. The FTIR measurements acquired from the best-manufactured cross were shown and compared to simulations obtained *via* RSoft's DiffractMOD and were successfully shown to agree with one another.

Cross-shape trenches were subsequently introduced for the purpose of making a multi-resonant meta-atom. An asymmetric cross-shape was decomposed into two symmetric cross-shapes and combined within one unit cell. Once again the procedure utilized to produce these metamaterials was delineated. The FTIR results shown that an expected double resonance does indeed occur when the two different cross-trenches are combined into one unit cell.

An important inclusion within this chapter was the documentation of different obstacles that presented themselves. This included, but was not limited to, two-tone colourings present upon SEM viewing; the construction of structures within the CAD; the role of PMMA and the instability of HSQ.

Finally, a cross-shaped trench with a reduced amount of metal surrounding the trench was presented. The notch-like qualities of a simulated version of this meta-atom were shown. Due to the inclusion of HSQ, the fabrication procedure is radically altered. All the subsequent changes necessary to produce this structure were documented along with the highest quality parameters. Alongside the simulated results of this metamaterial, the most successful FTIR results were also shown.

The FTIR measurements for both the U-shapes and cross-shapes were promising; while the fabricated notch filter does not display as profound a resonance as the simulations suggest, there is nevertheless a strong agreement between the two regimes. Given more time, this cross with reduced metal would be re-fabricated with more sensitivity, including a more rigorous dose test and altering the thickness of the metal film. This cross would then subsequently be placed in a meta-atom with another larger cross to deliberately ensure a double transmission resonance that we observed in the deconstruction of the original cross.

Bibliography

[1] S. Linden, C. Enkrich, M. Wegener, J. Zhou, T. Koschny, and C. M. Soukoulis, "Magnetic response of metamaterials at 100 terahertz", Science **306**, 1351 (2004).

[2] N. Katsarakis, Th. Koschny, M. Kafesaki, E. N. Economou, and C. M. Soukoulis, "Electric coupling to the magnetic resonance of split ring resonators", Appl. Phys. Lett. **84**, 2943 (2004).

[3] C. Enkrich, M. Wegener, S. Linden, S. Burger, L. Zschiedrich, F. Schmidt, J. F. Zhou, T. Koschny, and C. M. Soukoulis, "Magnetic metamaterials at telecommunication and visible frequencies", Phys. Rev. Lett **95**, 203901 (2005).

[4] S. Linden, C. Enkrich, G. Dolling, M. W. Klein, J. Zhou, T. Koschny, C. M. Soukoulis, S. Burger, F. Schmidt, and M. Wegener, "Photonic crystals: Magnetism at optical frequencies", IEEE Journal of Selected Topics in Quantum Electronics **12**, 1097-1105 (2006).

[5] V. A. Podolskiy, A. K. Sarychev, E. E. Narimanov, and V. M. Shalaev, "Resonant light interaction with plasmonic nanowire systems", J. Opt. A Pure Appl. Opt. **7**, S32 (2005).

[6] University of Washington, [Accessed 16th September 2018], Available from: https://ebeam.mff.uw.edu/ebeamweb

[7] E. J. Osley, C. G. Biris, P. G. Thompson, R. R. F. Jahromi, P. A. Warburton, and N. C. Panoiu, "Fano resonance resulting from a tunable interaction between molecular vibrational modes and a double continuum of a plasmonic metamolecule", Phys. Rev. Lett **110**, 087402 (2013).

[8] U. Fano, "Effects of Configuration Interaction on Intensities and Phase Shifts", Phys. Rev. **124**, (1866 Published 15 December 1961).

[9] S. Zhang, D. A. Genov, Y. Wang, M. Liu, and X. Zhang, "Plasmon-Induced Transparency in Metamaterials", Phys. Rev. Lett. **101**, 047401 (2008).

[10] B. Gallinet and O. J. F. Martin, "*Ab initio* theory of Fano resonances in plasmonic nanostructures and metamaterials", Phys. Rev. B **83**, 235427 (2011).

[11] B. Lukyanchuk, N. I. Zheludev, S. A. Maier, N. J. Halas, P. Nordlander, H. Giessen, and C. T. Chong, "The Fano resonance in plasmonic nanostructures and metamaterials", Nat. Mat. **9**, 707715 (2010).

[12] R. M. Roth, N. C. Panoiu, M. M. Adams, J. I. Dadap, and R. M. Osgood, "Polarization-tunable plasmon-enhanced extraordinary transmission through metallic films using asymmetric cruciform apertures", Opt. Lett. **32**, 3414-3416 (2007).

[13] P. G. Thompson, C. G. Biris, E. J. Osley, O. Gaathon, R. M. Osgood, N. C. Panoiu, and P. A. Warburton, "Polarization-induced tunability of localized surface plasmon resonances in arrays of sub-wavelength cruciform apertures", Opt. Exp. **19**, 25035-25047 (2011).

[14] A. Hutchison, D. M. OCarroll, T. Schwartz, C. Genet, and T. W. Ebbesen "Absorption-Induced Transparency", Angew. Chem. **123**, 2133-2137 (2011).

[15] Bruker, [Accessed September 16th 2018], Available from: www.brukerpmma

Chapter 7

Conclusions and Future Work

Due to their seeming ability to bend the laws of physics, metamaterials have experienced a busy flurry of activity since their inception. The benefits of patterning metals atop a substrate have lead to sci-fi dreams becoming a tangible possibility, with a plethora of applications in nanoprinting, invisibility cloaks, and earthquake protection. Currently the metamaterial community are making sure that no stone goes unturned; indeed, there seems no end of novel ideas being published that document potential new game-changing structures. As slight changes to a meta-atom's constitution appear to have rather strong consequences, it is of paramount importance to study the underlying theoretical framework that governs the laws of this field. Making use of the computational tools at our disposal, therefore, is an unavoidable necessity.

Ensuring that every metamaterial studied is theoretically sound is, however, often not enough. One of the cornerstones of this thesis has been to ensure that each meta-atom introduced to the reader has been designed in such a way so as to be experimentally verifiable. It is with this approach that tomorrow's technology will be created today; the abstractly theoretical structures, while rich with interesting physical phenomena, will, more often than not, stay confined to the pages of a journal. This principle is more easily stated than achieved, especially with regards to nonlinear physics.

Making sure that a nonlinear signal can be detected and measured from a fabricated meta-atom has therefore been one of the main aims of this thesis. The investigation and analysis of nonlinear signals arising from both centrosymmetric and non-centrosymmetric meta-atoms have been heavily undertaken in order to elucidate new insights. Firstly, a theoretical analysis of plasmonic and all-dielectric centrosymmetric meta-atoms documented how a common assumption regarding the treatment of the bulk media within dielectric metamaterials is unjustified. Secondly, an in-depth exploration of the nonlinear signal arising from an all-dielectric non-centrosymmetric meta-atom delineated how a nonlinear toroidal dipole can be engendered.

Another aspect of my work was to investigate and fabricate metamaterial notch filters in such a way that multiple notches can be incorporated within the design of one meta-atom. An analysis of multi-resonant metamaterials was undertaken and documented alongside the fabrication procedures of each metamaterial created in the London Centre for Nanotechnology. The optical results measured by Fourier Transform Infrared Spectroscopy were also shown to match the results of simulations. Additionally, the theoretical idea of combining a metamaterial notch filter with a Bragg grating was outlined, with computational results showing that by placing a metamaterial on top of the surface of a Bragg grating, many layers of a pure Bragg grating can be removed.

The following sections discuss the contributions of my work to both nonlinear and notch metamaterials and outline the future goals that this work can help achieve.

7.1 Contributions

With regards to the physics arising from nonlinear metamaterials, the achievements of this thesis can be split into two regimes: centrosymmetric and non-centrosymmetric. Regarding the centrosymmetric framework, it has been a common assumption throughout metamaterial literature that the contribution to the nonlinear signal arising from the bulk of an all-dielectric metamaterial is negligible, and can therefore be ignored in computational calculations. Furthermore, the bulk of plasmonic metamaterials is neglected for the same reason. These assumptions were, for the first time, rigorously addressed for a general centrosymmetric cruciform meta-atom of varying size.

Utilizing in-house code, the surface and bulk contributions of both a plasmonic and all-dielectric meta-atom were calculated and compared. Due to an empirical rule known as Miller's Rule, the validity of which is a controversial topic for centrosymmetric crystals, results were obtained for both with and without the inclusion of this rule.

The linear results of this cruciform structure were first analysed, the common recipe throughout this thesis due to the fact that the nonlinear results that are investigated all stem from the activity of the linear regime. The linear results show that the dielectric case is much more rich with activity than the plasmonic case; while only one simple resonance is observed for the gold cross, several resonances appear in the linear spectra of the silicon case. These resonances are shown, upon analysis of the multipole expansion, to belong to different multipole excitations.

The nonlinear results show several intriguing phenomena: firstly, the surface contributions of the plasmonic cruciform outweigh, by orders of magnitude, the contributions of the bulk to the nonlinear signal. Furthermore, it is the *smallest* plasmonic structure that generates the strongest nonlinear signal. Regarding the dielectric case, while the

surface contributions do, as in the plasmonic case, outweigh the bulk contributions, the surface and bulk signals are much more comparable in magnitude, and thus the bulk contribution cannot *a priori* be neglected. Additionally, although the smallest dielectric cross is responsible for the largest nonlinear signal, it is the largest dielectric cross that has the more impacting bulk activity.

The non-centrosymmetric nonlinear investigations do not revolve around testing a commonly-held assumption. Rather, it is the creation and analysis of new physics that is the primary goal. An all-dielectric meta-atom is introduced that is designed to be experimentally verifiable through size considerations and embedding it in a glass background. Instead of being composed of one structure, the meta-atom consists of four parallelepipeds placed close enough to one another such that their electromagnetic excitations can interact.

As in the centrosymmetric case, the linear results are analysed firstly to become acquainted with the underlying physics that is prevalent. Through analysis of the most important multipoles from the multipole expansion, it is found that a linear toroidal dipole is primarily responsible for the linear signal arising from this meta-atom. This toroidal dipole arises through the coupling of the four individual components of the meta-atom. The nonlinear results that are subsequently analysed are hence nonlinear signals produced by a linear toroidal dipole.

The calculated nonlinear signals document an interesting physical effect: the linear toroidal dipole is producing a nonlinear field that is itself toroidal in nature. Furthermore, plots that are produced to highlight the underlying current density distributions show that there are in fact two toroidal loops that are squeezed into the structure. It is the unequal balance in these two vectors that causes one loop to be more prevalent than the other.

An investigation was undertaken to create a multi-resonant meta-atom. Starting with an asymmetric cross that is therefore polarization-dependent, two symmetric crosses were generated from it; one symmetric cross arose from the smaller asymmetric arm, the other symmetric cross from the larger arm. The effects of periodicity were firstly investigated for a single meta-atom. The reason for this is knowing how far apart multiple meta-atoms can be placed so as to not interfere with one another. An example is given whereby two different meta-atoms that are placed too closely together are included in a metamaterial. The example shows that no clear resonance arises from this case. Putting the two symmetric crosses together within one structure, two distinct resonances were shown to be possible. The manufacture of this meta-atom is explored in detail, whereby the process of collecting the results through Fourier Transform Infrared Spectroscopy is elucidated. The measured results show that the simulations were indeed correct.

The discussion then moved on to developing a notch filter, i.e. a metamaterial transmission filter that blocks only a small number of wavelengths, transmitting all other wavelengths outside this range. The process of acquiring the structural parameters of this notch filter through utilising DiffractMOD's MOST optimizer is discussed, and the simulated transmission spectra are shown. The structure involves reducing the amount of metal that surrounds the metamaterial pattern, thus increasing the transmission of most wavelengths. The entire fabrication process of this metamaterial is again given. While the simulations and measured results both depict a resonance at a wavelength of 2.7μm, the response of the fabricated metamaterial is not quite as sharp as the simulations. However, the given meta-atom offers fruitful results. A combination of this notch filter with other similarly-designed but differently-sized notch filters would allow a multi-resonant notch filter metamaterial to exist.

Finally, a computational analysis is described in detail to answer the following question: by placing a metamaterial notch filter on top of a Bragg grating, is it possible to reduce the number of layers that make up the Bragg filter, i.e. can the metamaterial act as a replacement for a number of layers within the Bragg filter? The mathematics and computational set-up of the problem are depicted, with the role that the number of layers plays being shown. The notch filter from the previous discussion is then incorporated into the set-up. The results of this endeavor, however, are still ongoing.

7.2 Future Work

Metamaterials have shown their potential to have applications in numerous fields. Advancing the collective knowledge of these nanostructures, therefore, can have a dramatic impact on the shape of future technology. The computational, theoretical, and experimental procedures discussed throughout this thesis not only provide new insights into the underlying physics, but offer a springboard from which further as-yet-unseen physical phenomena can be investigated, as shall now be outlined.

Firstly, it would be of great interest to see just how far the bulk contribution of centrosymmetric all-dielectric meta-atoms can be pushed. Would it be possible for the bulk contribution to outweigh the surface contribution, and what optical consequences could this have? The meta-atom provided in this thesis lays out in detail the starting point from where this investigation could begin.

Achieving experimental verification of a nonlinear toroidal dipole would be the first of its kind. As this thesis depicts an all-dielectric meta-atom that is manufacturable along with the wavelength of maximal nonlinear toroidal excitation, achieving this is not an unrealistic possibility. The set-up of this meta-atom encourages a few more prospects

for the investigation of new physics. Firstly, if the two nonlinear toroidal loops that are generated could cancel with one another, this may lead to a nonlinear anapole moment. Secondly, an exciting prospect would be to see if toroidal dipoles can be excited at the *third* harmonic.

Incorporating all of the fabrication goals into one fully-functioning meta-atom would have enormous applications for laser protection. By having a multi-resonant meta-atom, where each constituent acts as a notch filter for a small group of wavelengths, a multi-notch filter could be created for any wavelengths by tuning the scale and pattern of the constituents. Furthermore, the multi-notch filter could be modified to become a wide band-pass filter by having the individual notches effectively overlap. Naturally, a more robust metamaterial-Bragg filter composite could prove to reduce costs on fabricating an effective transmission filter through radically altering the number of layers required. The details of how this could be achieved are delineated in the next section.

7.2.1 Bragg Gratings

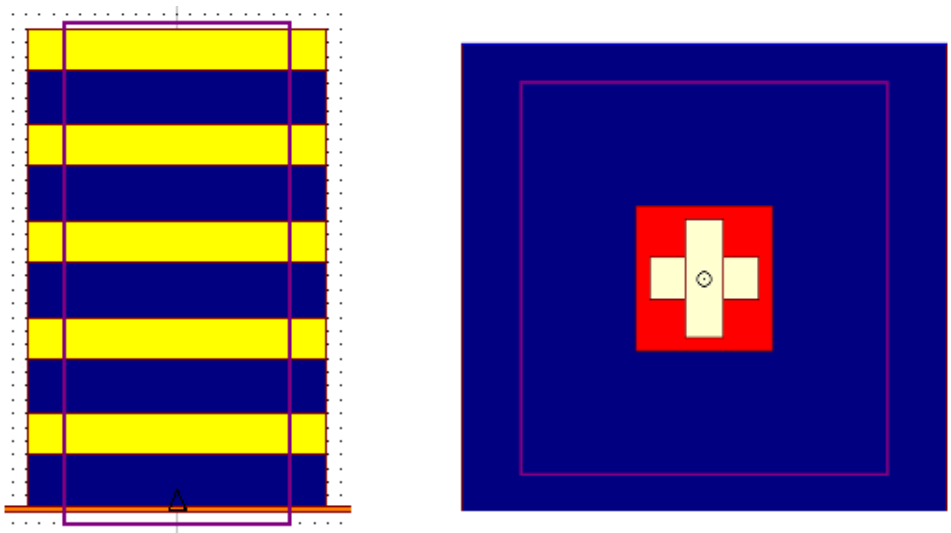

Figure 7.1: The metamaterial is now placed on the Bragg grating. Left - a view of the xz-plane. Right - a view of the xy-plane.

An interesting side project was the idea of seeing what would happen when a metamaterial transmission filter was placed on top of a Bragg filter, which is a combination of alternating layers that enables certain modes of light to cancel with one another. The more layers that are included, the more the Bragg filter acts as a complete transmission filter. The question that arises when placing a metamaterial on top of this Bragg filter is the following: how many Bragg layers can be removed, i.e. that are superfluous, due to the presence of the metamaterial?

To explore this problem, a Python script was written that solved the Chebyshev polynomials and hence the characteristic matrix equation (Equation 2.56). As we saw, this allows the reflection and transmission coefficients to be computed. The results of a pure Bragg grating are shown in Figure 3.16. The orange, green, and blue curves correspond to 3, 5, and 7 periods of the two materials, respectively, i.e. 6, 10, and 14 individual layers, respectively.

Rather than inputting a wave with uniform power across all wavelengths, a modification was made that enables the metamaterial to be simulated: a reverse Gaussian signal is given as the input. The Gaussian signal is dependent upon three parameters:

$$G(a, b, c) = 1 - ae^{\frac{-(x-b)^2}{2c^2}} \tag{7.1}$$

Hence, by choosing the parameters a,b,c correctly, we can engineer a Gaussian that resembles the transmission signal emitted from a metamaterial notch filter. For the following results, the two alternating layers, l_1 and l_2, correspond to Silicon Dioxide (SiO_2) and Hafnium Dioxide (HfO_2), with the heights of each layer being 400nm and 300nm respectively. The refractive indices are plotted for both of these materials across the wavelength range of interest in Figure 3.17.

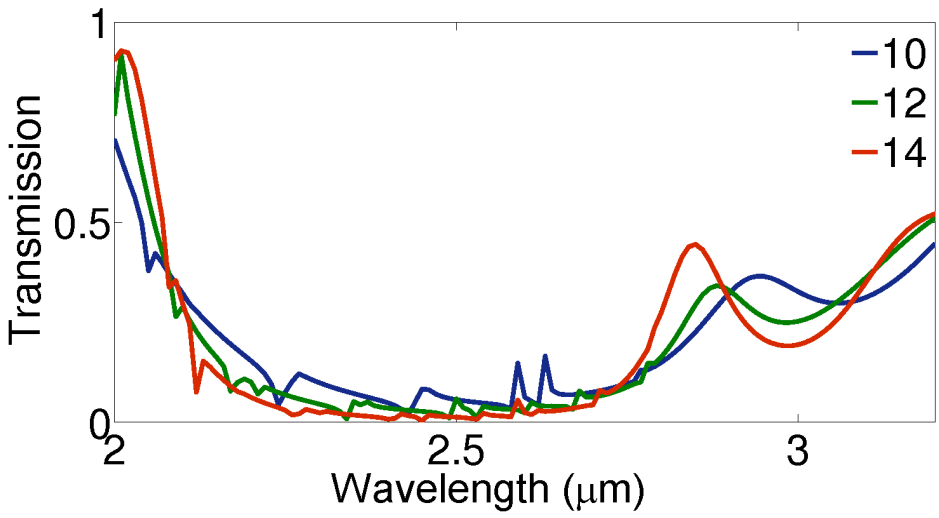

Figure 7.2: The results of the metamaterial-Bragg composite shown in Figure 7.1. 10, 12, and 14 layers are calculated. The notch-like qualities are not exactly present; an additional resonance at 2.7μm is seen that appears to 'throw-off' the full notch effect.

Figure 3.18 shows the culmination of the discussion so far. In the top panel, the blue curve shows the reverse Gaussian signal that is input into the Chebyshev equations. It is clearly centered at a wavelength of 2.6μm with a high quality factor, resembling the transmission spectra of the metamaterial filter. The orange curve shows the Bragg filter

consisting of 10 layers 'in isolation', i.e. the results of purely the Bragg filter with no metamaterial or Gaussian signal involved. A deep transmission can be seen owing to a number of modes of the light that are reflected or absorbed due to the contrast of the refractive indices of the layers. The green curve take the Bragg filter and applies the Gaussian as an input. It is clear that adding this Gaussian, i.e. fixing a metamaterial on top of this Bragg filter, can increase the strength of the resonance, making it more notch-like than the filter alone.

To highlight the role of the number of layers, the lower part of Figure 3.18 shows three curves, each one corresponding to a different number of layers within the Bragg composite. It is clear that as the number of layers increases, the Bragg filter acts increasingly as a notch filter.

These simulations were further corroborated by implementing RSoft's DiffractMOD. Figure 3.19 shows the effect of altering the number of layers in the simulations. Again, a sharper and deeper resonance is observed when the number of layers is increased. The metamaterial was subsequently fitted onto the top layer of SiO_2, as in Figure 7.1. The inclusion of the metamaterial gives the results in Figure 7.2 for 10, 12, and 14 layers. This structure currently does not give the full filter-like results that we expect to see. Given more time, this metamaterial-Bragg composite would be more rigorously examined.

To sum, the investigations described throughout this thesis have offered insights to further the collective knowledge of metamaterial physics. The rapid pace of this field combined with its seemingly limitless applications makes this an exceptionally exciting and revolutionary field to be a part of.

Appendices

Appendix A

Multipole Origins

Here, the origins of the multipole expansion is shown mathematically, as a complement to the analysis of Maxwell's equations in Chapter 2. It was seen that the sources of electromagnetic radiation are the oscillating charge and current distributions. An important parameter characterizing electromagnetic fields is the vector potential, $\mathbf{A}$:

$$\mathbf{A}(\mathbf{x}) = \frac{\mu_0}{4\pi} \int \mathbf{J}(\mathbf{x}') \frac{e^{i\mathbf{k}|\mathbf{x}-\mathbf{x}'|}}{|\mathbf{x}-\mathbf{x}'|} d^3\mathbf{x}' \tag{A.1}$$

This is the vector potential at x due to current density distributions at x'. The source electric and magnetic fields can be equivalently written in terms of this potential. Explicitly:

$$\mathbf{H} = \frac{1}{\mu_0} \nabla \times \mathbf{A} \qquad\qquad \mathbf{E} = \frac{i}{\mathbf{k}} \sqrt{\frac{\mu_0}{\epsilon_0}} \nabla \times \mathbf{H} \tag{A.2a}$$

The basis of the multipole expansion comes from the consideration of the denominator within the integral of equation *A.1*. It can be shown mathematically that:

$$\frac{1}{|\mathbf{x}-\mathbf{x}'|} = 4\pi \sum_{l=0}^{\infty} \sum_{m=-l}^{l} \frac{1}{2l+1} \frac{r_<^l}{r_>^{l+1}} Y_{lm}^*(\theta', \phi') Y_{lm}(\theta, \phi) \tag{A.3}$$

Where $r_<$ ($r_>$) is the smaller (larger) of $|\mathbf{x}|$ and $|\mathbf{x}'|$. Hence, the vector potential - and consequently the electromagnetic source field - is an infinite sum which gives rise to the multipole family. Before the multipoles are analysed, a brief inspection of the Y_{lm} terms must be undertaken.

A.0.2 Spherical Harmonics

The spherical harmonics arise from the ansatz to the Laplace equation in spherical coordinates:

$$\frac{1}{r}\frac{\partial^2}{\partial r^2}(r\Phi) + \frac{1}{r^2\sin\theta}\frac{\partial}{\partial\theta}(\sin\theta\frac{\partial\Phi}{\partial\theta}) + \frac{1}{r^2\sin^2\theta}\frac{\partial^2\Phi}{\partial\phi^2} = 0 \tag{A.4}$$

By considering the angular factors of this equation, it is possible to construct a complete set of orthogonal functions, $Y_{lm}(\theta,\phi)$ known as the spherical harmonics. Explicitly:

$$Y_{lm}(\theta,\phi) = \sqrt{\frac{2l+1}{4\pi}\frac{(l-m)!}{(l+m)!}}P_l^m(\cos\theta)e^{im\phi} \tag{A.5}$$

P_l refer to the Legendre polynomials, succinctly expressed by Rodrigues' formula:

$$P_l(x) = \frac{1}{2^l l!}\frac{d^l}{dx^l}(x^2-1)^l \tag{A.6}$$

Where x=cos θ.

Equation *A.6* contains a modified form of the Legendre polynomials, $P_l^m(\cos\theta)$. This notation, combined with Rodrigues' formula, explicitly denotes:

$$P_l^m(x) = \frac{(-1)^m}{2^l l!}(1-x^2)^{m/2}\frac{d^{l+m}}{dx^{l+m}}(x^2-1)^l \tag{A.7}$$

A.0.3 Electromagnetic Multipoles

The potential of a system is dependent upon the aforementioned polynomials:

$$\Phi(\mathbf{x}) = \frac{1}{\epsilon_0}\sum_{l,m}\frac{1}{2l+1}[\int Y_{lm}^*(\theta',\phi')r'^l\rho(\mathbf{x}')]\frac{Y_{lm}(\theta,\phi)}{r^{l+1}} \tag{A.8}$$

The integral in the square brackets in the above equation are referred to as the multipole moments. It is the expansion of this series that gives rise to the phenomena that was particularly prevalent in Chapters 4 and 5.

This section is intended to show that at the heart of all electromagnetic sources, there is an infinite series consisting of terms of varying significance. It is these terms which are responsible for the characteristic behaviours of each system. As was seen in Chapter 4, only several terms of the series are usually analysed in most electromagnetic models, as the higher-order terms are negligible when considering observable phenomena. How this series manifests itself physically is also detailed in Chapter 4.

Appendix B

Derivation of the Toroidal Dipole Power

For a rigorous analysis of the toroidal dipole power, most prevalently discussed in Chapter 5, it was helpful to have this quantity in S.I. units for a direct comparison with the other multipoles given in [1]. This derivation is the subject of this appendix. Firstly, the method of comparing the power of the electric dipole between CGS and S.I units is worked through for brevity.

Jackson [1] states:

$$\mathbf{E}_p = \frac{1}{4\pi\epsilon_0}[k^2(\mathbf{n}\times\mathbf{p})\times\mathbf{n}\frac{e^{ikr}}{r} + [3\mathbf{n}(\mathbf{n}\cdot\mathbf{p}) - \mathbf{p}](\frac{1}{r^3} - \frac{ik}{r^2})e^{ikr}] \tag{B.1}$$

where $\mathbf{E}_p$ is the electric field associated with the electric dipole in S.I. units. Fedotov [2] gives the associated electric dipole field as:

$$\mathbf{E}_p = [\frac{\mathbf{r}\cdot\mathbf{p}}{c^2r^2}F(k,r)\mathbf{r} - \frac{G(k,r)}{c^2}\mathbf{p}]\frac{e^{ikr}}{r} \tag{B.2}$$

where:

$$\begin{aligned} F(k,r) &= c^2(-k^2 + \frac{i3k}{r} + \frac{3}{r^2}) \\ G(k,r) &= c^2(-k^2 + \frac{ik}{r} + \frac{1}{r^2}) \end{aligned} \tag{B.3}$$

There are two small tools that enable us to complete the comparison:

$$\begin{aligned} &\mathbf{r} = r\mathbf{n} \\ &\mathbf{n}\times\mathbf{p}\times\mathbf{n} = \mathbf{p} - \mathbf{n}(\mathbf{p}\cdot\mathbf{n}) \end{aligned} \tag{B.4}$$

By substituting the first part of Equation B.3 into Equation B.2, we obtain:

$$\mathbf{E}_p = [(\mathbf{n}\cdot\mathbf{p})\mathbf{n}(-k^2) + \frac{(\mathbf{n}\cdot\mathbf{p})\mathbf{n}i3k}{r} + \frac{3(\mathbf{n}\cdot\mathbf{p})\mathbf{n}}{r^2} + \mathbf{p}k^2 - \frac{\mathbf{p}ik}{r} - \frac{\mathbf{p}}{r^2}]\frac{e^{-ikr}}{r} \tag{B.5}$$

Now implementing the second part:

$$\mathbf{E}_p = [k^2(\mathbf{n}\times\mathbf{p})\times\mathbf{n} + [3\mathbf{n}(\mathbf{n}\cdot\mathbf{p})](\frac{ik}{r} + \frac{1}{r^2})]\frac{e^{ikr}}{r} \tag{B.6}$$

Two transformations bring us from the above CGS-units equation to that in Jackson's renowned work: firstly, Jackson's system here has assumed the notation '-i' instead of 'i'. A simple switch does not change the physics. Secondly, by multiplying the CGS-unit system by $1/4\pi\epsilon_0$ brings the two systems to agreement.

We can now proceed to the toroidal dipole, where we use Fedotov's formula:

$$\mathbf{E}_T = [\frac{ikG}{c^2}\mathbf{T} - \frac{ik(\mathbf{r}\cdot\mathbf{T})F\mathbf{r}}{c^2r^2}]\frac{e^{-ikr}}{r} \tag{B.7}$$

Where F and G are as above. Proceeding with the relations in Equation B.2, we obtain:

$$\mathbf{E}_T = [ik^3(\mathbf{n}\cdot\mathbf{T})\mathbf{n} - ik^3\mathbf{T} + \frac{3k^2(\mathbf{n}\cdot\mathbf{T})\mathbf{n}}{r} - \frac{k^2}{r}\mathbf{T} - \frac{3ik}{r^2}(\mathbf{n}\cdot\mathbf{T})\mathbf{n} + \frac{ik}{r^2}\mathbf{T}]\frac{e^{-ikr}}{r} \tag{B.8}$$

Rearranging and applying the transformations in Equation B.4:

$$\mathbf{E}_T = \frac{1}{4\pi\epsilon_0}[-ik^3(\mathbf{n}\times\mathbf{T})\times\mathbf{n}\frac{e^{ikr}}{r} + [3(\mathbf{n}\cdot\mathbf{T})\mathbf{n} - \mathbf{T}](\frac{k^2}{r^2} + \frac{ik}{r^3})e^{ikr}] \tag{B.9}$$

In the far-field, this equation reduces to:

$$\mathbf{E}_T = \frac{-ik^3}{4\pi\epsilon_0}(\mathbf{n}\times\mathbf{T})\times\mathbf{n}\frac{e^{ikr}}{r} \tag{B.10}$$

Hence, we are now in a position to write the full equation for the power emitted by an array of periodic electric dipoles, magnetic dipoles, electric quadrupoles and toroidal dipoles together with their interferences:

$$I_\omega = \frac{Z_0\omega^2}{8A_0^2\cos^2\theta_i}|(\mathbf{n}_0\times\mathbf{p}_0)\times\mathbf{n} - \mathbf{n}\times\mathbf{m}_0 - \frac{ik}{6}(\mathbf{n}\times\mathbf{Q}_0)\mathbf{n} - ik(\mathbf{n}\times\mathbf{T}_0)\times\mathbf{n}|^2 \tag{B.11}$$

where Z_0 is the impedance of free space, θ_i is the angle of the incident exciting light wave, A_0 is the area of the unit cell. It is clear that upon the condition $\mathbf{p}$=-$ik\mathbf{T}$, the electric and toroidal fields cancel with one another.

Bibliography

[1] J. D. Jackson, *Classical Electrodynamics* (John Wiley and Sons, 1962).

[2] V. A. Fedotov, A. V. Rogacheva, V. Savinov, D. P. Tsai, and N. I. Zheludev, "Resonant transparency and non-trivial non-radiating excitations in toroidal metamaterials", Sci. Rep. **3**, 2967 (2013). Supporting Information.